Computational Methods for Micromechanics Characterisation: Application to and Experimental Investigation of Metal Additive Manufacturing and Heat Treatment Processes

Yuhui Tu

Supervisors: Dr. Noel Harrison and Prof. Sean Leen

A thesis submitted to the National University of Ireland as fulfilment of the requirements for the Degree of Doctor of Philosophy

Mechanical Engineering, National University of Ireland, Galway.

July 2022

Contents

Abstract

Powder bed fusion (PBF) is an additive manufacturing process in which finely focused thermal energy is used to selectively melt target regions within thin layers of metal powders. Due to the complex thermal conditions associated with the rapidly moving micro-melt pool and the layer-by-layer deposition of material, the resulting printed product in, for example, CoCr, Ti-6Al-4V, and 17-4PH stainless steel have unique and anisotropic microstructure, compared to traditional manufacturing processes. Another significant process within industrial PBF manufacturing is post-built heat treatment (HT). This step modifies the microstructure (as well as relieves residual stress), adding complexity to the processing parameters design. It is thus necessary to develop a further understanding of the process-structure (HT) and structure-property (PBF) relationships in PBF manufacturing.

Multi-physics computational models are developed, based on experimental characterisation, to investigate the process-structure-property relationship in PBF. Particular attention is paid to model construction and maintaining a faithful representation of real PBF grains and sub-grain features. Direct microscopy microstructural characterisation is performed using electron backscatter diffraction of as-built and post-heat treatment specimens, where measures of texture and grain morphology are extracted and used to construct Voronoi tessellation-based or real image-based micromechanics models.

Crystal plasticity finite element (CPFE) modelling is a micro-scale computational method to predict mechanical performance based on microstructure and crystallographic properties. CPFE model with physical dislocation mechanisms is employed to quantify the effect of the PBF microstructure variation (grain size, phase, morphology, and crystallographic orientation) on mechanical properties (tensile and fatigue). Phase-field method (PFM) is implemented to investigate the effect of heat treatment on grain growth and is then integrated with CPFE to offer an efficient method for an in-depth

understanding of the relationship between thermo-processing, microstructural evolution and mechanical properties. This thesis also utilizes a large database of input-output samples from CPFE modelling to develop a trained deep neural network (DNN) model which instantly estimates the output (strength prediction) associated with a given input (microstructure) of multi-phase PBF stainless steels.

The EBSD-based method for CPFE model generation is shown to give approximately 10% improved agreement for fatigue life prediction, compared with the more commonly-used Voronoi tessellation method. The effect of PBF inhomogeneity and post-built HT on the structure-property relationship was investigated using a dual-phase strain gradient crystal plasticity model based on physical dislocation mechanisms, based on the as-built and HT microstructure of Ti-6Al-4V, with a notable increase in lath width post HT. The effect of as-built lath width gradient in a single component on bulk stress-strain relationship exists but is minimal (1% variation in yield strength), whereas a greater effect (9% reduction in yield strength) is found in the post-heat treatment specimen. The PFM model is utilized for analysing the grain growth behaviour during the post-built heat treatment process through the simulation of grain boundary migration. It predicts five times grain growth in lath area from 0.59 to 3.0 um^2, after 100 minutes of annealing at 1127 K. The evolved lath prediction reaches close agreement compared to the EBSD measurement. Finally, the CPFE-based deep learning (DL) model exhibits high accuracy for the structure-property relationship as a surrogate predicting tool compared to CPFE while significantly reducing the computational cost to a few seconds.

Acknowledgements

First, I want to thank my supervisors Dr. Noel Harrison and Prof. Sean Leen for their constant helpful supervision over the last four years. Their broad knowledge and kindness help me successfully obtain my PhD degree while living an enjoyable life in Galway. They also never hesitate to offer me guidance and assistance in ensuring the high quality of my presented work. The comments and feedback alone are usually half the word count of my draft! from which I benefited and progressed considerably as a non-native speaker. I am also impressed by their easy-going style as well as the free academic atmosphere. I have been allowed and encouraged to develop new research directions based on my personal background and interest. They supported me when I was considering learning and employing the phase-field method and arranged the relative supports. Later, they supported me again to work with Singapore and USA researchers for the deep learning work. This thesis could never include the abundant interdisciplinary content it now has, without the unconditional support from my supervisors. As an international student, I always receive kind consideration from my supervisors, for example, regarding accommodation and visa issues, my physical health and mental condition especially when the Covid-19 pandemic occurred. Even still, they are providing support and advice for my future career development.

I also want to acknowledge the support from my sponsor, I-Form, Science Foundation Ireland, for providing funding for this research project, under Grant number 16/RC/3872. I acknowledge HEA and The National University of Ireland Galway / University of Galway for funding the last 7 months of the project, and the Irish Centre for High-End Computing (ICHEC) for the provision of computational facilities and support.

Then the author would like to acknowledge Dr. P. J. Ashton, Dr. Yaoyi Geng and Dr. Xinyu Yang for the helpful discussions. It is a pleasure to have you guys around, in the lab, the office, or the pub.

Finally, I want to thank my parents. Actually, my mom insisted and strongly recommended me to start this PhD study, which turned out to be a superb decision. My

father, as an experienced automobile engineer, has been giving useful and professional suggestions, both on engineering knowledge and more importantly, life-coaching. I enjoy the unique relationship with my parents, like the closest peers, with whom I never hesitate to share my real feelings regardless of pains or joys.

List of Publications

The following two peer-reviewed journal papers were published from the research in this thesis.

Yuhui Tu, Sean B Leen, Noel M Harrison. *A high-fidelity crystal-plasticity finite element methodology for low-cycle fatigue using automatic electron backscatter diffraction scan conversion: Application to hot-rolled cobalt–chromium alloy*. Proceedings of the Institution of Mechanical Engineers, Part L: Journal of Materials: Design and Applications. 2021;235(8):1901-1924. doi:10.1177/14644207211010836

Yuhui Tu, Zhongzhou Liu, Luiz Carneiro, Caitriona M. Ryan, Andrew C. Parnell, Seán B Leen, Noel M Harrison. *Towards an instant structure-property prediction quality control tool for additive manufactured steel using a crystal plasticity trained deep learning surrogate*, Materials & Design, 2022; 213, doi:10.1016/j.matdes.2021.110345

Acronyms List

2D	Two-dimensional
3D	Three-dimensional
BCC	Body centre cubic
CoCr	Cobalt Chromium
CPFE	Crystal plasticity finite element
EBSD	Electron backscatter diffraction
EDX	Energy-dispersive X-ray spectroscopy
FCC	Face centre cubic
FCI	Fatigue crack initiation
FIB	Focused ion beam
FIP	Fatigue indicator parameter
GND	Geometrically necessary dislocation
HCP	Hexagonal close packed
IPF	Inverse Pole Figure
LCF	Low-cycle fatigue
PBCs	Periodic boundary conditions
SEM	Scanning electron microscope
UMAT	User material subroutine
UEL	User element subroutine
SSD	Statistically stored dislocations
VT	Voronoi tessellation
AM	Additive manufacturing
PBF	Powder bed fusion
DL	Deep learning
CNN	Convolutional neural network
DNN	Deep neural network
RMSE	Root mean squared error
MAE	Mean absolute error
YS	Yield stress
SS	Stainless steel

Nomenclature List

Parameter	Unit	Description
$\boldsymbol{X}$		reference global vector
$\boldsymbol{x}$		current configuration vector
$\boldsymbol{u}$		displacement vector
$\boldsymbol{F}$		global deformation gradient
$\boldsymbol{F_e}$		elastic deformation gradient
$\boldsymbol{F_p}$		plastic deformation gradient
$\boldsymbol{L_p}$		plastic velocity gradient tensor
$\dot{\gamma}^{\alpha}$		rate of slip along the slip system α
$\dot{\gamma}^{0}$	[s^{-1}]	reference strain rate
α		current slip system
$\boldsymbol{s}^{\alpha}$		unit vectors along slip direction
$\boldsymbol{m}^{\alpha}$		unit vectors normal to slip plane
$\dot{a}$	[s^{-1}]	reference strain rate component
n		strain rate sensitivity
g_0	[MPa]	initial critical resolved shear stress
g_∞	[MPa]	stage I stress
$h^{\alpha\alpha}$	[MPa]	self-hardening moduli
$h^{\alpha\beta}$	[MPa]	latent-hardening moduli
x^{α}	[MPa]	kinematic hardening back stress
$C_i\ D_i$	[GPa]	parameters which define the back-stress hardening
b_α	[m]	Burgers vector
$\rho_{SSD}^{m,\alpha}$	[m^{-2}]	mobile SSD density
$\rho_{SSD,i}$	[m^{-2}]	immobile SSD density
${\rho_{GND}}^{\alpha}$	[m^{-2}]	GND density
ν	[s^{-1}]	frequency for mobile dislocations
ΔH	[J]	Helmholtz free energy
T	[K]	Temperature

k	[JK^{-1}]	Boltzmann constant
p		accumulated effective crystal slip
W	[MJ/m^{-3}]	accumulated strain energy dissipation
N_i		fatigue crack initiation life

1 Introduction

1.1 General

Global industries such as medical devices, automotive, aerospace and the military have led the adoption of metal additive manufacturing (AM) as a process of choice for next-generation manufacturing. AM, also referred to as digital fabrication, rapid prototyping, or 3D printing, is a computer-aided design (CAD) assisted manufacturing approach in a layer-by-layer manner. AM techniques, according to the ISO/ASTM S2900:2021 terminology standard [1], are primarily classified into seven categories: (1) powder bed fusion (PBF), (2) directed energy deposition, (3) binder jetting, (4) material jetting, (5) vat polymerization, (6) material extrusion and (7) sheet lamination. A graphical summary of these seven processes is shown in Figure 1-1. This thesis focuses on PBF AM using metal alloy powder materials.

Figure 1-2 shows a general PBF workflow and the printing system components. A PBF printer firstly deposits the powder layers on a (often preheated) substrate using a blade or roller layering apparatus. Then a laser or electron beam heats and melts the powder layer selectively according to the sliced CAD profile and process controlling system. Subsequently, the build plate moves downwards to allow the manufacturing of the next layer [2]. Finally, post-built processing including surface polishing, heat treatment, and machining [3, 4] are carried out on the fabricated part to improve the mechanical performance.

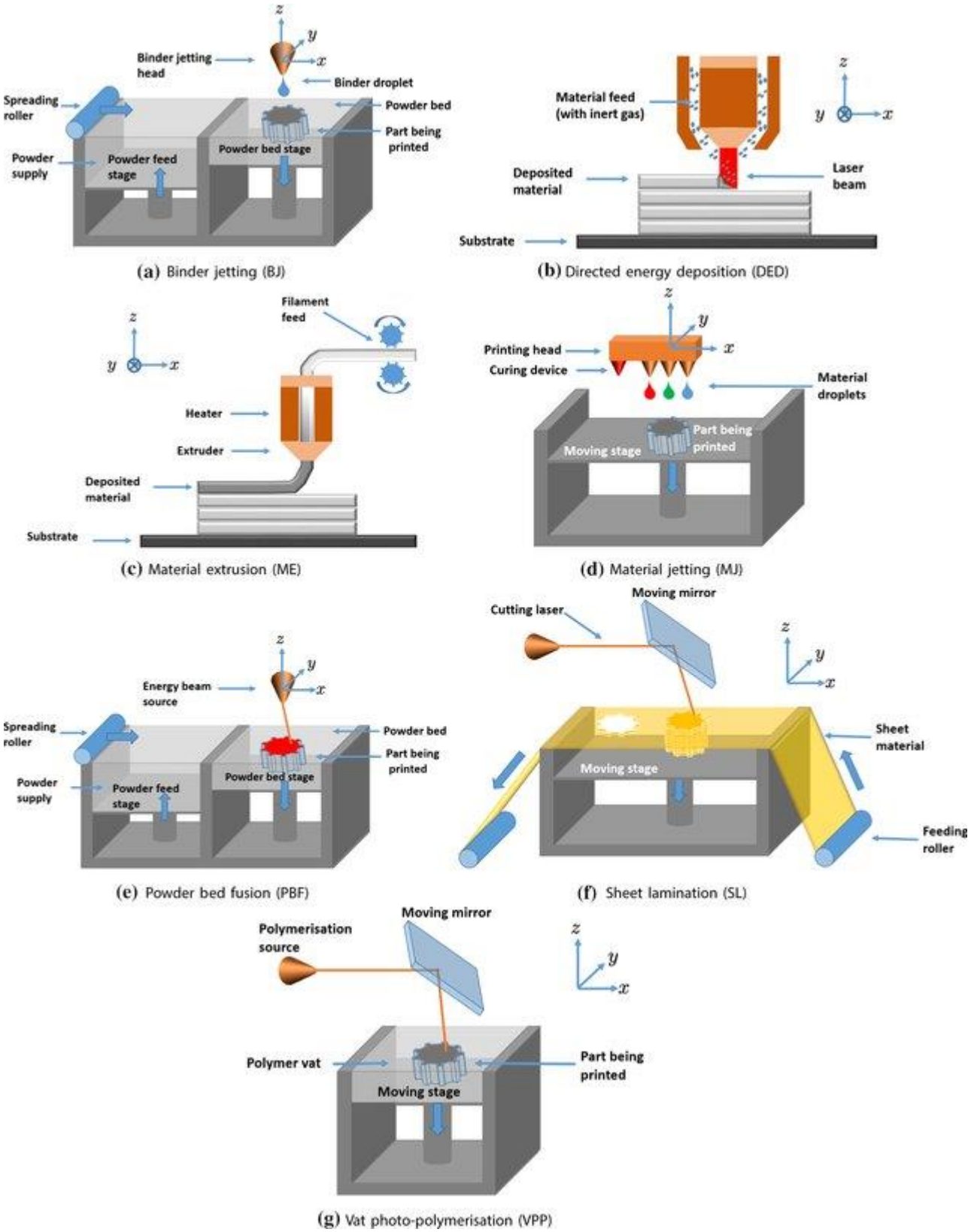

Figure 1-1. Classification of the seven different AM process, image obtained from [5].

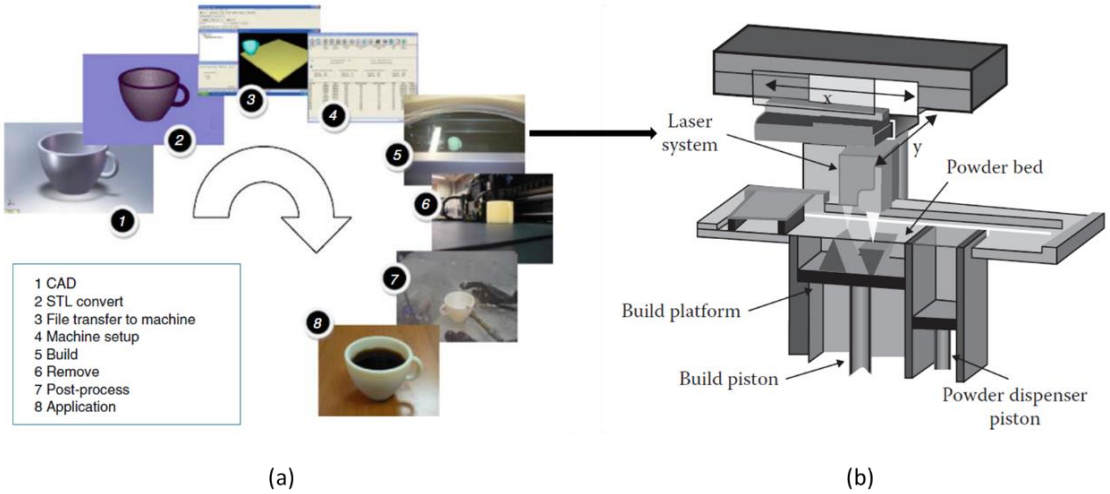

Figure 1-2. (a) Generic steps of AM fabrication, from CAD part design to end-use product application, not including heat treatment, image obtained from [6].

PBF is the most promising AM technique for manufacturing small and complex metallic products. Within the PBF category, there are two main subcategories, differentiated by the form of energy beam in use- laser beam (PBF-LB), or electron beam (PBF-EB). PBF-EB (suitable only for metal printing) built parts exhibit lower oxidation in because PBF-EB takes place under a vacuum environment compared to the inert gas environment used for PBF-LB [7]. PBF-EB parts also exhibit lower residual stresses post-built due to the higher chamber and pre-heat temperatures, compared to PBF-LB [8]. However, PBF-EB is not as popular as PBF-LB, due to the higher printer cost, and the reduced resolution (minimum feature size of 100 μm compared to 40 μm in PBF-LB) [9]. This thesis focuses on PBF-LB technology only, and the following PBF terms, if not specially specified, all refer to the PBF-LB fabrication type.

Current PBF research focuses on improving our understanding and control of the process for various metals or alloy products. PBF has been widely used to fabricate metal products including titanium alloy, cobalt chromium alloy, aluminium alloy, nickel-based superalloy, and a range of stainless steels [10]. This will enable the industrial manufacture of next-generation components with complex structures or with added functionality, that are not suitable for conventional fabrication techniques (casting, forging, machining). The main benefit of PBF includes high flexibility in structure design and the unique capability

of building complex lattices or detailed geometries for engineered materials [11]. PBF can achieve accurate 3D structure especially complex net-shape shapes, which is impossible or troublesome through conventional manufacturing approaches such as subtractive machining or casting etc [12]. PBF has enabled the development of new metal products and a new era of innovation, such as in orthopaedic design [13, 14]. PBF has also positively impacted industrial tooling availability and design, in particular for low-volume production, prototyping or rapid customised fabrication, reducing the dependency on costly traditional machined moulds and dies [6]. Material waste and energy consumption are the two issues when estimating environmental influence. PBF is generally assumed to be more environmentally sustainable in particular for manufacturing complete parts [15].

Recent years have witnessed explosive growth in the AM business due to the expiration of key hardware patents, recognition of the new product design freedoms, and the emergency of smart design tools, particularly in weight-sensitive applications such as topology optimization. The aerospace magnate Boeing company has adopted AM to produce over 200 different parts for 10 aircraft platforms [16]. In 2017, Boeing adopted AM to produce four titanium-alloy based parts for its model 787, and expect future production to extend AM to more than 1000 parts, with an estimated saving of $3 million per airplane [17]. Another aircraft company Airbus replaced the machined aluminium alloy part with AM titanium part which brought a 30% weight reduction [18]. NASA engineers are also using PBF processes to fabricate rocket injector part for the next-generation space launch engine, which has reduced the required injector part numbers from 155 to 2 only, together with the decreased production cycle from months to weeks [19].

In order to further enable industry's ability to capitalise on the advantages of PBF and move to large-scale production capability with industry-standard quality, the following research challenges and knowledge gaps need to be addressed [11, 20]:

1. The complex combination of process parameters, build conditions and post-built heat treatment leads to various possibilities of thermal history, leading to varying microstructure and ultimately inconsistent product mechanical properties. This

leads to difficulties in PBF parameter optimization and stable product quality control.

2. Difficulty in characterizing the inevitable inhomogeneous PBF product performance. Directional microstructure induced from layer-by-layer built features and the associated anisotropic mechanical properties, which might be either beneficial or undesired, cannot be eliminated.

3. Lack of an industry-ready predictive model for PBF quality prediction. Current quality monitoring sensors in PBF hardware track secondary parameters such as temperature history, and lack the responsive capability to determine the consequence of temperature variations on material properties. Rapid or in-situ quality predicting tools based on observed microstructure are urgently required.

In recent years, major advances in microstructural imaging, including electron backscatter diffraction (EBSD) and synchrotron X-ray diffraction tomography technique, have enabled accurate visual characterisation of grain structures and their orientation [21, 22]. In parallel, advances in computational modelling methodologies, including crystal plasticity finite element (CPFE) modelling, deep neural network (DNN) modelling, and phase-field modelling (PFM), have permitted advanced microstructural mechanical simulation and prediction [23, 24]. Prediction of microstructure and associated mechanical properties of AM materials is key to addressing current industry concerns with PBF.

1.2 The Significance of Micromechanics

It is well understood that the mechanical performance of metal in-service is largely dependent on its microstructural features such as phase composition, crystallographic orientations, grain morphology as well as grain size distribution [25]. The mechanical performance can be more explicitly quantified as the yield strength, ultimate strength, fatigue toughness, and hardness etc. In general, the strength of a material is inevitably linked to the failure behaviour. Micromechanics is the study of these interrelationships and is a branch of mechanics of materials, that can be dated back to Eshelby's study [26].

The benefit of a micromechanics study is to understand the macroscopic mechanical behaviour of polycrystalline materials or composites based on the characterisation of their microstructure, imperfections and inhomogeneities, by implementing the theories of elasticity and plasticity. Micromechanics includes the definition of micro-scale structures and the numerical analysis to predict a range of macroscopic mechanical behaviour such as elasticity, plasticity, fracture, and fatigue [27].

Figure 1-3 illustrates the interdependency of the process-structure-property relationship. Process: PBF printer parameter and post-built heat treatment; Structure: microstructural grain morphology, grain size, phase, crystallographic orientations, and grain boundary; Property: mechanical strength, fatigue and fracture. The critical significance of characterisation of the interrelationships between the manufacturing process, microstructure, material properties and mechanical performance (structural integrity) [28, 29] has been highlighted by a recent aeroengine fan hub failure investigation [30, 31]. This report provides detailed proof of the serious risks associated with not considering these relationships, particularly for fatigue crack initiation in real applications, in this case, an aeroengine fan hub failure of Ti-6Al-4V alloy, not previously considered susceptible to facet fatigue.

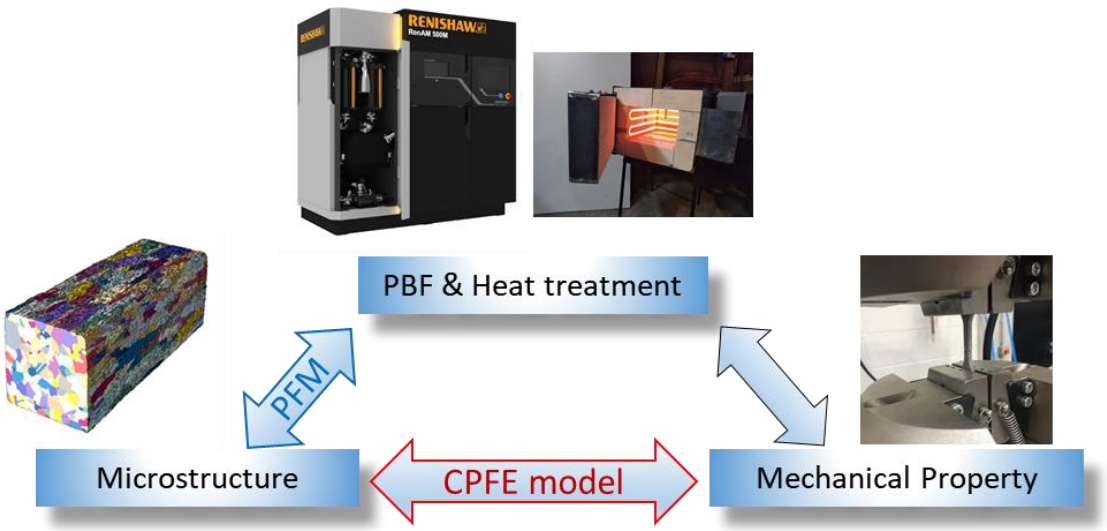

Figure 1-3. The process-structure-property interdependency in PBF study.

1.3 Micromechanics in Additive Manufacturing

The structure-property relationship in PBF fabricated metals has become a significant area of research and is considered by some to be the main bottleneck for PBF exploitation in industry [32]. The complex layer-by-layer solidification process and intricate thermal history of metal PBF parts present complexities in predicting material microstructures in printed parts. Grain size, texture and grain morphology in metal AM structures are believed to be highly dependent on temperature profiles induced by AM processing variables. The variety of PBF process parameters, material effects and part size design all contribute to uncertainty when determining the resulting mechanical behaviour. The inhomogeneity and anisotropic feature of PBF product also require multi-directional material characterisation, for e.g., microstructural sectioning and mechanical tests along both parallel and perpendicular (compared to build direction) surfaces. The mechanical properties that are commonly shown to be different include but are not limited to tensile behaviour, creep and fatigue [33].

Titanium alloys can be classified into five groups according to the $\alpha - \beta$ phase compositions [34]. Ti-6Al-4V has received the most popularity in PBF industry considering its high strength-to-weight ratio. The commonly used PBF-LB precipitate hardening steels include 17-4PH SS, 15-5PH SS, and 440 SS and have good corrosion resistance due to higher Cr content compared to other austenite materials. Microstructure features such as morphology and crystallographic orientations, raise new requirement for the micromechanics modelling work, such as high-fidelity microstructural representation tool, as well as implementing anisotropic tensors when calculating the deformation. This is because PBF-generated microstructures are usually more complex than conventionally manufactured counterparts due to the layer-by-layer and continuous-spot mode of the melting and solidification. AM microstructure is largely determined by the laser spot size (usually between 50-100 mm), the spot moving (scan) speed, and the overall power level. The grain morphology resulting from PBF is often observed to have columnar or lamellar grain morphology and the measured grain size is finer than conventional method such as wrought or forging [35]. One example is PBF manufactured Ti-6Al-4V alloys, which display lamellar shape and dual-phase $\alpha + \beta$ morphologies within prior β-grains

compared to equiaxed $\alpha + \beta$ morphologies observed in wrought sample [36]. Another example, the microstructure of PBF as-built austenitic stainless steel such as 17-4PH, has been observed to have columnar grain morphologies with fine grain size with a columnar width of less than 8 μm due to the rapid solidification process compared to an average diameter of 15 μm in wrought samples [25, 37]. Another important difference is the crystallographic orientation distribution, also referred to as texture when groups of grain aggregates tend to elongate along similar direction [38]. In PBF produced alloy, the parent grains tend to elongate along the build direction, leading to textured fibres. These neighbouring parent grains usually have large grain boundary angles. After the cooling process, the smaller transformed grain form within their parent grain, sharing very similar crystallographic orientations.

Micromechanics of PBF metal alloys is a complex matter but is key to improving our understanding and exploitation of PBF. Micromechanics-based modelling tool offers a reliable approach to predict the macroscopic response of new materials while reducing the reliance on experimental testing. Assisted with the experimental method, microstructural-based, especially high fidelity representative numerical simulations [39], are believed to offer reliable PBF process-microstructure- mechanical property linkage. Challenges with real-time quality control and process-structure-property awareness, are also limiting the further uptake of PBF, and next-generation PBF technology development [40]. Such a platform, possibly developed based on big data micromechanical modelling, will enable us to directly investigate the thermal history of metal powders and the process design tool, thus integrating a software interface for data acquisition and micromechanics measurements. The PBF industry can benefit from such algorithms, to optimize, test, and validate a real-time and closed-loop control of PBF processes [41].

1.4 Motivations and Objectives

There is a priority need to establish a robust understanding of the links between as-built PBF microstructure and mechanical properties, and the effect post-built heat treatments may have on this relationship. The objective of the thesis is to advance our understanding

of the process-structure-property relationship for AM metals through microscopy image-based microstructural-sensitive micromechanical modelling and solid-state kinetic microstructural evolution. Note that although the effect of solidification on phase transformation and microstructure, this thesis does not address the solidification process. Among these applications, three popular AM alloys are presented in this thesis as examples, including single phase FCC crystallographic lattice biomedical graded L-605 CoCr, BCC + FCC 17-4PH stainless steel, and HCP + BCC Ti-6Al-4V alloys, thus the introduced methodology can be further extended to any type of alloy database.

To summarise, this PhD thesis aims to:

1. Develop and demonstrate a tool for automatically converting EBSD data into high-fidelity CPFE models, including accurate representation of grain morphology and orientation, for improved mechanical property prediction.

2. Develop physically based strain gradient CPFE to investigate microstructural-sensitive effects including built gradient and heat treatment of PBF Ti-6Al-4V.

3. Introduce a coupled computational framework that integrates solid-state grain growth phase-field modelling (PFM) with CPFE modelling, to investigate the process-structure-property relationships for post-processing heat treatment of AM Ti-6Al-4V alloy.

4. Develop a deep learning model which instantly estimates the output property associated with a given input structure of multi-phase PBF stainless steel.

1.5 Outline of Thesis

Chapter 2 provides the literature review of the key subjects in this thesis. This chapter first starts with the experimental characterisation of the process-structure-property interdependency, by including the effect of printing and post-built treatment process and parameters on the resulting microstructure and mechanical performance. Then the developed computational models applied to such process-structure-property investigation

are introduced and potential linkage between the models is presented. The equations and theory implemented in this thesis for the relative computational modelling, including crystal plasticity modelling, phase-field method, and deep learning, are also detailed.

Chapter 3 details the experimental work used in microstructural characterisation and PBF testing approaches, including (1) PBF part build and post-built heat treatment; (2) microscopy sample preparation, EBSD characterisation, microstructure post-processing and analysis methodology, and micro-CT quality check; (3) tensile and low cyclic fatigue mechanical testing.

Chapter 4 introduces a detailed methodology for automatically converting EBSD data into high-fidelity CPFE models, including an accurate representation of grain morphology and orientation. This EBSD-CPFE methodology is applied in the prediction of grain size effects for cyclic plasticity and fatigue crack initiation in biomedical-grade CoCr alloy for fatigue life prediction, compared with the more commonly used Voronoi tessellation method.

Chapter 5 introduces a physically based CPFE model to characterize the lath size and gradient effects for PBF Ti-6Al-4V. The improved CPFE model implements a length-scale effect for characterizing the size effect without the need to modify the input constitutive parameters. This more advanced CPFE model captures the dependence of the mechanical responses on alpha phase lath size by investigating the geometrically necessary dislocation (GND) density distribution.

Chapter 6 adds in a quantitative PFM to simulate grain growth during post-processing heat treatment such as annealing and hot isostatic pressing, which are necessary to homogenize microstructure and eliminate initial defects. The proposed PFM takes into account both temperature-dependent grain boundary mobility and thermal driving force. The evolved microstructure from the PFM prediction is firstly compared to measurements from EBSD analysis and then imported into a CPFE modelling tool for prediction of the mechanical performance. This work utilizes the EBSD-based model generating tool introduced in Chapter 4, and the size-sensitive strain gradient model developed in Chapter 5.

Chapter 7 introduces an interdisciplinary coupling of the CPFE model with a machine learning approach employed in computer science, to produce an industry-ready strength prediction tool. This work is motivated by the heavy computational cost in CPFE analyses and aims to present a more user-friendly and efficient process-structure-property predicting tool with satisfying predicting accuracy. This work utilizes a large database of input-output samples out of CPFE modelling to produce a trained DNN model which instantly estimates the output property associated with a given input structure of the multiple-phases PBF stainless steels.

Chapter 8 summarizes the conclusions of this PhD project. Discussions on the key findings and relative illustrations are presented. Based on the findings and outcomes of the thesis, potential future works are suggested to further develop the capability of the developed multi-physics modelling framework, for more advanced and practical applications in PBF research and industry.

2 Literature review

2.1 PBF-LB process parameters

The laser beam, along the scanning direction, forms single tracks. The morphology of these tracks is one of the significant features, which can be assessed by the following definitions: (i) good quality and continuous; (ii) transitional tracks; (iii) balling effect [42] (showing particle chains due to non-optimal parameters) and (iv) humping effect [43] (a surface defect observing swelling zone). Other single-track defects also include cracks and droplets. Figure 2-1 shows the typical geometry of the melting pool. The geometry of the track is usually described by its penetration depth, width, height, and contact angle and width of the remelted area.

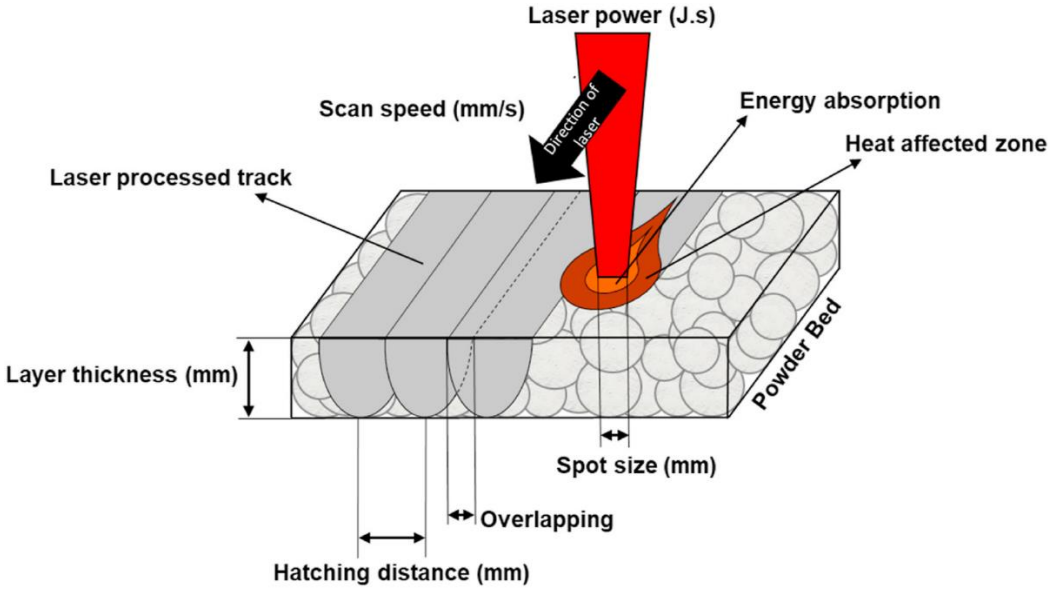

Figure 2-1. Schematic of the cross-section of the sintered PBF track [44].

The geometry of the cross-section (width and depth) of the track depends on the laser power density and irradiation time [45], shown in Figure 2-2. The track geometry is determined by the spot size and layer thickness [46]. The hatch space and the scanning strategy affect the morphology of the PBF layer.

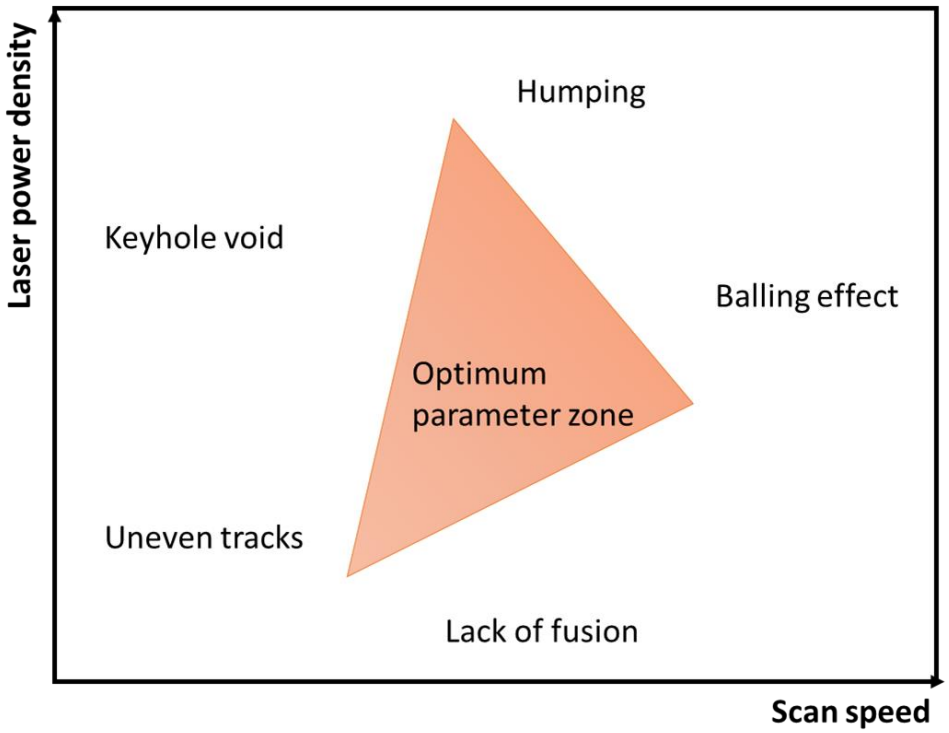

Figure 2-2. Effect of PBF parameters (laser power density and scan speed) on the sintered powder bed track (Adapted from Ref [45]).

Many researchers adopt the idea of "integral" parameter to optimize the PBF process, e.g., the volumetric energy density (VED) [47]:

$$VED = \frac{P}{Vht_l} \tag{2-1}$$

where P is laser power, V is laser scanning speed, h is the hatch spacing distance, and t_l is the layer thickness.

Some also consider laser spot diameter [48] when estimating this VED value. It is not possible to quantify the accurate energy density using the concept of VED. The same integral energy density can be obtained, e.g., by increasing the scanning speed with a thinner layer, but possibly resulting in a different property. Thus, VED is usually used as a metric for comparing PBF processing effects rather than quantification. The direct influence of PBF processing parameters on the product includes: (i) quality such as defects and porosity, and (ii) solidified microstructure (discussed in section 2.3.1). Figure 2-3

shows the relationship between the processing parameters and the defects, for PBF-LB Ti-6Al-4V alloy built with EOS M290[49]. A lack of fusion with irregular voids was observed when the power and scan speed are low. Porosity also increased with combined high laser power and scan speed, due to the beading-up conditions.

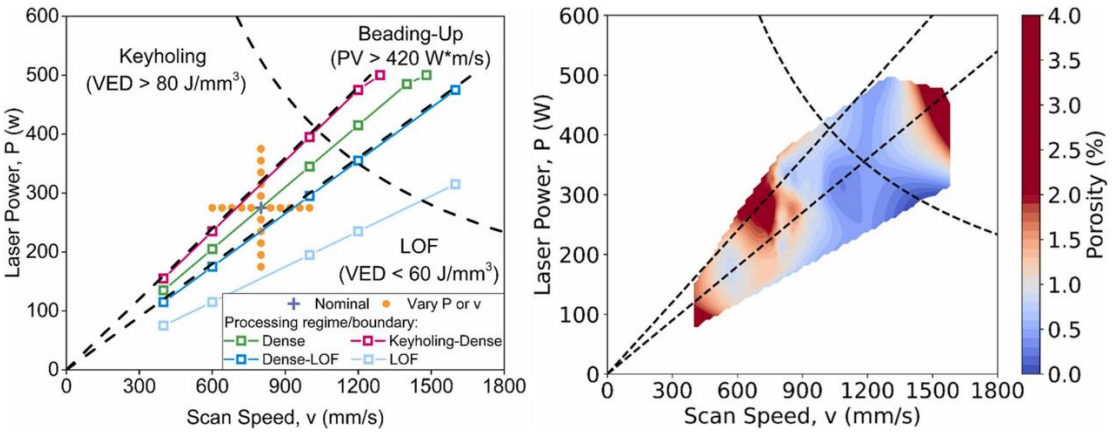

Figure 2-3. PBF processing parameter induced defects and porosity contour map [49].

2.2 Post-built heat treatment

Post-built heat treatments (HT) are important to improve the PBF-LB product properties, compared to the as-built conditions [50]. A HT process is also necessary to minimise the residual stress artefacts from PBF-LB product [51]. Meanwhile, HT homogenises the localized or graded microstructure observed in PBF parts, leading to uniform and isotropic mechanical performance. The suitable HT process adopted for PBF-LB materials includes stress relief annealing, solution annealing [52], aging [53], and hot isostatic pressing (HIP) [54]. HIP is a proven post-processing HT approach for improving the ductility and fatigue performance, by reducing the voids using uniform pressure on the part surface [55].

The temperature gradient induced along the built direction (BD) during the PBF process leads to notable directional microstructural phenomena such as grain size irregularity observed within the melting pool interfaces and along the built direction. Solution annealing at 1150 C reduces the micro-segregation of PBF-LB 17-4PH stainless steel (SS) to homogenize the solute distribution [56].

Besides homogenizing the microstructure and reducing potential defects, HT also offers the opportunity to tailor the desired mechanical property. Available HT parameters including temperature, HT time, heating rate, and cooling rate, as well as the HT types have been shown to affect the microstructure and the corresponding mechanical properties. After HT, the microstructure removed the Laves phase which has a detrimental influence on the material property, with the Laves phase solved from coarse to discrete particles for the PBF-LB Inconel 718 alloy [51]. A novel HIP process was developed to maintain the strength behaviour of the Ti-6Al-4V alloy compared to the as-built condition. HIP treatment was found to modify the lath aspect ratio, but also get rid of internal porosity and remove the microstructural heterogeneities [54]. Industrial recommended post-built HT process was tested for a stress relief annealing process for AM 17-4PH stainless steel and it showed little influence on the directional dendrite grain morphology (grows along favourable crystallographic direction along the laser source) but altered the phase fraction of BCC/martensite volume fraction. This phase change led to significantly increased Vickers micro-hardness (from 258 to 312 VHN) [56]. Through a comparison between solution HT and aging at different temperatures, post-built HT has proved to influence the hardness and recrystallization microstructure of the PBF fabricated Al alloy [57]. An investigation on Ti-6Al-4V alloy found that after HIP, the microstructure evolved to dual $\alpha - \beta$ lamellar phase and the mechanical properties was altered to have a lower strength, but significantly improved ductility. After HT, the Ti-6Al-4V samples also showed improved fatigue performance under dynamically loaded conditions [58].

Another benefit of HT is to alleviate residual stress. Steep residual stress gradient is caused by the layer-by-layer feature, together with a high-temperature gradient and rapid cooling speed of PBF-LB process (typically $10^3 - 10^8$ °C/s [59]), leading to part distortion in the as-built product. Typical residual stress profiles include high tensile stress observed in the surface zone and the magnitude is influenced by the substrate [60]. Tensile residual stresses were observed localized at the edges alongside the BD, with a higher magnitude 150% - 160% compared to the nominal yield strength of the 316L SS [61]. Compressive residual stress has also been observed in the as-built PBF-LB Inconel 718 (IN718) alloy, which mostly appeared in the longitude cross-section surface along the BD, due to the inhomogeneity microstructure of the part. The measured compressive residual

stress using the contour method had a peak value of 378.4 MPa, about 1/3 of the yield strength, which decreased to 140.6 MPa measured in the HT sample [51].

Post-built HT can reduce defects such as voids and lack of fusion. Porosity is one challenge for PBF-LB fabricated products, including pores caused by lack of fusion [62], keyhole pores caused by laser spot movement [63], and gas pores caused by entrapped gases [64]. Post-built HT is potentially effective in reducing the near-surface porosity defects. Through X-ray computed tomographic examination, it was found that the Ti-6Al-4V samples show fewer porosity values (from 2.4% to 1.2%) due to high temperature and uniform pressure, after HIP treatment [65]. Another research [66] using the X-ray computed tomography (XCT) as the measuring tool has quantified the reduction of the defects: (i) Lack of fusion from 0.35% to 0.0039%; (ii) keyhole pore fraction from 0.298% to 0.0007%; and (iii) contour pores from 0.911% to 0.643%, after HIP treatment for the PBF-LB Ti-6Al-4V alloys.

2.3 Microstructure of PBF-LB metals

2.3.1 Effect of PBF-LB process on solidified microstructure.

The PBF-LB fabricated metallic alloys have different microstructure compared to their conventionally manufactured counterparts, mainly due to the layer-by-layer deposition and the incremental formation manner during the PBF-LB process, and other factors such as temperature gradient and repeating thermal cycles. The microstructure is determined by this thermal gradient within the melt pool [32]. Thermal gradient is described as the ratio of the temperature difference along the normal direction to the solid-liquid interface [67]. One microstructural feature in PBF-LB cooling process is phase transformation, where sub grains (grains having low-angle grain boundary) nucleate from the parent phase (prior-β substrate in Ti-6Al-4V) and inherent similar crystallographic orientations.

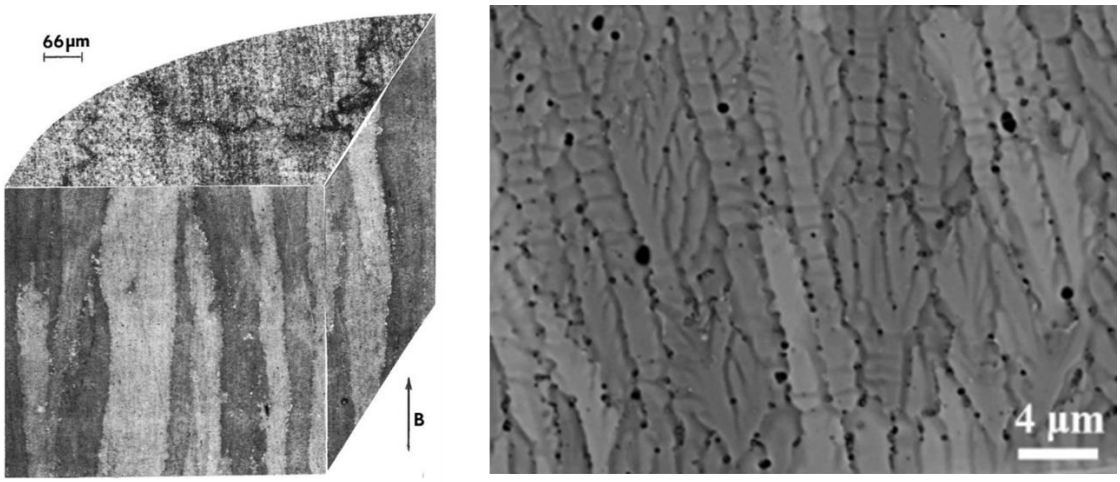

Figure 2-4. SEM images showing the columnar grain and dendritic structure in PBF titanium alloy [68].

Another unique feature compared to casting or machining, is the widely observed cellular or dendritic columnar grain morphologies, as shown in Figure 2-4 [68]. Rapid cooling speed [59] (typically $10^3 - 10^8\ °C/s$) during PBF-LB solidification causes rapid non-diffusion transformation and crystallization, also referred to as growth rate [69]. Such high growth rate in the melting pool generates solute-rich boundary layers along the solid-liquid interface and causes the material to reach the supercooling condition (Cooling the liquid below solidified point). Crystallization becomes unstable under this condition, thus forming cellular/lamellar (also referred to as basketweave) grain morphology, shown in Figure 2-5. The above two unique microstructural features have been widely observed in a range of PBF metallic alloys, including biomedical graded CoCr alloys [70-72], Ti-6Al-4V alloys [20, 73], and 17-4PH stainless steels [74, 75]. Figure 2-6 shows a comparison between PBF-LB fabricated resulting microstructure and their conventionally manufactured samples such as wrought products. The near- α Ti-6Al-4V exposed to the fast cooling speed in PBF-LB process leads to the generation of needle shape and fine size α' lath transformed from β.

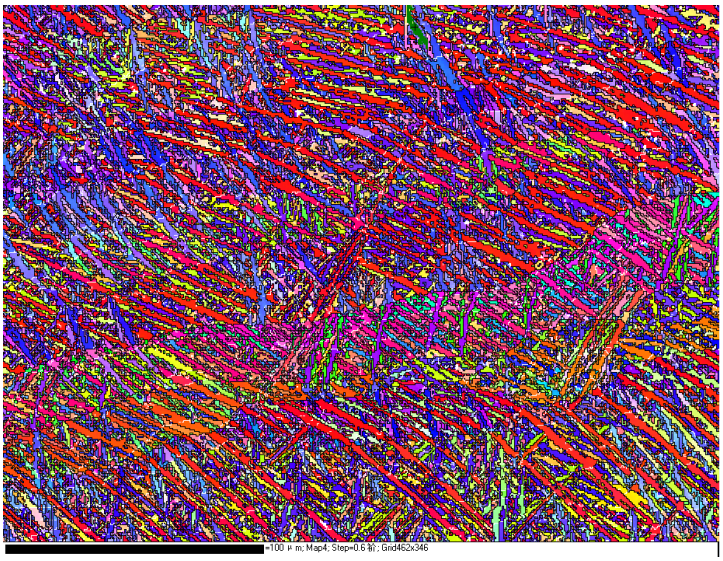

Figure 2-5. Basket-weave microstructure in a PBF-LB Ti-6Al-4V EBSD image [76].

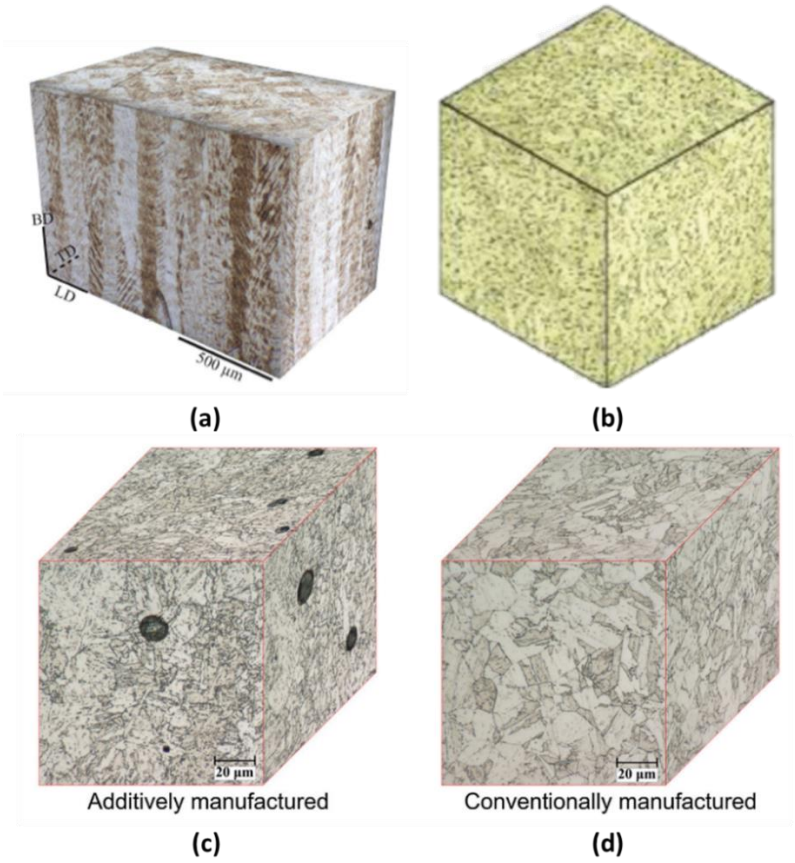

Figure 2-6. Reconstructed 3D SEM grain image comparison: (a) PBF Ti-6Al-4V[77], (b) wrought Ti-6Al-4V [78], (c) PBF 17-4PH SS [79], (d) wrought 17-4PH SS [79].

Increasing the energy density (higher VED) means increased solidification and cooling rate, and smaller thermal gradient. Laths width, or the dendritic arm spacing are used to measure the size of PBF lamellar structure. The PBF-LB Ti-Al alloy was observed a cellular structure with the dendritic arm spacing ranging from 0.165 to 1.765 μm using a laser power of 150 W and a scanning speed of 200 mm/s. The solidified microstructure was found to be more sensitive to the cooling rate rather than the thermal gradient, and finer laths were observed at the centre of melt pool due to the higher cooling speed [80]. The prior-β grain size in Ti-6Al-4V increased when a higher energy density was applied. As the VED increases, the grain morphology transits from columnar to equiaxed due to the higher driving force induced from the constitutional supercooling condition [49]. The grain diameter increased from 101 μm to 224 μm with the laser power increasing from 127.5 W to 161.5 W for 17-4PH SS [81].

2.3.2 PBF-LB strategies on crystallographic texture.

The PBF-LB strategies mainly include built direction (BD), scanning strategies, powder bed preheating, and support type. The PBF-LB solidified grain usually forms alongside the BD, resulting in an anisotropic microstructure with strong texture. The epitaxial nucleation feature during the crystallization and solidification process causes the sub-grains to have similar crystallographic orientation compared to the parent phase grain, which is largely determined by the BD. In some dual-phase alloys such as Ti-6Al-4V and 17-4PH alloy, the martensitic transformation occurs during cooling. The martensite phase can be related to its parent phase via Burgers vector relationship and the reconstructed parent grain map can be used to track the texture during PBF [82]. This dominant crystallographic orientation is referred to as texture. One popular tool for calculating the texture direction and strength is a probe plugin of a scanning electron microscope called electron backscatter diffraction (EBSD). Figure 2-7 shows the EBSD measured grain morphology of an PBF-LB 316L stainless steel showing strong texture along its BD and obvious anisotropic microstructure compared to the longitude cross-section plane. Dendritic arm spacing is a quantitative microstructural parameter determining local solidification rate [83]. Dendritic arm spacing also affects tensile strength, wear and

fatigue behaviour [84]. The microsegregation is the composition variation across cells or dendrites in a solidified alloy [85, 86].

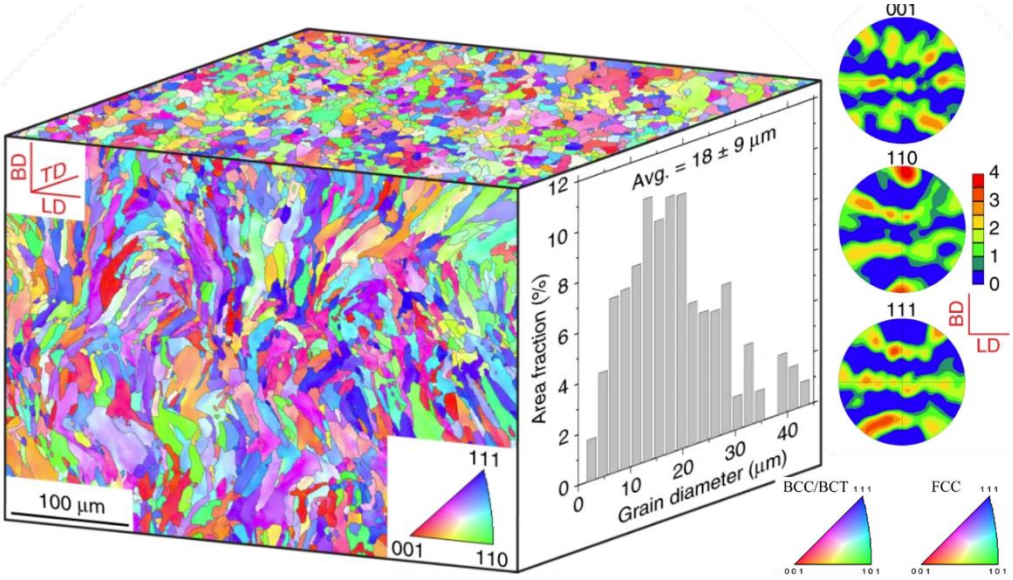

Figure 2-7. The 3D EBSD image of PBF-LB 316L stainless steel showing the grain morphology, orientation by inverse pole figure, and the calculated grain size distribution [87].

The crystallographic texture can be controlled or modified through suitable processing parameters or post-built processing. Niendorf et.al. [88] found that the 316L SS can maintain a strong <100> texture along the BD, given that a laser power of 1000 W is adopted. Texture was observed across the successive deposited layers in the PBF Ti-6Al-4V alloy [89]. A similar conclusion was addressed for Inconel 718 with a laser power higher than 400W [90]. Scanning strategies also affect the overall crystallographic texture, as shown in Figure 2-8. The hexagonal scanning strategy shows a <100> texture parallel to BD, while the remelting strategy generates multiple texture peaks. Also, a smaller grain size is observed with lower laser power [81]. Undesired texture can be reduced by post-built HT. E.g., the <100> texture observed in as-built 17-4PH steel disappeared after the solution HT [37].

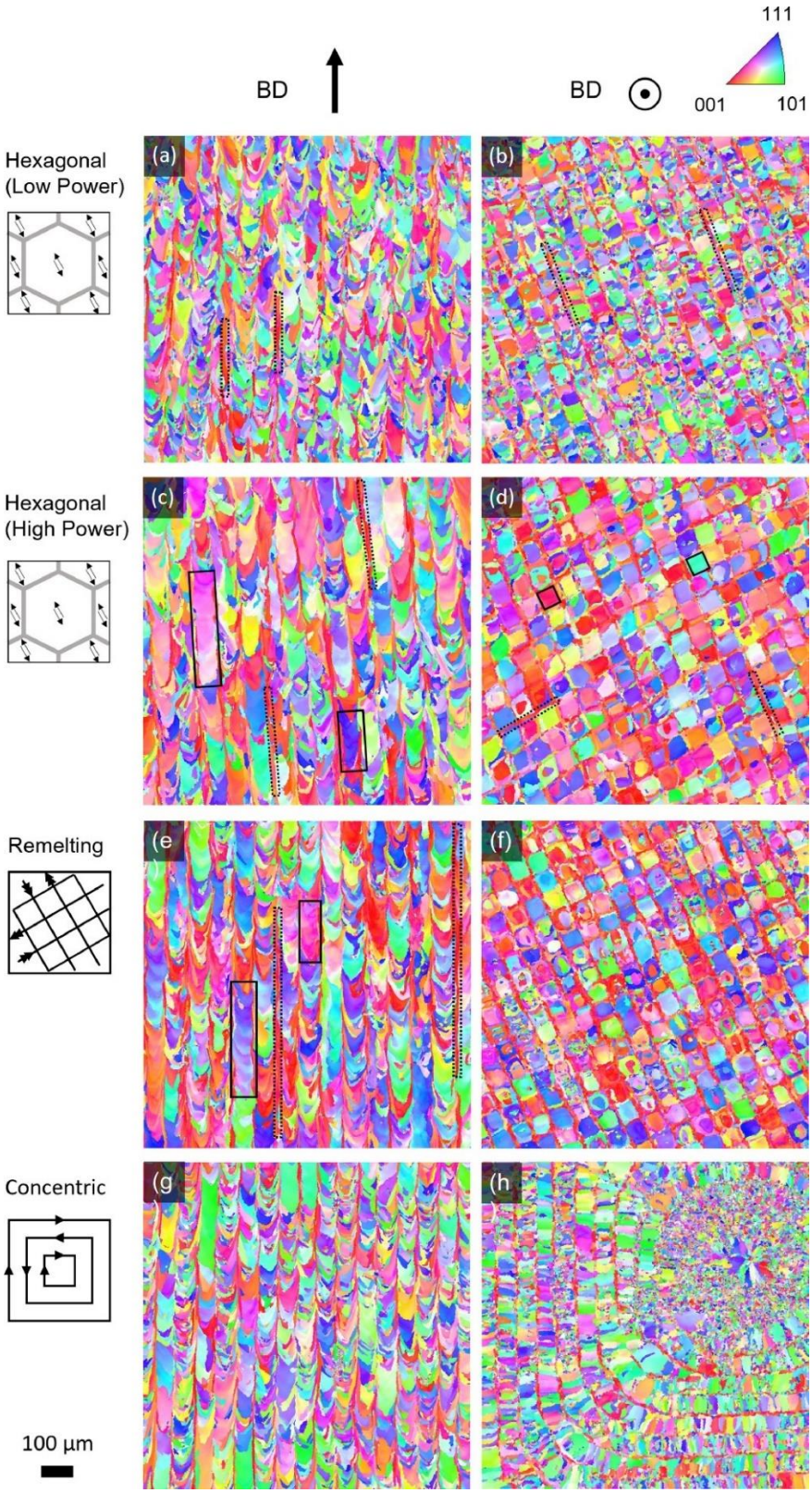

Figure 2-8.IPF EBSD grain maps taken from central regions of 17-4PH SS with different scanning strategies [81].

2.3.3 Effect of post-built heat treatment on the microstructure of PBF-LB alloys.

It is recommended that the HT be performed immediately after completion of the PBF build and before the parts are cut from the plate, in order to improve the homogenize the structure and improve the property. CoCr and β-Ti display softening and grain growth during HT at high temperatures [91]. HT of PBF-LB Ti-6Al-4V alloy usually results in more uniform $\alpha - \beta$ microstructure and disappearance of dislocation and twining structures [34]. In-situ high temperature XRD [92] was used to analyse and quantify the phase transition during HT for PBF-LB Ti-6Al-4V. The retained β phase was detected when the HT temperature was higher than 500 °C, while there was no α phase once the temperature reaching 1200 °C. The HT effect on grain size evolution is the focus of this thesis, and more HT induced grain growth applications are discussed in Chapter 5 and 6.

2.4 Surface roughness

The layer-by-layer principle of the PBF process inherently causes a rougher surface than other manufacturing methods. SEM images shown in Figure 2-9 gives a comparison between the surface height map of plate and cylinder samples using the same printing parameters. The surface roughness of PBF-LB products is usually in micrometre scale and can be controlled by post-built surface processing techniques. 60% higher surface roughness was observed in a cylindrical part compared to flat ones in 17-4PH SS [93]. Roughness average (Ra) of a surface was measured highest, 8.38 μm for a 17-4PH SS sample, which decreased to 0.015 μm after polishing and machining, compared to 0.01 μm in the wrought sample [94]. Besides, post-built surface processing is sometimes challenging, for products with complex shapes. Such surface roughness cannot be improved through HT or HIP without milling [95]. The main factors influencing surface roughness include the size of powder particles, ejection of particles, the morphology of the melting pool track, stair-stepping effect, and layer thickness [96, 97].

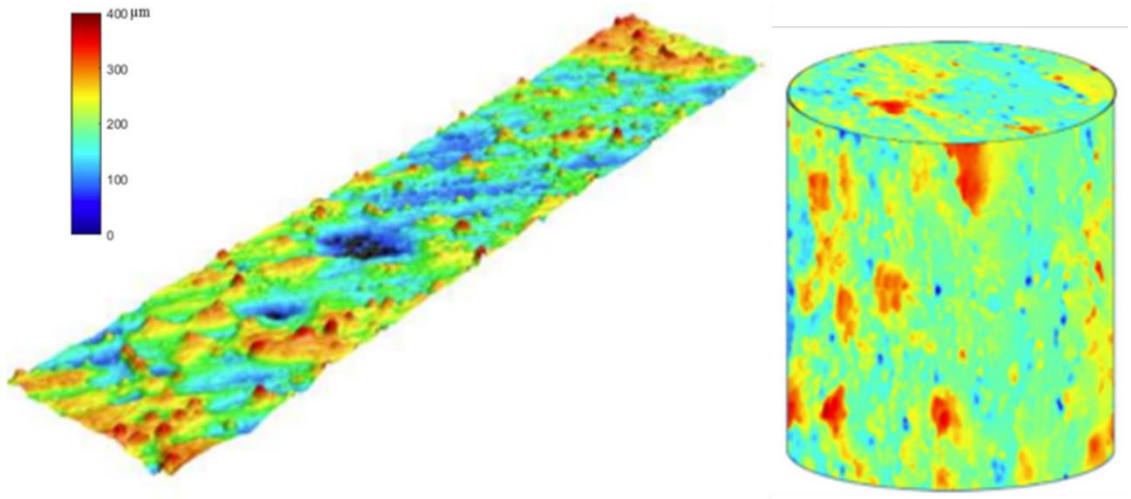

Figure 2-9. Surface height distribution map for plate tensile sample (left) and cylindrical sample (right) respectively of PBF-LB manufactured SS 17-4PH alloy [93].

The fatigue performance of the PBF sample is highly sensitive to surface quality and defects, thus requiring careful consideration of post-built quality improvement for low cyclic fatigue test, especially at a relatively higher strain range. The roughness associated with PBF marts may be of benefit in certain medical device applications, for example, cementless orthopaedic implants where the ability for bone tissue to attach to the implant is increased with increased surface roughness. Another significant impact of surface roughness is the ability to withstand crack initiation at the part surface under fatigue loading, and more details are covered in section 2.5.2. Machined or surface etched Ti-6Al-4V showed the increased fatigue life from 2×10^4 to 8×10^5 in stress-controlled tests after surface machining [98]

2.5 Mechanical performance

2.5.1 Tensile behaviour of PBF-LB components.

PBF-LB manufactured stainless steels such as 17-4PH and P91, are usually dominated by martensite with retained austenite phase [56]. 8% to 21% retained austenite were

reported in the previous PBF-LB 17-4PH SS research, with the reported yield stress (YS) ranging from 570 to 660 MPa, and a UTS ranging from 900 to 1250 MPa [25, 79, 99]. The PBF lamellar microstructure morphology leads to higher strength and hardness but lower ductility in the as-built Ti-Al-4V alloy. The as-built parts have reported UTS values of between 1035 and 1407 MPa compared to the UTS values from 870 to 995 MPa for wrought fabricated parts [100]. 17-4PH SS can have higher tensile strength after HT, due to the precipitation of nanoparticles in martensite. However, this effect was largely reduced given the retained volume fraction of austenite is higher [101]. HT on Ti-6Al-4V usually aims at trading some strength for better ductility. PBF-LB Ti-6242 [102], after annealing at 850°C for 3 hours, followed by air cooling, the UTS has dropped from 1437 MPa to 1185 MPa, however, its strain at failure doubles, from 5.7% to 9.3%.

2.5.2 Fatigue behaviour of PBF-LB components

A common concern with PBF-LB components is the fatigue behaviour, due to the existence of defects such as voids, surface roughness, and the existence of residual stresses. This shortcoming is especially notable for the as-built parts without a suitable post-built treatment processing and has prevented wider adoption of AM application by industry [103]. The fatigue tolerance estimation, consequently, needs to consider microstructure, defects, and surface condition. As-built PBF-LB Ti-6Al-4V has poor fatigue performance due to the dominant volume fraction of martensite phase and as a result, HT is recommended to eliminate this phase [104]. Besides microstructure, fatigue cracks are believed to initiate from surface roughness and voids close to the surface [105].

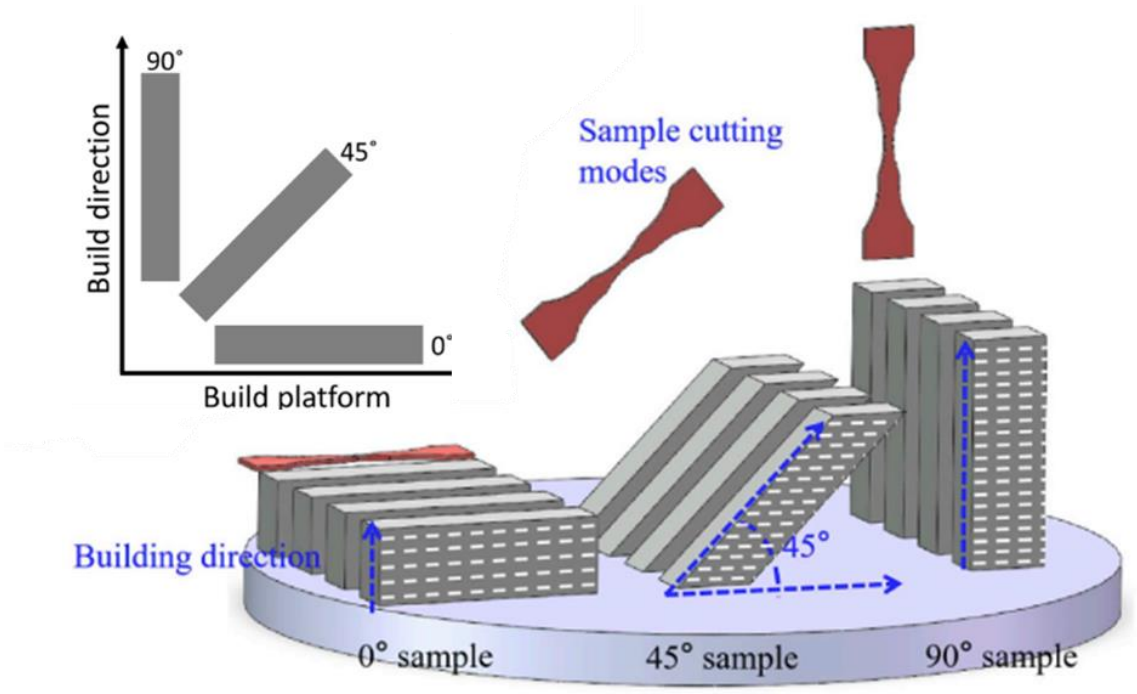

Figure 2-10. Experimental design for studying the crystallographic texture effect on mechanical response caused by three different built directions.

Anisotropic microstructure induced fatigue performance has been studied, including LCF [106, 107] and HCF tests [108]. The vertical direction build sample exhibits fewer crack propagation resistance due to the weaker bonding interfaces between the layers. Such anisotropic mechanical response features caused by the directional AM process have been studied with samples varying in printing orientation. Figure 2-10 shows a typical design trial with horizontal, 45 degrees, and vertical built samples respectively. Their crystallographic texture effect on the different behaviour in stress-strain curves [106], fatigue crack initiation [109], fatigue crack propagation [107, 110], as well as high cyclic fatigue performance, have been quantified and also explained with microstructural characterisation results. Agius et al, [106] stopped the fatigue tests with strain amplitudes ranging from $\pm 1.0\%$ to $\pm 2.0\%$ reaching 200 cycles, which obtained sufficient testing data for plotting the hysteresis loops but not failure life. Table 2-1 shows the main results obtained from the previous experimental research on the mechanical behaviour of three different orientated AM Ti-6Al-4V samples. The crack propagation data [107] was obtained through a load-controlled fatigue test with R-ratio of 0.1 and the crack

propagation rate was fitted using the NASGRO equation [111]. High cyclic fatigue test [108] was carried out using a stress ratio of 0 up to 2×10^6 cycles.

Table 2-1. The mechanical behaviour of Ti-6Al-4V samples varying in built directions.

Sample	Elastic modulus (GPa)	Yield stress (MPa)	Ultimate stress (MPa)		ΔK_{th}	ΔK_{Ic}		HCF crack initiation	HCF failure life
Horizontal	95.2	1000	1182		14.3	55		2×10^4	5×10^5
45 degrees	100.0	1100	1254		23.4	60		-	-
Vertical	103.7	1037	1181		11.1	55		8×10^3	1×10^5

2.6 Process monitoring and non-destructive testing

Efforts in PBF process and materials research and industrial quality control would benefit from greater availability of detailed high resolution and fast-rate sensor data from within the manufacturing process. The currently implemented sensors include in-situ process monitoring systems and thermal imaging cameras. Non-destructive tests (NDT) is a group of quality check techniques that inspects parts for defects without damaging the part. Methods for in-situ process sensing and monitoring and in-situ NDT are detailed in a review [112].

Current process monitoring systems have three main challenges:

(i) Lack of automatic operation tuning tool based on the feedback from monitors [113]. The variation nature of PBF makes the calibration and tuning algorithms development a difficult task. The training dataset for such an algorithm needs to be representative while the physical phenomenon within each layer might differ, adding complexity to the process assessment.

(ii) The efficiency of dealing with big data monitoring information. PBF monitoring data involves multiple formats, such as images, thermal signals, and video, which easily occupy hundreds of gigabytes of storage [114].

(iii) Instant data analysis and synchronization [115]. The monitoring sensor needs to be rapidly located at the target location, or even use images to construct 3D data. The sensor also needs to be synchronized with the layer's behaviour.

2.7 PBF modelling framework

2.7.1 General

Based on the modelling scale, the computational models addressing the structure or property calculation can be classified into four main types [116], as shown in Figure 2-11: (1) Quantum simulations (not discussed in this thesis), (2) Molecular dynamics (MD) simulation, (3) micro-meso scale simulation such as crystal plasticity finite element (CPFE), phase-field method (PFM), Monte Carlo (MC), and Cellular automata (CA), (4) macroscale modelling, also known as continuum simulations. Models can interact to establish a multiscale modelling framework, e.g., homogenize the microscale CPFE models to represent the macroscopic behaviour.

PBF-LB is a multi-scale and multi-physics process. During PBF-LB the micro-scale powders interact with each other within each layer of the powder bed, requiring particle flow models to capture the physical behaviour of the powder [117, 118]. These in-situ PBF-LB process are not the focus of this thesis. After the laser beam is activated, heat transfer, particle sintering, melt pool dynamics, and solidification become dominant processes. This work focuses on the solidified microstructure from as-built parts and evolved structure after post-built heat because it directly determines the mechanical properties of the PBF-LB alloys. Figure 2-12 illustrates an example modelling framework integrating thermal-based FE predicting thermal history, phase-field method predicting solidified microstructure based on temperature evolution, and crystal plasticity finite element (CPFE) model predicting mechanical strength based on microstructure, to characterize the process-structure-property interdependent relationship for AM Ti-6Al-4V alloys. This section discusses the developed computational models to investigate the process-structure-property concerns in PBF-LB fabrication.

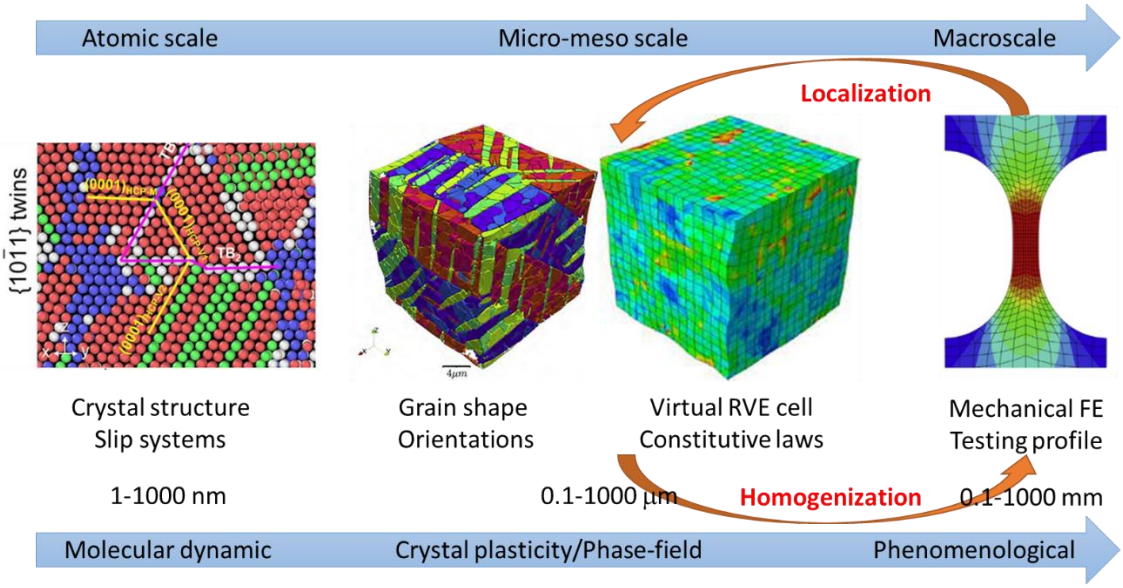

Figure 2-11. Micromechanics models at ranges of modelling scale [118, 119], and the idea of homogenizing micro-scale models for representing macroscopic behaviour of the test profile.

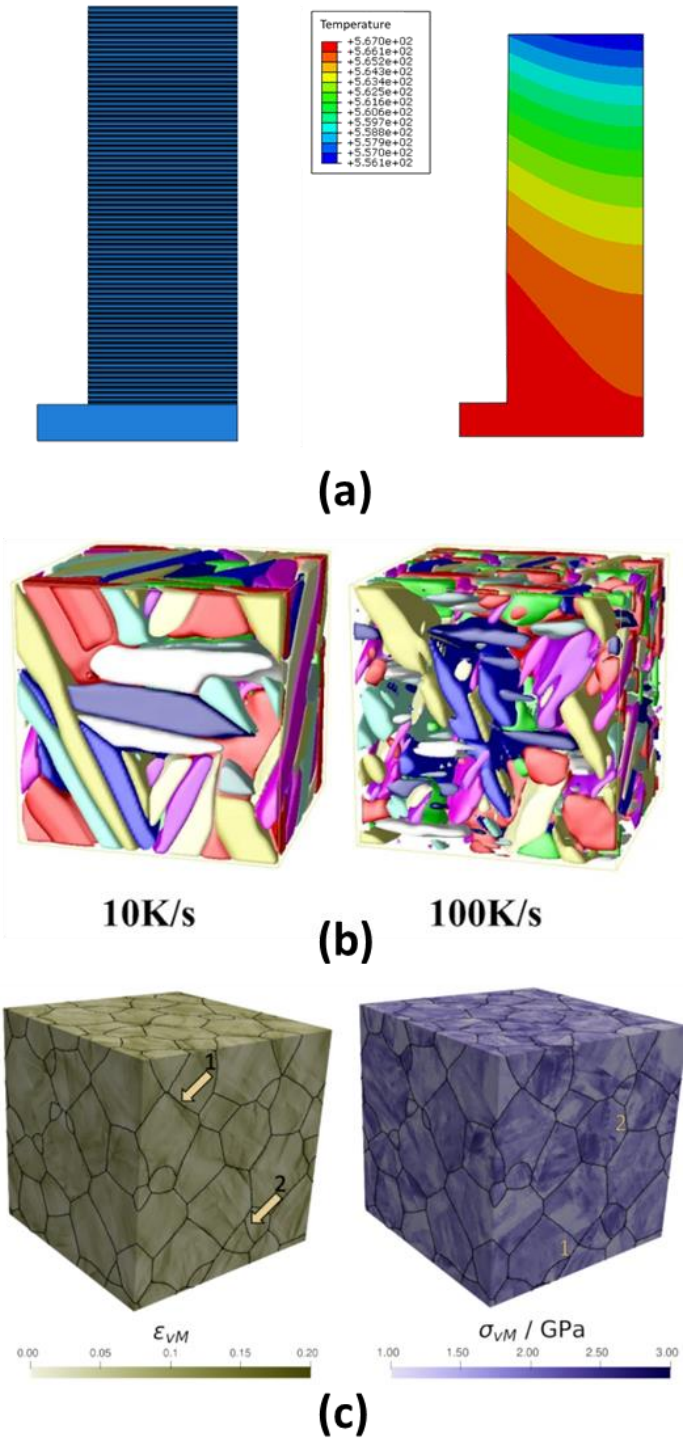

Figure 2-12. Integrated modelling framework, coupling (a) thermal FE model [120], (b) phase-field method for solidified microstructure under different cooling speed [121], and (c) CPFE modelling predicting mechanical response[122], to investigate the process-structure-property independency.

2.7.2 Representative volume element

The heterogeneous material property depends on the microstructural features. Micromechanics, different to the conventional continuum macroscopic modelling, considers the features inside the structure, and requires the concept of a representative volume element (RVE) as a repeating unit cell, to represent the material as a whole part [123]. An RVE is the minimum volume which contains sufficient statistical microstructural data to account for behaviour, and further increasing the volume should not affect the mechanisms [124].

Numerous artificial methods have been adopted for generating idealised polycrystalline RVE models, such as homogenised regular shape microstructures [125, 126], Voronoi tessellation (VT) based 2D maps consisting of irregular (but idealised) grain morphologies defined by straight grain boundaries [127] and the 3D polycrystalline aggregate cube [128, 129] methods. These methods have some important limitations:

- The polyhedral-shaped structures typically generated by VT do not represent the real measured morphology of grains, which has been shown to influence the evolution of intra-granular misorientation and inter-grain deformation [130-132].
- VT generated models fail to include accurate orientation information for grain-neighbourhood effects, especially for materials with strong texture [133].
- VT algorithms produce unique models from each run, due to the use of random nucleation generators within the model generation codes. This produces an inherent scatter in modelling results which, while sometimes useful, cannot be eliminated [134].

In recent years, researchers have realised the significant influence of phase composition and grain morphology on mechanical behaviour [135]. Of particular interest to the broader context of the present work are complex microstructure morphologies like those of Ti6Al4V alloy [20]. The traditional VT method is not sufficient to represent such multi-phase lamellar or bimodal structures [20-22]. Efforts to address these shortcomings include the open source software Neper [22], which uses an extension function, based on the traditional VT rule, to provide an absolute mean grain size and standard deviation, using the lognormal fit, to achieve a wider range of grain size distribution and higher grain

sphericities compared with the simplified polyhedral-shaped standard VT method. This improved extension is also capable of providing a sub-tessellation meshing option, based on the centre of the grain mass, to imitate realistic morphology and grain boundary shape [23]. The Dunne group introduced a 27-grain polycrystal model to investigate elastic anisotropic in cold-dwell fatigue of a titanium alloy [31]. This 2D model used 5- to 8-(straight) sided polygons to represent the grain morphology and random orientations were assigned to each grain. The group also developed another sketching method to generate a real image-based model integrated with the extended finite element (xFEM) method to model slip-dominated crack growth through polyhedral line grain boundary drawing with 2D surface crack assumption [136]. Real microstructural morphologies (grain shape and size), measured using scanning electronic microscopy [137, 138] or diffraction contrast tomography [139, 140], has been utilised in image-based CPFE models to enhance accuracy and demonstrate the errors associated with artificially-generated microstructure models. However, details of the model generation process have been limited and its application to fatigue crack initiation has not previously been addressed.

A solution to include both accurate morphology and texture in CPFE models is through direct and complete EBSD conversion [141, 142]. Bronkhorst et al. [143] applied EBSD-based structural reconstruction with a single-crystal theory model for the tensile behaviour of wrought and additively manufactured stainless steel to investigate the effects of the manufacturing-induced differences in texture. Kapoor and co-workers [144, 145] applied a similar method to study strain localization and residual stress of lamellar Ti6Al4V alloy. Although Euler angle data available from EBSD measurements has been used to define grain orientations in CPFE models [146-149], the comparative and quantitative benefits vis-à-vis artificially-generated (e.g. VT) models for FCI has not previously been addressed. Furthermore, a systematic exposition of this approach, addressing imaging artefact issues such as imprecise or incomplete Kikuchi band indexing and pattern matching [150] and grain reconstruction strategy, has not previously been presented.

2.7.3 Modelling of PBF process and heat transfer

Laser power, scan speed, and hatch spacing are the three most important parameters during this process [2]. To model the PBF-LB powder material, variables including heat capacity, thermal conductivity and material density are considered.

The core theory to study heat transfer is defined by solving a time-dependant fluid energy problem [151] taking into account physical variables such as the flow velocity u, temperature T, the energy loss $Q$and the fluid density ρ.

Based on the background above, finite element methods [120] have been developed to predict the heat conduction, thermal distribution, and residual stress during PBF-LB process, with particular attention to the effect of scanning strategies [152]. Discrete element methods were also developed for quantifying the effect of process parameters, for example, laser power, scanning speed and hatch space, on the powder bed temperature field. Models are usually validated by comparing the predicted powder flow and heat conduction, with the experimentally measured temperature distribution in the powder bed. Laser hatch spacing, while not hugely affecting the temperature field on the powder bed, causes severe microstructural inhomogeneity and discontinuity[153].

2.7.4 Modelling of microstructural evolution during PBF process.

2.7.4.1 Kinetic Monte Carlo (kMC) modelling

Kinetic Monte Carlo (kMC) is a mesoscale modelling approach for predicting the solidified grain microstructure, including the grain morphology size, and the densities. KMC can describe the sintering mechanism which cannot be explained through finite element modelling. Besides, it is also capable of modelling high density systems which is the limitation of discrete element method. The kMC requires the construction of a representative volume element (RVE) to initialize the microstructure which can be reconstructed from real microstructure image using micro-CT pr X-ray microtomography facilities [154]. The popular kMC package, open-source suite SPPARKS, has been adopted to analyse the dependency between the grain morphology and the AM parameters,

such as the lathes size and their preferential growth orientations, for Ti-6Al-4V alloys [155].

2.7.4.2 Cellular Automata (CA) modelling

Cellular automata (CA), similar to kMC, is another mesoscale modelling approach and also requires RVE to initialize the microstructure. The simulation domain is meshed into cells containing variables that represent the properties necessary for predicting the volume evolution of itself and the neighbouring cells, and these predictions sum up to the final predicted solidified microstructure. CA was first introduced by Gandin et al. [156]. CA applications in AM usually contain two steps, melting and solidifications, simulated by solid-liquid cell definition and the boundary nucleation from the fusion lines.

CA has been integrated with computational fluid dynamics (CFD) models to predict the solidified microstructure of the PBF fabricated 316L stainless steel [157]. The coupled CFD-CA model predicted more fraction of columnar morphology grains and finer grain size when increasing the laser scanning speed. The PBF solidified microstructure morphology was also predicted using a 3D CA model focusing on dendritic grain growth and validated against the microstructural characterisation of PBF 316L [157] and Inconel 718 [158] samples. Another common approach is the coupled CA and finite element approach referred to as CA-FE, which was improved to evaluate the solidified texture for PBF 316L [159], and Ti34Nb alloys [160].

2.7.4.3 Molecular Dynamics (MD) modelling

MD modelling method can be integrated with other modelling approaches to obtain necessary variables such as temperature to simulate the evolution of energy difference to predict the solid/liquid or phase transition evolution [161]. Another integrated modelling framework coupled the discrete element method with the MD model to predict the evolution of temperature and microstructure of the Ti-6Al-4V alloys, by modelling the interaction between the non-spherical powder grains [162]. The capabilities include the

prediction of the effect of powder morphology and PBF parameters on solidified microstructure features such as phase composition and grain morphology.

2.7.4.4 Phase-field method (PFM) modelling

The PFM predicts the microstructural evolution using a group of field variable across the interfacial, and the evolution of the field variables are determined by Allen-Cahn relaxation (time-dependent Ginzburg-Landau) equation [24]. PFM, similar to kMC and CA, predicts the microstructural evolution at the mesoscale. One significant limitation of the CA numerical method is the possibility of introducing artificial anisotropy in the growth kinetics due to the Cartesian mesh (square grid) [163]. kMC can have difficulty predicting the three-dimensional microstructural evolution [164]. Furthermore, PFM can afford a better resolution around the grain boundary and triple junction areas, around the joints of at least three neighbouring grains. PFM can better predict the grain boundary segregation. MD modelling is computationally expensive and not suitable for mesoscale or bigger timeframe modelling work.

Current PFM approaches mainly cover three different processes: (i) solidification; (ii) grain growth [165, 166].; (iii) phase transformation. Figure 2-13 shows the typical applications of the PFM for PBF material modelling[167].

A PFM model studying solidification of Ti-6Al-4V has captured the effect of processing parameters on dendrite grain morphology, with ~15% reduction in the dendrite arm spacing size when increasing scanning speed from 200 to 800 mm/s or increasing the temperature gradient from 2000 to 3000 K/mm [168]. Another work by Wang et al. [169] integrated PFM with the finite element method and applied such multi-scale model to study the morphology of Laves phase particles. This model was used to predict hot cracking resistance property at the regions where neighbouring grains share bigger misorientation angles. An integrated CFD-PFM model was developed for predicting solidified microstructure for PBF Inconel 718. CFD predicted the printing parameter-based track characteristics using a numerical volume-of-fluid based method. These characteristics were then imported into the PFM as variables to predict grain

microstructure including segregation of phase elements in this binary alloy, dendrite width as well as dendrite orientation [83]. PFM has been used and developed for predicting solid state grain growth behaviour of the aluminium alloys [170] in PBF and martensitic steel [171]. Specific advances in PFM modelling include complexity was added for developing the capability of predicting abnormal grain growth by distinguishing grain boundary types [172], and grain growth in porous polycrystalline materials[173].

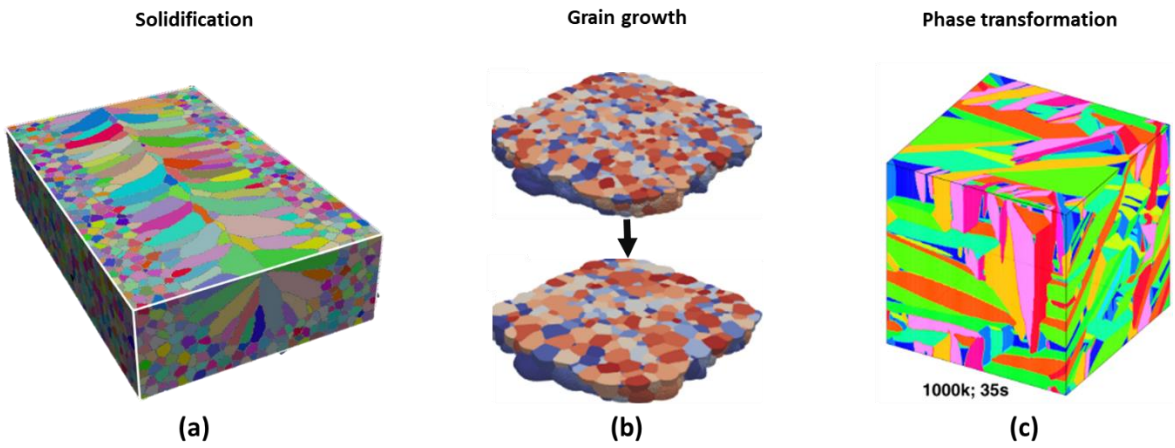

Figure 2-13. Schematic showing the widely-adopted applications of PFM approach, in predicting (a) the effect of laser power and scanning pathways on the columnar grain solidification evolution prediction in the anisotropic temperature field [135]; (b) Example of the MARMOT model predicting the grain growth behaviour of the reconstructed 1620-grain polycrystalline aggregates, whose grain size increases by a factor of 2.7 after 85 simulating steps [133]; (c) PFM predicted weave-basket morphology alpha lath transformed from their parent phase, prior beta grains, at a temperature of 1000K for a duration of 35 seconds [85].

2.7.5 Modelling of mechanical properties of PBF alloys.

2.7.5.1 Mechanical strength property

Finite element (FE) modelling is widely used for predicting the mechanical strength properties, e.g., the yield strength (YS) and ultimate strength (UTS) during the tensile tests. The macroscopic FE model is mainly used for structural topology optimization to achieve the desired mechanical property or stress distribution analysis. A FE model was developed to predict the tensile curve loaded from different directions until failure, for Ti-6Al-4V brackets components, using geometry designs varying in wall thickness [174]. FE model was also adopted for cellular structure optimization, to achieve a light-weight product

while meeting the strength requirement [175]. Another macroscopic FE model studied the effect of artificial voids on the tensile behaviour of 17-4PH SS [176].

Molecule dynamics modelling has been used to characterize the mechanisms of powder sintering behaviour at atomistic scale. Some studies also tried to link the AM product strength with the powder's sintering behaviour. Molecular dynamics (MD) is another computational modelling tool to describe the interaction action of powders. The MD method implemented in AM simulation usually requires multiscale modelling framework, e.g., thermal history from CFD modelling. The MD modelling packages LAMMPS [177] and LIGGGTS [178] were adopted for predicting the elastic modulus, tensile plastic strain, yield stress, and residual stress for the PBF-LB printed nickel particles' sintering behaviour [179].

CPFE modelling has been utilized to quantify the phase composition effect on tensile behaviour [180, 181], the higher ductility and strength caused by finer grain size structure [182, 183], the strengthening effect of grain boundaries [184, 185], as well as manufacturing direction-induced texture effect [186, 187]. This predictive capability has been applied to investigate AM metals and processes within manufacturing and materials research, requiring post-built sectioning, polishing, imaging, model reconstruction. One important advantage leading to the popularity of CPFE is the flexibility of implementing various constitutive flow laws with the aim of studying different microstructural-sensitive mechanical responses [188]. A Ramberg-Osgood and Hall-Petch based plasticity finite element model was developed for predicting the yield stress of PBF-LB Ti-6Al-4V [189]. CPFE modelling is the focus in this thesis, and more applications can be found in Chapter 4 to 7.

2.7.5.2 Fatigue and failure

The development of computational prediction methods for microstructure-sensitive fatigue crack is an important problem that will benefit a wide range of industries, including aerospace [182], medical-device [190], and power generation [146, 191]. The critical importance of characterisation of the interrelationships between manufacturing process,

microstructure, material properties and mechanical performance (structural integrity) [28, 29] has been highlighted by a recent aeroengine fan hub failure investigation [30, 31]. This report provides detailed proof of the serious risks associated with not considering these relationships, particularly for fatigue crack initiation in real applications, in this case, an aeroengine fan hub failure of Ti-6Al-4V alloy, not previously considered susceptible to facet fatigue.

Different methods have been introduced for evaluating the fatigue life of metals. The linear damage approach S-N curves, also referred to as stress-based approach is commonly adopted. The curve information can be used for deriving the constants in Paris' law [192, 193]. Basquin [194] firstly raised up the idea of using power law for illustrating the relationship between the applied stress amplitude and fatigue life. Coffin-Manson [195] provided similar relationship for studying the type of loadings when fatigue life is affected mainly by plastic strains:

$$\frac{\epsilon_p}{2} = \epsilon_f'(2N)^c$$

where ϵ_p is the plastic strain amplitude, c is the ductility constant, ϵ_f' is the fatigue ductility coefficient and N is the fatigue life.

The failure of ductile material goes through yield before fracture. Thus, fatigue modelling needs to consider two main steps: plastic deformation, and fatigue damage accumulations. The primary damage accumulation theory assesses the failure through accumulative plastic strain and strain energy concepts. The procedure of finite element fatigue modelling parameter fitting includes optimization of the hardening parameters derived from hysteresis loop, as well as damage evolution parameters.

A S-N curve (relationship between fatigue stress versus the number of cycles to failure) predictive model was developed to study the relationship between laser power and fatigue life for the PBF 316L. The fatigue fracture behaviour was explained with the void fraction using an inverse-square-root equation [196]. Yadollahi et al. [197-199] used Ramberg–Osgood relationship to represent the stabilized hysteresis loops during fully reversed fatigue tests, and used Coffin-Manson relationship for fatigue prediction of the AM 17-

4PH SS. In another modelling work of AM 15-5 PH SS, four back stresses were implemented, and four constants were used to fit the Coffin-Manson-Basquin law [200].

2.7.5.3 Thermal residual stress and distortion

The PBF-LB process often leads to large and anisotropic residual stress. High speed energy beam spot causes the nonuniform temperature field, plus the effect of hatch overlap and complex part geometry, residual stress prediction becomes difficult and hinders further uptake of PBF technology [201].

Finite element modelling methods are used for predicting the residual stress by calculating strain/stress tensors during the deformations. For the purpose of calculating residual stress, the finite element model needs to be capable of predicting both thermal and a mechanical PBF model. A coupled thermal-mechanical finite element method was developed for capturing the strain rate influenced by annealing process [202] and scanning strategies [152], for PBF Ti-6Al-4V alloy. Residual stress modelling results can be validated against measurements taken via Synchrotron X-ray diffraction [203]. Residual stress is also predicted at a microscale grain-level through CPFE modelling and validated via high resolution digital image correlation, for AM Ti-6Al-4V alloy [144]. The residual stress was predicted based on a geometrically necessary dislocation (GND) density initialized constitutive laws and the prediction was directly compared and validated against EBSD calculation with the Nye's tensor-based approach.

2.7.5.4 Toughness and distortion.

The effect of printing parameters [204], build orientations [205, 206] and temperature [207] on the toughness of PBF material have been previously studied experimentally. Charpy impact experiment was adopted for estimating the impact energy to quantify the toughness property. Johnson-Cook phenomenological flow stress constitutive law [208] together with the damage criteria were implemented in a finite element model by Sagar et al. [209] to simulate the impact energy when the striker impacts the 15-5 stainless steel

specimen. Distortions were predicted using a part-scale FE thermos-mechanical for PBF-LB Ti-6Al-4V through a sequential heating method [210].

2.7.5.5 Void defects

Voids and porosity are common defects in AM metals. Predicting the existence and fraction of void is important for controlling the product quality and to avoid significant damage to the mechanical strength [104]. The excessive AM source energy setting leads to keyhole-induced pores while insufficient heat input also leads to voids due to lack of fusion [211]. This means careful control over the heat energy input is required in the print parameter settings. A numerical Multiphysics model was established to predict the melt pool evolution and key-hole void formation for Ti-6Al-4V [212]. This model was further modified for predicting lack-of fusion type void for Inconel 718 alloy [213]. In another study, a CPFE model with a circular hole in the middle of the square model was developed with a 2D rate-dependant constitutive law. This single-crystal model [214] of AM aluminium alloy confirmed severe plastic deformation around the void and a significant influence on the stress-strain curve was observed from the shape of the void (aspect ratio), and the crystallographic orientations. DEM and CFD models were integrated as a meso-scale modelling framework for predicting the formation of inter-layer void due to lack of fusion [215]. The DEM-CFD model predicts the size of the pores. Meanwhile, it suggests using contour and layer-wise interlace scanning strategy to reduce the voids.

2.8 Crystal Plasticity Finite Element (CPFE) modelling.

2.8.1 CPFE applications to investigate the structure-property relationship

Accurate computational simulation of the macroscale strength of metals or alloys typically requires microstructure definition. Finite element analysis, involving grain boundary and crystal orientation specifications, along with constitutive and damage model parameters, are referred to as crystal plasticity finite element (CPFE) methods [188, 216-218]. CPFE model is a suitable tool for solving structure-property problem of anisotropic

materials. The deformation of the polycrystalline grain aggregates is dependent on the external loading direction and its own orientation. CPFE requires an accurate and reliable representative volume element (RVE) to statistically contain the equivalent microstructural information in the sample, such as grain size distribution, phase composition, grain morphology, and texture.

It has been shown that manufacturing-induced texture has an important influence on response to both monotonic and cyclic loading, with regards to yield stress and ductility [106]. Unfortunately, the crystallographic orientations in such studies do not correspond to the realistic microstructural characterisation. Other than the orientational-dependent slip system, a special misorientation relationship, twinning boundary also needs to be considered and activated for alloy structures dominated with hexagonal close packed (HCP) [219]. Ali et al. [220] implemented the initial texture of annealed aluminium alloy into an equiaxed cubic VT model where the crystallographic orientation distribution is statistically equivalent to that from pole figure measurement. McDowell and co-workers [221, 222] developed a microscale dual-phase titanium model capturing the texture effect and found that (i) the accumulative effective plastic strain of the basal-textured material was ~25% lower than the transverse case and (ii) the effective plastic strain distribution changes significantly if neighbouring misorientation relationships are omitted. In the latter work, orientation distribution was extracted and assigned to lamellar colony 3D models through the measured probability density distribution. This method successfully revealed distribution of absolute orientation and initial texture [223]. The Cailletaud team [224] introduced a customized grain boundary misorientation relationship in a regular 2D hexagonal model to predict FCI behaviour using the maximum value of shear strain amplitude as well as accumulated viscoplastic strain. The distributions of the two fatigue parameters were shown to depend on the misorientation relationships between grains. It was concluded that individual crystal orientation is insufficient for microstructure-based fatigue prediction. Rather, neighbouring grains and misorientation relationships need to be considered.

Currently, most CPFE studies are based on VT idealised (grain morphology and linear grain boundaries) RVEs that statistically represent the real microstructure [225-227].

Other recent CPFE studies have introduced high-fidelity models based on realistic characterisation images from scanning electron microscope (SEM) or EBSD scans, to include realistic and detailed microstructural information such as grain morphology and neighbouring misorientation relationships [31, 141, 228]. Such EBSD-based modelling frameworks, while containing more accurate information, have two challenges. Firstly, imaging artefacts lead to non-indexed noise pixels, adding difficulty to phase fraction determination, especially when a minor phase (below 10%) exists in the sample. The difficulty in determining accurate minor phase content has led some researchers to approximate dual phase materials as single phase (Ti-6Al-4V [229], 316L steel [143] and P91 steel [146]), though dual phase CPFE studies on AM Ti-6Al-4V [180, 229] have been reported. Secondly, extra experimental efforts are required for both EBSD sampling preparation and increased computational cost as, typically, mesh density of EBSD based CPFE model is highly dependent on the high resolution EBSD images [144]. Thus EBSD data undoubtedly provides valuable raw source data for microstructural modelling; however, VT-based CPFE models informed by EBSD-derived parameters may be a more widely-adopted approach, especially for model sensitivity investigation.

The next three sections introduce the constitutive laws implemented in this thesis.

2.8.2 A phenomenological CPFE modelling approach

The phenomenological crystal plasticity model is based on large deformation theory [230] and the deformation is described solely by the slip displacement along crystal slip systems. The motion and generated dislocations along the crystal slip direction cause shear deformation along slip planes. Crystal slip occurs on a given slip system once the shear stress exceeds the critical resolved shear stress. These slip systems determine the velocity gradient during plastic deformation.

According to large deformation kinematics, current position vector $\boldsymbol{x}$ is defined in terms of reference original position vector $\boldsymbol{X}$ and displacement $\boldsymbol{u}$, as follows:

$$\boldsymbol{x} = \boldsymbol{X} + \boldsymbol{u} \tag{2-2}$$

and the deformation gradient tensor $\boldsymbol{F}$ is used for describing the transformation of the deformation from reference global vector $d\boldsymbol{X}$ to the current configuration vector dx:

$$d\boldsymbol{x} = \boldsymbol{F}d\boldsymbol{X} \tag{2-3}$$

The deformation gradient $\boldsymbol{F}$ can be further decomposed into elastic and plastic parts:

$$\boldsymbol{F} = \boldsymbol{F}^{\mathrm{e}} \cdot \boldsymbol{F}^{\mathrm{p}} \tag{2-4}$$

where $\boldsymbol{F}^{\mathrm{e}}$ represents rigid body rotation and elastic stretch while $\boldsymbol{F}^{\mathrm{p}}$ represents plastic deformation. The inelastic velocity gradient $\boldsymbol{L}^{\mathrm{p}}$ is implemented as follows:

$$\boldsymbol{L}^{\mathrm{p}} = \dot{\boldsymbol{F}}^{\mathrm{p}} \cdot (\boldsymbol{F}^{\mathrm{p}})^{-1} = \sum_{\alpha} \dot{\gamma}^{\alpha} \boldsymbol{s}^{\alpha} (\boldsymbol{m}^{\alpha})^{\boldsymbol{T}} \tag{2-5}$$

where the velocity gradient $\boldsymbol{L}$ is the differential form of the deformation gradient $\boldsymbol{F}$. Plastic deformation is only affected and determined by crystallographic slip here; the velocity gradient can also be written as the accumulated value of the rate of slip along the slip system α where $\dot{\gamma}^{\alpha}$ is the rate of slip, and $\boldsymbol{s}^{\alpha}$ and $\boldsymbol{m}^{\alpha}$ are the slip direction and slip normal direction vector for slip system α, respectively.

In the present work, a user material subroutine (UMAT) for ABAQUS (Release version 2017) is employed, initially developed by Huang [231], and modified by Sweeney et al [232] modified to include back stress definitions for predicting non-linear kinematic hardening behaviour. This UMAT adopts a phenomenological power law flow rule for the rate of crystallographic slip $\dot{\gamma}$, as follows:

$$\dot{\gamma}^{\alpha} = \dot{a}\mathrm{sgn}(\tau^{\alpha} - x^{\alpha}) \left\{ \frac{|\tau^{\alpha} - x^{\alpha}|}{|g^{\alpha}|} \right\}^{n} \tag{2-6}$$

where $\dot{a}$ is the reference strain rate component and n is a rate sensitivity exponent. x^{α} is the back stress which is defined later in Equations 14 and 15. g^{α} is isotropic strain hardening parameter, defined by Peirce and co-workers [233] as:

$$g(\gamma_a) = g_0 + (g_{\infty} - g_0) \tanh \left| \frac{h_0 \gamma_a}{g_{\infty} - g_0} \right| \tag{2-6}$$

where γ_a is the accumulated plastic slip over all slip systems, defined below in Equation 16. g_0 is the critical resolved shear stress, g_∞ is the saturated stress, and the euqaitons for self and latent hardening can be derived from:

$$h^{\alpha\alpha} = h^{\alpha\beta} = h(\gamma_a) = h_0 \mathrm{sech}^2 \left| \frac{h_0 \gamma_a}{g_\infty - g_0} \right| \tag{2-7}$$

where h_0 is the initial hardening modulus, α and β refer to two specific slip systems. The self-hardening modulus $h^{\alpha\alpha}$ $(\alpha = \alpha)$, and latent hardening modulus $h^{\alpha\beta}$ $(\alpha = \beta)$ are assumed to be equal here. More details about self-hardening and latent-hardening moduli definitions can be found in prior literature [234-236].

The evolution of the hardening parameter is defined as the following:

$$\dot{\boldsymbol{g}}^{\boldsymbol{\alpha}} = \sum_{\boldsymbol{\beta}} \boldsymbol{h}^{\boldsymbol{\alpha\beta}} \dot{\boldsymbol{\gamma}}^{\boldsymbol{\beta}} \tag{2-8}$$

The original Huang UMAT was extended to include non-linear kinematic hardening by Sweeney et al [232], with the total back stress x^α, defined as a summation of two individual back-stresses (one for short and one for long range strains) defined by individual Armstrong-Frederick evolution rules as follows:

$$x^\alpha = x_1^\alpha + x_2^\alpha \tag{2-9}$$

$$\dot{x}_i^\alpha = C_i \dot{\gamma}^\alpha - D_i x_i^\alpha |\dot{\gamma}^\alpha| \tag{2-10}$$

where i = 1, 2; C_i and D_i are the material parameters which define the asymptotic limit and rate of decay of each non-linear back-stress evolution.

Accumulated crystallographic slip over all slip systems, which is key to the fatigue indicator parameters (FIP) for crack initiation in the present work, can be obtained by integrating over time, as follows:

$$\gamma_a = \sum_\alpha \int_0^t |\dot{\gamma}^\alpha| \, dt \tag{2-11}$$

2.8.3 A physically-based strain gradient CPFE modelling approach.

In order to evaluate the effects of grain size, a user defined element (UEL) subroutine with a strain gradient constitutive law, was developed by Dunne and co-workers [237], based on the incorporation of GND [238] effects. This slip rate calculation flow rule is established on the assumption of occurrence and pinning behaviour of gliding during the plastic deformation. GNDs act as barriers to mobile dislocations such as the statistically stored dislocations (SSDs) [239]. The flow rule is modified from the Gibbs creep rate equation [240, 241]

$$\dot{\gamma}^{\alpha} = \rho_{SSD}^{m,\alpha} v (b^{\alpha})^2 \exp\left(\frac{\Delta H}{-kT}\right) \sinh\left(\frac{(\tau^{\alpha} - {\tau_c}^{\alpha})\gamma_0 \Delta V^{\alpha}}{kT}\right) \tag{2-12}$$

where $\rho_{SSD}^{m,\alpha}$ and b^{α} are the mobile SSD density and Burgers vector, respectively, on the slip system α. ν describes the frequency of attempts for mobile dislocations to jump over the energy barriers whether successful or not. ΔH is the Helmholtz free energy, T is the temperature and k is the Boltzmann constant. ${\tau_c}^{\alpha}$ is the critical resolved shear stress and γ_0 is the reference slip.

$$\Delta V^{\alpha} = \frac{(b^{\alpha})^2}{\sqrt{\rho_{SSD}^{s}}} \tag{2-13}$$

$$\lambda_p = 1/\sqrt{\psi\left(\boldsymbol{\rho}_{SSD,i} + \boldsymbol{\rho}_{GND}\right)} \tag{2-14}$$

The activation energy ΔH is related to the pinning actions by SSD and GND over the associated activation volume ΔV, determined by the pinning distance λ_p, and the Burgers vector magnitude b^{α}. The pinning distance is related to the sum of immobile SSD density $\boldsymbol{\rho}_{SSD,i}$ and GND density $\boldsymbol{\rho}_{GND}$. ψ is the constant that defines the percentage of SSD or GND acting as pinning points of gliding. The mobile and immobile SSD density are assumed to be equal for simplification in this thesis.

The GND density ${\rho_{GND}}^{\alpha}$ is further decomposed to three separate components based on the types of dislocations, by two edge dislocations and one screw dislocation:

$$\sum_{\alpha=1}^{nslip} (\boldsymbol{\rho}_{\mathrm{s}}^{\alpha} \boldsymbol{b}^{\alpha} \otimes \boldsymbol{s}^{\alpha} + \boldsymbol{\rho}_{\mathrm{et}}^{\alpha} \boldsymbol{b}^{\alpha} \otimes \boldsymbol{n}^{\alpha} + \boldsymbol{\rho}_{\mathrm{en}}^{\alpha} \boldsymbol{b}^{\alpha} \otimes \boldsymbol{t}^{\alpha}) = curl(\boldsymbol{F}^{\mathrm{p}}) \tag{2-15}$$

where $\boldsymbol{s}^{\alpha}$ and $\boldsymbol{n}^{\alpha}$ are the two vectors parallel and perpendicular to the slip plane. $\boldsymbol{t}^{\alpha}$ is defined as product vector of the slip direction and slip normal, as ($\boldsymbol{s}^{\alpha} \times \boldsymbol{n}^{\alpha}$). $\boldsymbol{\rho}_{s}^{\alpha}$ **is** screw dislocation and $\boldsymbol{\rho}_{e}^{\alpha}$ is edge dislocation vector.

The GND density ${\rho_{GND}}^{\alpha}$ is defined as a function of the plastic deformation gradient:

$$\sum_{\alpha=1}^{nslip} \boldsymbol{b}^{\alpha} \otimes {\boldsymbol{\rho}^{\alpha}}_{GND} \;=\; \mathrm{curl}(\boldsymbol{F}^{\mathrm{p}}) \tag{2-16}$$

The circuit equation can be expressed in a surface integration format through Stokes' theory:

$$\boldsymbol{B} = \iint_{S} \left(\sum_{\alpha=1}^{nslip} \left(\boldsymbol{b}^{\alpha} \otimes {\boldsymbol{\rho}^{\alpha}}_{GND}\right)\right) \boldsymbol{r}\, dS \tag{2-17}$$

where $\boldsymbol{r}$ is the unit normal vector on an arbitrary surface S along the failure circuit.

The plastic deformation occurred within a crystal lattice generates a Burger's circuit $\boldsymbol{B}$ along the closure failure path, Γ. According to Nye's GND theory, the relationship between the deformation gradient and circuit can be expressed by:

$$\oint_{\Gamma} \boldsymbol{F}^{p}\, dx = \boldsymbol{B} \tag{2-18}$$

The critical resolved shear stress (CRSS) for a slip system α is calculated by:

$${\tau_c}^{\alpha} = {\tau_{c0}}^{\alpha} + MGb^{\alpha}\sqrt{\rho_{GND} \;+\; \rho_{SSD}^{s}} \tag{2-19}$$

where M is the Taylor factor [242] and G is the material shear modulus, and ${\tau_{c0}}^{\alpha}$ is the initial CRSS value.

The evolution of immobile SSD density ${\rho_{SSD,i}}^{\alpha}$ is implemented as follows:

$${\dot{\rho}_{SSD,i}}^{\alpha} = \frac{|\dot{\gamma}^{\alpha}|}{b}\left[\sum_{\alpha}\left(H^{\alpha\beta}\left({\rho_{SSD,i}}^{\alpha} + {\rho_{GND}}^{\alpha}\right) - 2cy_c{\rho_{SSD,i}}^{\alpha}\right]\right. \tag{2-20}$$

where c is a constant and y_c is the critical annihilation distance. The coefficients $H^{\alpha\beta}$ describe immobility relationships between dislocations, assigned a value of 0 when dislocations share the same or coplanar slip system, and a value of 1 for all the other cases.

The accumulated slip on a certain slip system α, after a modelling step Δt can be expressed as:

$$\gamma_{t+\Delta t}^{\alpha} = \gamma_t^{\alpha} + \int_t^{t+\Delta t} |\dot{\gamma}^{\alpha}| dt = \gamma^{\alpha} + |\dot{\gamma}_{t+\Delta t}^{\alpha}| \Delta t \tag{2-21}$$

Newton iteration is implemented in this model to determine the stress increment after each modelling step. The calculated stress is updated iteratively until the residual is below the defined tolerance (10^{-8} MPa).

2.8.4 Fatigue crack initiation (FCI) prediction with CPFE modelling

A key challenge for the prediction of microscale crack initiation, is the identification of suitable, scale-consistent fatigue indicator parameters (FIPs) [138, 243].

Dunne [244] and co-workers have shown for a C263 alloy, that accumulated effective crystal slip, aggregated over all slip systems, can be successfully implemented with CPFE to predict high and low cycle fatigue, including the effects of mean stress and even temperature. This parameter is denoted here as *p* and defined as follows:

$$\dot{p} = \left(\frac{2}{3}\boldsymbol{L}^{\mathrm{p}} : \boldsymbol{L}^{\mathrm{p}}\right)^{\frac{1}{2}} \tag{2-22}$$

$$p = \int_0^t \dot{p} dt \tag{2-23}$$

A further development of this approach is the accumulated strain energy dissipation *W* parameter. Compared to *p* which measures the effect of slip only, FIP *W* takes both microscale shear stress and slip rate into consideration, giving more accurate prediction in FCI. This FIP sums up the energy consumption on all the crystal slip systems as follows:

$$W = \sum_{\alpha} \int_0^t \tau^{\alpha} \dot{\gamma}^{\alpha} dt \tag{2-24}$$

Several other FIPs have been developed, e.g., the Fatemi-Socie FIP_{FS} and grain boundary impingement FIP_{GBI}, for fatigue crack initiation prediction of Ti-6Al-4V [245]. A new Dang Van criterion donated as FIP_{DV}, [246] measured the combined effects of the shear stress on individual slip systems and the hydrostatic stress and was used in aluminium alloy fatigue study. FIP_{FS} and FIP_{DV} are the two slip-dependent FIPs, which emphasize the influence of heterogeneous microstructure.

It has been shown that the cyclic values of these parameters, p_{cyc} and W_{cyc} typically evolve to a stabilised saturated value, so that the numbers of cycles for FCI is then predicted by dividing a critical FIP value by that of the stabilized fatigue cycle, shown below:

$$p_{\mathrm{cyc}} = p(t) - p\left(t - \Delta t_{cyc}\right) \tag{2-25}$$

$$W_{\mathrm{cyc}} = W(t) - W\left(t - \Delta t_{cyc}\right) \tag{2-26}$$

$$N_{i,p} = \frac{p_{\mathrm{crit}}}{p_{\mathrm{cyc}}} \tag{2-27}$$

$$N_{i,w} = \frac{W_{\mathrm{crit}}}{W_{\mathrm{cyc}}} \tag{2-28}$$

The experimental FCI life for LCF test was approximated from the total life fatigue data according to a damage approach [235]:

$$D = 1 - \left[1 - \left(\frac{N}{N_f}\right)^{\frac{1}{1-x}}\right]^{\frac{1}{y-1}} \tag{2-29}$$

where x and y are two parameters identified against all strain range tests to allow the best fit. FCI (N_{i}) is identified with a critical damage value D_c taken as 0.0125, based on an assumed crack initiation size equal to the RVE standard element size at the free surface.

2.9 Phase-field method (PFM) in grain growth modelling.

As introduced in section 2.7.4, PFM displays superiority when studying 3D polycrystalline and grain boundary evolution problems, compared to other modelling tools such as CA and MD. PFM can also be integrated with CPFE model, due to similar input variables and FE meshing tool. Thus, PFM is adopted in this thesis for grain growth simulation. A PFM based approach from MOOSE [247] is introduced below, for calculating the grain boundary (GB) migration process to predict the grain growth behaviour, at fixed temperature.

The governing equation for PFM simulation is the Allen-Cahn equation [248] :

$$\frac{\partial \eta_i}{\partial t} = -\mu \frac{\delta F}{\delta \eta_i}, i = 1,2,3 \dots N \tag{2-30}$$

where μ is the grain boundary (GB) mobility and f represents the free-energy functional. The evolution of variables is defined below by a modified Cahn-Hilliard equation:

$$\frac{\partial c_i}{\partial t} = \nabla \cdot M_i \nabla \frac{\partial F}{\partial c_i} \tag{2-31}$$

where c_i is the conserved variable, and M_i is the mobility. The local free energy density f_0 is a function of all concentrations and order parameters η_i, which can be expressed in the format:

$$\begin{aligned} F &= \int_V f\left(\eta_1, \dots, \eta_p, \nabla\eta_1, \dots, \nabla\eta_p\right) dV \\ &= \int_V \left[m f_0\left(\eta_1, \eta_2, \dots, \eta_p\right) + \frac{\kappa}{2} \sum_{i=1}^{p} \left(\nabla\eta_i\right)^2 \right] dV \end{aligned} \tag{2-32}$$

where an individual grain is represented by η_i, which equals to 1 within the grain and 0 in other grains.

The molar volume is assumed to be constant and the system is assumed to be under thermal equilibrium condition. κ is the energy gradient coefficient and should be always positive. Different grain orientations can be represented as a large set of non-conserved field variables.

The free energy is calculated as a function of the phase field variables and their gradients, in a homogeneous free energy format mf_0. The local free energy f_{loc} for the model can be further assumed using N conversed variables c_i as:

$$F = \int_V [f_{loc}(c_1, \dots, c_N, \eta_1, \dots, \eta_M)]dV \tag{2-33}$$

The evolution of order parameter in individual grains is described as:

$$\frac{\partial f}{\partial \eta_i} = \mu\left(\eta_i^3 - \eta_i + 2\gamma \sum_{j>i}^{N} \eta_i^2 \eta_j^2\right) \tag{2-34}$$

The homogeneous free energy is assumed to be zero within grains; thus the integral calculation from Equation (2-30) represents the total grain boundary energy within a system under the assumptions. The phase field evolution is then modified to be time-dependant by implementing the Ginzburg-Landau equation [249]:

$$\begin{aligned} \frac{\partial \eta_i(\mathbf{r},t)}{\partial t} &= -L \frac{\delta F(\eta_1, \eta_2, \dots, \eta_p)}{\delta \eta_i(\mathbf{r},t)} \\ &= -L\left[\frac{\partial f(\eta_1, \eta_2, \dots, \eta_p)}{\partial \eta_i} - \kappa \nabla^2 \eta_i\right] \end{aligned} \tag{2-35}$$

where γ, L and κ are model parameters determined by the GB surface energy σ_{GB}, the GB width for diffusion w_{GB}, and the GB mobility μ.

The definition by Equation (2-35) guarantees a continuous decrease in the total GB energy through the calculation of GB migration caused by the high temperature condition. An analytical model for two-grain configuration is derived when considering only the interaction between two grains indexed by i and j:

$$\frac{d\left(\frac{d\eta_j}{dx}\right)}{d\left(\frac{d\eta_i}{dx}\right)} = \frac{\eta_j^3 - \eta_j + 2\gamma_{i,j}\eta_i^2\eta_j}{\eta_i^3 - \eta_i + 2\gamma_{i,j}\eta_i\eta_j^2} \tag{2-36}$$

The equation 2-37 was developed for constructing the test function ϕ_m:

$$\begin{aligned} &\left(\frac{\partial c_i}{\partial t}, \phi_m\right) = -\left(\kappa_i \nabla^2 c_i, \nabla \cdot (M_i \nabla \phi_m)\right) \\ &-\left(M_i \nabla\left(\frac{\partial f_{\text{loc}}}{\partial c_i} + \frac{\partial E_d}{\partial c_i}\right), \nabla \phi_m\right) + \langle M_i \nabla(\kappa_i \nabla^2 c_i) \cdot \vec{n}, \phi_m \rangle \\ &-\left\langle M_i \nabla\left(\frac{\partial f_{loc}}{\partial c_i} + \frac{\partial E_d}{\partial c_i}\right) \cdot \vec{n}, \phi_m \right\rangle + \langle \kappa_i \nabla^2 c_i, M_i \nabla \phi_m \cdot \vec{n} \rangle \end{aligned} \tag{2-37}$$

Thus, the Equation 2-35 can be rewritten in the following format, for the use of respective interior and boundary integrals:

$$\left(\frac{\partial \eta_j}{\partial t}, \phi_m\right) = -L(\kappa_j \nabla \eta_j, \nabla \phi_m) - L\left(\frac{\partial f_{loc}}{\partial \eta_j} + \frac{\partial E_d}{\partial \eta_j}, \phi_m\right) + L\langle \kappa_j \nabla \eta_j \cdot \vec{n}, \phi_m \rangle. \quad (2\text{-}38)$$

2.10 Deep learning application in AM.

2.10.1 Deep learning development in process monitoring and quality control.

Currently, the most widely accepted idea of applying deep learning (DL) [250] algorithms in AM, is defect detection using in-situ thermographic monitoring. Compared to manual detection, DL is more effective and avoids potential human bias. Previously developed DL models [251] have reached an accuracy of 96.8% when recognizing the delamination and splatter defects from the thermal sensor images, as shown in Figure 2-14. This DL tool is light on computational cost and can be easily modified for detecting other defect types. Another convolutional neural network (CNN) -based DL model fulfilled a correlation accuracy of 85% validated against CT results, and further upgraded to an automatic defect detection and classification system for PBF-LB Ti-6Al-4V alloys [252, 253]. DL was also used to optimize the process parameters for Ti-6Al-4V [254].

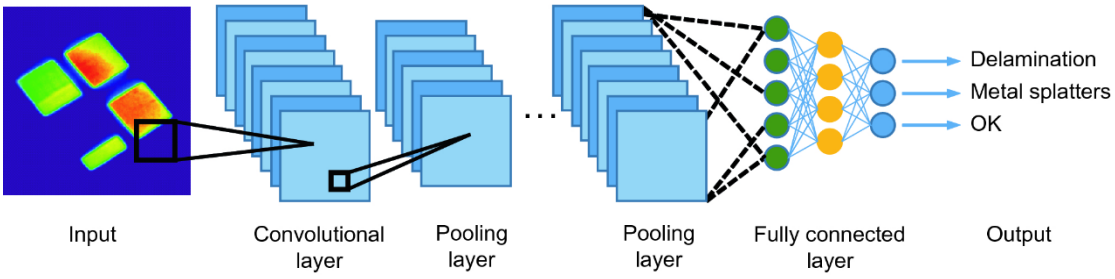

Figure 2-14. Application of CNN to detect defects, delamination and splatters from PBF imaging sensor [255].

2.10.2 Deep learning development in microstructural prediction.

CNN based DL has been used for automatic microstructure image recognition [256, 257]. However, there is still relatively little work on using DL models to predict microstructural evolution considering the limited possible alternative for real-time predictions or direct measurement. DL also helps quantify the microstructural variation in PBF, as shown in Figure 2-15 [258]. A genetic algorithm [259] was developed to determine the optimum AM parameters to get desired microstructure zones, with 30000 different scan paths as the training dataset, which could be improved and further investigated with a variation on other parameters.

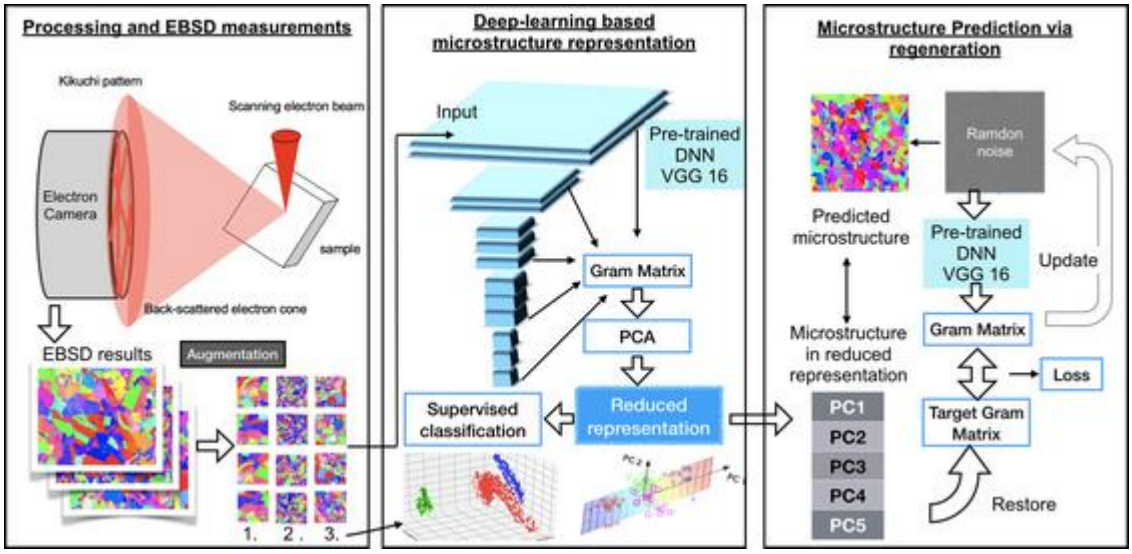

Figure 2-15. EBSD analysis for solid-state PBF materials [258].

2.10.3 Deep learning development in structure-property relationship.

Some studies have considered integrating DL with the structure-property prediction models to either assist decision making [260-263] and non-destructive quality control [264, 265], improve efficiency [266, 267] or predict mechanical properties [268] . Existing DNN-FE coupled methods focus on decision making and computational cost reduction [269, 270]. CNN, a subclass type of DNN model, was adopted as the encoder to study the crystallographic texture effect on the stress-strain behaviour [271] and orientation evolution [272] of a synthetic RVE morphology. CNN methods have been shown to give accurate DL predictions compared to CPFE simulations but with a greatly reduced

computational cost per run (order of milliseconds runtime). Yamanaka et al. [269] developed a DNN tool to read in 3D orientation maps including the 32 × 16 × 32 pixels Euler angle information of aluminium sheet material and applied this to estimate the biaxial stress-strain behaviour. The mean squared error (MSE) between CPFE modelling and DNN-3D prediction was less than 7% of the true stress extracted from nine points, and an approximate 3% error was calculated for predicted maximum stress at 0.05 strain. Compared to the DNN-2D modelling tool which read in a 32×16 pixel 2D pole figure, DNN-3D improves the MSE accuracy when predicting stress ratio in the biaxial tensile tests but also with a 50% longer running time. Miyazawa et. al [270] compared a two-point correlation (with 2-point features as inputs) with DL approach for the fatigue behaviour of a ferrite-pearlite dual phase steel. Mangal [273] used CNNs to predict stress localization and capture "hotspots" for the potential crack initiation locations.

While previous studies have successfully implemented DL techniques with various structure-property models, to the author's knowledge, such tool that captures the effect of phase and crystallographic orientation in AM materials has not been previously developed. CPFE model is generated based on the microscopic image, and such high contrast image format is intrinsically a favourable input for DL. The complex PBF parameters and the associated varying microstructure also require an effective and reliable characterisation tool, for processing quality control and parameter optimization. The next section introduces a DL algorithm developed for training a CPFE-based instant structure-property tool.

2.10.4 Deep learning training for CPFE-based data.

Over recent years, DL, a subclass of the general term machine learning (ML), has become a popular tool due to its ability to deal with big data efficiently. Compared to traditional ML techniques [274] such as Gaussian processes, regression trees, and linear regression, which often impose unrealistic or rigid assumptions about the input feature relationships, DL provides greater flexibility via an artificial neural network where successive transformations (known as hidden layers) of the inputs extract useful information from the previous layers to predict the final output, with minimal human bias. DL produces predictions by training and updating the implicit parameters in these layers

via a back-propagation algorithm which allows the model to run on extremely large data sets [275]. DL generates a pipeline-like structure, where data is input and flows through many layers, each with different transformation functions, according to the task at hand.

The base module of the DNN model implements CNN [276] as the kernels to extract information from the groups of images, and the design of the CNN contains the following layers:

Fully connected layer: this layer implements a perceptron for nonlinear transformation on the input data defined as:

$$y = \emptyset(wx + h) \tag{2-40}$$

where x is the high-dimensional feature input data, w and h are trainable parameters and $\emptyset$ is the activation function [277]. The fully connected layer is a non-linear transformer capable of handling arbitrary complexity and is widely used in DNN design [271]. Although the fully connected layer is effective in modelling data features, it is not suitable for image processing [278]. Since it cannot capture the local characteristics of an image, especially when the size of the image increases, the resulting number of parameters greatly affects DNN efficiency. In this work, each input image has $100 \times 100 \times 3$ pixels, further action is required to condense the size of the data. The further layers introduced are:

Convolution layer: this layer is used to capture local characteristics of an input 2D array such as an image [279]. A convolution layer consists of several small filters; each filter can capture one type of local characteristic within the input data. Unlike the fully connected layer which takes the whole image as the input, the convolution layer only needs a small part for each computation (usually 3 x 3 or 5 x 5), resulting in a much smaller number of parameters. The feature map generated by filters shows the distribution of the specific characteristic on the data (i.e. in which part the characteristic is more significant and in which part it is less significant, also denoted by a weight parameter). The stress-strain property of each instance is influenced by different characteristics of the data. The goal of the convolution layer is to determine the implicit characteristics that contribute to the stress property.

Pooling layer and dropout layer: these DNN layers are usually adopted to prevent overfitting. Overfitting can lead to the loss of the generalization power of a DNN. The pooling layer can smooth some intermediate characteristics to let the model be adapted to different settings (or sources) of the data. The dropout layer randomly drops a specific proportion of parameters during the training step. It would be helpful to reduce the model complexity during DNN optimization process to save computational cost. By training different DNNs, the generalization power is improved, and overfitting can be prevented.

The fully-connected multi-Layer perceptron developed by TensorFlow 2 is converted to a CNN by constraining the matrices. Take a 2D image input format **X** for example, its 2D hidden representations H has the same shape and spatial structure. The expression of the fully-connected layer is:

$$\begin{aligned}\mathbf{H}_{i,j} &= [\mathbf{U}]_{i,j} + \sum_k \sum_l [\mathrm{W}]_{i,j,k,l}[\mathbf{X}]_{k,l} \\ &= [\mathbf{U}]_{i,j} + \sum_a \sum_b [\mathrm{V}]_{i,j,a,b}[\mathbf{X}]_{i+a,j+b}\end{aligned} \tag{2-41}$$

where I and j donate the relative pixel coordination in the 2D input image. The tensors are re-indexed by $k = i + a$ and $l = j + b$ respectively. After convolution through invariant translation, the equation is converted to:

$$[\mathbf{H}]_{i,j} = u + \sum_a \sum_b [\mathbf{V}]_{a,b}[\mathbf{X}]_{i+a,j+b} \tag{2-42}$$

The value $[\mathbf{H}]_{i,j}$, after convolutional translation, can be obtained effectively by weighting pixels at the $(i + a, j + b)$ location. This conversion can be further condensed by ignoring the pixels too far away from the target by assuming a zero value of $[\mathbf{V}]_{a,b}$ once the distance exceeds the range tolerance Δ. Under this new assumption, the relationship can be re-written in the format:

$$[\mathbf{H}]_{i,j} = u + \sum_{a=-\Delta}^{\Delta} \sum_{b=-\Delta}^{\Delta} [\mathbf{V}]_{a,b}[\mathbf{X}]_{i+a,j+b} \tag{2-43}$$

The new format is a typical CNN layer, where **V** is referred to as a convolutional filter or kernel which determine the weight factor of the layer when determining the predictive output. The kernel is usually learnable and trainable, through optimization algorithms, to improve the predicting accuracy and efficiency.

The challenge of kernel and hidden layer optimization lies in the minimizing the objective function, rather than the generalized error. The optimization algorithm design is closely associated with the input data structure and is usually determined through training and validation group performance. More details on CNN layer architecture design and modification are shown in Chapter 7.

CNN is an important tool in practical DL application, especially when dealing with big data learning jobs. The billions of parameters in image recognizing works can be condensed to less than a thousand, without sacrificing the dimensional structure.

2.11 Gaps between current research and future PBF needs.

PBF industry grows rapidly due to its unique advantages. Publications containing PBF as the key word have increased by eight times in 2020 [280]. Based on the literature review presented in this chapter, future development of PBF needs better PBF product quality control, extended manufacturing capability, and improved efficiency and productivity. Some key challenges identified in the current applications are as follows:

(1) The microstructure of PBF, metal is more complex than its conventionally manufactured counterpart. Thus, realistic representative model including precise grain morphology, grain boundary misorientation, texture, and grain size, should be developed for better prediction of the micromechanical behaviour. No clear integrated method to develop such models exist.
(2) Need to better understand the microstructure-property relationship and develop better predictive capability. The PBF process allows for gradients in composition and thus have the gradient properties within a part.
(3) Need for coupled multi-scale and multi-physics models to establish a through process modelling framework. The PBF process includes different multi-scale and multi-physics phenomena that are typically impossible to describe sufficiently in a single model. Further effort is therefore required to integrate modelling tools for process-microstructure-property interdependence investigation.

(4) Need for an instant quality control tool to avoid process-structure-property uncertainties that hinder the PBF process. To address this issue, on the one hand, further development of in-situ and feedback systems especially on microstructure monitoring are required. On the other hand, the modelling time are usually much longer than that of the practical operation and process, if combined with multi-scale modelling method for process-structure-property. Artificial intelligence technologies, such as deep learning, have the potential to facilitate much rapid calculation. This technology can be implemented within the in-situ monitoring system or modelling framework for development within AM digital twins.

(5) Heat treatment (HT) and hot isostatic pressing, as the post-built thermal treatment required for stress relief and mechanical properties enhancement, need more comprehensive investigation. The capability of a bigger HT chamber is needed for larger scale PBF part. An emerging technology, in-situ HT saves the cost and time for PBF fabrication, however, requires a novel monitoring tool to check the in-situ HT temperature and the associated microstructure evolution.

3 Experiments: PBF-LB processing, microstructural characterisation, and mechanical testing.

3.1 Introduction

The computational models and tools developed and employed in this research require experimental characterisation, including microstructural measurements and mechanical testing, for parameter identification and overall model calibration and validation. This chapter first introduces the manufacturing processes (specimen design, printing parameter, post-built heat treatment) for the following materials: L605 CoCr (Chapter 4), Ti-6Al-4V (Chapter 5 and 6), and 17-4PH stainless steel (Chapter 7). It also introduces the microscopy protocol with special attention to the EBSD technique as it motivates the high-fidelity (the most direct source of microstructure data) modelling framework, see section 3.4. Finally, the mechanical testing protocol including tensile and fatigue are demonstrated.

3.2 Sample manufacturing and post-processing.

3.2.1 Processing parameters and sample design.

The PBF-LB Ti-6Al-4V samples used in Chapters 5 & 6 were manufactured from extra-low interstitial powder provided by Renishaw. The powder particle size was measured to range from 20-100 μm and had low thermal expansion and conductivity [281]. Figure 3-1 shows the Renishaw RenAM 500M model, located at the Irish Manufacturing Research centre, that was used for printing the Ti-6Al-4V specimens. This printer uses a 500 W pulsed wave emission laser as the energy beam source, with a wavelength of 1020 nm, with an argon atmosphere. Table 3-1 lists the PBF-LB process parameters adopted. A meander scanning strategy was also specified in the fabrication for consistent specimens without large deformation [282]. The specimen was vertically printed with the axial direction perpendicular to the powder bed.

Table 3-1. RenAM 500M printing parameters.

Power	Point distance	Exposure time	Layer height	Hatch distance
250 W	50 μm	90 μs	30 μm	0.1 mm

Figure 3-1. Renishaw RenAM 500M PBF-LB metal printer (left) for fabricating the Ti-6Al-4V alloys, 3D Systems ProX DMP 100 printer in NUI Galway (right) for 17-4PH SS, with inset image of view of buid chamber during specimen fabrication.

A build plate consisting tensile test specimens was configured in the 3D Systems 3DXpert build software at NUI Galway. However, hardware and access issues at that time prevented build completion at that time. Therefore published test data [79] on 17-4PH SS specimens was used for tensile and fatigue test data. The primary author of that study (Luiz Carneiro) thus collaborated on the publication of the paper emanating from Chapter 7 [283] in terms of tensile test data provision. The specimens used in Chapter 7 were fabricated by the Sentinent Corporation company in USA, using a PBF-LB machine, under the protection of the argon atmosphere. These 17-4 PH SS samples were orientated with the axial direction aligned with the build direction (vertically printed) and were of ASTM-E8 specification (Figure 3-2). Details about the specific PBF-LB machine were not fully disclosed by the company in charge of specimen manufacturing. The PBF specimen was then subjected to the recommended post-built heat treatment, this standard annealing process are described later in section 3.1.2.

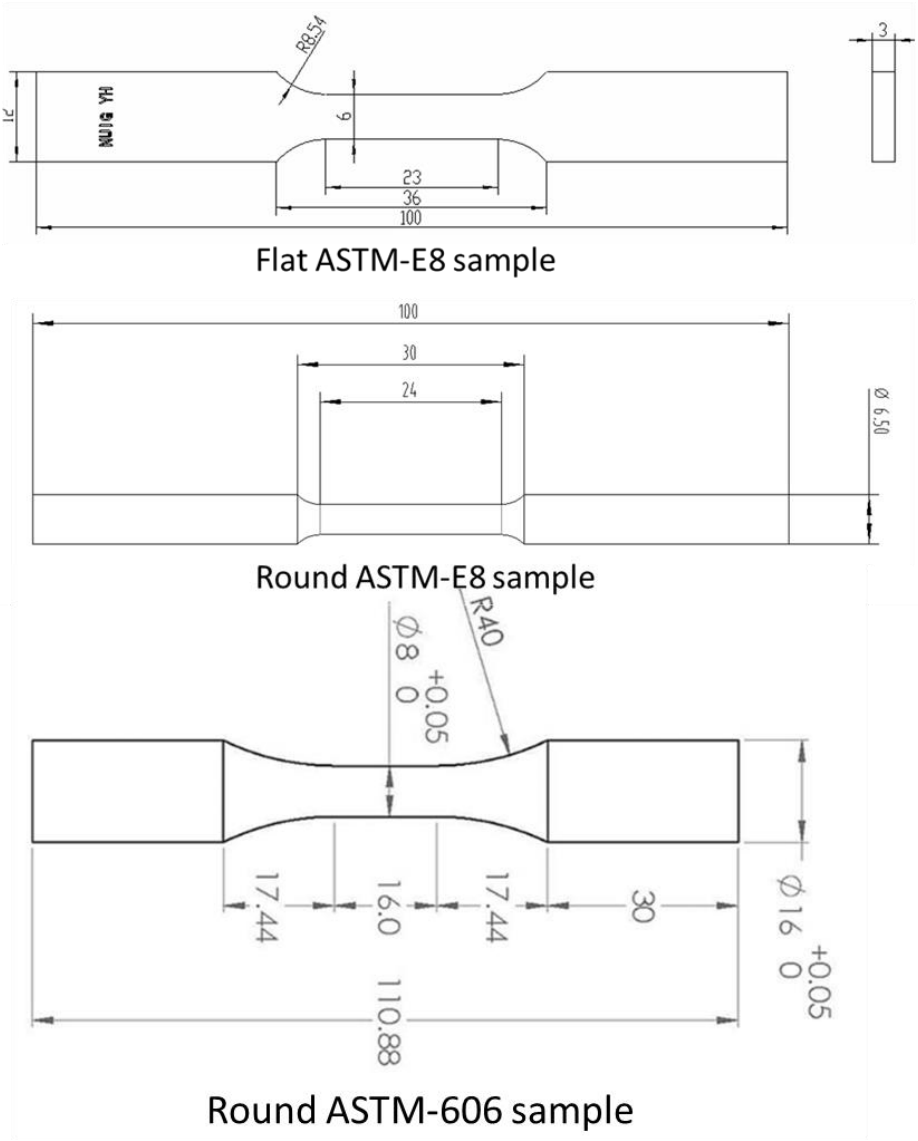

Figure 3-2. Designed geometry for the PBF-LB built samples: plate and round ASTM-E8 samples for tensile test, and ASTM-E606M sample for fatigue testing.

Figure 3-3 shows (a) the printed flat and cylindrical Ti-6Al-4V samples, following the ASTM-E8 standard recommendation, and (b) the cylindrical 17-4 PH SS samples, following the ASTM-E606 standard. Ti-6Al-4V specimen had a length of 16 mm and a diameter of 8 mm at the gauge section, The shoulder radius of the testing specimen was 40 mm. The grip section had a diameter of 16 mm. 17-4PH SS specimen had a length of

16 mm and diameter of 8 mm at the gauge section, The shoulder radius of the testing specimen was 40 mm. The grip section had a diameter of 16 mm. The mechanical test protocol employed in this test programme followed the ASTM-E8 [284] and the ASTM E606 standard [285] recommended for tensile and fatigue mechanical testing respectively

(a)

(b)

Figure 3-3. (a) RenAM 500M printed Ti-6Al-4V samples following ASTM-E8 standard. (b) PBF-LB 17-4PH SS following ASTM-E606 standard.

3.2.2 Heat treatment

Post-built heat treatment (HT) of PBF-LB alloys used in an electric Nabertherm oven (max temperature 3000 °C) in NUI Galway. Ti-6Al-4V samples were annealed 900 °C, for two different durations 50 & 100 minutes. The heated samples were then air cooled

(unassisted) to room temperature. Abrasive paper (Grit 400) was used on the samples to slightly smooth the surface. Figure 3-4 shows the four samples after HT. These samples were used for comparison and validation against modelling, with regards to their microstructure evolution and tensile properties in Chapter 6.

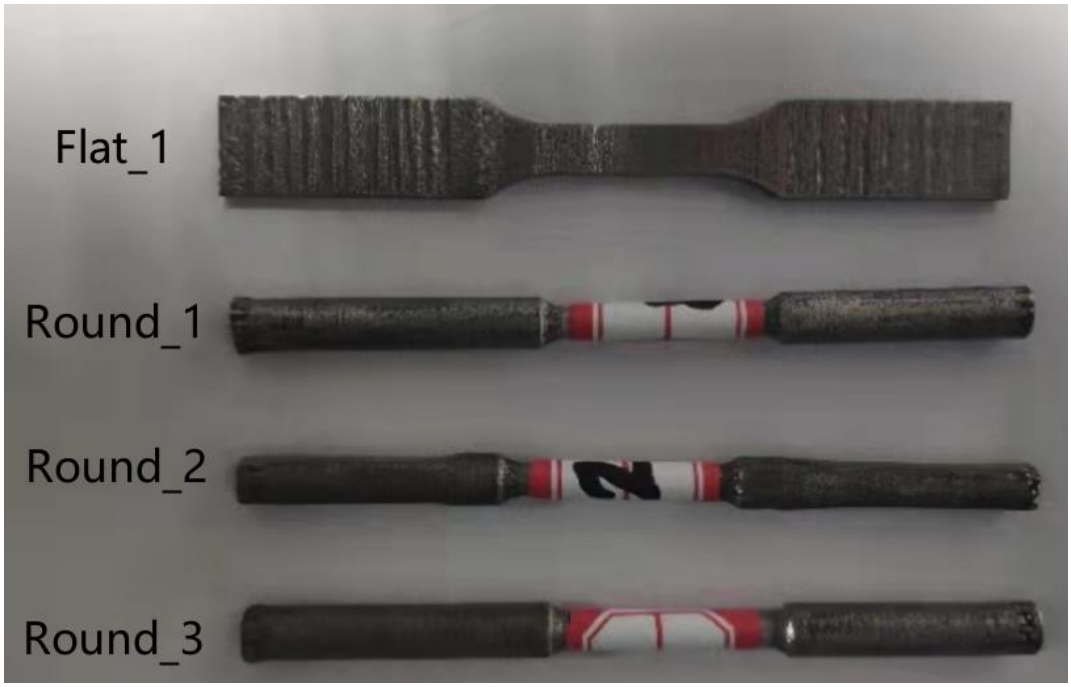

Figure 3-4. PBF-LB Ti-6Al-4V samples after HT with different HT time for comparison.

The post-built heat-treatment of all the PBF-LB 17-4PH SS samples also followed the standard HT H1100, which consists of solution annealing at approximately 1050 °C, air cooling, and then age hardening at 593 °C for 4 hours, followed by air cooling at room temperature. After the heat treatment process, grit blasting was conducted to improve the surface quality and the polished average surface roughness was measured as 60.1 μm.

The material of focus in Chapter 4 (L-605 CoCr alloy), was not PBF-LB manufactured but did undergo solution annealing at 1250 °C for 2.5 hours, and was the basis of previous published study from the group [183].

3.3 Microstructural characterisation.

Non-destructive inspection methods such as micro-CT is first used on the printed metal samples to check the porosity, internal defect, and surface roughness. For microstructural characterisation, such as EBSD, the samples need to be sliced, mounted, gritted using a succession of papers and polished with silica colloidal. A final etching step is also required for an investigation under an optical microscope or SEM. Energy Dispersive X-Ray spectroscopy (EDX) is necessary prior to EBSD scanning if the phase composition of the sample is unknown. The determined crystalline type from EDX helps input necessary crystal symmetry information when setting up EBSD analysis, ensuring reliable texture information.

3.3.1 Micro-CT scan and detection.

The cabinet cone-beam microCT, Scanco Medical μCT100 (shown in Figure 3-5) was used to scan the as-built part to check the overall manufacturing quality (porosity). The highest energy available (70 kV) and the highest intensity settings were set for the scans. Each sample scan contains 855 slices with a resolution of 3072×3072 pixels, corresponding to a 11.4 micron isotropic resolution. The raw data, image sequence data (.isq), was generated by combining these slices. A contouring drawing method was adopted for segmentation and threshold of the gauge transition area of the cylindrical or irregular sample. After contouring, the .isq file was converted to a graphical object, and was finally reconstructed as a 3D scan after thresholding, suitable for porosity and density evaluation.

Figure 3-5. Scanco Medical Micro-CT 100

Each scan included one ASTM-E8 flat sample and another round sample. Two scans were made per sample. The first scan checked the area at the bottom end of the sample directly attached to the powder bed during PBF while the second scan checked the necking area at the end of the gauge length where some failure took place. The micro-CT raw data was proceeded through a customized MATLAB code [286]and extracted 800 slices of the cross-section area were for a void and porosity check. Those slices have not detected obvious pores and the volume was calculated based on the reconstructed 3D files.

3.3.2 Sample preparation for microstructure analysis.

The L-605 CoCr alloy used in Chapter 4 was polished with a sequence of polishing paper and paste up to a final polish with 0.02 μm diamond suspension paste.

Chapter 5 and 6 details the micromechanical characterisation of Ti-6Al-4V. The sample preparation for PBF-LB titanium alloy is more challenging due to the harder alpha phase and higher surface smoothness requirement for revealing the complex lamellar

morphology. The detailed procedure below was based on and improved from the Buehler guide [287].

(i) Wet grinding with SiC paper down to 400, 800 (1200 optional) grits with water cooled, 240 rpm rotating speed using the Buehler AutoMet 250 polisher (shown in Figure 3-6), and apply 30N force to press at the centre top of specimen.

(ii) Change to a new abrasive paper and polishing mat, continue polishing using a 9 μm suspension on UltraPad under 25N load force for 10 mins.

(iii) Use 0.05 μm final polishing suspension on a soft, porous, chemically resistant synthetic polishing pad, ChemoMet supplied by Buehler, under 20N load force for a minimum of 20 minutes until obtaining plane surface through optical microscope check. This improved polishing protocol reduces the loading force to avoid undesired manually generated deformation twinning, but increases the polishing time in the final step to deal with the roughened part surface exposed to non-melted powder in the PBF process.

(iv) Rub with ethanol and ultrasonic cleaning before EDX testing.

Figure 3-6. Buehler AutoMet™ 250 Grinder-Polisher.

After going through the polishing protocol, the specimen needs to be etched to reveal different phase contrast and grain boundaries. CoCr was etched using a mixed chemical reagent of 100 ml HCL and 5ml 30% H_2O_2. The Kroll's reagent 187 (HF and Nitric acid by 2:1) supplied from Etchants UK was used to reveal the grain boundary of Titanium alloys. Hydrofluoric acid (HF) etches glass, therefore all HF processing is carried out in polyethylene or polymethyl pentene containers only. Ti-Al alloy is easy to be etched, and the etching process is complete once the colour of the surface changes (approx. 10 seconds). However, the etching job for Ti-6Al-4V is trickier due to no visible colour changes. In-house trails of various etching approaches concluded that using a pipette for dropping etching onto PBF Ti-6Al-4V samples offered the best etching depth control. A separate study on the effect of etching time and method types on image characteristics is available in Appendix A. The surface change (dimmed colour and scratched texture) is evident after the first drop. 3-5 drops are sufficient (cross-section of ASTM-E8 samples).

Table 3-2 summarizes the recommended procedures after several trails and optimization steps, for PBF-LB Ti-6Al-4V sample preparation.

Table 3-2. Recommended polishing and etching procedures.

Surface	Abrasive size	Load (N)	Base speed (rpm)	Rotation	Time
Carbimet	P400	30	300	Same	5:00
CarbiMet	P800	30	300	Same	Until Plane
UltraPad	9um Diamond	25	150	Opposite	10:00
ChemoMet	0.05um Silica suspension	20	150	Opposite	10:00
ChemoMet	0.05um Silica suspension	15	150	Opposite	Until Plane
Etching	Kroll's reagent. 5 drops. Dropping interval = 1 second.				

Chapter 7 investigate the structure-property relationship of 17-4PH SS. The 17-4PH SS sample was etched with Ralph's reagent to reveal the grain structure.

Etching is not performed on samples for EBSD characterisation because it roughens the surface around the grain boundary. Instead, for EBSD, further polishing steps are

performed which result in a surface smoothness capable of yielding sufficient diffraction data points (above 90%). The pre-etching process described above leads to 40 – 70 % valid EBSD points, which would result in significant missing data points in the grain map construction. The further polishing steps include:

(v) Vibrating polishing with the colloidal silica suspension on the VibroMet vibratory polisher for 1-2 hours and,

(vi) Ion polishing using the focused ion beam until achieving the optimal condition for EBSD measurement. A focused ion beam (FIB) generated from excited ions vaporises and exposes the sample surface to be directly suitable for an EBSD scan. The FIB milling uses 10 keV ion gun for a rapid milling, followed by 2 keV gentle polishing and cleaning until smooth, as observed under FIB-SEM.

3.3.3 Optical and Scanning Electron Microscopy

The etching process has revealed the different phases by varying colour depth and most importantly, it has made the grain boundary obvious for the ease of polycrystalline map reconstruction. The optical microscopy image in Figure 3-7 shows the general microstructure by stitching four 4:3 ratio images along the PBF printing direction, using the Olympus microscope and the associated Fujitsu post-processing tool (shown in Figure 3-8). The basket-weave lath within the parent phase prior-beta grain varies associated with the solidification process determined by the PBF process and cannot be characterized clearly in this macroscopic image. However, this is a good example showing the typical highly anisotropic prior-beta grains along the build direction. The columnar shape prior-beta grains in this Ti-6Al-4V sample have a length ranging from 100-1500 μm.

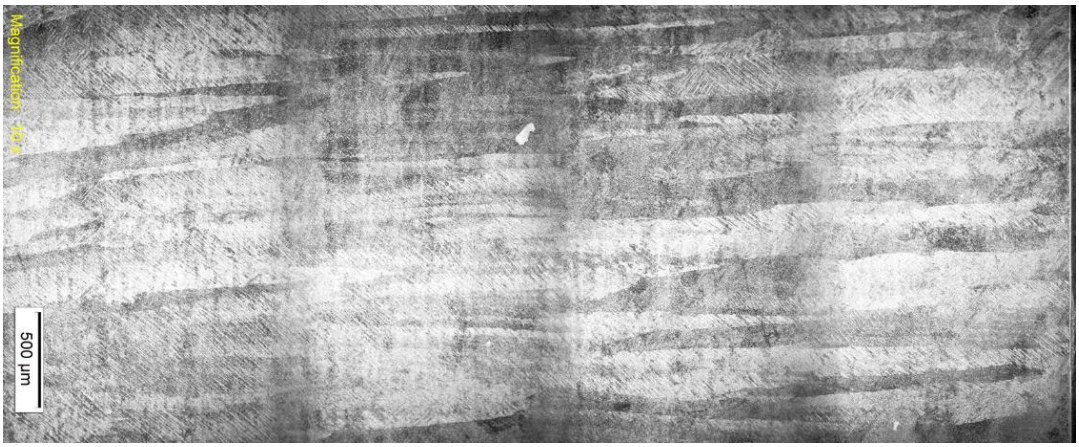

Figure 3-7. Optical microscopy image of PBF Ti-6Al-4V showing the macroscopic microstructure.

Figure 3-8. Olympus optical microscopy systems.

The cold field emission high-resolution SEM, Hitachi S-4700 (Figure 3-9) was used to reveal the microstructure at a higher resolution. For high magnification examination the etch depth should be shallow, while for low magnification examination a deeper etching yields better image contrast.

Figure 3-9. Hitachi S-4700 FE-SEM.

Figure 3-10 shows the SEM images of the etched PBF Ti-6Al-4V samples. (a) (b) and (c) show the microstructure of the cross-section surface along the build direction, at different magnitude scales. It is observed that the laths in this cross-section plane have a preferable growth direction as well as the segregated smaller needle α' lath in between the thicker laths. However, image (d) shows the SEM of the bottom surface of the sample attached to the powder bed directly. As a result, the microstructure does not show directional preference because it represents the solidified laths out of a single layer. All the Ti-6Al-4V images indicate a very fine lath width of the segregated alpha phase during the melting pool solidification.

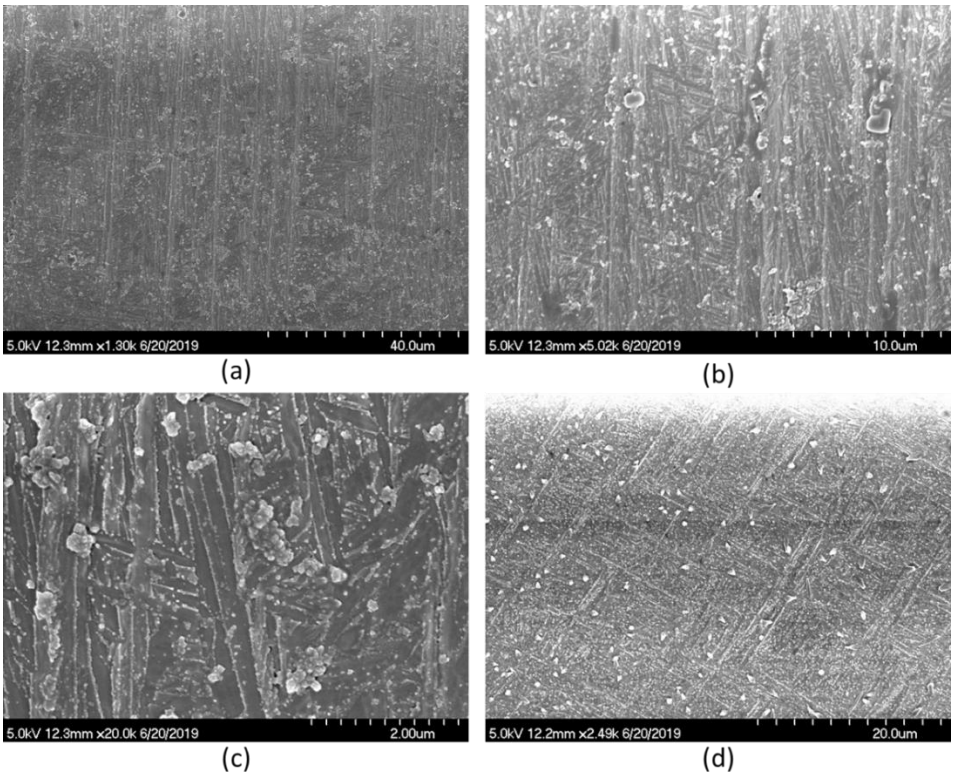

Figure 3-10. SEM microstructural images of two PBF Ti-6Al-4V samples from different cross-section surfaces.

3.3.4 Energy-dispersive X-ray (EDX) spectroscopy.

The EDX spectroscopy, also referred to as energy dispersive X-ray (EDX) analysis can be used either before or after polishing of the sample, to characterize the chemical composition of the surface. The EDX spectroscopy facility system associated with the scanning electron microscope model Hitachi S-4700 located at NUI Galway microscopy centre, was used in this thesis to quantify the chemical composition of the two near-alpha titanium alloys. During EDX scanning, SEM needs operate in high magnitude mode with the analysis mode activated. Figure 3-11 shows the EDX spectrums and the quantified element weight fraction for (a) as-build PBF Ti-6Al-4V, (b) Ti-6Al-4V samples after polishing and etching and, (c) Ti-Al sample after polishing and etching. The polishing step seems to have little influence on the EDX calculation. However, the scans of some specimens that did not receive complete cleaning detected up to 8% carbon, due to contamination. In such cases, this material needs to be removed via ethanol before repeat measurement.

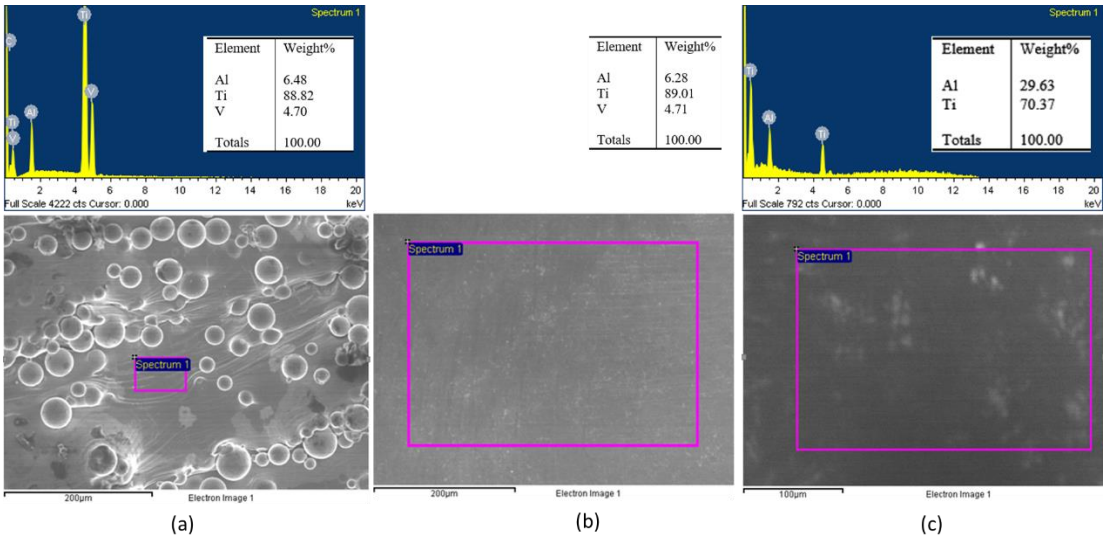

(a) (b) (c)

Figure 3-11. EDX spectroscopy results for the two PBF near-alpha alloys.

3.4 Electron backscatter diffraction (EBSD) measurement.

3.4.1 EBSD scan and measurement

Although various algorithms have been developed to measure grain morphology (e.g. intercept length method) from SEM images [288], such approaches require high contrast images as the measurement accuracy is highly dependent on the shape of the grain boundary, particularly for high-aspect ratio grains. As an advanced characterisation tool, EBSD offers quantitative microstructural feature measurement by directly counting the pixels within certain phase groups and grain aggregates. This tool is invaluable when studying irregular grain morphology materials such as those found in PBF metals. EBSD also provides crystallographic orientation data for individual grains, which assist in determining the texture, misorientation and anisotropy features in PBF samples. Due to the above reason, EBSD is the key characterisation tool in this thesis, for both microstructural inspection (grain map, phase data and orientation data) and as direct-from-source raw data for computational model construction.

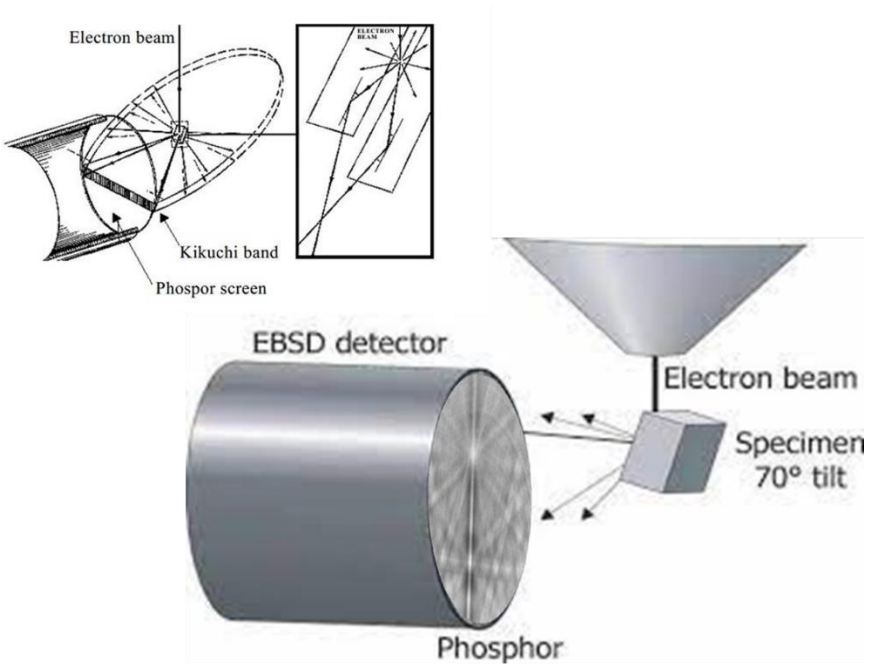

Figure 3-12. Principle of EBSD, diffraction, Kikuchi band, and texture detection [289].

EBSD scans of Ti-6Al-4V were taken using the FEI (Thermo) Helios G4 CX DualBeam instrument system equipped with the focused ion beam (FIB) and the Oxford EBSD detector located at Bernal Institute, University of Limerick (UL), shown in Figure 3-13. The Ti-6Al-4V sample used in Chapter 5 and 6, was cut from the cross-section along the build direction with the scan area of 38×25 μm with the resolution (step scanning increment) of 0.05 μm. EBSD scans of SS 17-4PH were outsourced to a Jeol JSM-7100F field emission SEM located at the University of Nevada, Geology department, equipped with an Oxford EBSD detector. A microstructural sample was cut from the gauge area using a scan area of 300×300 μm and a resolution of 0.5 μm to detect the austenite and martensite phases together with their crystallographic orientation texture.

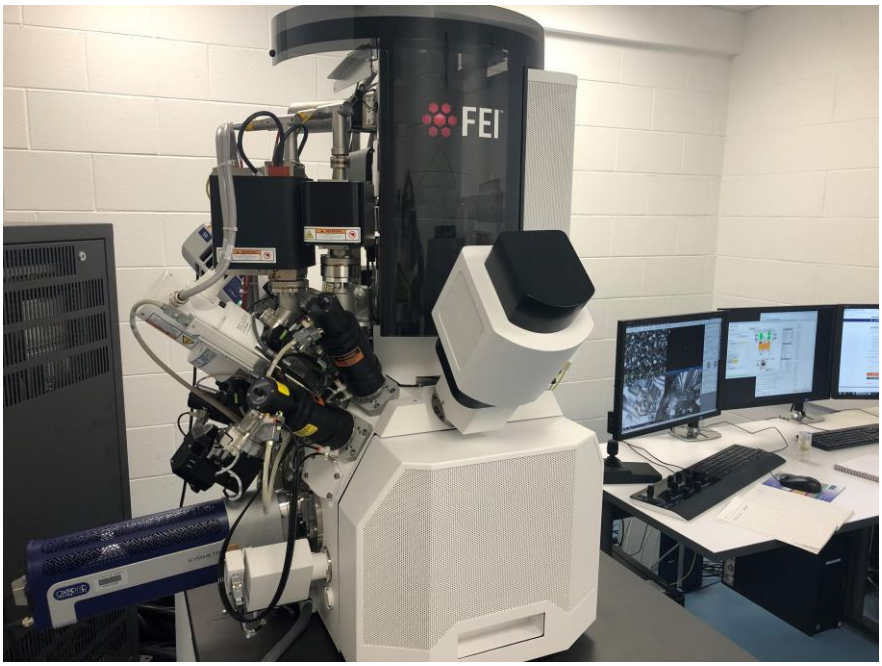

Figure 3-13. FEI Helios G4 CX SEM system, equipped with the Oxford Instrument EBSD prob.

Figure 3-14 shows the sample preparation and settings for EBSD scanning. The specimen needs to be either mounted in an electrically conductive resin or stuck with a conductive band. During EBSD measurement, the electron beam firstly hits the sample surface at a tilt angle of 70°. Y axis in the scan was defined to be alongside the built direction. The backscattered electrons contact the crystal and generate two diffraction cones, which later interact with the phosphor screen to form the bands. The position of the cones, the bandwidth and symmetry of the crystal together determine the final indexing process through the Hough transformation [290].

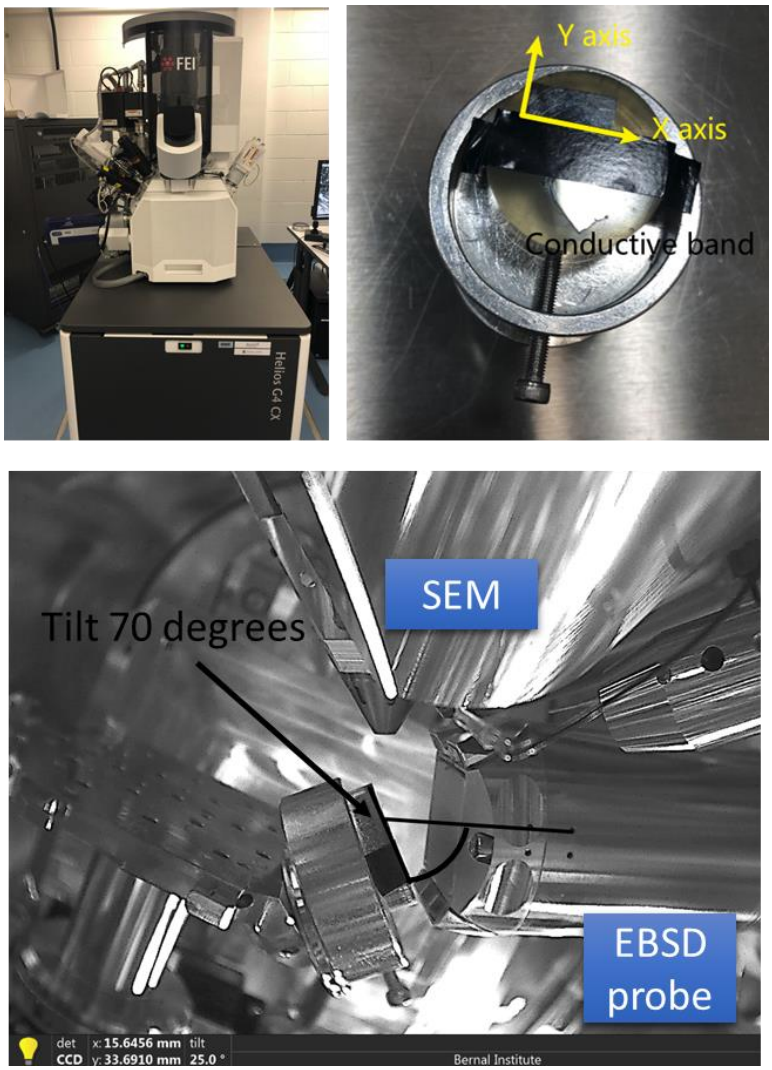

Figure 3-14. EBSD sample preparation and internal placement in the vacuum chamber, image taken in UL.

FEI Helios DualBeam FIB-SEM system generates up to 30 kV accelerating voltage from the Schottky field emitter energy source, with the ion beam current ranging from 0.8 pA to 22 nA. The resolution is up to 0.8 nm scanned under a voltage of 15 kV, while 1.4 nm at 1 kV. The EBSD probe has a symmetry detector which permits efficient generation and indexing of the scanned pixels. It takes 30 minutes to complete a scan containing 1 million pixels, with high resolution grid of 50 nm, corresponding to a sample area of 140 μm × 87 μm.

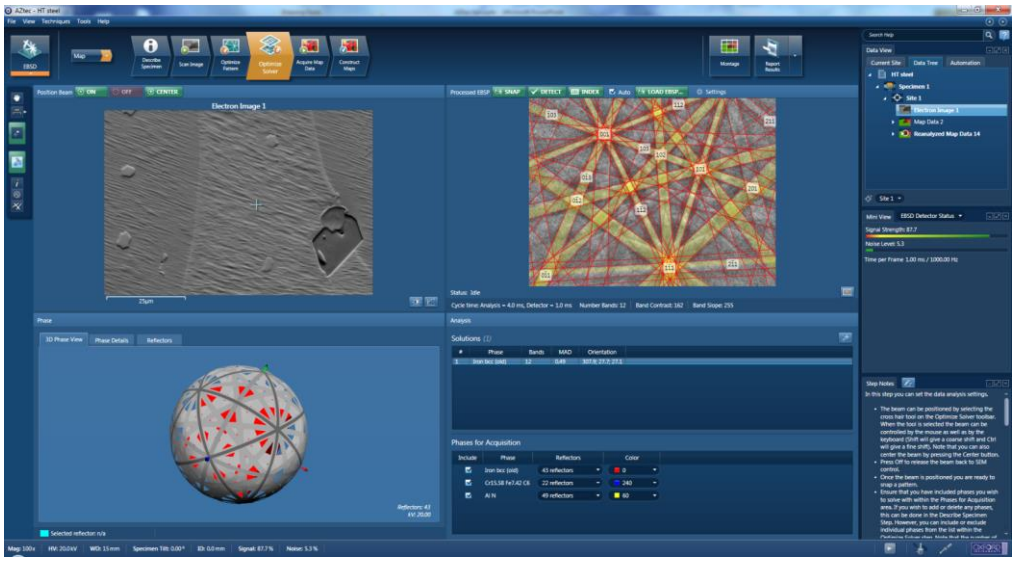

Figure 3-15. User interface of AZtec for diffraction calculation and Kikuchi band indexing, during the process of scanning Ti-6Al-4V sample used in this thesis.

3.4.2 Polycrystalline grain map reconstruction

The capabilities of EBSD include grain microstructure analysis through post-processing on the Oxford Channel text file (ctf) file to reconstruct the polycrystalline grain map including information such as grain size, grain shape, and phase distribution. Figure 14 shows a snapshot of the commercial software package AZtec user interface when the probe is fetching and indexing the grain map data, based on the crystallographic relationship, for the Ti-6Al-4V sample. Figure 3-15 shows the EBSD pixel acquisition and data indexing from the diffraction bands.

Figure 3-16. EBSD probe is indexing a PBF-LB Ti-6Al-4V scan, ~25% progress.

The grain map reconstruction usually contains two steps, clean-up and grain segmentation. The clean-up process replaces the non-indexed or noise with more reasonable indexed data through neighbouring grain relationships (neighbour correlation). MTEX [291] provides a grain erosion and dilation algorithm to successfully fill the bad data when the non-indexed region is less than 30%. The most popular approach for segmenting the grains is known as the burning algorithm by picking a random location as the starting scanning point and adding the nearest neighbouring pixels into its aggregate if less than the specified threshold tolerance. This approach is adopted by MTEX [292], ATEX [293] and DREAM3D [294]. The detailed parameters and optimization process is introduced in Chapter 4 methodology section.

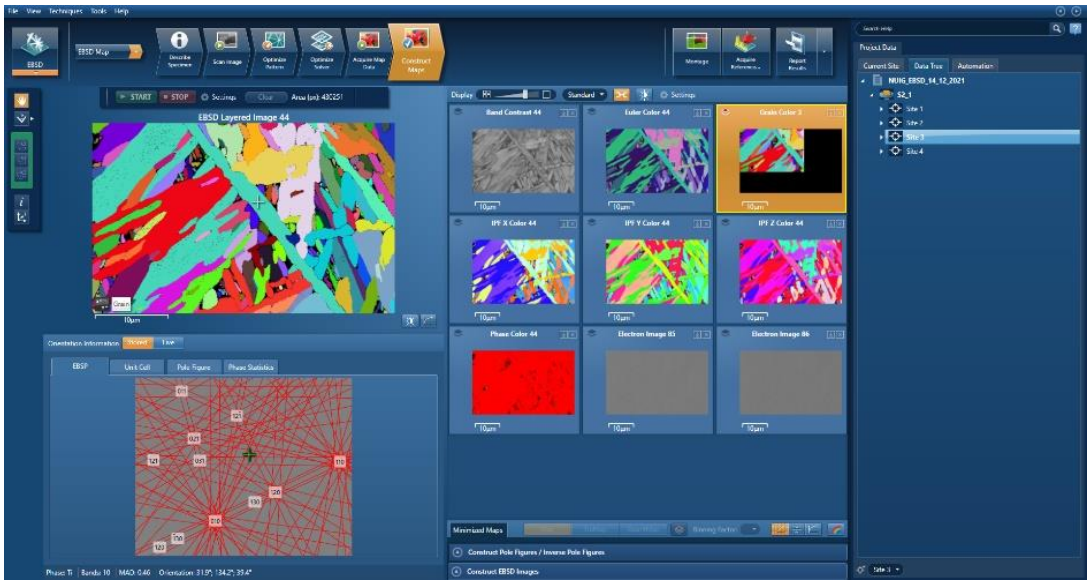

Figure 3-17. Full grain map reconstruction, colouring and editable file extraction in AZtec.

3.4.3 Texture analysis

This thesis uses HKL standard coordinates to record the crystallographic orientation. The specimen coordinate transformation is defined through three Euler angles in Bunge definition: φ_1, Φ, and φ_2. The Bunge Euler angles make the second rotation about the x-axis compared to Roe, Matthies and Kocks angles which rotate about the y-axis.

The Bunge Euler angles are calculated to plot the orientation distribution in three types: (i) pole figure showing the general texture on a projected crystal plane, (ii) inverse pole figure (IPF) emphasizing the texture direction and strength on a projected sample plane, (iii) orientation distribution functions (ODF) focusing on the intensity of Euler angles projected in a Euler space. Figure 3-17 shows a reconstructed grain map example, coloured according to the Euler angles and crystallographic types, as well as the conversion of the raw data into .ctf type data, a more common and user-friendly format for analysis.

After grain reconstruction and texture analysis, it is also feasible to calculate the misorientation distribution function (MDF) through the similar approach adopted by ODF

measurement. In this thesis, the Kernal averaged misorientation method is used to calculate the misorientation relationships.

These Euler angles are finally converted to a rotation matrix, which links the grain orientation with the three user-defined subroutine introduced in Section 2.7, in finite element modelling work. The three rotations are calculated as:

$$\boldsymbol{g}_{\varphi_1} = \begin{pmatrix} \cos\varphi_1 & \sin\varphi_1 & 0 \\ -\sin\varphi_1 & \cos\varphi_1 & 0 \\ 0 & 0 & 1 \end{pmatrix}$$

$$\boldsymbol{g}_{\Phi} = \begin{pmatrix} 1 & 0 & 0 \\ 0 & \cos\Phi & \sin\Phi \\ 0 & -\sin\Phi & \cos\Phi \end{pmatrix}$$

$$\boldsymbol{g}_{\varphi_2} = \begin{pmatrix} \cos\varphi_2 & \sin\varphi_2 & 0 \\ -\sin\varphi_2 & \cos\varphi_2 & 0 \\ 0 & 0 & 1 \end{pmatrix}$$

Thus, the rotation matrix is obtained by multiplying these matrices in sequence:

$$\boldsymbol{g} = \boldsymbol{g}_{\varphi_1} \cdot \boldsymbol{g}_{\Phi} \cdot \boldsymbol{g}_{\varphi_2}$$

3.5 Tensile and fatigue tests

3.5.1 Axial tensile test

The mechanical behaviour of PBF metals was measured through experimental testing to facilitate constitutive behaviour calibration and validation of the CPFE model. The stress-strain curve, as well as the fatigue life are compared to the CPFE predicted result shown in result section of Chapters 4-7.

The tensile behaviour of three PBF-LB Ti-6Al-4V samples following ASTM-E8 standard was first tested on Instron-4467 at NUI Galway under room temperature. This machine does not support extensometer control/data logging. Thus the testing result is only adopted for a quick estimation of yield strength and ultimate strength of the sample, but is not used for modelling validation. Details on the test results from Instron-4467 are provided in Appendix B1. Ti-6Al-4V samples introduced in Chapter 5 & 6 were all tested

on an Instron 8500 servo hydraulic machine at NUI Galway using flat jaws, equipped with a clip-on strain extensometer. The V-shaped jaws were also used to test the cylindrical specimen; however, the gripping force was not sufficient, and the grip became loose during the test. The tests were only able to continue after some adjustments to the sample geometry modification. The initial tensile speed was set at 1.25 mm/min and increased to 2.5 mm/min after yield.

As for the 17-4PH SS samples used in Chapter 7, axial tensile test was conducted under ambient air conditions using a servo-hydraulic tension-torsion Instron load frame equipped with the 8800 controller, located at the University of Nevada, as detailed in a prior publication from that research group [79]. The test machine has a maximum loading force capacity of 222 kN to characterise the plasticity behaviour of the 17-4PH SS material.

Figure 3-18. Instron 4467 (left) and 8500 hydraulic machines (right) for tensile and fatigue testing at NUI Galway.

3.5.2 Fatigue test

The L-605 CoCr sample was tested at room temperature on an Instron 8500 servo hydraulic machine using V-shaped jaws, as previously published [295]. The strain-controlled LCF behaviour tests with a cyclic strain ratio of -1 were carried out at four different strain ranges. Closed-loop control of strain-range and strain rate (0.01 s^{-1}) was monitored via a clip-on extensometer. The critical fatigue crack initiation (FCI) values have previously been identified by comparison of predicted and measured FCI data for sample tests, with validation against other independent data.

The strain-controlled LCF test of PBF Ti-6Al-4V was also on Instron 8500 machine with the clip-on extensometer to accurately monitor the strain deformation. The strain rate was set as 0.001 s^{-1} with an interval of 0.002. The fatigue test was tested on $\pm 0.5\%$ only due to the poor ductility of the sample. The details of this fatigue test are provided in Appendix B2.

The strain-controlled fatigue tests of PBF 17-4PH SS samples were equipped with an extensometer with a gauge length of 12.7 mm to monitor and measure the strain evolution. The tensile test was conducted under displacement control with an approximated strain rate of $8 \times 10^{-4}\ s^{-1}$. Fully reversed strain-controlled fatigue tests were conducted with the testing frequency from 0.2 Hz to 10 Hz according to the strain amplitude ranging from 1.5×10^{-3} to 1.0×10^{-2}. The strain limit is 40% in the monotonic tensile test and ±10% in the fatigue test. During individual cycles in the fatigue test, a minimum of 200 data points were recorded, and the fatigue failure was considered to take place once the maximum stress was reduced by 5% compared to the stabilized peak value. The fatigue tests under four different strain ranges are compared to the modelling prediction, in Chapter 7.

4 A high-fidelity EBSD-CPFE modelling tool for grain size sensitive fatigue crack initiation assessment in CoCr alloy.

The core contents of this chapter have been published in as [Tu Y, Leen SB, Harrison NM. A high-fidelity crystal-plasticity finite element methodology for low-cycle fatigue using automatic electron backscatter diffraction scan conversion: Application to hot-rolled cobalt–chromium alloy. Proceedings of the Institution of Mechanical Engineers, Part L: Journal of Materials: Design and Applications. 2021;235(8):1901-1924. doi:10.1177/14644207211010836] ….

4.1 Introduction

CoCr alloys are employed in the medical device industry for a number of important applications, including cardiovascular stents [296] and orthopaedic hip implants [297, 298], where design against premature fatigue failure is of critical importance. In recent years, major advances in microstructural imaging, including electron backscatter diffraction (EBSD), have enabled accurate visual characterisation of grain structures and their orientation [21]. In parallel, advances in computational modelling methodologies, including crystal plasticity finite element (CPFE) modelling, have permitted advanced microstructural mechanical characterisation [23]. The common approach to CPFE modelling for load-bearing prediction of metallic structures involves the simulation of simplified grain morphology and substructure detail. The methodology generates high-fidelity CPFE models, by directly converting measured EBSD metal microstructure grain maps into finite element microstructural models, and thus captures essential grain definition for improved microstructure-property analyses.

This chapter provides a detailed systematic procedure including the development of an automatic tool for EBSD processing to convert data directly into image-based realistic

CPFE models for high-fidelity EBSD-based micromechanical predictions. Attention is focused on the cyclic plasticity and low cycle fatigue (LCF) crack initiation response for the biomedical-grade CoCr alloy, previously experimentally characterized by Sweeney et al. [183, 235, 296]. The latter presented experimental testing characterisation, and FE modelling, J2 continuum plasticity and CPFE, based on a VT methodology. To demonstrate the reliability and accuracy of the new method, comparisons are made with VT-generated models as the conventional and convenient CPFE method, and also against the experimental test data.

This chapter details a methodology for predicting the structure-property effect of as-manufactured microstructure, including true grain morphology and orientation, on cyclic plasticity and fatigue crack initiation in biomedical-grade CoCr alloy. As a starting point, this work distinguishes the performance between two commonly adopted representative volume element (RVE) methods; Voronoi tessellation (VT) and real image-based models, as detailed in Chapter 2.7.2. The convergence of the minimum RVE sizes for both models need to be quantitatively determined, e.g., the sufficient volume of RVE required to either obtain a reliable stress-strain relationship, or address the "hot spot" location leading to fatigue crack formation. These outputs offer useful criteria and significant guidance for RVE generation method, cropping size selection, and scattering elimination in the following studies, Chapter 5-7.

4.2 Methodology

4.2.1 High-fidelity EBSD image-based methodology

A key objective of the present work is to develop an optimum methodology for the rapid and accurate construction of image-based computational microstructural models. The methodology is predicated on the use of EBSD, which is an advanced microscopy technique, based on scanning electron microscopy as described in Section 3.4 and [21] [299]. This methodology is motivated by the two new types of information obtained from the automated EBSD technique: (i) quantitative orientation for each individual crystal and

(ii) ability to represent texture. The capability for detection with high pixel resolution facilitates a high accuracy, high-resolution grain boundary demarcation process. The reconstructed grain maps based on the quantitative orientation map, in turn, represent the grain morphology and grain size information with high resolution [300]. Before mechanical tests, EBSD imaging was conducted on the polished L605 CoCr surface, to produce crystallographic orientation maps parallel to the central axis of the cylindrical specimen [295]. An initial grain reconstruction attempt was performed on the EBSD raw data using an open-access toolbox MTEX [291] with a segment tolerance angle of 5 degrees. Figure 4-1 shows the segmented grain map, coloured with inverse pole figure definition. Each colour represents a unique orientation, defined by the set of three Euler angles, corresponding to the perpendicular plane direction projected on the colour legend.

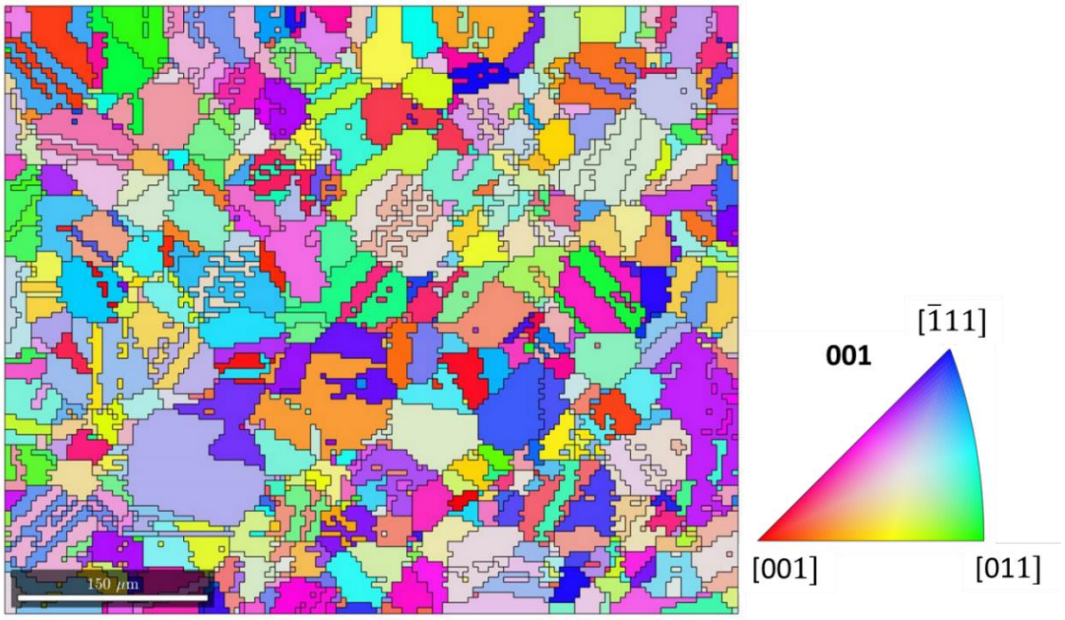

Figure 4-1. Reconstructed 576 μm × 476 μm grain map of CoCr alloy from electron backscatter diffraction (EBSD) scan.

The mean orientation values of the pixels within the same segmented grain were then calculated and projected to generate the scatter pole figure and the inverse pole figure, as shown in Figure 4-2. Plane projections on the three pole figure reference spheres only show very small areas of red, where similar orientations are shared. The indicated texture

strength is calculated as 1.2% by MTEX, which is equal to the fraction of projected orientations within a 10-degree difference compared with the direction of the vector orthogonal to fibres (a presumed directional texture that is mostly orthogonal to all the grains) in the (001) pole figure. The quantitative texture strength analysis indicates negligible preferred crystal orientation, i.e., random orientation. Consequently, in the more conventional VT method for CPFE model generation, as described below, random orientations are assigned for the cubic cell RVE model.

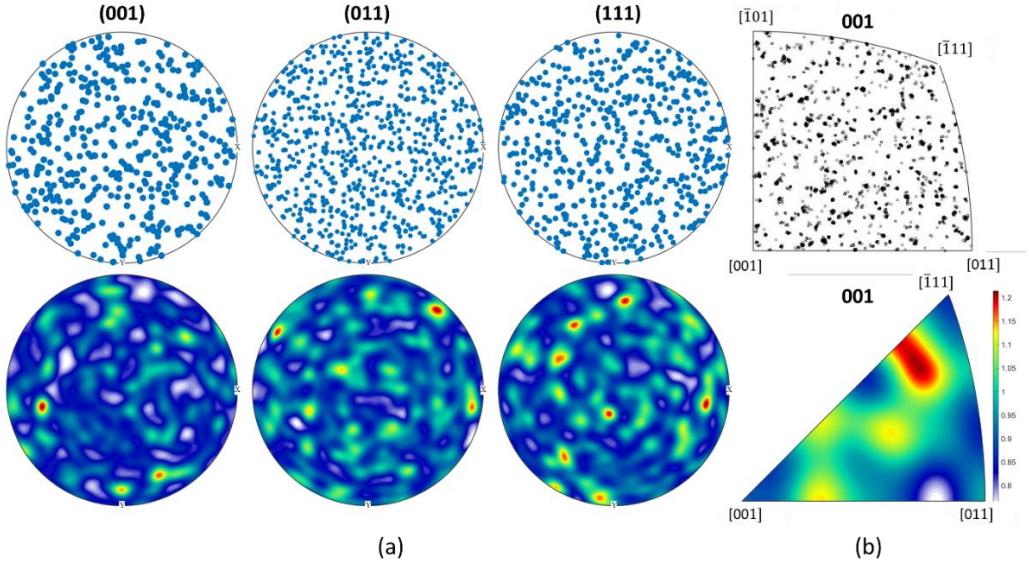

Figure 4-2. (a) Grain orientations are projected on three reference sphere planes (001) (011) and (111) to plot pole figures for CoCr alloy and (b) texture strength of 1.2% obtained through inverse pole figure analysis.

The proposed new methodology for converting EBSD data into a high fidelity CPFE is developed in the commercially available programming language MATLAB (MathWorks) [301]. The MATLAB code calls a number of other software tools, including MTEX, DREAM3D (Digital Representation Environment for the Analysis of Microstructure in 3D) [294, 302] and Python, for microstructure manipulation and mesh generation etc. Figure 4-3 shows a graphical illustration of the conversion process used for the present CoCr alloy, starting from EBSD raw file processing, microstructural information conversion, to linkage with CPFE constitutive laws. Unlike other digital microstructural reconstruction tools running from the command line, DREAM3D works

through a pipeline consisting of several filters with unique functions. The EBSD information including the pixel coordinates and the associated orientations are input into the pipeline structure which contains the EBSD reader and FE mesh writer functions. Outputs from such generated pipeline clearly define data containers with reconstructed and meshed grain information. This structure provides flexibility for customized plug-ins and makes it easier for combined use with Python to import necessary reconstructed imaging information for CPFE simulation in the commercially available general purpose FE solver ABAQUS [303].

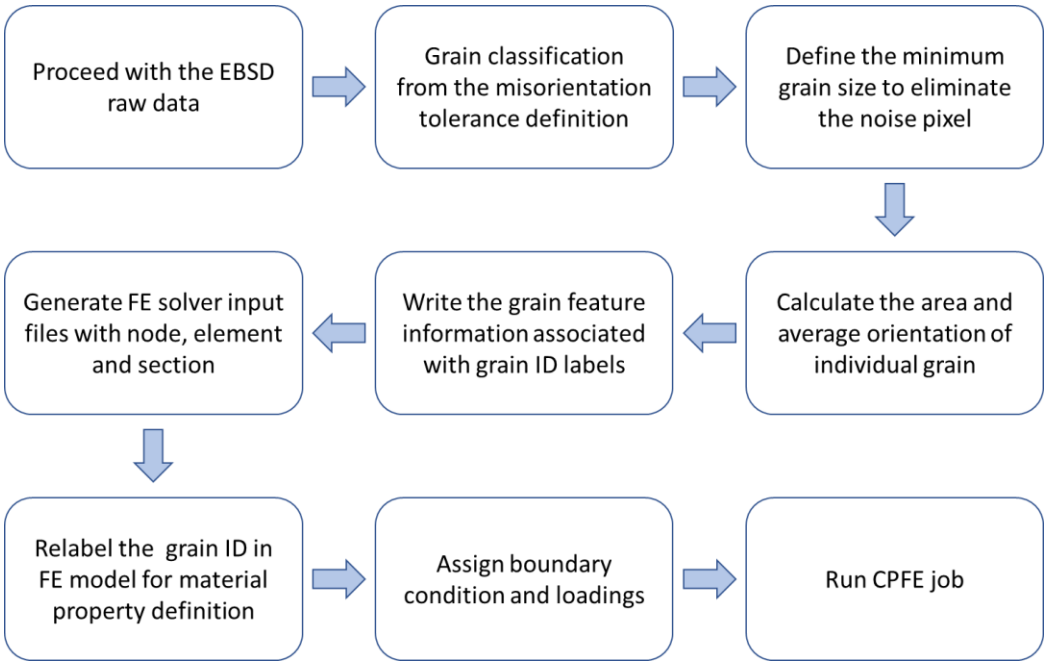

Figure 4-3. Flowchart of the overall steps of generating a realistic CPFE model based on the EBSD characterisation.

The microstructure information acquired by the EBSD measurement technique is shown in Figure 4-4 (a) with planar dimensions of 576 μm × 476 μm. The EBSD raw data was firstly processed with MTEX. The microstructure morphology was processed in a series of image cleaning steps, involving:

- specification of feature recognition tolerances,
- eliminating poor-quality pixel and
- minimum grain size removal, in order to minimise noise artefacts.

In this grain reconstruction procedure, the grain segmentation process depends largely on the quantitative orientation measurement of EBSD; non-indexed regions, as shown by the small white dots in Figure 4-4, were assigned to the surrounding grains [304]. Consequently, the algorithm [305] merges the voxels sharing similar orientations into the same grain ID list, by comparing the misorientation angle with the critical tolerance between the seed voxel and each of its neighbours. After each loop a new reference seed voxel is chosen to write up another grain list, and this process repeats until all the voxels are indexed. Hence, this process is sensitive to the precise value assigned to the relative misorientation tolerance, as it determines if a pixel belongs to the same grain as a neighbouring element or is a separate grain or feature. Too large a misorientation tolerance angle allows too many voxels for the same feature, especially with respect to lack of sudden misorientation change in deformed material. Too small an orientation tolerance will overpopulate the model with excessive independent features. However, a significant amount of imaging artefacts was observed when processing the EBSD raw data. The spurious data is possibly due to the presence of pores or precipitates or, are unindexed grain boundary points due to duplicate data from adjoining grains, thus distorting the pattern recognition. One solution to this issue is to increase the misorientation tolerance angle during grain segmentation [300].

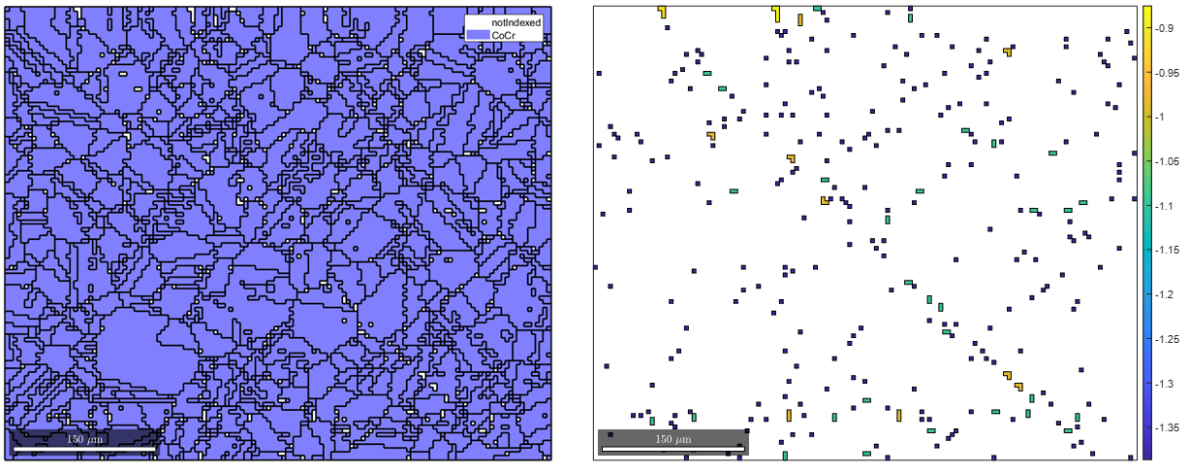

Figure 4-4. (a) EBSD measurement with noise before post proceeding. The non-indexed pixels are shown in white regions and the FCC structure CoCr phase shown in blue. (b) Noise measurement through quotients between the noise pixel area and the boundary length.

Commonly used misorientation tolerance angles range between 5° and 10° [306]. Thus, four misorientation tolerance angles, 5°, 8°, 10°, 15° were tested on the same EBSD raw data. The proceeded maps with the four settings varied little with respect to the resulting total number of grains, viz. 1096, 1042, 1018, 988 respectively. The misorientation tolerance angles range has minimal influence on the resulting grain segmentation in this work, and 10° was chosen as the critical tolerance angle for grain reconstruction considering the relatively high grain boundary misorientation angles and small size poor data points. Then, the minimum grain size limitation in terms of number of the voxels ($4\,\mu m^3$) was set to merge extremely small 'grains' into surrounding grains. The key parameter for this criterion is the choice of minimum grain for the sample, as well as the suitable minimum numbers of voxels required to represent the grain morphology. The measurement of grain size in the EBSD-converted CPFE model adopted the same definition as in the EBSD image analysis, viz. 2-D circular equivalent diameter assumption. In this study, the minimum grain size was defined as 3 voxels which is the maximum area size of non-indexed spots, so that grains with fewer than 3 voxels were combined into a neighbouring grain and were assumed to be artificial noise in the EBSD

scan. Finally, the orientation information for individual grains was captured by the inverse pole figure with a unique colour identification scheme, as shown by the arrows in Figure 4-5 (a). These orientation details were written in the form of Euler angle datasets (three Euler angles). The Euler angles datasets were converted to a rotation matrix dataset, as input material properties for the CPFE UMAT, representing the crystallographic slip systems of different grain sets in the polycrystalline model.

The resulting grain data was relabelled and discretized to a voxel FE mesh by reorganizing and grouping the nodes and setting the orientation property in the FE mesh to correspond to the Euler angle value in the EBSD map. In this 8-node element FE model, the 3D RVE was generated by extending the 2D map along the z direction by one-element thickness, resulting in a columnar grain shape in the third dimension in this quasi-3D model. In this method, grain boundaries have zero thickness, however some computational studies have included explicit representation of the grain boundaries in small sample sizes [307]. The grain ID lists were used to define sections in ABAQUS. Three grains labelled A, B and C are highlighted in both images in Figure 4-5 to emphasize the complete equivalent relationship between the EBSD image and the CPFE model.

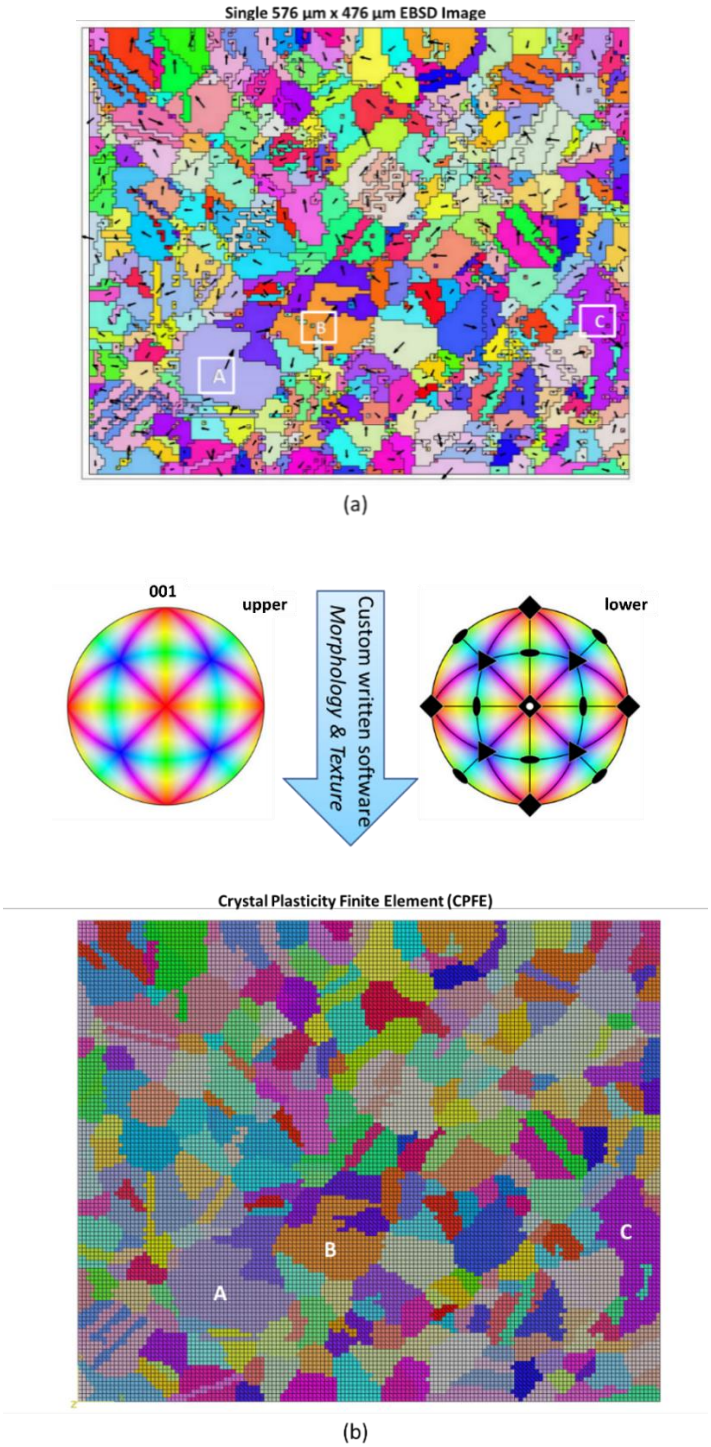

Figure 4-5. Output schematic during image-based CPFE generation procedure showing direct mapping of grains from 576 µm × 476 µm EBSD into CPFE model. (a) Arrows show the projected orientation for individual grains. Three randomly picked grains labelled A, B and C are highlighted here for reference and comparison to the converted and meshed CPFE model in (b).

4.2.2 A statistically equivalent RVE model approach

The commonly-used VT approach for the generation of CPFE models representing measured microstructures is an obvious comparator for the proposed image-based (EBSD-based) methodology described above. Initial testing of 2D VT models demonstrated an 18.8% error in the predicted mechanical performance (maximum cyclic stress) compared with the experimental results. This compares to a predictive accuracy within 5% for the 3D VT or quasi-3D (one-element thickness) models. Knezevic et al. [308] have previously reported the same limitation of 2D VT CPFE models. The key concept here is to develop a statistically-equivalent RVE model to represent the microstructure, in this case of the hot-rolled biomedical grade L605 cobalt chromium alloy previously characterised by Sweeney et al [235] via EBSD and fatigue testing. For the present work, a Voronoi tessellation methodology was developed to generate an FE cubic RVE cell. The Python library SciPy (Version 1.5.0) [309] was called to generate the nuclei points through the Delaunay triangulation algorithm, and then the edge of each polygon shape was connected based on the circumcircle around the nuclei points, thus forming the grain boundaries. The grain boundary coordinates were recorded and later read by ABAQUS. The grain size of the EBSD characterisation was determined through an equivalent circular diameter definition. There exists an argument that partial grains (on the edges) should be removed when measuring the averaged grain size to avoid introducing a bias since most partial grains are large. Thus, the average grain size measurements were calculated based on EBSD map (i) with all grains, and (ii) without partial grains, respectively. It was found that the partial grains comprised 26% of the total number of grains. The calculated equivalent circular diameter was 27.3 μm measured from the full grain map, and this value increased to 27.8 μm from the map without partial grains. Considering that the EBSD-based modelling uses full grain map conversion and a relatively small difference between the two calculations (1.8% difference), the grain sizes in this study were measured using full grain EBSD data. The grain size of the 3D VT model was represented using the equivalent spherical diameter. The grain volume was calculated by the number and size of the voxel mesh within the same grain. The grain size distribution was represented using a log-normal distribution fit to the measured data of mean and standard deviation of the grain sizes, as shown in Figure 4-6. The equivalent spherical diameters d of the grains are

extracted and regrouped to plot probability distribution. The grain size distribution was represented using a log-normal distribution fit to the measured data of mean grain (equivalent spherical diameter d) and standard deviation. The definitive RVE model thus contains the necessary statistically representative microstructural information.

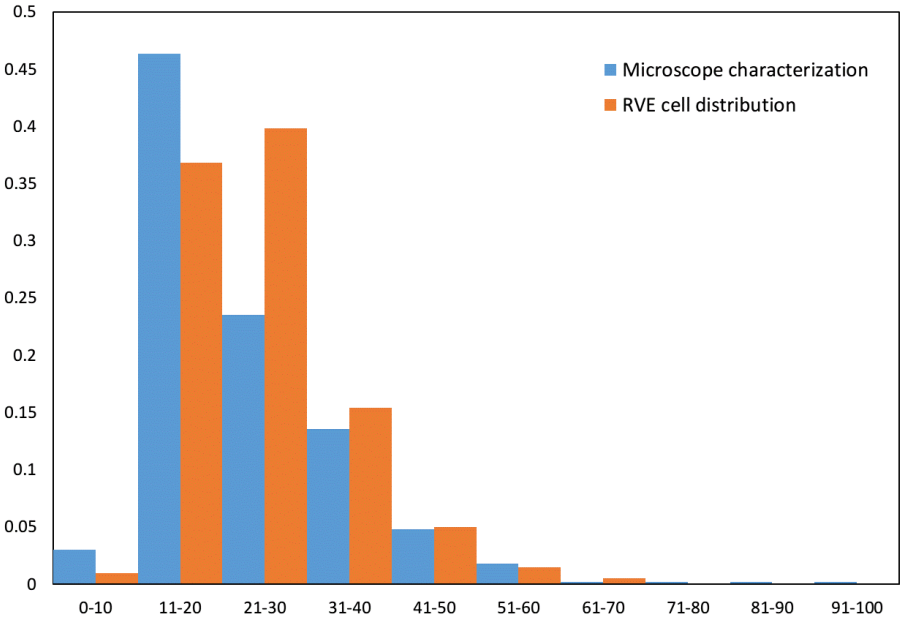

Figure 4-6. Comparison of measured grain size distribution from EBSD measurement with RVE cell distribution in VT based CPFE model.

Two boundary condition configurations were considered here: simply constrained boundary condition (i.e. fixing the model at the bottom and left side) and periodic boundary condition (PBC). Some studies have suggested that it is not necessary to use PBCs for micromechanical models under tensile loading [137]. Other authors have shown that due to PBCs linking the response between boundary surfaces, there is a significant benefit in reducing the minimum required model size for a definitive RVE [221, 310]. A definitive RVE model has sufficient microstructural information to fully represent the general macroscopic performance. Computational cost is high when running 3D fatigue constitutive models. The runtime required increases exponentially as the polycrystal geometry size scales up. In addition, PBCs are considered capable of providing accurate mechanical behaviour prediction with fewer variations to achieve complete convergence as the number of grains grows to a critical value [311]. PBCs are assigned to all FE nodes along the free edges of the unit cell shown in Figure 4-7, through a custom-written Python

script [234]. N, E, S, W are the four boundary lines and NW, NE, SE, SW refer to the four corner nodes and z-direction is perpendicular to the square. Boundary constraints for the displacement $\boldsymbol{U}$ obey the following equations:

$$\boldsymbol{U}_E(x) = U_{SE}(x) + \boldsymbol{U}_W(x) \tag{4-1}$$

$$\boldsymbol{U}_N(y) = U_{NW}(y) + \boldsymbol{U}_S(y) \tag{4-2}$$

$$\boldsymbol{U}_S(x) = \boldsymbol{U}_N(x) \tag{4-3}$$

$$\boldsymbol{U}_W(y) = \boldsymbol{U}_E(y) \tag{4-4}$$

$$U_{SW}(x, y, z) = U_{NW}(x) = U_{SE}(y) = 0 \tag{4-5}$$

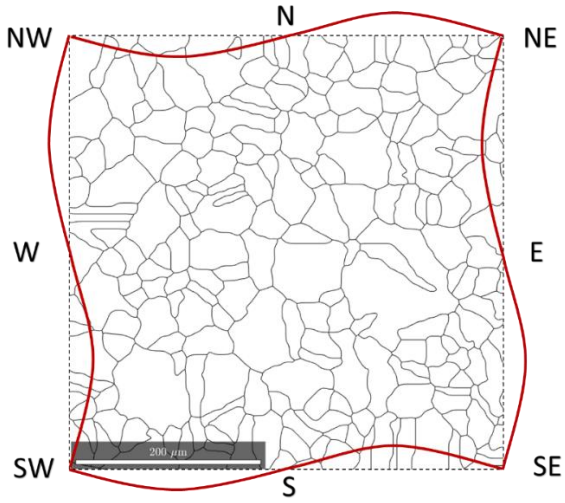

Figure 4-7. A cropped EBSD map to illustrate the principle of periodic boundary condition (PBC). N, E, S, W refer to the four edge surfaces of the model while NE, SE, SW and NW are the four corner points. Red curve around the model shows a typical deformed shape with PBC definition

In addition to PBCs, a periodic grain boundary (PGB) geometry was generated using the DREAM3D function "pack the primary phases". This filter generates a PGB for the microstructure that combines the grains along the surface bounds to be of the same specification. Figure 4-8 shows the generated periodic grains within the resulting CPFE model.

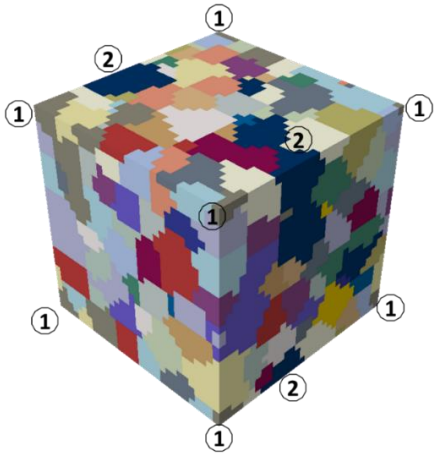

Figure 4-8. Illustration of the periodic grain boundary (PGB) in the polycrystalline RVE morphology. Labels 1, 2 highlight grain examples with PGB definition where the grains along the edge surfaces of the RVE model are bounded to the same section (grain) definition.

The definitive RVE model thus contains the necessary statistically representative microstructural information (as shown in the comparison of Figure 4-6) for prediction of the macroscale mechanical behaviour, as illustrated in Figure 4-9.

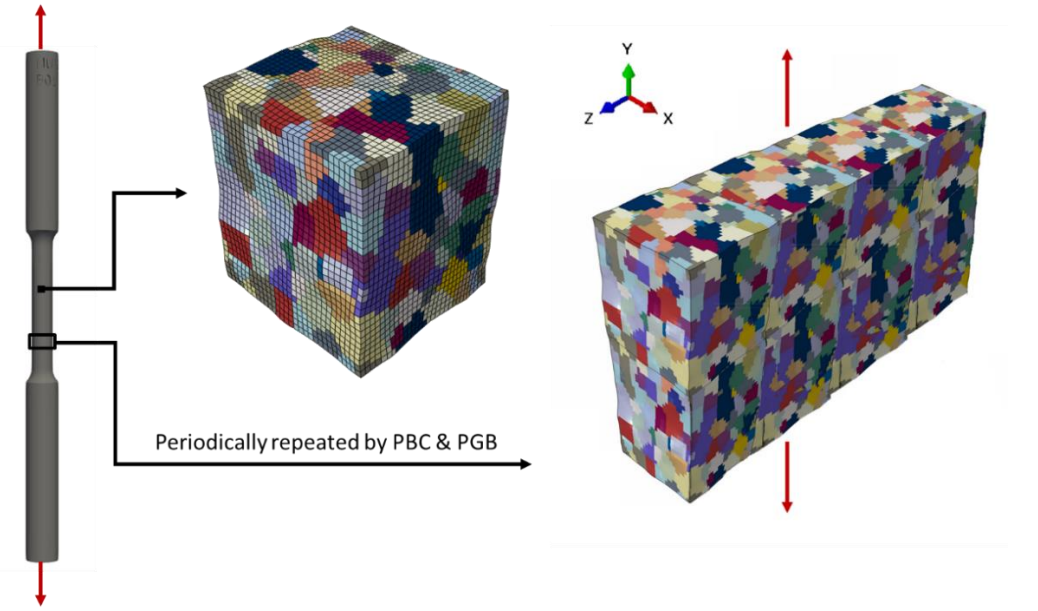

Figure 4-9. The concept of periodically repeated RVE model to predict mechanical property. Microstructure characterisation information obtained from a partial area of the sample is used for generating RVE unit cell model, which is then repeated periodically using the PBC and PGB definitions to predict macroscopic deformation.

In the present work, the cyclic plasticity responses of the two sets of boundary conditions were compared for strain-controlled simulations corresponding to strain ranges of ±0.5%, ±0.8%, ±1.0% and ±1.2%, viz. low cyclic fatigue loading cases, using the 3D VT CPFE models presented below. It was thus established, using the phenomenological CPFE constitutive model described in Chapter 2.3.2, that the simply constrained approach over-predicts local von Mises stress by between 10 to 20% relative to the PBC approach, the 0.5% comparison case, as shown, for example, in Figure 4-10. The remaining models, both VT and EBSD-based, in this thesis, thus use a PBC-based approach.

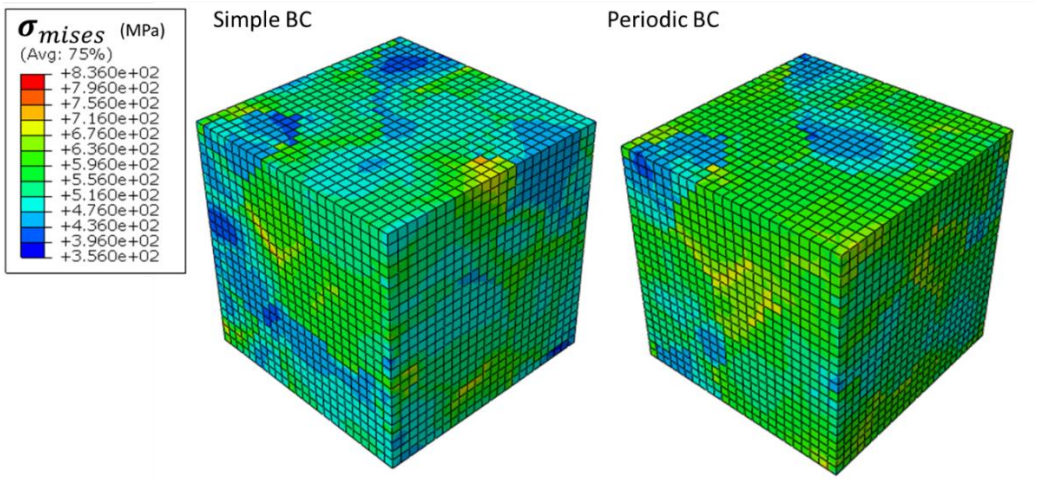

Figure 4-10. Effect of assumed boundary condition on localised von Mises stress. Finite element contour plots of the von Mises stress distribution for 0.5% strain-range case using simple boundary condition (BC) and periodic BC definition.

4.3 Results

4.3.1 RVE converged model size determination.

4.3.1.1 Determination of a converged definitive VT model.

The determination of a suitable (minimum) size is the first step in RVE modelling. CPFE models can lead to noticeable scatter in maximum principal stress [312] and initial yield strength when the number of grains is below 20 along cross-section area [313]. Hojun et al. observe that the predicted Von Mises stress values have a scatter of up to 11.7% when fewer than 100 elements are defined in individual grains [314]. This quantitative RVE convergence study ensures that the resulting simulation scatter due to

inherent VT algorithm shortcomings is minimized to a reasonable level so that both VT and EBSD models represent the (statistically) same grain size distribution. One benefit of the VT method is convenience with respect to studying RVE convergence; this is due to the artificial nature of the model, whereby it is straight-forward to generate models with increasing numbers of grains for the same grain size distribution. Hence, RVE convergence is first established here using the VT-based models. The constitutive material parameters of CoCr alloy for this study were previously calibrated by Sweeney et al [315], as shown in Table 4-1.

Table 4-1. Material parameters for CoCr alloy.

Parameter	Value
$\dot{a}$	$0.002\ s^{-1}$
n	50
g_0	$100\ MPa$
g_∞	$130\ MPa$
h_0	$100\ MPa$
C_1	$80\ GPa$
D_1	750
C_2	$1.25\ GPa$
D_2	0.001
b^α	$2.56 \times 10^{-10} m$
v	$1.0 \times 10^{11} s^{-1}$
ΔH	$2.85 \times 10^{-20} J$
T	$293K$
k	$1.38 \times 10^{-23} JK^{-1}$
γ_0	1.0×10^{-3}
$\rho_{SSD,m}$	$5 \times 10^{10}\ m^{-2}$

Figure 4-11 shows a typical example of the scatter predicted for three realizations of the statistically equivalent grain distributions on a 30-grains RVE mode. Although the average mesh density of 900 elements/grain is sufficiently refined, based on the findings of Harewood [316], for example, and both periodic boundary condition and grain boundary geometry were adopted, the predicted bulk stress values for an applied strain of 0.5% strain are 502.7 MPa, 507.4 MPa and 492.7 MPa, i.e. 3% difference between maximum and minimum. As for FIP *p*, the scatter in incremental values from the third cycle is 32.2%, with similar associated scatter in predicted FCI life.

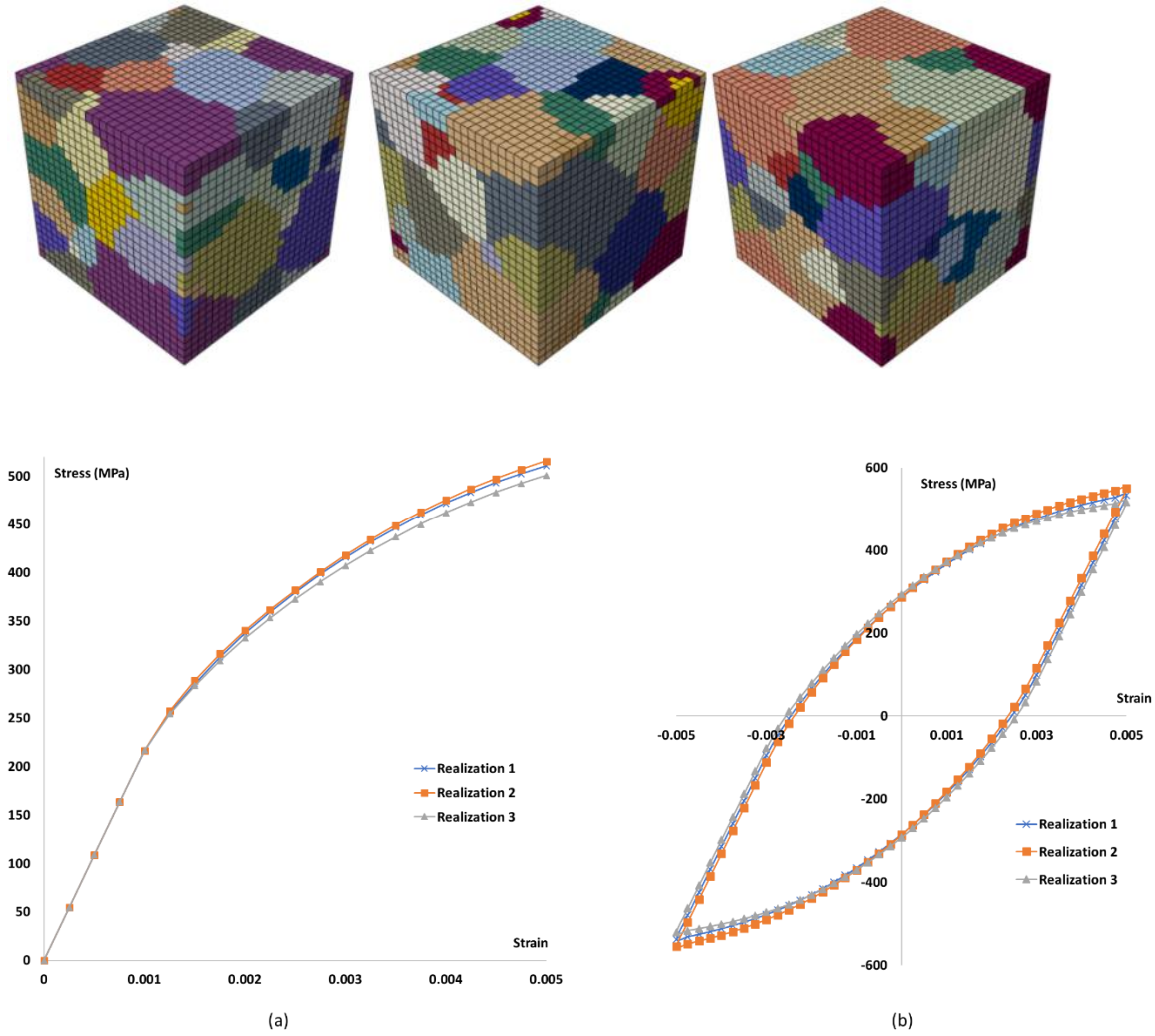

Figure 4-11. Comparison of predicted responses from different realisations of VT-based RVE (30-grain case) with same grain size distribution. Three realisations with different markers show (a) stress-strain behaviour for 0.5% applied strain and (b) stabilized hysteresis loops for ±0.5% strain-controlled cyclic case.

In the literature, there is significant variation in RVE sizes, in terms of the number of grains, e.g. [137]. The size of the definitive RVE depends on material properties such as elastic modulus, shear modulus and plasticity [317] and typically needs to be quantified individually for each application, including local considerations such as boundary and loading conditions, as well output criterion for convergence.

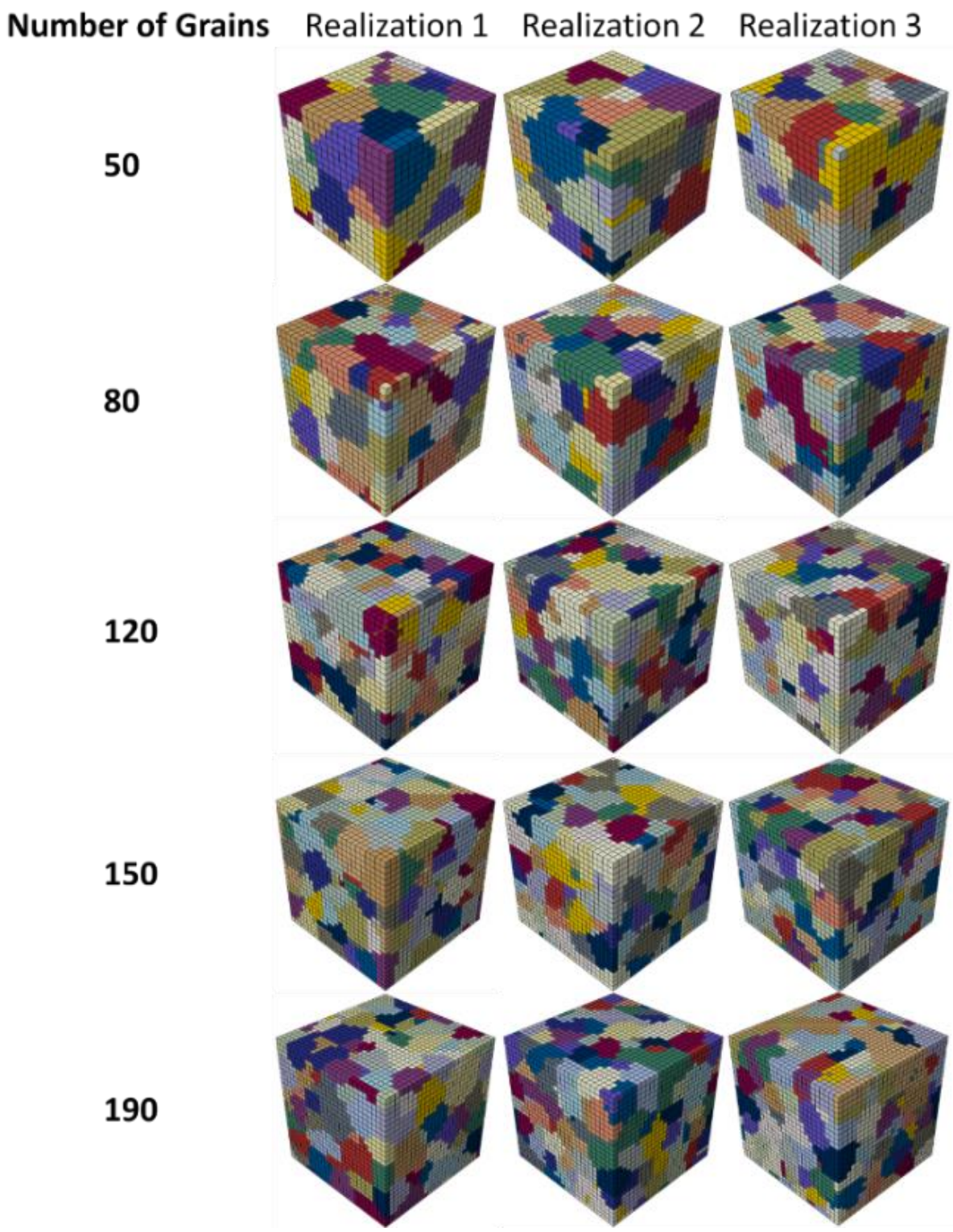

Figure 4-12. VT-generated CPFE models used for RVE convergence study with five groups differing in numbers of grains: 50, 80, 120, 150 and 190.

This study aims at ensuring a reliable prediction of elastic-plastic behaviour for an applied tensile strain of 0.5%. In order to facilitate this, a matrix of RVEs consisting of different random realisations for different numbers of grains, all using the same grain distribution (mean grain size and deviation) data, was generated using VT. Recent work by Farukh et al. [137], for 2D RVE convergence, concluded that a 169-grain RVE was sufficient for convergence under strain-controlled tensile deformation. As shown in Figure 4-12, the numbers of grains considered were 50, 80, 120, 150, and 190 respectively, for each of the three realisations. Each group includes three realizations for the specified number of grains. All the models have the same grain size distribution (as measured from EBSD analysis, see Figure 4-6) and element density (100 elements/grain). The FE mesh density was set constant at 100 elements per grain, according to a previous study demonstrating that 98 elements per grain were a sufficient density for converged results [318].

Figure 4-13(a) shows the effect of number of grains on scatter in predicted macroscopic stress, and the computational cost for the different RVE sizes are shown in Figure 4-13(b), based on a Windows workstation, consisting of a quad-core Intel i7 processor and 32 GB (4 × 8 GB) with ABAQUS multi-core accelerating assist. Simulation run-time needs to be balanced carefully against scatter when deciding the size of definitive RVE model, because the required computational cost multiplies for fatigue (cyclic loading) cases.

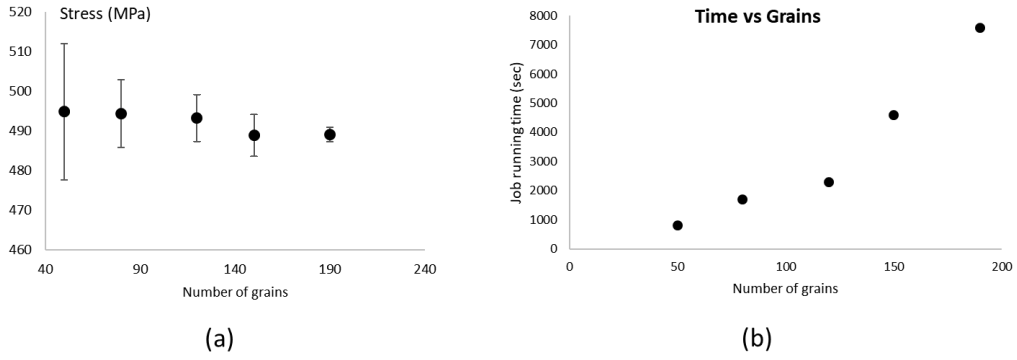

Figure 4-13. (a) Effect of number of grains from 50 to 190 in RVE model on maximum principal stress, with error bars representing the standard deviations across the three realizations; (b) effect of number of grains in RVE model on computational cost for 0.5% strain tensile test.

The predicted scatter in mechanical response is due to the scatter in randomly generated microstructural RVEs. Artificial variations in micro-structure occur when the total RVE volume is not sufficiently large. Figure 4-14(a) shows comparisons of the probability density plots of grain size distributions for different realisations of the 30-grain RVE and the 190-grain RVE. The scatter is significantly less for the 190-grain RVE. Furthermore, Figure 4-14(b) shows the corresponding comparison between the 190-grain RVE and the measured EBSD data, illustrating that the 190-grain model correlates closely to the EBSD. Hence, the establishment of a converged RVE is critical for minimizing the errors (artificial scatter) from VT-generated CPFE models of microstructures. The remaining CPFE-VT results in this chapter correspond to the 190-grain RVE.

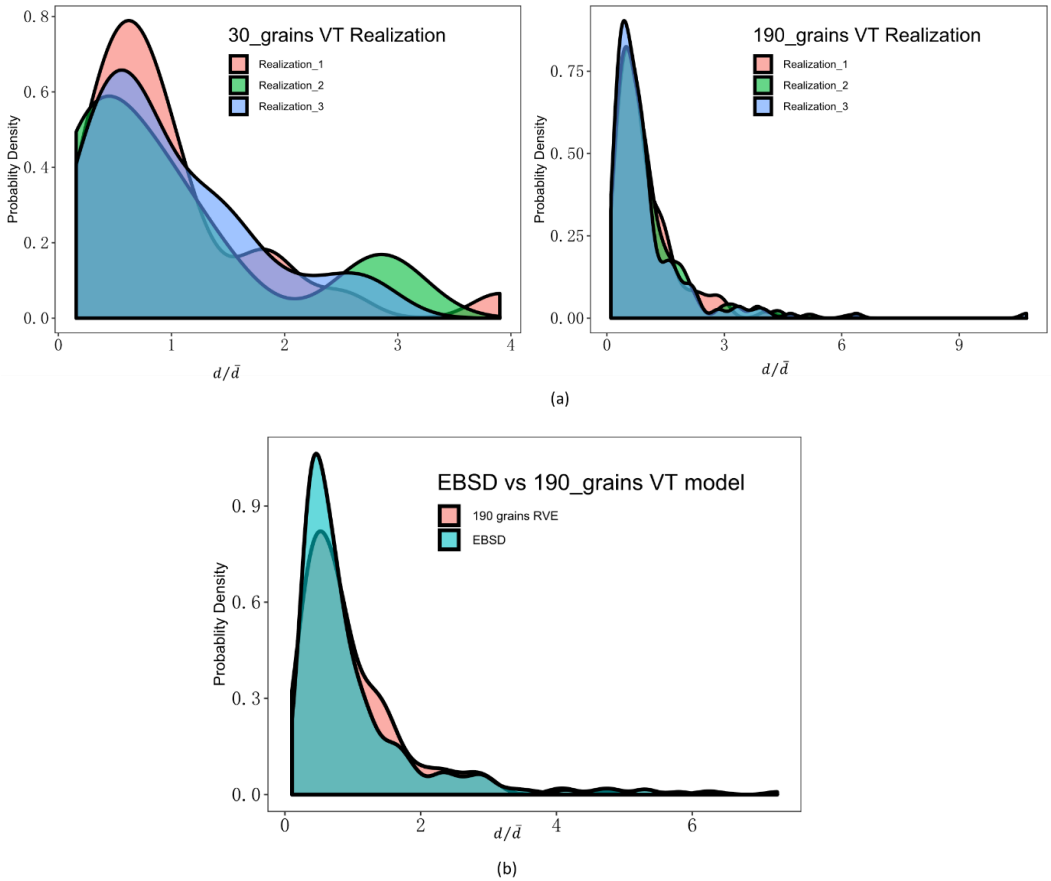

Figure 4-14. Comparisons of probability density distributions for grain size. $\bar{d}$ is the averaged grain diameter and is equal to 27 μm. (a) grain size distribution for three different realisations of 30-grain and 190-grain RVE models. (b) Comparison of grain size probability density distribution of 190-grain RVE (in red) with measured EBSD distribution (in blue).

4.3.1.2 Determination of a converged EBSD model.

The convergence investigation for the EBSD-based model focuses on the effect of ratio of EBSD map length to average grain size *(l/d)* using five cropped regions to construct the comparison sets, as shown in Figure 4-15. The dashed rectangular window indicates the cropped model and the value on the right-top of this window gives the relative (l/d) ratio. Unlike a strictly regular grain model, the averaged grain size slightly varies and is recalculated in each case of the cropped EBSD map; consequently, the *l/d* ratio is not completely linear with respect to the edge length *l* along the *x* axis direction.

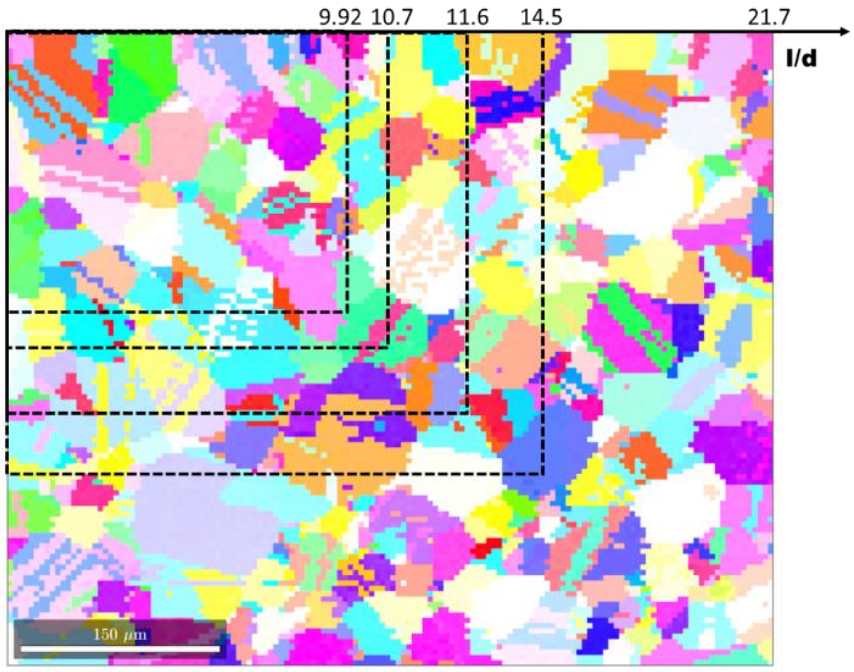

Figure 4-15. Illustration of the five cropped areas with different EBSD map length to average grain size l/d ratios for convergence study.

These five models were subjected to fully-reversed 0.5% cyclic strain. Consistent with the previous VT-RVE convergence study, the difference in stress-strain hysteresis response is negligible, being only an 8 MPa (1.42%) difference in maximum stabilized principal stress. This is attributed to the number of grains in the smallest cropped EBSD model being 272, which exceeds the above-identified convergence limit of 190 grains in an (VT-generated) RVE. However, *l/d* ratio was observed to marginal influence predicted FCI life, as shown in Figure 4-16. The predicted FCI life was found to decrease by factors of 1.12 for *W* and 1.23 for *p* as *l/d* increased from 21.7 to 9.9, with a negligible increase for

l/d > 14.5. These results are consistent with previously-presented results in a fretting fatigue study [234] and a failure strain [236] study. It was found that predicted life is more stable with respect to *l/d* for *W* than for *p*. It is important to note that all subsequent CPFE results meet the convergence requirements of more than 190-grain for VT models and *l/d* > 21 for EBSD models.

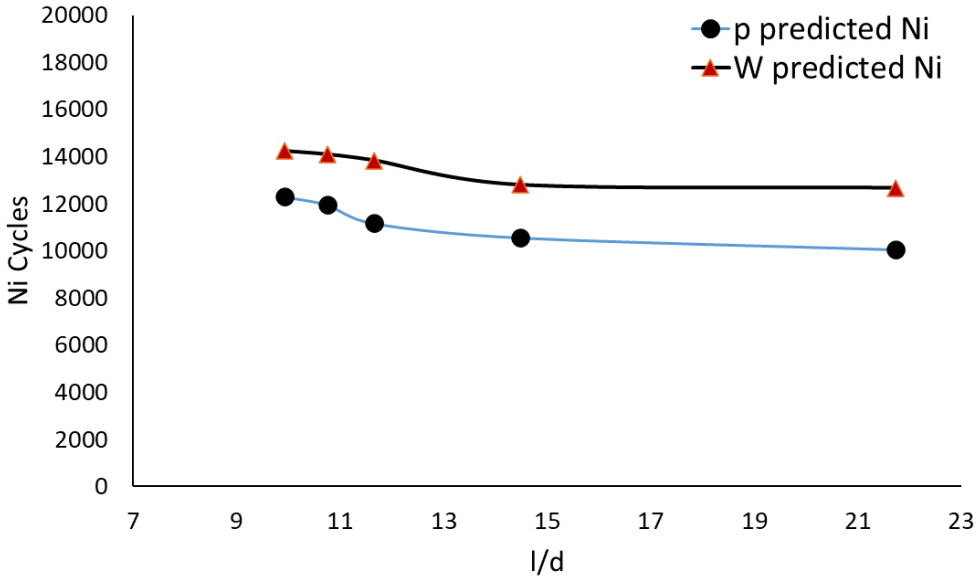

Figure 4-16. The effect of l/d ratio on predicted FCI life for the EBSD-based CPFE model, as predicted via FIP p and FIP W. l/d ratio is observed to have marginal influence on predicted FCI life.

4.3.2 Stress-strain response during cyclic deformation.

Figure 4-17 shows a comparison of the CPFE models with the experimental data [315] for four different applied strain ranges, demonstrating close agreement of both methods with the test data. Similar to the finding of a previous martensitic steel study [319], in general, the macroscopic stress results from the two methods show only slight differences in terms of stress-strain response. Both models, viz. VT- and EBSD-based methods, provide a satisfactory prediction of the hysteresis stress-strain relationship, although the VT method predicts slightly less accurate maximum tensile stress for the lowest and highest strain-ranges. The predicted responses show the close agreement of both methods with the test data, with the EBSD predictions showing slightly higher fidelity, particularly for the tensile part of the lowest and highest strain ranges.

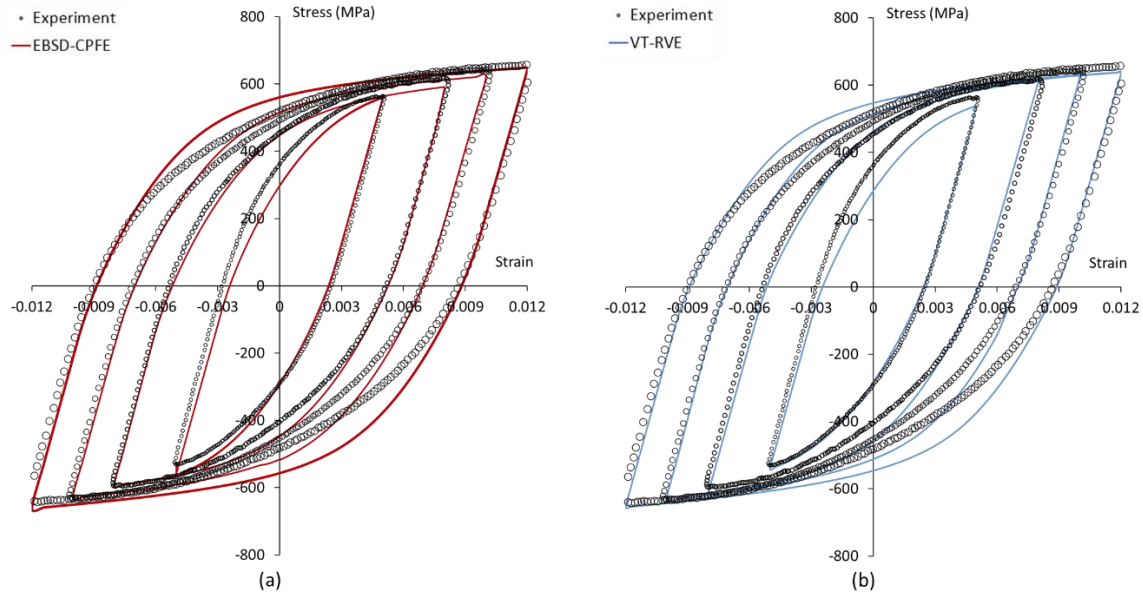

Figure 4-17. Comparison of measured and CPFE-predicted stabilised hysteresis stress-strain loops behaviour for strain-ranges of 0.5%, 0.8%, 1.0% and 1.2% for (a) EBSD-based CPFE model and (b)VT-based RVE response.

To further characterize the difference between these two polycrystalline generating methodologies, Figure 4-18 (a) shows a comparison of the predicted stabilized stress-strain responses from the EBSD- and VT-based CPFE models. Figure 4-18 (b) gives the stress values at different strain ranges from experimental measurements and CPFE predictions.

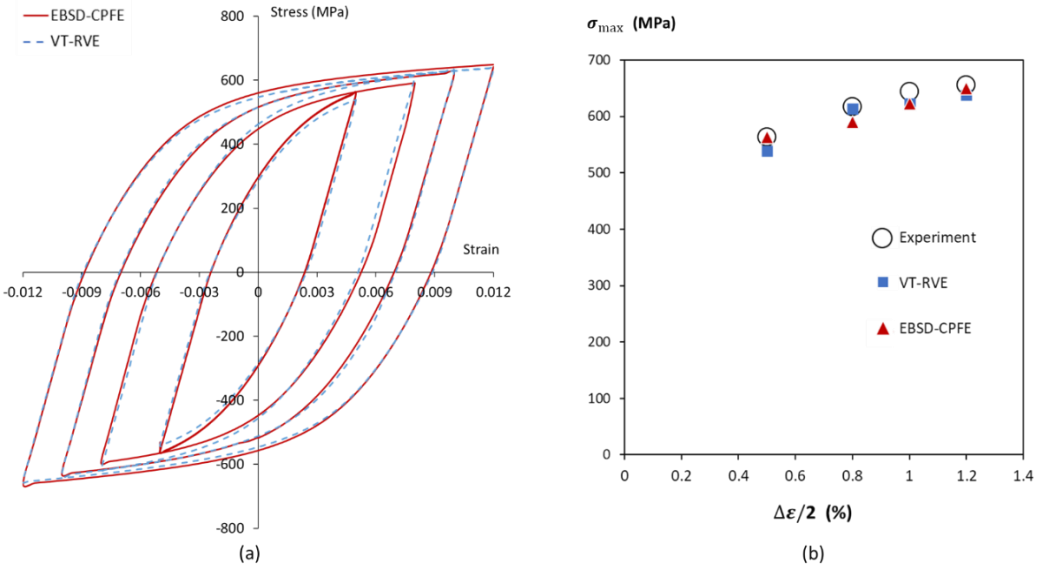

Figure 4-18. (a) Comparison of stabilised hysteresis stress-strain loops from VT- (blue dashed line) and EBSD-based CPFE models (red curve). (b) Comparison of maximum stress values at four strain ranges of 0.5%, 0.8%, 1.0% and 1.2% between experimental measurement (circle, VT- (blue square) and EBSD-based CPFE models (red triangle).

4.3.3 Fatigue crack initiation prediction.

The FIP_{cyc} values are calculated by the difference between successive cycles after the stress-strain response has stabilized, taken here as the 7th cycle. The critical FIP values are calibrated using the equation $FIP_{crit} = FIP_{cyc}N_i^{exp}$ at a sample strain range, in this case, the 1% case. Table 4-2 shows the identified critical FIP values against FCI life. The FCI life identified from the test data was 15,690 [315].

Table 4-2. FIP critical values determination of the original fine grain sample for strain-range of 1%.

Model type	p_{crit}	W_{crit}
VT	312.6	132123
EBSD	380.2	148920

Figure 4-19 shows a contour plot of the measured grain boundary misorientation angle along with the corresponding CPFE-predicted equivalent (von Mises) stress distribution, p-distribution and W-distribution, at 0.5% tensile strain. Grain boundaries are not

explicitly modelled here as per [307] but it is clear that the ESBD construction data provides an accurate geometric representation of grain boundaries for the microstructure RVE being modelled. A significant benefit of the EBSD-based CPFE model is the ability to capture the localization of crystallographic plastic slip and discontinuity stresses at the grain boundary interface regions of the microstructure. This is critical for an accurate and realistic representation of the discontinuity in crystallographic orientations between adjacent grains, which plays a key role in fatigue crack nucleation [32]. It is important to note that the VT method is limited to straight-line polyhedral boundaries and thus fails to provide a realistic neighbour relationship between adjacent grains. Hence, the VT method cannot provide realistic representations of the localized stresses and slips.

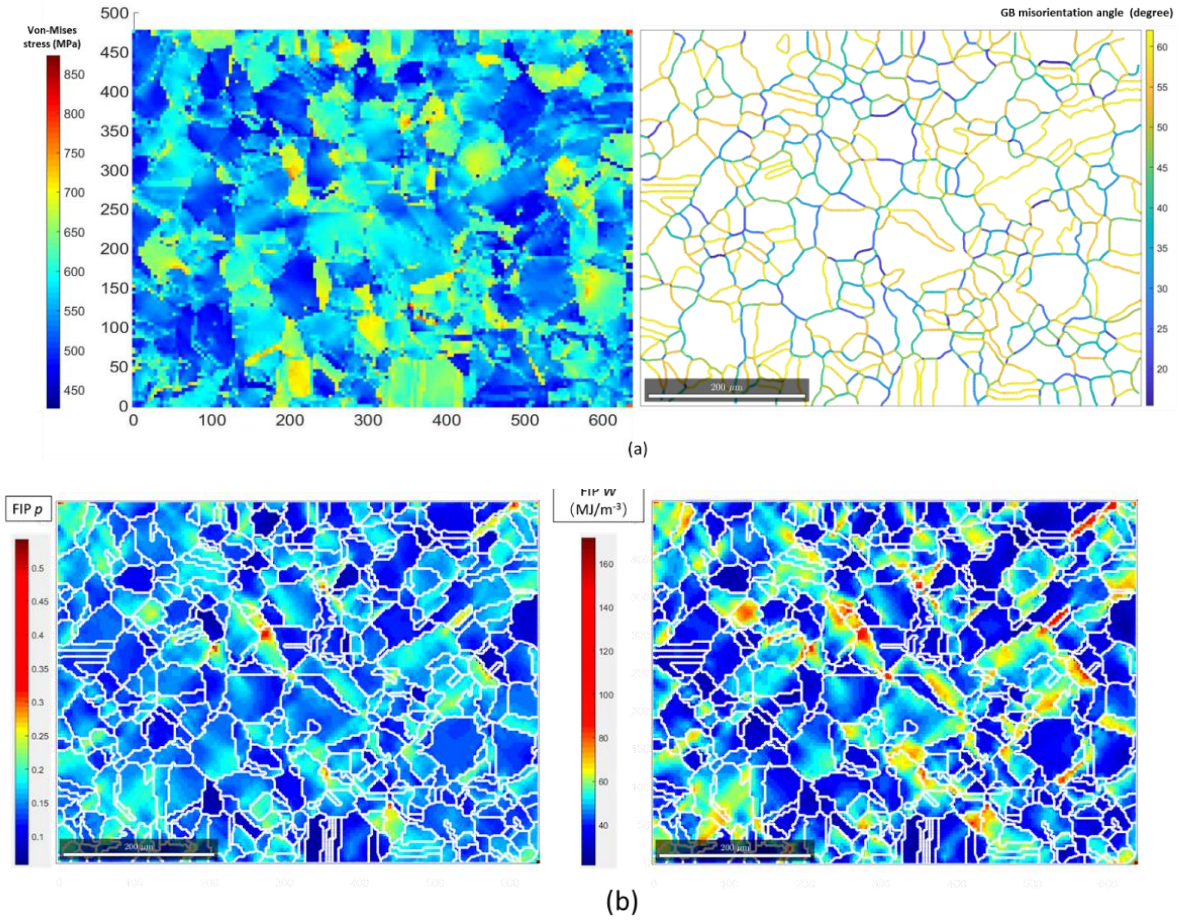

Figure 4-19. CPFE-predicted contour plots showing distributions of (a) von Mises stress at 0.5% strain after 6 cycles with grain boundary misorientation angle information where the boundary curve is coloured based on the orientational angle difference between the neighbouring grains and (b) fatigue indicator parameters, effective plastic strain p and accumulative energy dissipation W for EBSD-based RVE, at 0.5% tensile strain.

Figure 4-20(a) shows the comparison of the EBSD model for both FIPs with the experimental data across the full set of strain ranges. Although accurate FCI prediction was achieved using both FIPs, the *W* parameter is found to be more accurate across the full range. Figure 4-20(b) shows the comparisons of the VT-based and EBSD-based FCI predictions with the test data. The EBSD-based RVE model predictions are more accurate than those of the VT-based models. The EBSD-based *p*- and *W*- predictions are all within 25% and 23%, respectively, of the test data; in comparison, the corresponding errors for the VT-based model are 37% and 30%, respectively. A $\pm$30% error area is provided for the ease of predicting accuracy comparison. Although accurate FCI prediction is achieved using both FIPs, the W parameter is more accurate across the full range. Figure 4-20(b) indicates that the EBSD-based RVE model predictions are more accurate than those of the VT-based models.

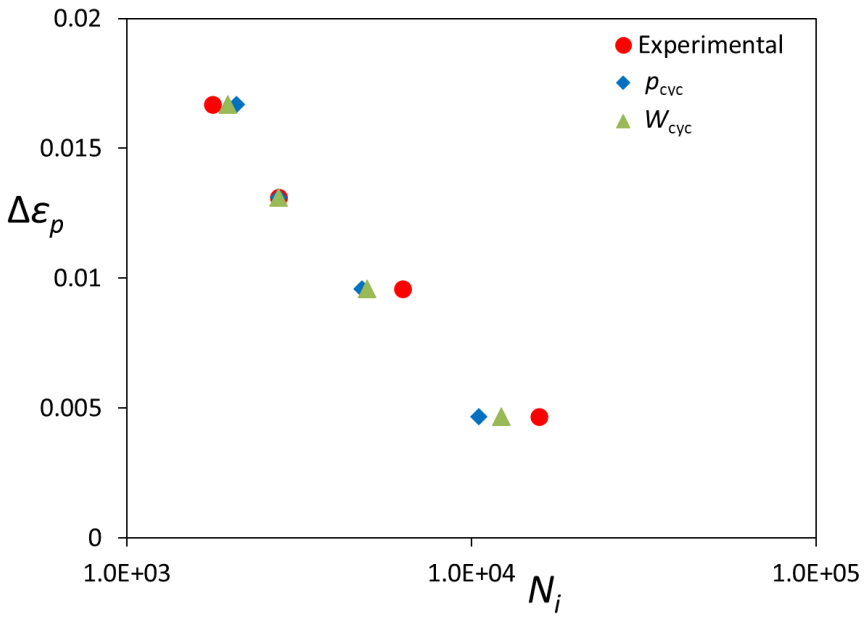

(a)

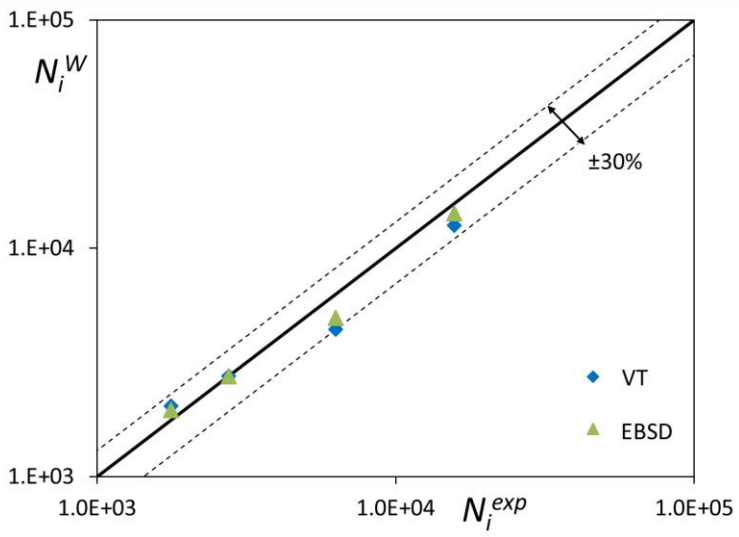

(b)

Figure 4-20. (a) Comparison of the predicted FCI from EBSD-based RVE with experimental results (red circle), for FIP p (blue diamond) and FIP W (green triangle), and (b) comparison of VT-based and EBSD-based FCI predictions against measured data for W parameter.

4.3.4 GND induced strain gradient length-scale size effect.

In this section, the evolution of the immobile GNDs during deformation is captured in order to predict the effects of grain size on FCI performance. More dislocations are required to overcome curvature obstacles in the crystalline lattice induced by deformation. Smaller grains result in a higher plastic strain gradient thus leading to a higher localized hardening along the slip systems of smaller grains [50, 51]. The original material was annealed to increase the grain size. The grain size was defined by the averaged value of equivalent spherical diameter *d* from EBSD analysis. The EBSD-based CPFE model was assigned the strain gradient constitutive formulation to simulate the LCF behaviour of both the original fine grain (d = 27 μm) and the coarse grain (d = 209 μm) CoCr alloys, using the modified constitutive law specified in Chapter 2.3.2.

Table 4-3. Comparison of W-based FCI life prediction using EBSD-based modelling for two fine- and coarse-grain CoCr.

Grain size	***Strain range***	N_i^{exp}	N_i^{pred}
Fine	0.5%	15690	8820
	1.0%	2752	2740
Coarse	0.5%	8697	6186
	1.0%	2376	2375

Two fatigue tests were carried out on this annealed alloy at the strain ranges of ±0.5% and ±1.0%. Figure 4-21 shows the predicted hysteresis loops compared to experimental loops for the two different grain sizes. It is clear that a key effect of the coarsened grain size is the reduction in loop size and, hence, in cyclic strength, i.e. softened response. This is well captured by the present EBSD-based strain-gradient CPFE model for both strain ranges. In order to demonstrate FCI prediction for the two different grain sizes, the *W*-based method was adopted, due to its established superior predictive ability above. A value $W_{\text{crit}} = 83934$ MJ/m^{-3} was identified using the fine grain, ±1.0% data. Table 4-3 shows the resulting comparisons between the predicted and experimental FCI data for both original fine-grain and coarsened-grain material for the two strain-ranges. It is seen that for the higher strain-range, the model is very accurate, while for the lower strain-range, it is somewhat conservative.

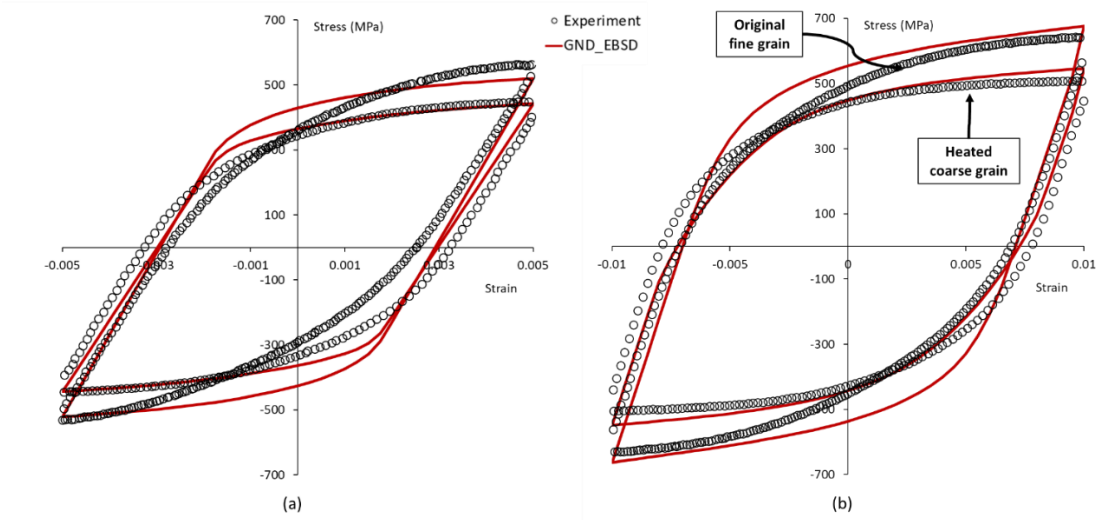

Figure 4-21. Comparison of experimental measurements (black circle) and EBSD-based model results (red curve) for original fine grain and coarse grain after annealing, at (a) 0.5% strain, and (b) 1.0% strain.

Figures 4-22(a) and (b) shows the grain boundary mis-orientation relationships for the fine and coarse grain EBSD images and FE models. Figure 4-22(c) and (d) show the CPFE-predicted GND density distributions for both levels of microstructure refinement. It can be seen from Figures 4-22(b) and (d) that there appears to be correspondence between high-angle grain boundaries and concentration of GNDs. For the fine-grain model, it is not possible to identify such direct correspondence; the dominant characteristic is the significantly higher GND values throughout, due to the reductions in grain size.

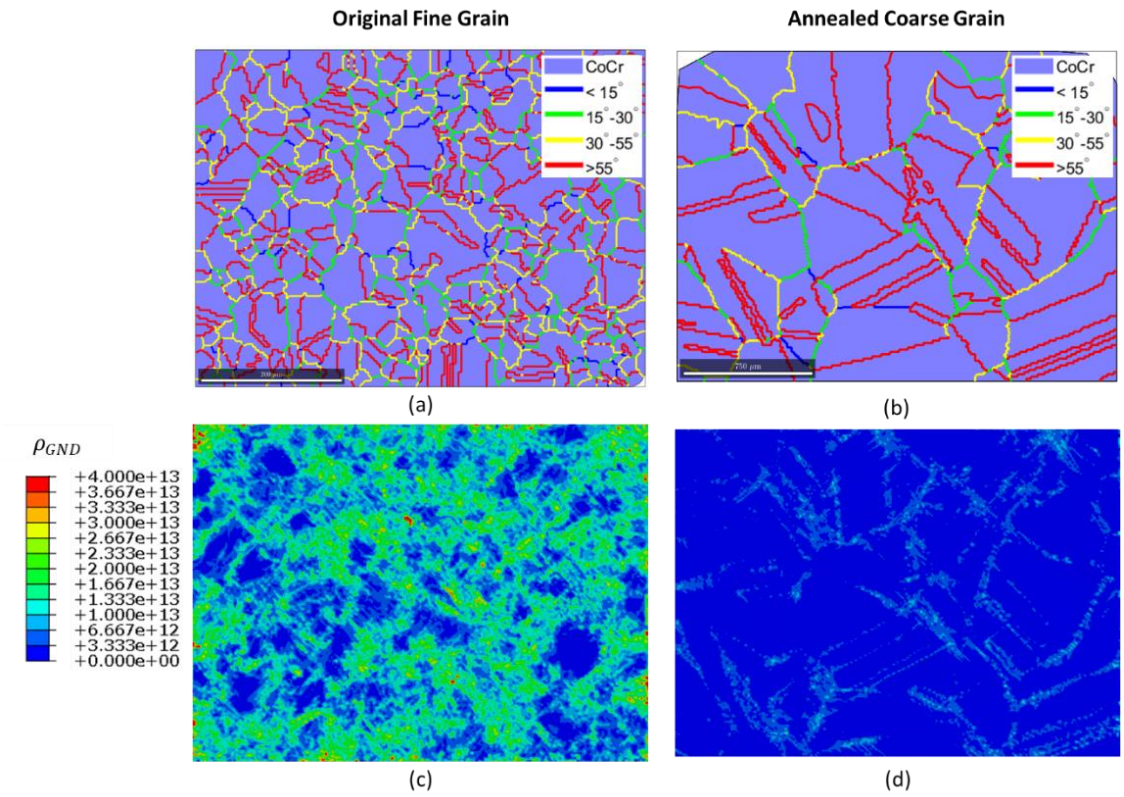

Figure 4-22. The grain reconstruction and mis-orientation relationship for the two grain sizes of (a) d = 27 μm (fine grain), (b) d = 209 μm (annealed, coarse grain) CoCr alloy. The mis-orientations are classified into four ranges by 15 degrees interval in blue, green, yellow, and red, respectively. Predicted geometrically necessary dislocation (GND) density distributions of (c) material-averaged diameter d = 27 μm and (d) d = 209 μm, at 1.0% strain range.

4.4 Discussion

The primary objective of this present work is to detail a new structure-property methodology to (i) systematically convert EBSD images directly into CPFE models and (ii) thus establish a micromechanics-based predictive method for fatigue crack initiation in realistic microstructure morphologies. Due to the inherent two-dimensional nature of the EBSD data, attention is limited here to 'quasi-3D' CPFE models, where grains are assumed to have one-element thickness in the out-of-plane direction. Thus, the grains are essentially columnar in this direction.

Another objective of this work is to compare the results between VT-generated and EBSD-converted CPFE model. Consequently, a definitive RVE model convergence study

is necessary to minimize the influence of scatter and ensure the reliability of the comparison conclusion. The scatter studied here refers to the inherent limitation of the VT algorithm in failing to accurately represent the realistic microstructure with an insufficient number of grains. Such scatter caused by the inherent deficiencies of artificial model-generating techniques (not microstructural scatter due to sampling region) is undesirable. The convergence study of the EBSD-based model is not simply a statistical size effects relationship [320]. FCI prediction is assumed here to be local, calculated based on the maximum or 'hottest' point in the map. As the l/d ratio increases, the size of EBSD map represented increases, so that the maximum 'hot-spot' value will be greater than or equal to the value from lower l/d values. This is consistent with the observation that fatigue life tends to decrease as part size increases [321] due to an increased probability of occurrence of fatigue-weak points. This trend is also consistent with the findings of Lucarini [322]. Figure 4-14 (a) shows decreasing tensile strength with an increasing number of grains, consistent with the results of Farukh [137]. In the following chapters, all the RVE models have the definitive size which is larger compared to the converged l/d ratio for EBSD-based, as well as the number of grains determined in this study, to ensure the minimum influence of scatter.

An important finding here is that the predicted cyclic hysteresis loops from both VT- and EBSD-based CPFE models are essentially the same. In contrast, for FCI prediction, EBSD-based models have improved the accuracy compared to VT-based models. The crystallographic work FIP, W, performs consistently better than crystallographic slip, p. W is able to capture more potentially dangerous hot spots by including the effects of both crystallographic slip and local crystallographic stress as indicated in Figure 4-20 (b). The EBSD-based modelling methodology is also applied to a coarsened-grain CoCr (heat treated) material and captures the grain size effect on (i) cyclic strength and hysteresis loop shape via incorporation of the GND-induced spatial gradient mechanism and (ii) FCI life via the crystallographic work parameter, W. FCI is a localized event specifically associated with microstructure discontinuities, such as grain boundaries with complex geometries, sudden changes of mis-orientation and facet nucleation. Compared with the coarse-boundary VT method, EBSD-converted models contain more accurate grain boundary morphologies and realistic neighbouring grain mis-orientation relationships.

Although the VT model, based on statistical information from SEM characterisation, is more convenient and arguably suitable for bulk stress-strain behaviour, it is important (and necessary), for capturing localised effects, to adopt the EBSD-based approach, due to the associated fidelity with respect to grain orientation, morphology, and microstructure-sensitive effects in particular. The latter has been shown here to give about 10% improvement for fatigue crack initiation life.

Despite the high-fidelity representativity and accurate prediction by EBSD-CPFE model, one significant challenge is the computational effort involved in such structure-property prediction. Considering that VT model can be easily controlled to alter the microstructural feature, and the invisible shortage in predicting tensile bulk stress, the dual-phase VT is implemented in Chapter 5 and 7, for lath width effect and phase composition study. EBSD-based approach is used in Chapter 6 where grain boundary morphology and texture are important.

4.5 Conclusion

This EBSD-based method for CPFE model generation is shown to give approximately 10% improved agreement for fatigue life prediction, compared with the more commonly-used Voronoi tessellation method. However, the added microstructural detail available in EBSD-CPFE did not significantly alter the bulk stress-strain response prediction, compared to VT-CPFE. The new EBSD-based method within a strain-gradient CPFE model is also applied to predict measured grain size effects for cyclic plasticity and fatigue crack initiation, and shows the concentration of geometrically necessary dislocations (GND) around true grain boundaries, with smaller grain samples exhibiting higher overall GND concentrations. In addition, minimum model sizes for VT-CPFE and EBSD-CPFE models are proposed for cyclic hysteresis and fatigue crack initiation prediction. Key conclusions from this work are as follows:

- A method is developed for converting electron back-scatter diffraction data images of microstructure into crystal plasticity finite element models, including grain morphology, size and orientation information. Details of the method are

provided and explained from reconstruction of the EBSD raw file to linkage with CPFE constitutive laws. The primary user inputs in this automated model generation tool are a definition of misorientation tolerance angle and of minimum feature size. The EBSD-based RVEs studied in this work are all one-element quasi-3D models due to the lack of 3D EBSD raw data; however the EBSD-CPFE conversion method used here can be extended to 3D EBSD-based model generation. This fully automatic procedure also allows the generation of large groups of models rapidly, providing potential for the application of machine learning and parameter control.

- The tool has been applied to generate image-based models of biomedical grade CoCr alloy and applied to the cyclic plasticity and low–cycle fatigue crack initiation prediction for multiple strain ranges.
- A minimum RVE size with an adequate number of grains is required to sufficiently reproduce real crystallographic texture. For this hot-rolled L-605 CoCr alloy sample and the CPFE models introduced in this work cyclically-loaded (under strain control) at ±0.5%, ±0.8%, ±1.0% and ±1.2% strain ranges, a definitive RVE convergence study confirms a minimum of 120 grains, preferably higher than 190 grains, in VT-generated CPFE models, to avoid detrimental scatter in the prediction of cyclic hysteresis behaviour. The size of the selected EBSD-based model (model dimension to grain size ratio) needs to be greater than 14.5 to ensure converged prediction of FCI.
- Until advanced multi-level Voronoi tessellation (VT) methods are developed for RVE generation, real microstructure conversion techniques (e.g. the EBSD-based RVE for micromechanical modelling) offer benefits in terms of FCI prediction. In this study, it has been shown that an improvement of up to 10% in fatigue life prediction is achievable in FCI behaviour prediction via EBSD-based micromechanical modelling based directly on observed microstructure, as opposed to using artificially generated VT microstructure models, even if the latter are based on approximate statistical equivalence to measured microstructure data.

- Modification of the constitutive law via a GND effect successfully captured the microstructural grain size effect on cyclic response and fatigue crack initiation life without the need to change model parameters.

5 Microstructure-based strain gradient crystal plasticity modelling of PBF-LB dual-phase Ti-6Al-4V

5.1 Introduction

A defining feature of metal AM processes is the gradual layer-by-layer formation of solid parts. In most metal AM processes, laser beam powder bed fusion (PBF-LB), for example, the process parameters (laser power, speed, layer thickness etc) remain unchanged during the build process. However, the complex thermal cycles, different combinations of printing parameter settings, and the directional fabrication features cause a large variety of microstructure features and inhomogeneity, leading to challenges and difficulties in product quality control. For example, the variation in thermal history along the PBF-LB build direction leads to non-uniform microstructure observed from different regions varying in distance from the powder bed base, even in the same metal parts. Even for fixed process parameters, it has been observed that an unintentional gradient exists in microstructural features, from the bottom of the part (nearest the build plate) to the top of the part, due to a variation in local thermal history along the build height [323].

Typical laser beam powder bed fusion (PBF-LB) printers usually produce Ti-6Al-4V with highly elongated prior β columnar grains along the build direction. Typical measured prior β grain sizes vary from 55 to 620 μm [324]. During the PBF-LB process, the β to α′ martensitic transformation occurs due to a very high cooling rate of more than about 410 K/s, compared to 20 K/s during air cooling [325, 326]. This high cooling speed has transformed most of the β phase into martensite α′ laths within their parent prior β grains, with very little retained β phase (typically less than 10%) surrounding the grain boundary [327]. Lath width was measured for PBF-LB fabricated Ti-6Al-4V part with the building height of 38 cm [323].

The columnar prior β lath width was observed to increase from an average value of approximately 86 μm measured at the bottom to 154 μm at top region of the part. Similar results were found for α lath with width increasing from 0.58 to 0.87 μm [328]. Another

study [329] carried out mechanical tests and found that the microhardness and tensile strength decreased as the building height increased in the Ti-6Al-4V specimen produced by electric beam melting. This phenomenon was explained by a slower cooling rate at the higher region during the AM process.

This inevitable gradient and inhomogeneity AM phenomenon in microstructure can lead to unexpected product performance and product quality control difficulties, as observed in industry. This also presents difficulty in PBF-LB material characterisation, as local variations in microstructure lead to local variations in mechanical behaviour. Typically, this inhomogeneity issue is addressed via post-built heat treatment, e.g. post-built annealing, as well as hot isostatic pressing (HIP), to regularise microstructure. The post-built heat treatment is also a standard process for reducing porosity, thus improving the ductility and fatigue properties of PBF-LB Ti-6Al-4V alloys [330]. However, such post-built processes, while homogenizing the structure, inevitably modify the grain size and phase composition. PBF-LB manufactured Ti-6Al-4V alloy, usually displays fully lamellar shape and dual-phase α+β morphologies within prior β-grains, after undergoing a fast cooling and solidification process [331]. The lath width size is highly dependent on thermal history and has been previously measured and quantified based on the Arrhenius equation with regards to the printing temperature cycle and primary phase kinetic [59]. The α lath width in PBF-LB Ti-6Al-4V was measured to be between 0.42 and 2 μm, which increases to between 3.2 to 4.65 μm after HIP [332]. Due to these microstructural changes after heat treatment, the mechanical tensile strength changes [333], with the UTS and YS decreasing from 1362 MPa and 1311 MPa, to 1180 MPa and 1115 MPa respectively after annealing at 600 °C.

PBF-LB processed Ti-6Al-4V has higher tensile strength but poorer ductility performance than conventional (e.g. wrought) Ti-6Al-V [331], due to the predominant acicular α′ martensite microstructure. The development of a suitable microstructural model for understanding such hierarchical microstructures influence in mechanical response, consequently, is important to assist AM alloy design and quality control in industry.

The mechanical performance of metals during loading is largely dependent on microstructural features, such as phase composition, crystallographic orientations, grain morphology as well as grain size distribution [25]. Crystal plasticity finite element (CPFE) modelling is a micro-scale computational method to predict mechanical performance based on these microstructure and crystallographic properties [188, 228]. The recent advanced Voronoi tessellation (VT) improved through an optimal Laguerre tessellations technique, has allowed more accurate representative model generation, thus increasing the fidelity for the modelling of typical lath microstructure like pearlite, bainite, and martensite in steels [122], as well as lamellar Ti-6Al-4V [22]. The lamellar morphology based CPFE models have been generated for studying the cyclic deformation of non-AM duplex titanium alloys and the localized micropillar behaviour of the TiAl alloy [221, 334]. Liu et al [335] directly import the morphology from microstructural predicting model viz. phase-field method, where the predicted alpha laths which solidified after phase transformation during the PBF-LB cooling process, were imported to CPFE for predicting mechanical properties.

The microscale polycrystalline aggregate-based model feature, and the localized deformation predicting capability, make CPFE a suitable and qualified tool for investigating the microstructural sensitive phenomenon, such as the important grain size, or lath size effects in this chapter, for Ti-6Al-4V alloy. CPFE has been previously adopted by the Max Planck Institute for characterizing the lath size effect of hierarchical compound structure from rapid cooled multi-phase steels, using phenomenological constitutive laws [122, 336]. Another phenomenological flow rule was adopted for characterizing the effects of grain size on the mechanical strength of the intentionally designed functionally graded alloys [180, 337]. One typical and common solution is to implement a size effect on the initial critical resolved shear stress (CRSS), in the constitutive laws. The Hall-Petch type and its extended format CRSS calculating equation were defined to simulate the effect of grain size on the number of cycles for fatigue crack initiation in two wrought IN718 samples varying in grain sizes [182]. Other efforts also include implementing physical length-scale dislocation effects through a strain gradient development, to further capture the size sensitivity. For example, Dunne and co-authors introduced a length-scale physically based CPFE model with HCP slip system definitions

[31], providing support for the modelling of titanium alloys. In this work, the length scale effects, determined by the plastic strain, contribute to the grain level stress behaviour based on dislocation glide and pinning obstacles due to the existence of geometrically necessary dislocations (GNDs). In recent years this physically-based CPFE model has also been successfully extended and implemented for investigating size effects in a wide range of alloys, such as CoCr [183, 228], polycrystalline copper [338], ferritic-pearlitic steel [339], and Ti-6242 [340].

This chapter aims to investigate the effect of such inevitable microstructural inhomogeneity and post-built heat treatment on the strength performance of the PBF-LB manufactured dual-phase Ti-6Al-4V parts, via strain gradient, microstructural sensitive lamellar CPFE modelling. Figure 5-1 illustrates the workflow from sample printing and microstructural characterisation, CPFE model generation and calibration, to mechanical tensile test validation. Section 5.2 describes direct microscopy microstructural characterisation using electron backscatter diffraction of as-built and post-built heat treatment specimens, where measures of texture and grain morphology are extracted from the bottom region and top region of PBF-LB specimens and used to construct Voronoi Tessellation based CPFE models. The model material parameters are fitted against experimental tensile stress-strain curves. Section 5.3 describes CPFE methods incorporating physical dislocation mechanisms to quantify the effect of the above AM phenomena, and of the heat treatment, on the tensile behaviour of Ti-6Al-4V. Key microstructural features exhibiting a gradient (between bottom and top) include lath width and phase fraction. Section 5.4 presents a separate lath width size effect study to further investigate the microstructural sensitivity, and the captured size effects are fitted and examined through macroscopic structure-property relationships in Section 5.5.

5.2 Methodology

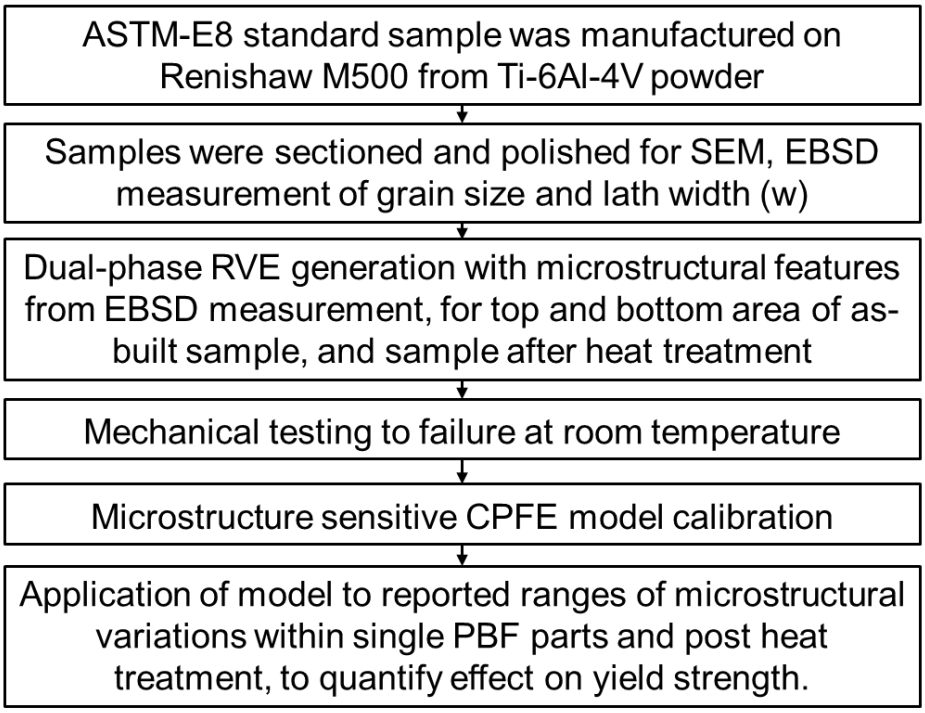

Figure 5-1. Overview of the research workflow, from sample printing, microstructural characterisation and associated RVE model generation, to the CPFE prediction and mechanical test for result validation.

Figure 5-1 introduces the workflow in this research, starting with PBF-LB Ti-6Al-4V specimen fabrication, then microscopy characterization of the inhomogeneous structure for localized samples along the built direction, as well as the HT specimen, finally to the generated representative CPFE modelling validated against experimental tests.

5.2.1 Experimental characterisations

The microstructure characterisation needs to reveal the high-resolution grain boundary morphology and provide texture information. Consequently, electron backscattered diffraction (EBSD) was considered a suitable microstructure scanning tool and adopted in this work to characterize the polished Ti-6Al-4V alloy. Some inevitable but undesired noise was observed from the raw EBSD detection, resulting in 7.4% non-indexed pixel information loss. This poor data percentage could be reduced by further improving the surface quality during sample preparation.

In this work, a neighbouring orientational relationship-based approach was implemented to assign un-indexed EBSD pixels, for a complete data set [150, 291]. The approach includes the main steps: (i) apply segment angle and minimum grain size for fundamental grain map reconstruction (taking 10 degree and 3 pixels per grain respectively here), (ii) apply an orientational median filter on the indexed data to filter out the random errors, (iii) define a suitable filter size (set as 3 in this work with an indexing neighbour window size of 7 × 7 pixels). (iii) fill data based on the previous step analysis and extract the newly written raw data file for final measurement.

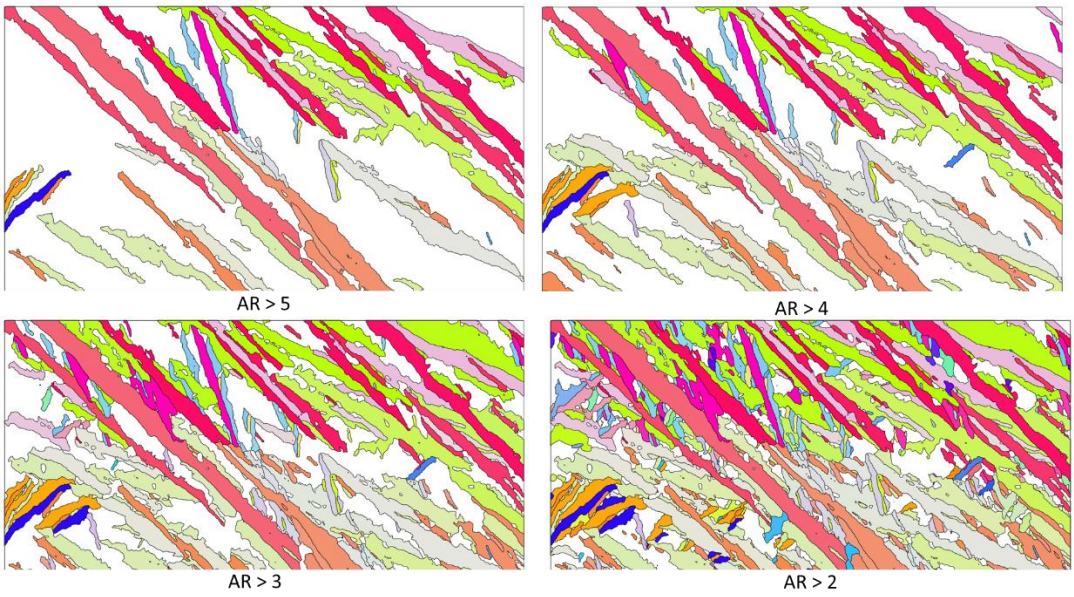

Figure 5-2. EBSD reconstructed 40 μm × 26 μm lamellar shape grains with minimum aspect ratio filters, showing laths with AR higher than 5, 4, 3 and 2. Coloured by IPF definition.

The first important feature is the grain size. One challenge in PBF Ti-Al-4V grain size demonstration is the special lamellar grain morphology, making it unsuitable to implement the equivalent spherical assumption. Figure 5-2 shows a new variable, aspect ratio (AR), which needs to be considered. Figure 5-3 shows an ellipse fitting process for measuring AR values for all the grains and obtains an average measured AR result of 3.09 for this EBSD image. The polycrystalline lath area S was determined as the product of pixel size and the number of pixels included in individual grain aggregates. The major and minor axis dimensions in the ellipse equation is equal to the corresponding fitted lath length and

lath width respectively. Finally, the equivalent lath width w, was again calculated based on the ellipse area equation:

$$S = \pi \times d_a \times d_b = \pi \times \frac{AR \times w}{2} \times \frac{w}{2}$$

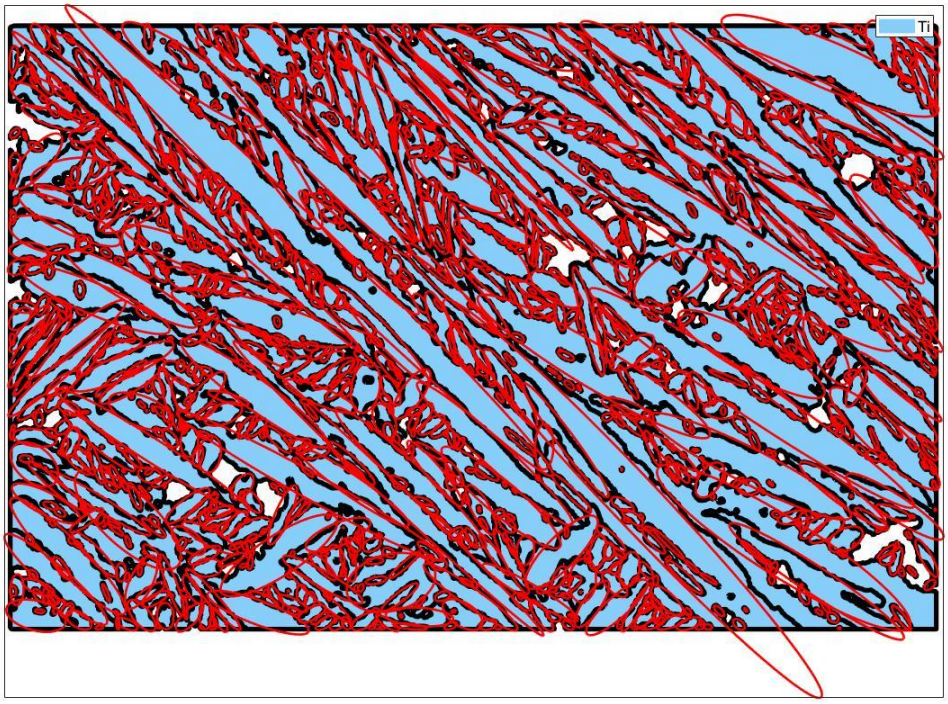

Figure 5-3. EBSD grain morphology fitted with ellipse assumption for measuring and calculating the aspect ratio value of alpha phase laths.

Figure 5-4 shows the reconstructed EBSD phase map with the alpha phase coloured in green. EBSD also helps quantify the material and crystallographic lattice constants required in the physically-based CPFE constitutive laws.

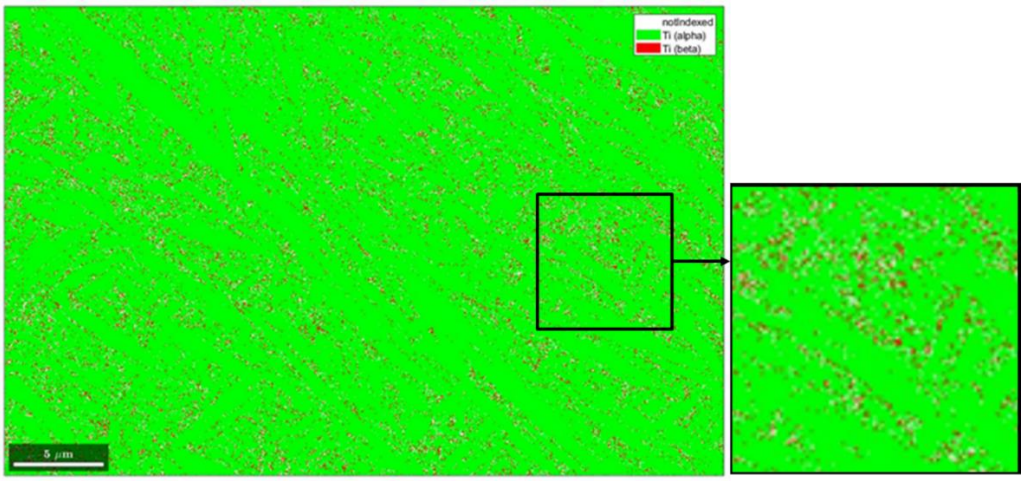

Figure 5-4. EBSD phase map, alpha HCP phase in green and beta BCC phase in red.

Other important information required is texture, or crystallographic orientation. Figure 5-5 shows the non-index filled and reconstructed EBSD grain map coloured according to the inverse pole figure (IPF) legend. Pole figures, IPF, and ODF were plotted to analyse the general crystallographic orientation distributions, texture strength along sample coordinate, and spatial distribution of the Euler angle sets, respectively. These orientation measurements were used as a criterion for determining the rotation matrix of finite element aggregates in the CPFE model.

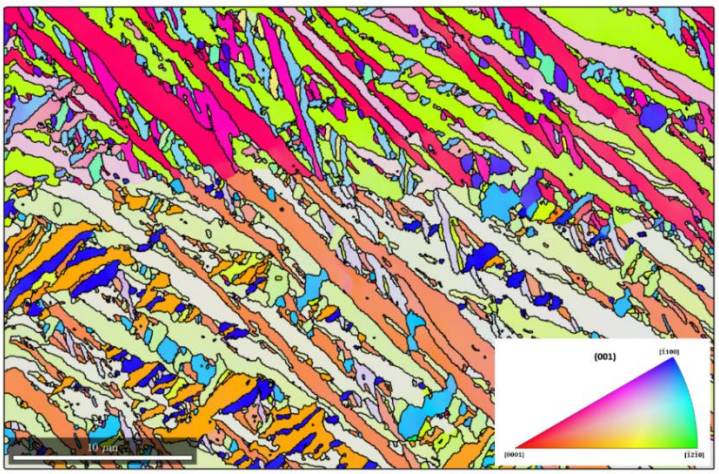

Figure 5-5. High resolution EBSD grain map after noise clean-up and filling process. The colour shows the crystallographic orientation for (001) plane based on the IPF.

5.2.2 Crystal plasticity modelling approach

5.2.2.1 Equivalent dual-phase polycrystalline model construction.

As a main objective of this work is to investigate the effect of graded microstructure, it is important to precisely represent the minor difference between the lath size and phase fraction. The EBSD-based method described in Chapter 4 is not suitable to do this parameter study because although morphologically accurate, an EBSD scan usually has ~5% unindexed noise, adding difficulties in phase fraction determination. Consequently, this chapter employs a novel VT algorithm to realize the required microstructure for consistency whilst maintaining specific model parameter control. An advanced multiple-tessellation poly-grain realization method [22] was developed to represent the dual-phase lamellar microstructure, including two main settings: lath width and lath aspect ratio. The sub-tessellation via the second level Laguerre cells discretization further divides the VT cells generated in the primary domain, into lamellar planes [341]. The developed dual-phase CPFE model differentiated the lath width ratio of α and β phase grains to represents the phase fraction. Figure 5-6 (a) shows a 3D example including complete prior-β morphology and the alpha laths in between. Unfortunately, such a model is too complex to analyse requiring prohibitive computational costs to analyse, with the current computational capability. This difficulty includes not only CPFE running effort, but the required input file generation, e.g., meshing, material property definition, as well as boundary condition settings. Consequently, one cuboid cut of a reasonable size from the 3D full model was adopted and the thickness of this model along the z axis (out-of-plane direction) was defined to be the same as the alpha lath width. Figure 5-6 (b) shows the constructed thin-slice and dual-phase lamellar CPFE model to represent the polycrystalline grains with an average β lath width of 0.0276 μm. The constructed RVE exhibits similar dual-phase morphology validated against the SEM image, showing darker regions of alpha phase, with few lighter regions around the lath boundary representing the retained beta phase laths.

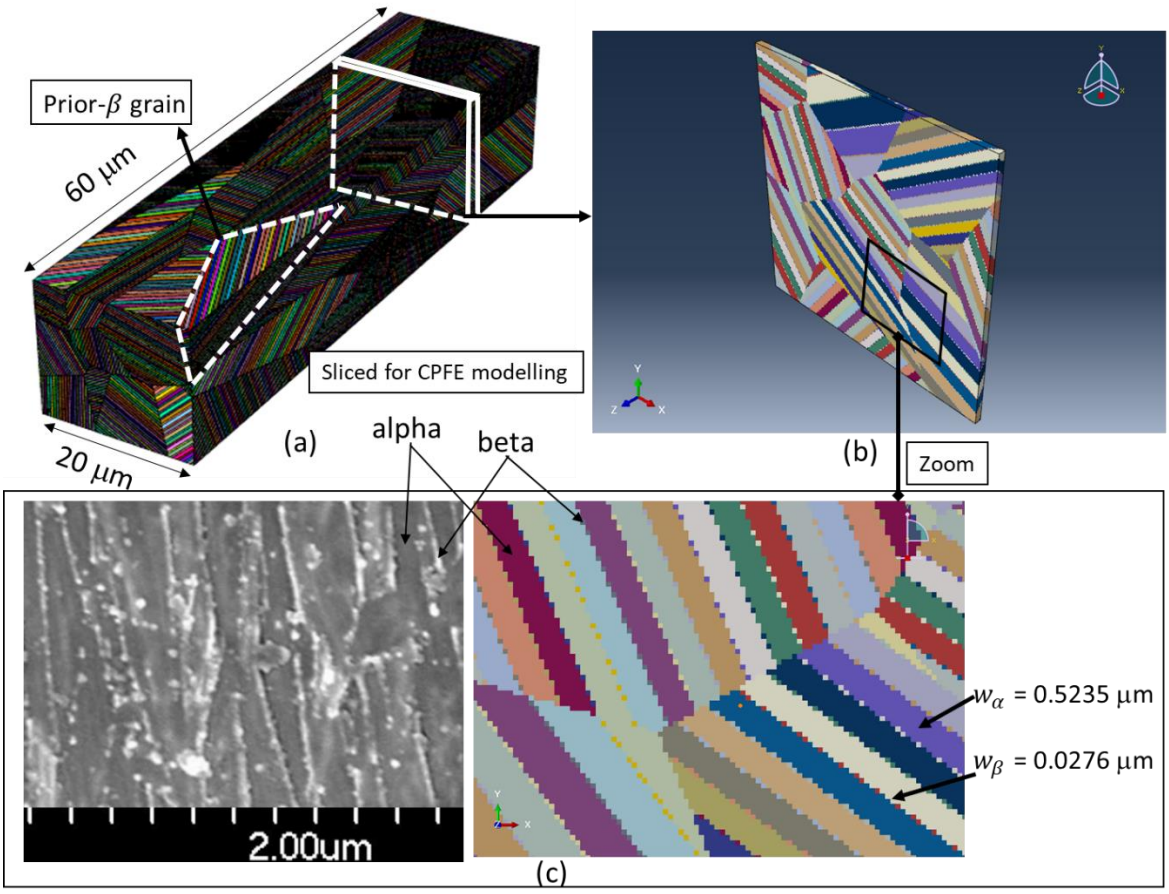

Figure 5-6. The methodology of constructing microstructural equivalent dual-phase lamellar CPFE model. The ratio of alpha and beta lath equals the phase volume fraction.

The orientation equivalent model is achieved by assigning the same orientation of the main grain aggregate (Figure 5-7 indicates 10 in total and highlighted with rectangles in the IPF) to generate the associated orientational dependant material data card in CPFE simulation. Figure 5-7 first shows the strategy for assigning the crystallographic orientation property in the CPFE model based on EBSD data. The IPF shows the texture distribution for 1571 grains in the reconstructed EBSD map. The IPF indicated ten fibres with strong texture, whose Euler angle set was then converted to a rotation matrix for the CPFE user subroutine. The generated VT with orientation definition was coloured using the same IPF legend through a customized-written code. The 10 generated prior-β grains orientations are shown in the IPF and the alpha laths within the same grains generally have the same orientation compared to its parent grain (prior-β).

Figure 5-7 finally compares the EBSD orientation analysis result with the CPFE model, through pole figures projected on the (0001) and $(10\bar{1}0)$ planes, as well as an ODF plot showing the spatial distribution of the three Euler angles. The EBSD analysis utilises 137 randomly selected grains which is the same as the CPFE model for plotting the orientation figures, thus the EBSD pole figure scatters slightly after each run. The orientation plots from the EBSD and CPFE model show close agreement of texture distributions.

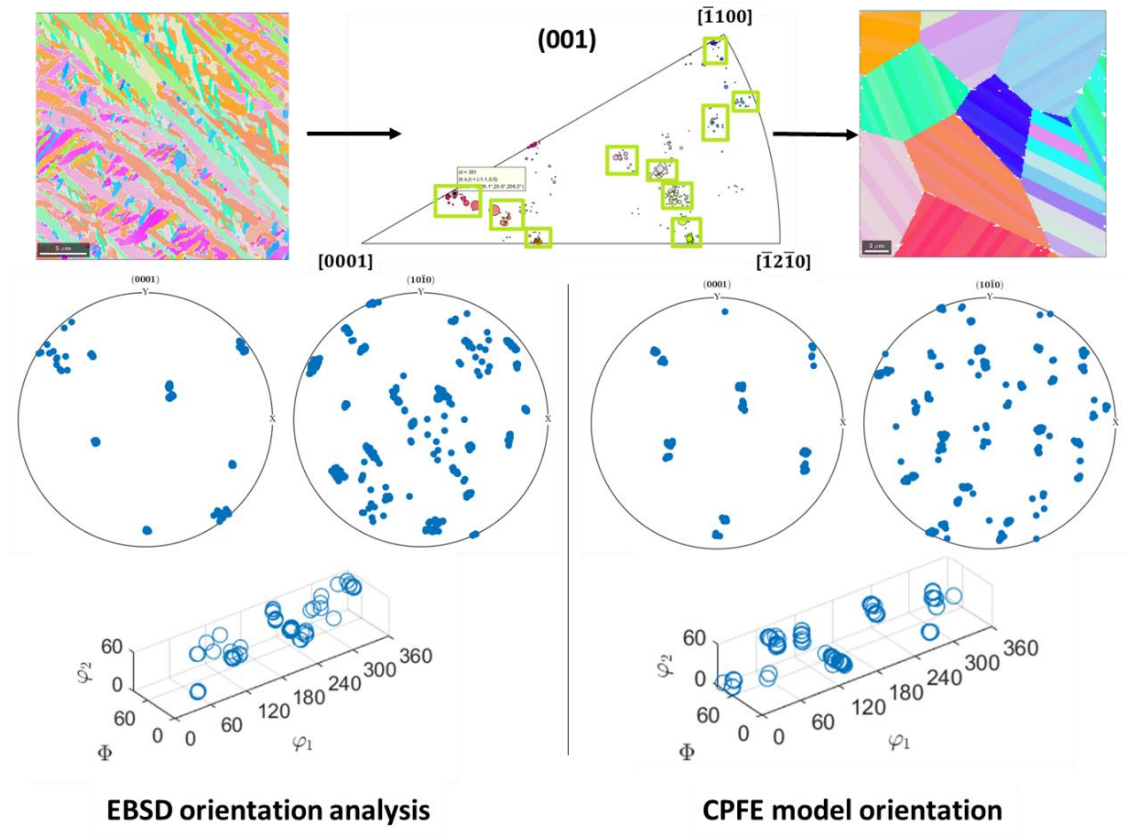

Figure 5-7. Schematic of assigning statistically equivalent texture in CPFE modelling and the orientation information comparison between EBSD characterisation and CPFE modelling.

5.2.2.2 Constitutive parameters calibration and fitting methodology.

Three main calibration steps were carried out to help determine the optimum set of constitutive parameters implemented here: (i) the material crystal lattice parameter measured from EBSD detection, (ii) the optimized parameters iteratively calibrated to the measured bulk tensile stress-strain response, and (iii) previously published parameters

established for the present $\alpha - \beta$ dual-phase titanium alloy and material models in previous research [28, 144].

The parameter optimization tool is developed based on the MATLAB toolbox non-linear least square (Lsqnonlin algorithm) which uses the Levenberg-Marquardt algorithm to minimize error with respect to a target, e.g., experimental test data. Lsqnonlin assists in automatic initial parameters modification to reach an optimized parameter set without time-consuming manual trials or unreliable human bias. This approach was successfully implemented for parameter optimization in studying the kinematic behaviour of MarBN steel[342] , and nickel-based superalloys [343]. Figure 5-8 illustrates the Lsqnonlin fitting workflow in this work, starting by defining the four parameters to be optimized and combining them into a matrix variable $\boldsymbol{x}$. Elastic parameters E_1, v_{12}, the two critical resolved shear stress (CRSS) for basal $\tau_{0,<a>}$ and pyramidal slip systems $\tau_{0,<a+c>}$ respectively. This matrix was altered and iterated by comparison with the monotonic tensile response to achieve minimum error. The CRSS for beta phase was calibrated as 280 MPa for a functional gradient Ti-6Al-4V alloy [337]. The initial dislocation densities were from previous modelling research on Ti-6242 [28], and other constants from the original research [31] which first introduced this flow rule. Table 5-1 lists the constitutive parameter values implemented in this work.

Periodic boundary conditions (PBC) were defined as previously shown in Figure 4-7, to constrain the adjacent boundaries of the CPFE polycrystalline model throughout the deformation simulation. Under such PBC definition, the laths are permitted to strain in the out-of-plane direction, but the deformation is constrained to be uniform.

Table 5-1. Constitutive parameters used in CPFE modelling.

Parameter	HCP Alpha lath	BCC Beta lath
$\tau_{0,<a>}$	322 MPa	280 MPa [337]
$\tau_{0,<a>}$	419 MPa	-
G_{12}	30137 MPa	54900 MPa
G_{13}	57900 MPa	54900 MPa
E_1	88000 MPa	82000 MPa
E_3	105000 MPa	82000 MPa
v_{12}	0.46	0.46
v_{13}	0.22	0.46
b <a>	2.95 x 10^{-4} μm	3.31 x 10^{-4} μm
b <c+a>	3.84 x 10^{-4} μm	-
M	0.8	
k	1.38 x 10^{-23} J K^{-1}	
T	293 K	
ΔH	7.58 x 10^{-20} J	
ν	1.00 x 10^{11} Hz	
γ_0	1.32 x 10^{-4}	
ρ_{SSD}^{m}	5.0 μm^{-2} [28]	
ρ_{SSD}^{s}	0.01 μm^{-2} [28]	

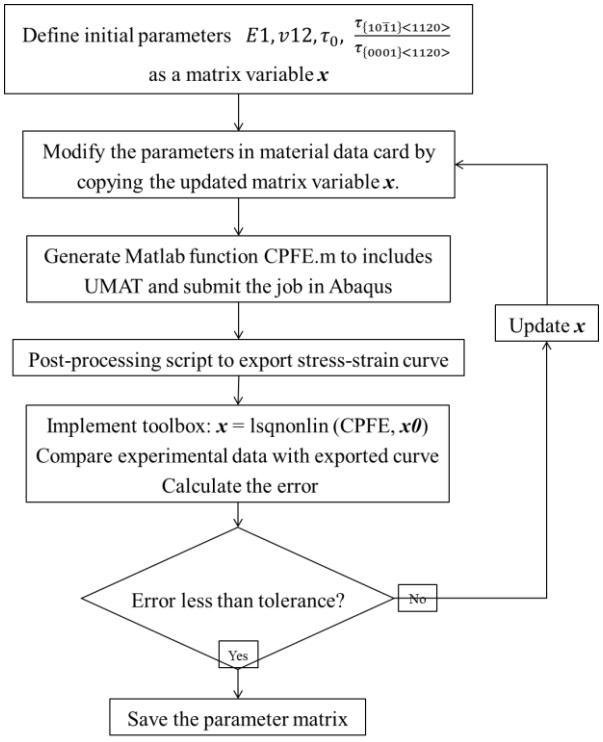

Figure 5-8. Workflow of an efficient and convenient curve fitting programme NL-Lsq, for parameter calibration, to determine elastic moduli and critical resolved shear stresses.

5.3 Results

5.3.1 Mesh convergence study

The converged mesh size was determined through the sensitivity of the computed stress-strain curve to different mesh designs and degrees of refinement. The CPFE modelling works are carried out using the high-performance computer, named Kay, the primary device for academic research in ICHEC. The modelling jobs are submitted on a cluster equipped with 2.4 GHz Intel Xeon Gold 6148 (Skylake) processors (4-core ABAQUS acceleration enabled), and the RAM of 192 GB. Five different element densities, with numbers of elements, show the different meshes considered ranging from 3200 to 86400 were defined to mesh an alpha phase only CPFE model with the lath width of 0.5 μm. The C3D20R voxel type element was assigned, and Figure 5-9 indicates minimal difference for refinement above 60000 elements. In this fully lamellar model, the predicted strength after yield increases with the mesh density. However, there is no obvious trend before yield as all five models predict only 1 MPa stress difference at a strain of 0.7%.

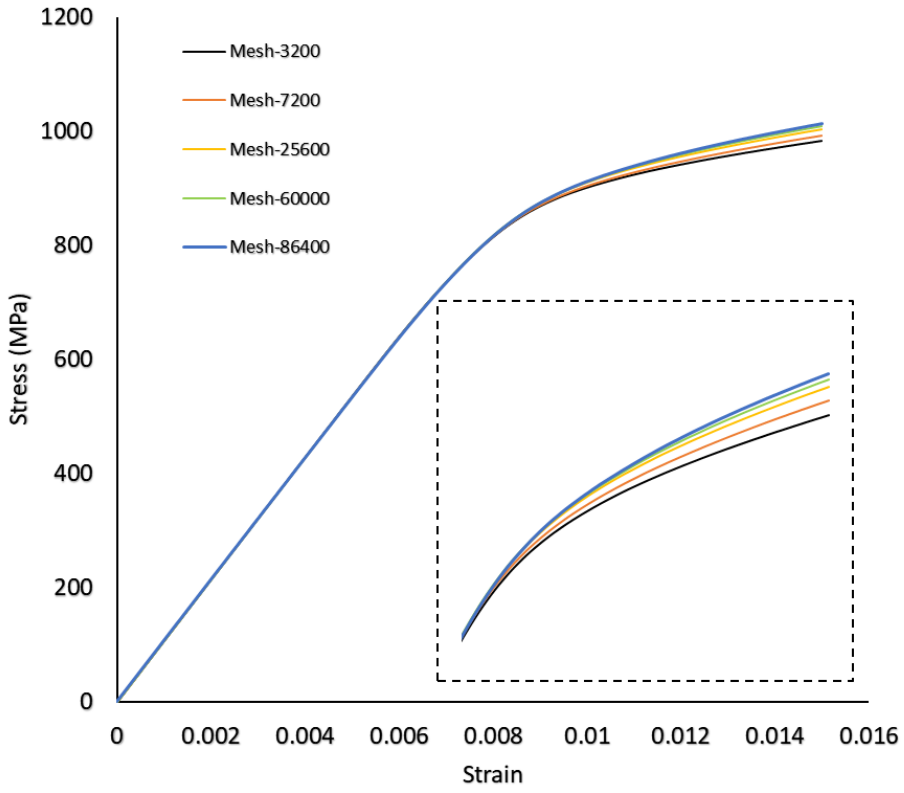

Figure 5-9. Effect of mesh refinement (no. of elements, uniform distribution) on CPFE predicted bulk tensile stress-strain curves.

The predicted stress at 1% strain was shown as the criterion for determining convergence. Figure 5-10 shows the relationship between this stress and the number of elements. The difference is less than 0.17% on increasing number of elements from 25600 to 60000 and this difference reduces to 0.05% on further increasing number of elements to 86400. Mesh density adds a heavy computational burden on the CPU core performance when assigning PBCs and running the job. The mesh with 60000 elements is then decided for the remaining models based on balancing the convergence performance and computational requirement.

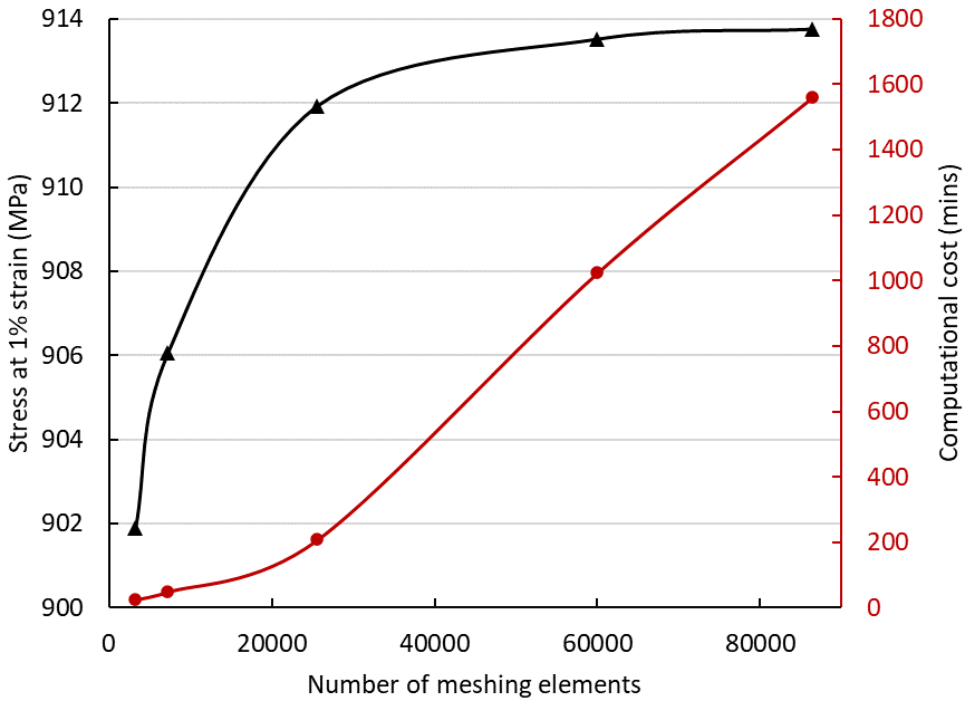

Figure 5-10. The relationship between the computational cost, predicted macroscopic stress at 1% strain for different numbers of C3D20R (uniformly spaced) elements.

5.3.2 Tensile behaviour prediction.

The tensile behaviour of the PBF-LB manufactured Ti-6Al-4V alloy was predicted by the statistically equivalent CPFE model where the physically-based strain gradient constitutive law determines the crystal plasticity deformation. The retained β phase fraction was determined to be 3% by calculating the $110_\beta/101_\alpha$ diffraction peak intensity [281] through X-ray diffraction (XRD). The average lath area was calculated as 0.665 μm^2 and the calculated average equivalent lath width $\bar{w}$ of the Ti-6Al-4V sample is thus 0.5235 μm.Table 5-1 shows the calibrated parameters used in this Chapter. After calibration and validation with the experimental measurement, the CPFE stress-strain curve shows close agreement with the tensile test up to 1.5% strain, as shown in Figure 5-11. The CPFE-predicted Young's modulus of 103.35 GPa and yield stress (0.2% offset) of 941.12 MPa compare favourably to corresponding experimental values of 104.9 GPa and 939.20 MPa respectively.

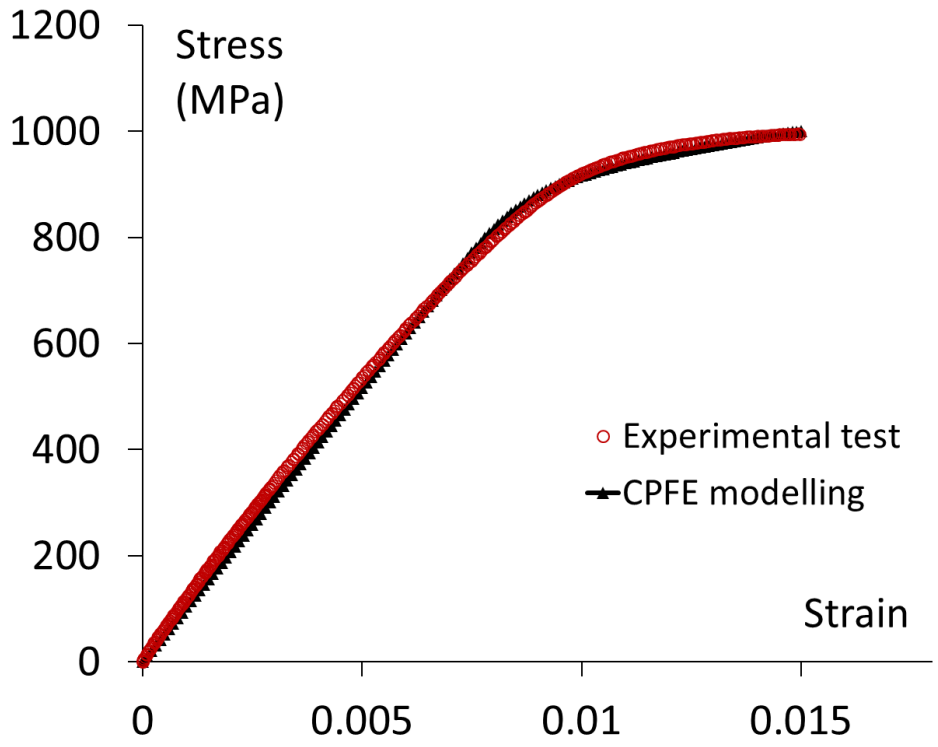

Figure 5-11. CPFE-predicted tensile response compared to the experimental measurement based on the calibrated constitutive parameters.

Figure 5-12 shows the CPFE predicted contour plots for this dual-phase lamellar sample, including the maximum principal stress, logarithmic strain, cumulative crystallographic slip p, as well as the GND density distribution, at 1.0 % strain. The CPFE predicted stress-strain curve gives a macroscopic flow stress of 916.2 MPa at this strain while the principal stress contour plot shows a maximum localized stress of 1763 MPa, corresponding to a localised (microstructural-induced) stress concentration factor of 1.92. Deformation strain inhomogeneity is observed between the neighbouring alpha lath within the same grain while the difference across prior-β grain boundaries. The Beta laths show higher accumulative crystallographic slip p (see Section 2.8.6), this accumulated deformation tends to be uniform among alpha laths within the same prior-β grain.

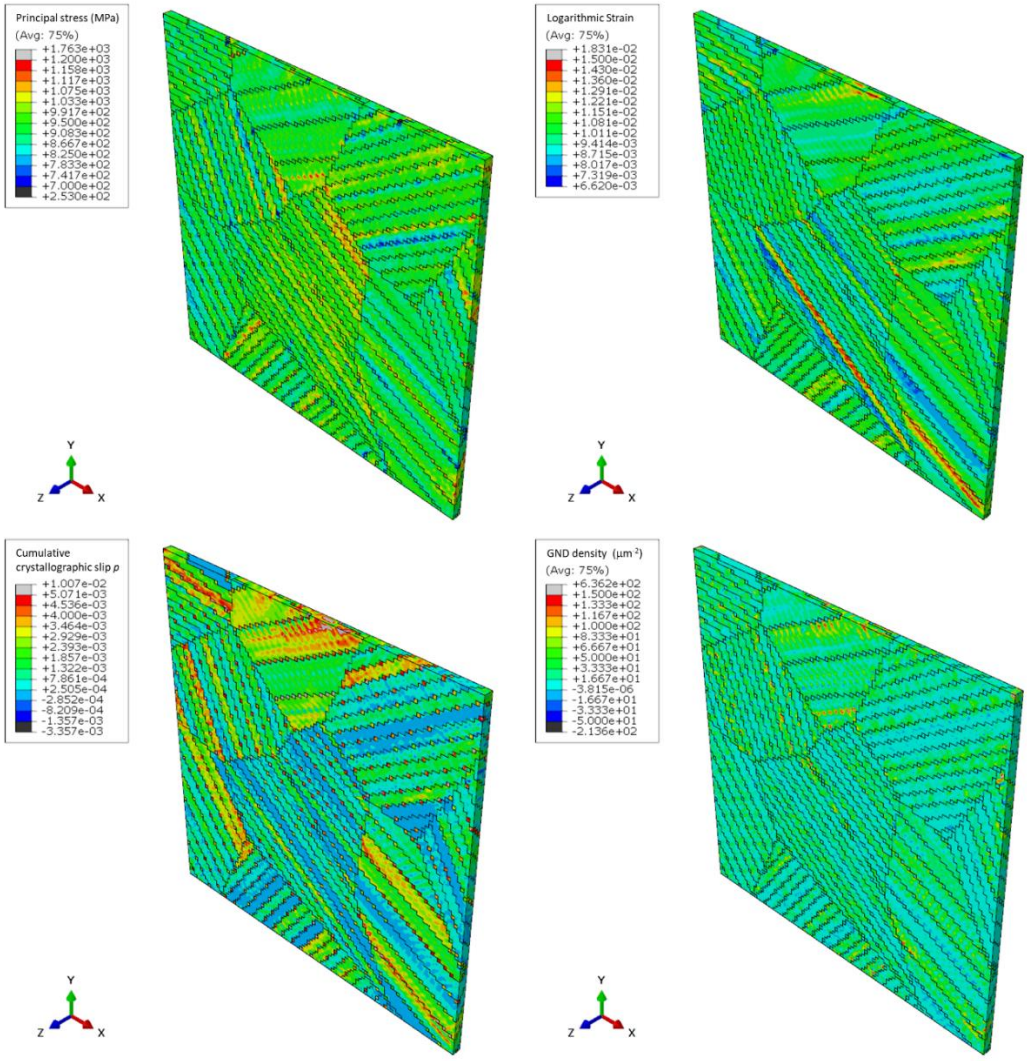

Figure 5-12. The contour plots showing principal maximum stress, logarithmic strain, cumulative crystallographic slip, and GND density distribution from CPFE modelling.

5.3.3 Inhomogeneous mechanical property characterisation.

The printed sample with long build height (~30cm) has exhibited various microstructure from bottom to top. Figure 5-13 shows the microscopy images scanned from the as-built bottom and, top areas, and the top area for post-built HIP, respectively. XRD was used to measure the phase fraction. Table 5-2 lists the measured average equivalent lath width and beta phase fractions for these three conditions [323]. As the distance (build height) from the building base plate increases, an increase in alpha lath width w_α from 0.7 to 1.1 μm is observed while the beta phase fraction increases from 3% to 8%.

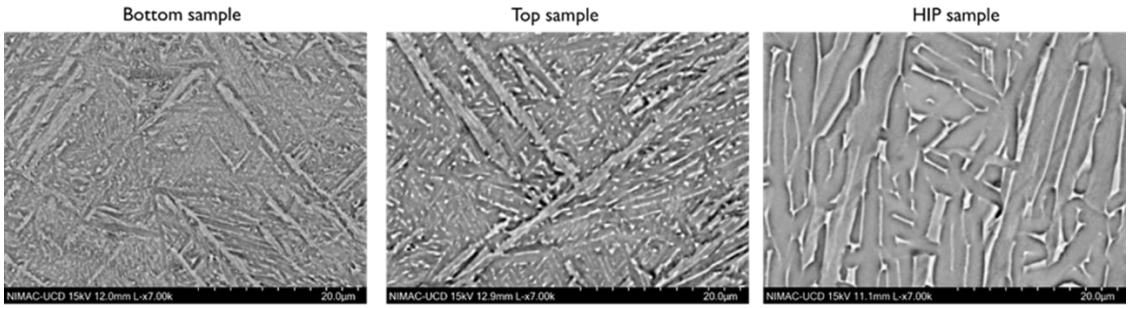

Figure 5-13. SEM images of AM Ti-6Al-4V alloys at the regions of bottom, top, and after HIP treatment on top region.

Table 5-2. Microstructural information characterized from XRD detection and SEM images, including lath width and the beta phase fraction.

Sample	w_α (μm)	Beta phase (%)
Top, as-built	1.06	8.8
Bottom, as-built	0.76	3.0
Top, post-built HIP	~5	9.5

Figure 5-14 shows the corresponding CPFE models generated to represent the microstructure for the three conditions. The CPFE model size was increased by a factor of five times with a total cuboid volumetric size of $100 \times 100 \times 5$ μm^3 to represent the HIP sample, compared to that of the as-built top CPFE model, to maintain the same grain morphology and texture distribution. As defined by the equivalent model generation method introduced in section 5.2.2.1, the three models all have the correct values of Beta phase (viz. 8.8%, 3%, 9.5%) and of w_α (viz. 1.06 μm, 0.76 μm, and 5 μm) respectively.

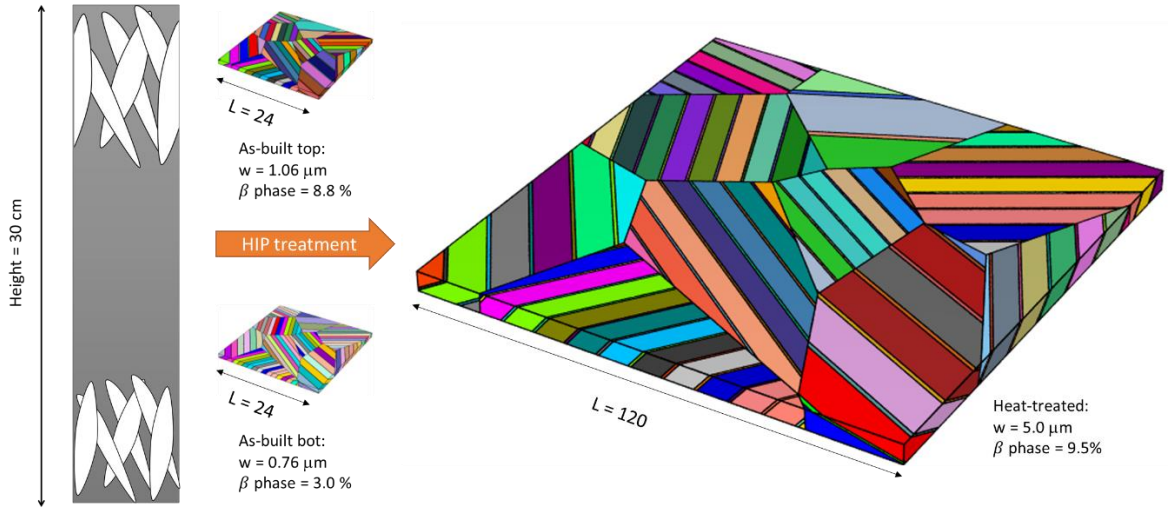

Figure 5-14. Schematic of the CPFE models' generation to represent the microstructural features including alpha lath width size and phase fraction ratio, for the three samples respectively.

Figure 5-15 shows the CPFE-predicted stress-strain tensile curves for the bottom, top, and HIP samples. The CPFE results are generally consistent with the mechanical test values [323]. Table 5-3 shows the yield stress from both experiment and CPFE modelling. The experimental test confirms that the sample after HIP treatment has the lowest strength, which drops by 10% compared to the as-build part. The inhomogeneous mechanical behaviour is captured between the bottom and top area of the as-build samples, the bottom yield stress is measured about 1% higher than the top in both model and test.

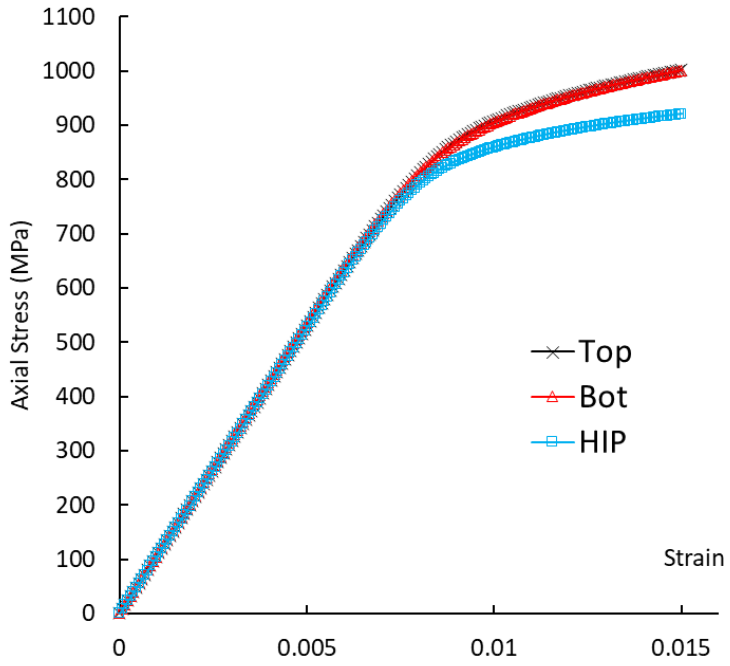

Figure 5-15. The tensile stress-strain curve of the as-received bottom sample, top area sample, and HIP sample, predicted by strain gradient CPFE model.

Table 5-3. Comparison of the yield strength difference between the three samples from experimental measurement and CPFE prediction.

Sample	Experimental YS (MPa)	CPFE predicted YS (MPa)
Top	903.6	914.90
Bottom	911.9	922.07
HIP	813.9	836.25

Figure 5-16 shows the GND evolution as the strain increases during the tensile deformation. For bottom as-built model. Figure 5-17 plots the probability density function of the maximum GND distribution at 1.5 % strain. The GND distribution map shows slightly lower GND density for the top microstructure compared to the bottom, with the heat-treated microstructures showing much lower GND density. The effect of as-printed lath width variation in a single component on bulk stress-strain relationship was minimal (1% variation in yield strength), whereas a greater effect (10% reduction in yield strength)

was found in the post heat treatment specimen. Most elements in top and bottom models have the GND density of around 20 μm^{-2} while the density peak is smaller in the top model. HIP model has smaller GND density where most elements have a GND density of less than 10 μm^{-2}.

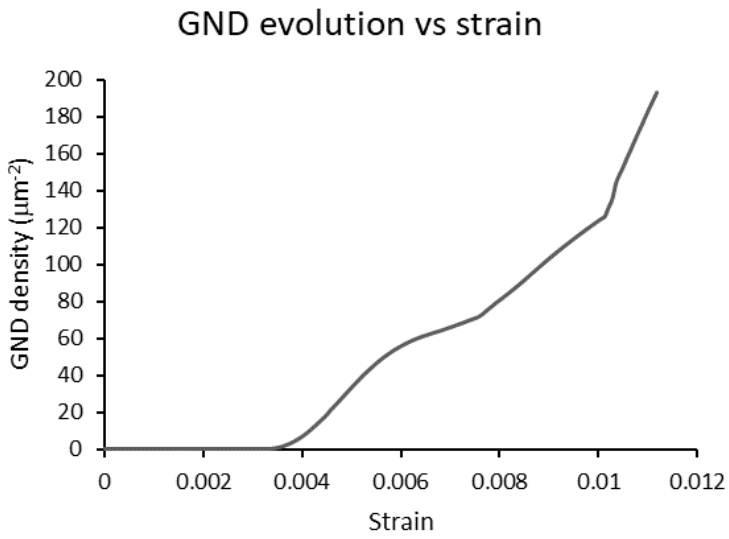

Figure 5-16. The maximum GND density evolution during the tensile deformation.

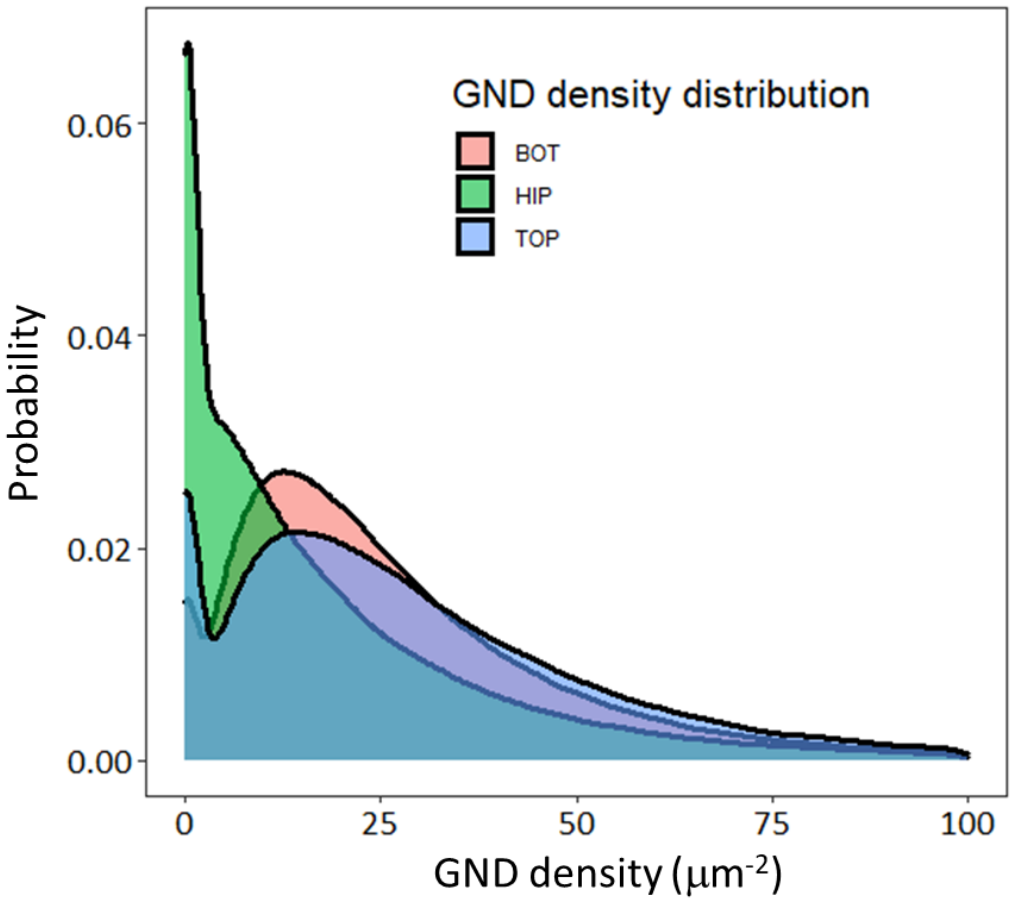

Figure 5-17. GND distribution plot of the bottom, top, and HIP CPFE models.

5.4 Model microstructural sensitivity analysis

5.4.1 Lath width size effect

The developed model successfully captures the microstructural sensitive effect when comparing as-built and post-built HIP samples. It is worth noting that the difference in mechanical response is contributed by both lath width and phase fraction. This means that the decrease in strength after HIP was caused by multiple factors such as the softer beta phase, the changing aspect ratio, and thicker lath. To quantify individual lath size effect and fulfil the advantage of computational modelling for strict single variable sensitivity, alpha phase models differing in lath width (w_α) only, were generated to quantity only lath

width size effect. This study is especially meaningful for metals having one dominating phase, like Ti-6Al-4V, mainly consisting of alpha phase in a near-alpha titanium alloy. Considering the motivation of avoiding the influence of unavoidable scatter of crystallographic orientation and number of grains among separate tessellations, the models in this lath width size effect study are all scaled based on the same morphology model.

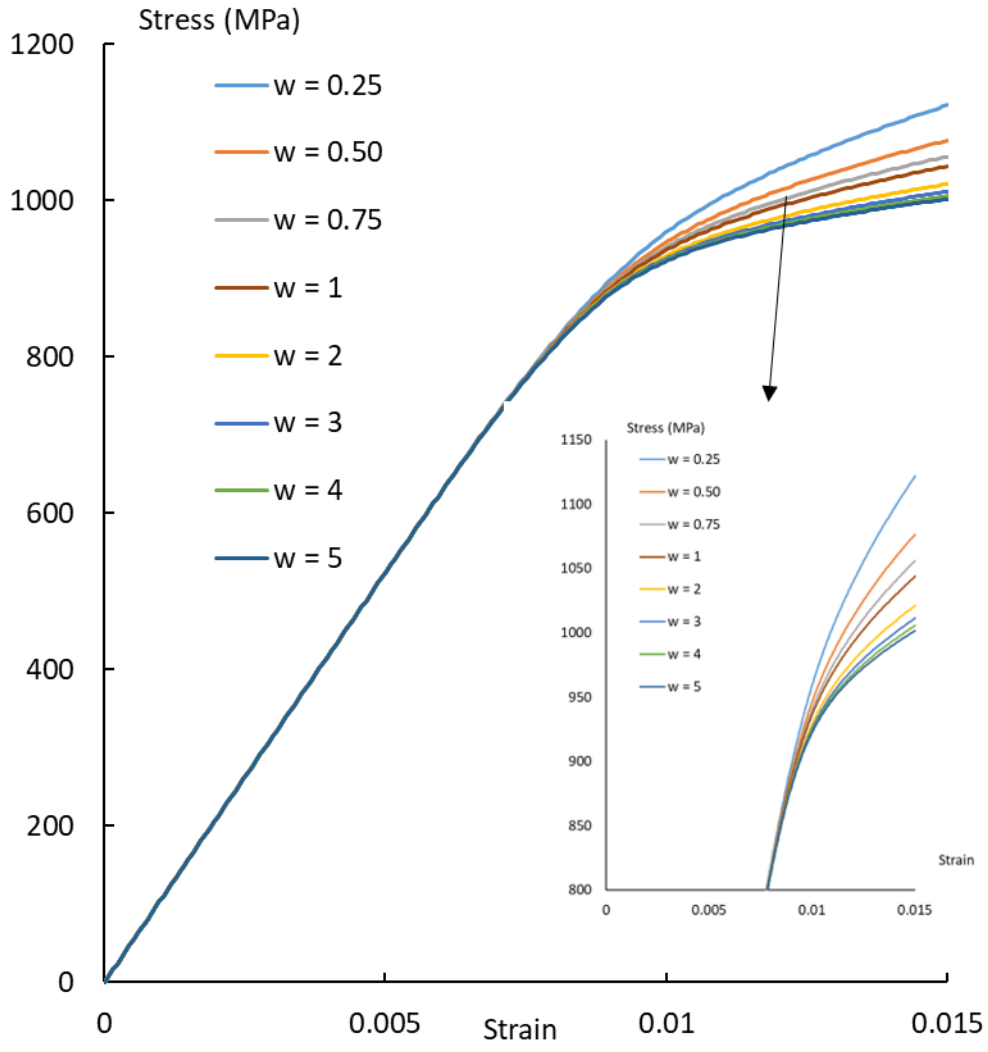

Figure 5-18. Tensile and yield behaviour predicted by CPFE models varying in lath width size.

CPFE models are generated with average lath width of 0.25 μm, 0.5 μm, 0.75 μm, 1 μm, 2 μm, 3 μm, 4 μm, and 5 μm to study size effect of the lamellar material. Figure 5-18 shows the predicted stress-strain tensile curve up to 1.5% strain, and Figure 5-19 shows the predicted relationship between maximum GND density at 1.5% strain and the average lath width. Increasing lath width causes a decrease in GND density, leading to reduced yield stress, consistent with the plastic deformation constitutive laws. GND density exhibits higher sensitivity to lath width for a smaller width. This calculated maximum GND density drops by 85% from 1417.0 to 210.4 μm^{-2} as lath width increases from 0.25 to 2.0 μm. Thus, the lath width change has a greater influence on the predicted yield strength when the lath width is smaller than 2.0 μm. An exponential equation can be used to represent the predicted relationship by: $\rho_{GND,max} = 401.32\, w^{-0.914}$.

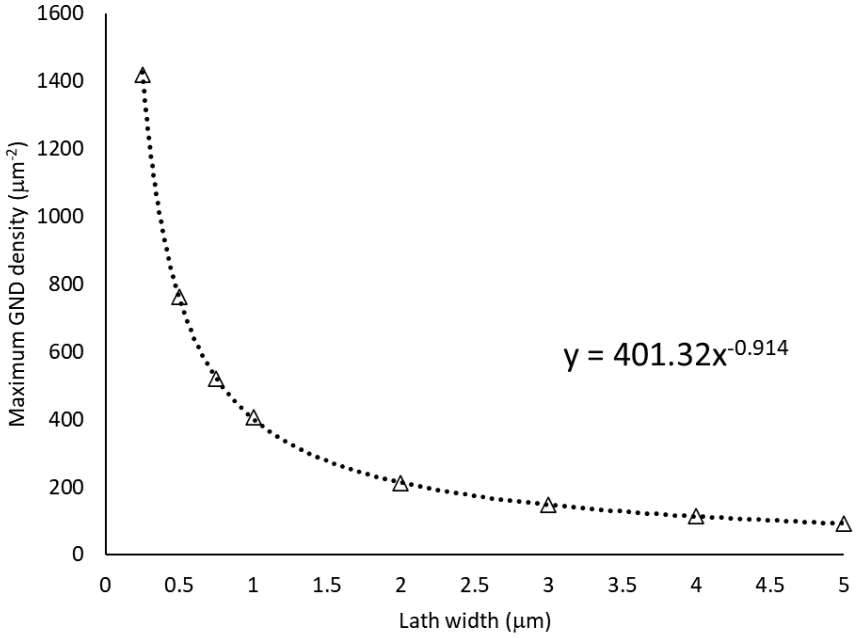

Figure 5-19. The relationship between the CPFE predicted GND density at the strain of 1% and the average CPFE model lath width.

5.4.2 Prior-β grain size effect

Two different CPFE model comparison groups were generated to investigate prior-β grain (PBG) size sensitivity. In both cases, the cuboid model size was kept constant while

changing the number of prior Beta grains. In each comparison group, four models were generated with different numbers of PBG (n_β) namely 2, 4, 7, and 10. The multiple Voronoi tessellation approach implemented so far has a constraint, with the generated lath width following a normal distribution. In this case, the alpha lath widths are dependent on parent PBG size and consequently not constant compared to the size within the different beta grains, as shown by the Group 1 model in Figure 5-20. Figure 5-21 shows the predicted tensile curve comparing the four models in Group 1. The elastic moduli are similar (107.4 to 108.6 GPa), but not equal due to the unique texture material feature and the anisotropic definition in constitutive laws. There is no obvious relationship between elastic behaviour and the number of grains because the Young's modulus is affected by crystallographic orientation and lattice type. However, an obvious difference can be noticed after yielding. Tensile strength drops from 1070 MPa to 1040 MPa (2.8%), as the n_β increases from 2 to 10.

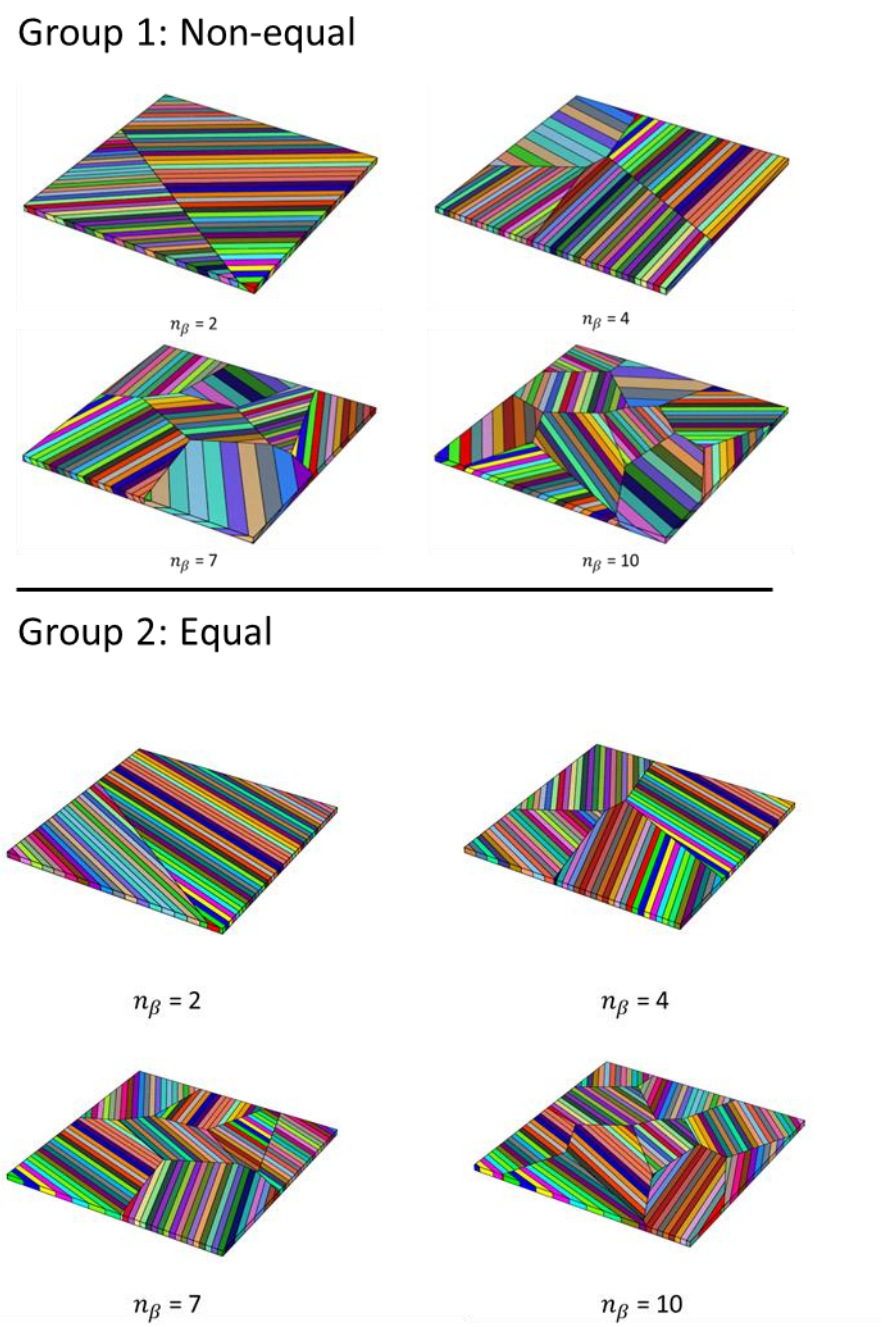

Figure 5-20. Schematic of the two constructed model groups for prior beta grain size study, with uneven and even alpha lath width, respectively. In each group number of prior beta grains were defined to range from 2 to 10 grains.

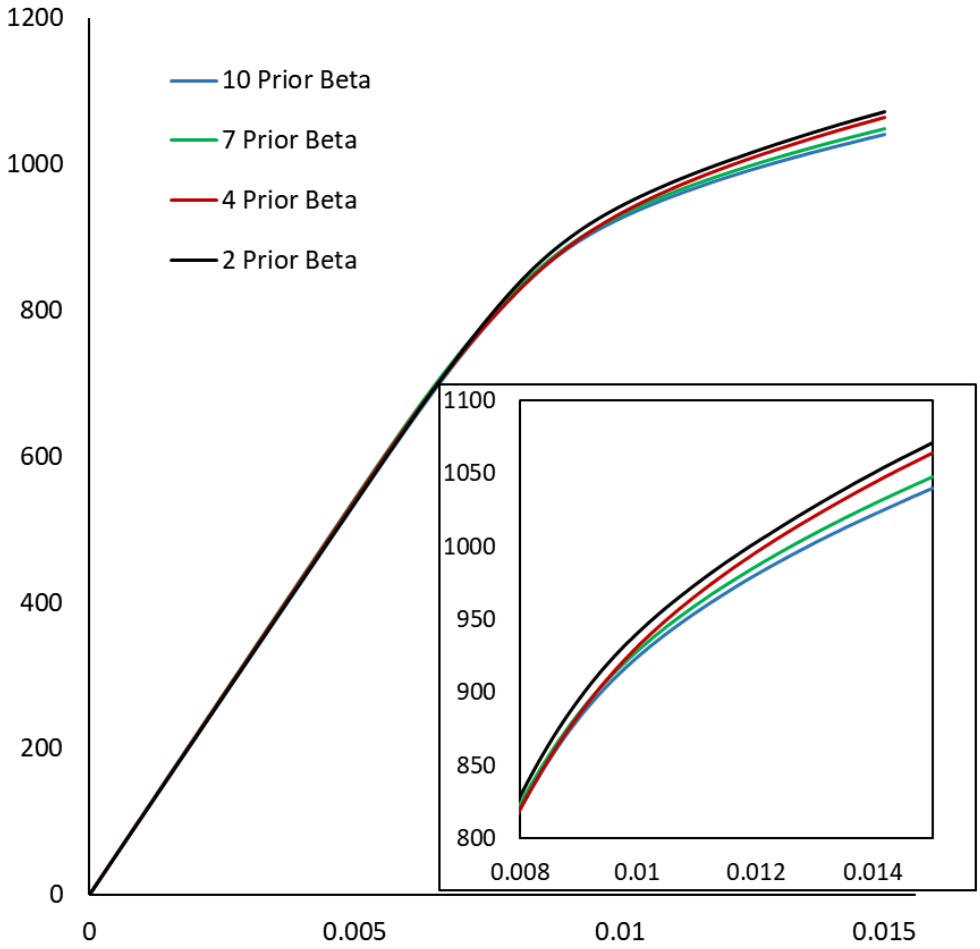

Figure 5-21. Tensile behaviour after yield predicted by the uneven alpha lath models group with the number of prior beta grains of 10, 7, 4, and 2.

The limitation for comparison Group 1, as mentioned, is the non-equal (non-uniform) alpha lath width. Then the VT algorithm was modified to remove the linkage between the alpha lath and parent grain, allowing equal alpha lath width for different number of PBGs, as shown in Figure 5-20 Group 2. In this case, a negligible difference is observed from the stress-strain curves. The largest difference is 0.34%, so the PBG size has a negligible effect on tensile response.

5.4.3 Grain morphology effect

This section investigates the effect of grain morphology, e.g., for the commonly-observed lamellar and equiaxed shape grains. Figure 5-22 shows the equiaxed polyhedron model and fully regular (the grains have similar aspect ratio) models. As well as the previously described lamellar model, the three models are defined to have the same model size and the same number of elements sets (137 grains in equiaxed or 137 laths in the lamellar model, in total), thus leading to the same equivalent spherical areas.

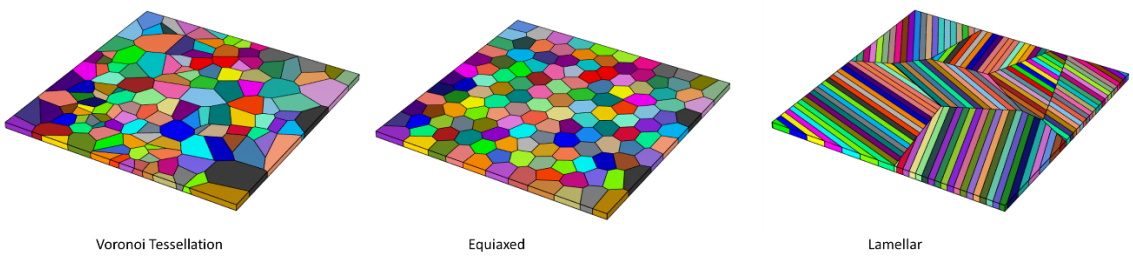

Figure 5-22. Schematic of the generated equiaxed, regular equiaxed, and lamellar CPFE model for grain shape effect study.

The modelling results show a negligible difference in terms of predicted macroscopic stresses, with only 4 MPa difference at the strain of 1% for the average stress of 1065 MPa. The regular model has the lowest strength, 1064.2 MPa. However, their predicted GND distributions show some differences, as shown in Figure 5-23. The GND density in the lamellar lath model has a bigger standard deviation due to the irregular lamellar shape, and sharper grain boundary. In the equiaxed grain model, the distribution is narrower, indicating that more elements have a similar GND density result, and this narrow region area grows slightly when the equiaxed grain morphology becomes more regular.

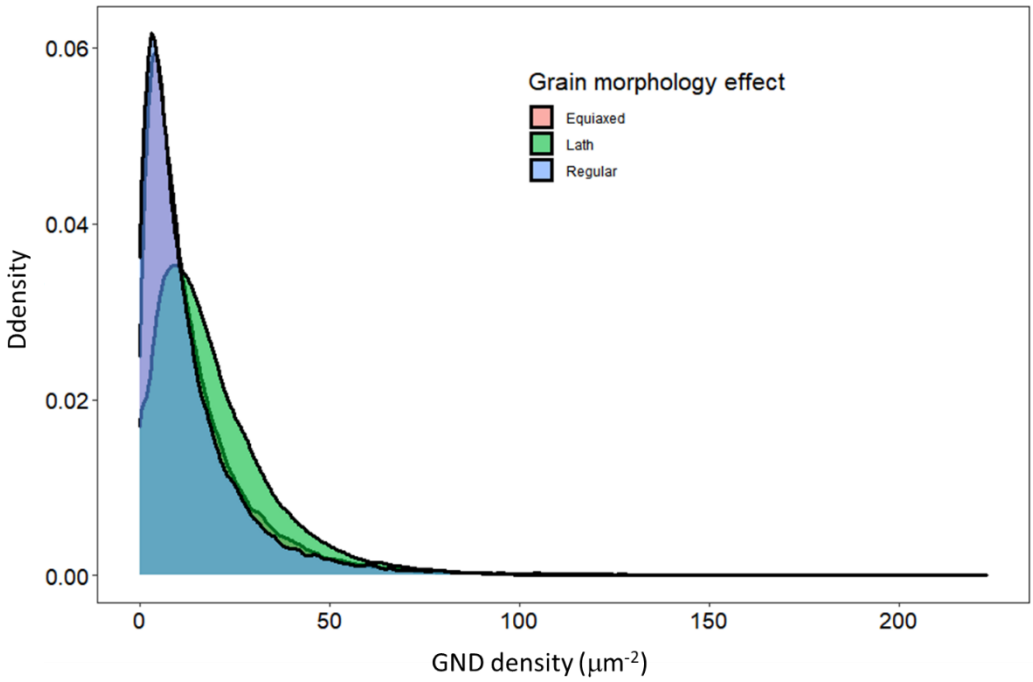

Figure 5-23. GND density plot for the lath, equiaxed, and regular equiaxed grain morphology samples.

5.5 Discussion

During the PBF-LB solidification process, the PBGs of Ti-6Al-4V solidify to a basket-weave morphology of α' laths. The cooling speed in the upper area of the vertically built sample is slower compared to that in the earlier layers. Previously printed layers also undergo more annealing cycles compared to the subsequent layers. These differences in local thermal history cause a graded microstructure along the built direction, with an associated graded mechanical behaviour. It is worth noting that the models used here for investigating the gradient phenomena as well as the heat treatment, take account of the lath width gradient, and the phase composition fraction changes. Section 5.4.1 considers only lath width effects and quantified the implemented strain-gradient size effect for the lath widths ranging from 0.25 to 5 μm, which covers the commonly reported range, thus confirming that the present strain-gradient CPFE is a suitable modelling tool for studying the PBF-LB Ti-6Al-4V alloy.

The columnar morphology prior-β usually has a length of ~100 μm, which is outside the size sensitivity of GND prediction from this CPFE model. The computational cost of

using the high-performance computer to run this full model can be estimated from the quantified relationship shown in Figure 5-10. Assuming the full model contains a height equal to the prior- β length, the model has twelve million elements (using the same meshing density). Thus, the estimated running time is 158 days with a linear fit. An even longer time of 554 days is predicted if using a power law to fit the computational cost versus the number of elements relationship. However, the methodology of generating this full model still has potential for future research, given the development of more efficient constitutive laws with optimized coding structure, and the capability of higher performance computational facilities.

The relationship between the lamellar microstructure and mechanical behaviour has not been quantified, for PBF-LB fabricated Ti-6Al-4V alloys. To provide a more efficient and less computationally intensive method for lath size sensitivity, relationships between microstructure and its macroscopic tensile behaviour are fitted to the CPFE-predicted results. The Lsqnonlin was adopted here.

Hall and Petch [344, 345] presented a phenomenological relationship between the grain size and the yield strength, as follows:

$$\sigma_{YS} = \sigma_0 + \frac{k_{\mathrm{HP}}}{w^n} \tag{5-1}$$

where σ_0 is an assumed YS of the polycrystalline material with a large grain size, while n and k_{HP} are two constants identified from a test data for different grain sizes.

The Hall-Petch relationship was calibrated against CPFE modelling data presented in Section 5.3.1. The calibrated form is as:

$$\sigma = 828 + \frac{103.69}{w^{0.2848}} \tag{5-2}$$

The fitted Hall-Petch relationship covers the reported tensile yield strength for the as-build Ti-6Al-4V samples ranging from 828 to 1166 MPa [4, 346].

The generalized size-dependent Taylor-strengthening relationship was introduced as [347]:

$$\sigma_{YS}/\mu = \left(\frac{\alpha}{w\sqrt{\rho_{GND}}} + \beta b\sqrt{\rho_{GND}}\right) M \quad (5\text{-}3)$$

where ρ_{GND} is the GND density, b is the Burgers vector, and M is the Taylor factor, 0.8 here. α and β are the two dimensionless constants requiring fitting, and their calibrated values are: $\alpha = 0.0041$, $\beta = 21.0465$. ρ_{GND} is provided from the CPFE prediction at yield, see Table 5- . ρ_{GND} can also be obtained from EBSD measurement.

Table 5-4. The GND density used for the calibration with varying lath width.

$\boldsymbol{w_\alpha}$ (μm)	0.25	0.5	0.75	1	2	3	4	5
$\boldsymbol{\rho_{GND}}$ (μm^{-2})	1417	761.3	521	405.2	210.4	147.1	113.3	92.3

The calibrated constants help quantify the size effect strength of the two parts: the intrinsic length effect of the grain size, and the normalized extrinsic length effect determined by the weakest dislocation and the Burgers vector magnitude.

A grain boundary strengthening relationship was introduced in order to help: (i) consider the strengthening effect of lath boundaries; and (ii) include evaluation of lath boundary effect as the lath becomes thicker, due to the accumulated dislocations around the grain boundary. This equation for YS is:

$$\sigma_{YS} = \sigma_{\mathrm{i}} + 8(\sigma_{\mathrm{b}} - \sigma_{\mathrm{i}})\frac{t}{w} - 16(\sigma_{\mathrm{b}} - \sigma_{\mathrm{i}})\left(\frac{t}{w}\right)^2 \quad (5\text{-}4)$$

where σ_{i} is the grain strength and σ_{b} is the grain boundary strength. ξ is a constant, taken here as 0.1. Grain boundary thickness t is determined by the lath width:

$$t = \xi w^{1/2} \quad (5\text{-}5)$$

The two stress constants were calibrated as: $\sigma_{\mathrm{i}} = 837.3$ MPa, $\sigma_{\mathrm{b}} = 979.4$ MPa.

Figure 5-24 shows the comparison between the CPFE predicted YS values and the fitted curves plotted from the four relationships. The Hall-Petch gives the best fitting result. Thus, this relationship will be implemented in Chapter 6 to study the effect of post-built heat treatment. A similar trend between the Taylor dislocation-based relationship and the CPFE models was observed because both the CRSS equation in the CPFE constitutive

law and this generalized Taylor relationship are dependent on dislocation densities. In the grain boundary strengthening relationship, a reversed Hall-Petch effect is activated when the size is below 150 nm.

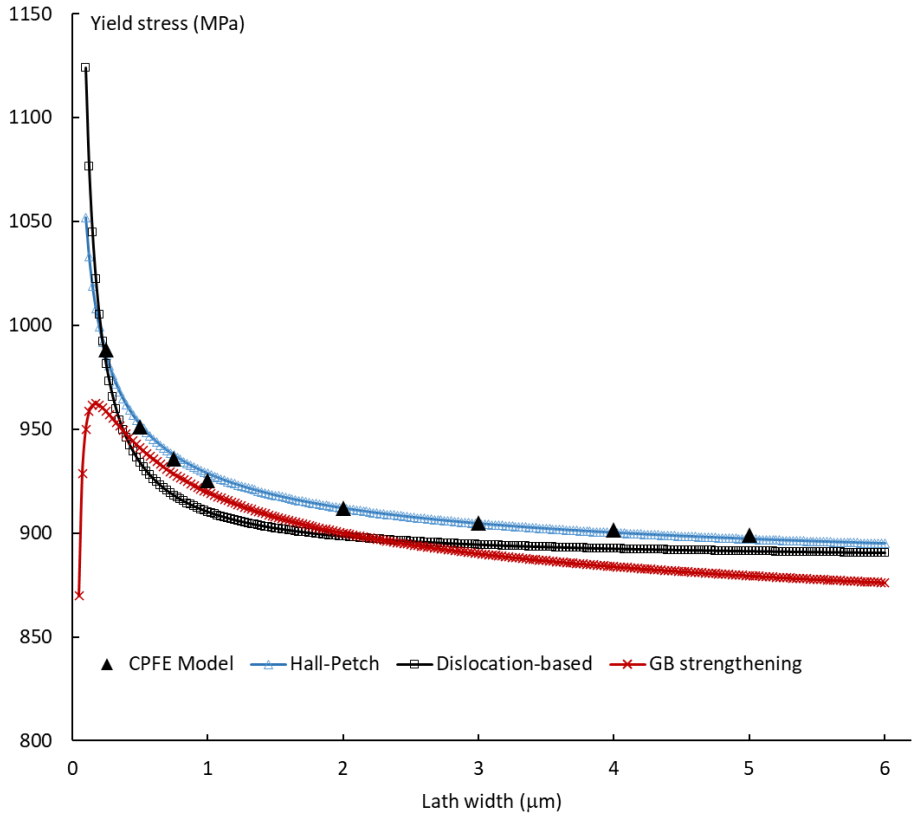

Figure 5-24. The CPFE predicted YS strength for the lath width ranging from 0.25 μm to 5 μm, compared to the three fitted grain size relationships.

5.6 Conclusion

During powder bed fusion, the dual-phase alloy Ti-6Al-4V undergoes fast cooling and solidification, leading to a complex and gradient α-β lamellar microstructure. A physically-based, strain-gradient micromechanical model can capture key microstructural variations and determine their effect on the tensile response of PBF-LB Ti-6Al-4V alloys. Some key findings of this study are:

1. A strain gradient crystal plasticity finite element model has been developed for the lath width size effect, and predicted close agreement to experimental tensile test data for yield strength of PBF-LB Ti-6Al-4V samples.
2. The dual-phase lamellar model predicts a marginal effect (0.8%) on tensile yield strength due to spatial position on a PBF-LB sample where 43% increase is observed in lath width (0.74 – 1.06 μm). However, the observed five-fold increase in lath width due to post build heat treatment HIP is predicted to cause a significant decrease in yield strength (~ 9 %) and tensile strength. The captured difference in mechanical response is consistent with the experimental test results.
3. An accurate lath width measuring approach and 3D dual-phase lamellar model generation method are introduced. The CPFE model generated from the methodologies represents statistically equivalent microstructural information compared to the SEM/EBSD characterisation, including lath size, phase fraction, lath morphology, and crystallographic orientation.
4. The models varying in alpha lath width have been constructed, and quantitively compared to separately study the lath size effect on the mechanical response. The relationship between the predicted macroscopic yield stress and average lath width is fitted into three size-sensitive strengthening equations.
5. In this developed strain-gradient model, GND density has a more significant influence on the alloys with a lath width smaller than 2 μm and thus is especially suitable for predicting the performance of powder bed fusion Ti-6Al-4V alloys.
6. The effects of prior-β grain (PBG) size and grain morphology (sphericity) are studied to investigate the microstructural sensitivity and other capabilities of the CPFE model. The PBG and grain morphology has negligible influence on the CPFE-predicted stress-strain curves. However, lamellar morphology results in a higher standard deviation in GND density compared to regular and equiaxed morphology.
7. Hall-Petch and Taylor model parameters have been identified to investigate the effect of lath width on yield strength of PBF-LB Ti-6Al-4V.

6 Investigation of the post-built heat treatment effect on grain growth and mechanical behaviour using integrated PFM-CPFE framework

6.1 Introduction

The PBF core process features of, localised heating, partial melting and rapid solidification lead to the existence of thermal gradients during the manufacturing process. This thermal gradient also leads to an inhomogeneous microstructure [323] along the built direction and the presence of more residual stresses in the as-printed part [144]. Consequently, post-built heat treatments (HT) such as annealing are necessary to regularize the microstructure, as well as minimise the residual stress [56, 333]. Such annealing processes release the stored distortion energy and cause microstructural evolution such as grain recrystallization, grain growth and phase transition, leading to a polycrystalline grain structure varying in grain size and orientation [348].

Linking the thermal history induced driving force with a defined microstructural equilibrium, the phase-field method (PFM) is capable of constructing the process-structure relationship. The PFM predicts the microstructural evolution using a group of field variables across the interfacial grain boundary [24], as detailed in Section 2.7. Recently PFM has been used to predict the evolved morphological material microstructure, such as titanium alloy solidification [349], and grain growth [165, 166]. To construct the structure-property relationship, one popular computational model is the crystal plasticity finite element (CPFE) approach which predicts mechanical response based on a certain microstructure, as introduced in Section 2.8. Although several applications, including the lath width research in Chapter 5 have demonstrated the capability of the CPFE method in studying grain size effect [183, 338], and texture effect [222], work on strength predictions based on an evolved microstructure due to a thermal process is still in the early stages of development. Some recent studies have integrated

modelling methods of solidification and as-solidified strength prediction to fulfil a through-process simulation. One such example is the coupled PFM-CPFE approach. This integrated method has been utilized for the prediction of evolved texture and the associated anisotropic mechanical property of steel [348], the as-built grain morphology and tensile property of the Ti-6Al-4V alloy manufactured by different printing strategies [335], and shear stress of recrystallized grain varying in orientations [350].

As discussed in Section 4.4 and 5.1, AM research requires accurate and realistic representative models considering their microstructures are usually more complex than conventionally manufactured counterparts including the PBF manufactured Ti-6Al-4V alloys, which display fully lamellar shape and basket-weave morphologies within prior β-grains. VT partitions space, it does not capture or use information/physics of metallurgy. In VT, there can sometimes be more than 3 grains meeting at one point, compared to the fact that only 3 grains could meet at one point. It generates models without considering thermodynamics or physics. Due to the complexity of local thermal history during the PBF process and repeated rapid cooling and heating rate, the resulting Ti-6Al-4V alloy has a martensite phase lamellar shape grains elongated towards the printing direction [331]. While grain size, anisotropic texture and grain morphology in metal AM structures are believed to be highly dependent on temperature profiles induced by AM processing variables, these microstructural features, in turn, influence the macroscopic mechanical behaviour. As introduced in Chapter 4, one of the novel challenges is to adopt real microstructure images, e.g. obtained from electron backscatter diffraction (EBSD) as the initial condition, for both microstructural measurements as well as computational modelling. The EBSD imaging allows accurate and detailed grain-level information like grain morphology, phase fraction, and recrystallization texture which are important features of PBF fabricated alloys. However, there are still few image-based microstructural evolution models for PBF metals, and limited high-fidelity through-process modelling research to the best of author's knowledge.

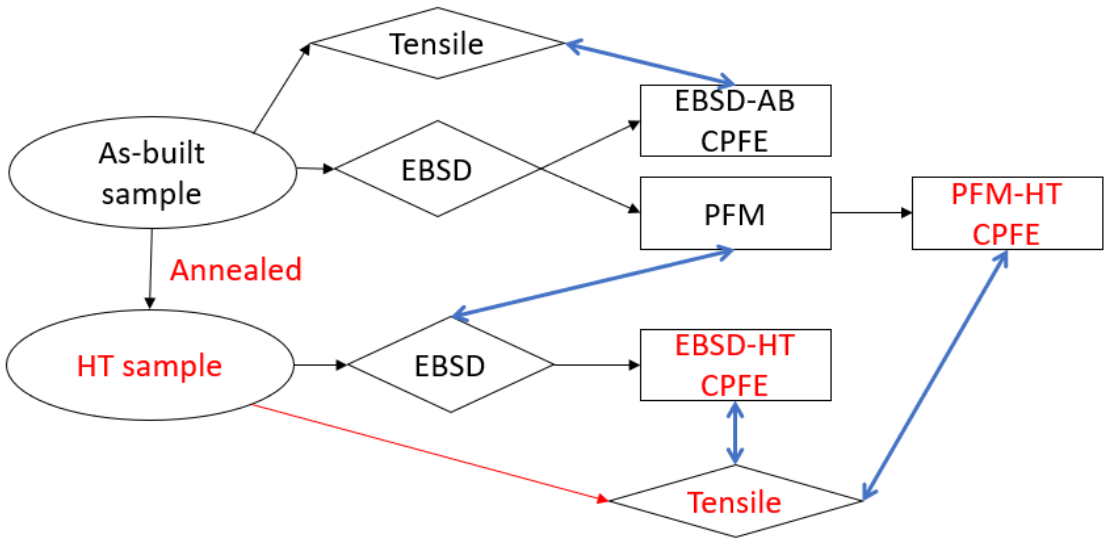

Figure 6-1. The schematic of post-built heat treatment, EBSD characterisation, tensile tests, PFM, CPFE modelling, and the validation process in this research.

This chapter aims to introduce a through-process approach that integrates the phase-field method (PFM) with the crystal plasticity finite element (CPFE) modelling for the prediction of microstructure evolution during the post-PBF heat-treatment and the associated change in mechanical performance. This work first introduces a real image-based model generation method for PFM to deliver high-fidelity representative models of the complex microstructure including realistic grain morphology and orientation. Then a seamless bridging tool linked to the microstructural-sensitive strain gradient CPFE model, detailed in Chapter 5, is developed to establish the coupled PFM-CPFE modelling framework. Such an integrated framework is introduced to establish a through-process HT-structure-property relationship for PBF manufactured Ti-6Al-4V alloy. The objective is to use real (not VT) microstructure images obtained from electron backscatter diffraction (EBSD) scans as the initial condition for both PFM and CPFE models. Figure 6-1 illustrates the workflow in this Chapter. The PFM model will be developed to predict grain growth during the post-built annealing process. Both the evolved polycrystalline microstructure from the PFM prediction and the original as-printed EBSD map will be analysed via a CPFE model for the prediction of mechanical response. The experimental validation is shown by the blue arrows, including the microstructural comparison between heat treated EBSD image and PFM prediction, tensile curves from three CPFE models for

both as-built and annealed samples compared to the mechanical tests respectively. Thus, this combined modelling approach will determine the effect the post-built heat treatment process has on the microstructural evolution and the associated mechanical properties.

6.2 Methodology

6.2.1 Sample fabrication and microstructural characterisation

The PBF-LB Ti-6Al-4V samples followed the ASTM-E8 standard and were fabricated with the Renishaw RenAM 500M metal printer located at the Irish Manufacturing Research centre, using a 500 W constant pulsed laser power as the energy beam source. The specimen geometry design was introduced in Section 3.1.1 of this thesis. Post-built HT of Ti-6Al-4V samples involves annealing in a Nabertherm oven under 900 °C for 100 minutes, and then cooling at the ambient air temperature. The samples were sectioned along the built direction longitude surface, shown in Figure 6-2, for EBSD characterisation, by the FEI Helios DualBeam SEM-FIB system located at Bernal Institute, the University of Limerick. The voltage was set as 20 kV with a current of 12 nA, and the resolution was defined as 0.05 μm per pixel. A bigger 139×87 μm area was scanned to provide an overall grain morphology of the material, while smaller regions with the size of 40×26 μm were also obtained for finite element model generation, considering the likely computational cost. Both the as-built and HT samples show less than 5% retained β phase, as reported in the EBSD detection. Aside from the relatively small area fraction, the retained β phase is also hard to distinguish and represent, considering their small size (width of ~0.1 μm) and ~8% indexed pixels in the EBSD raw file. Consequently, this works adopts a single-phase assumption to simplify the model generation, material data input requirements and solution stability.

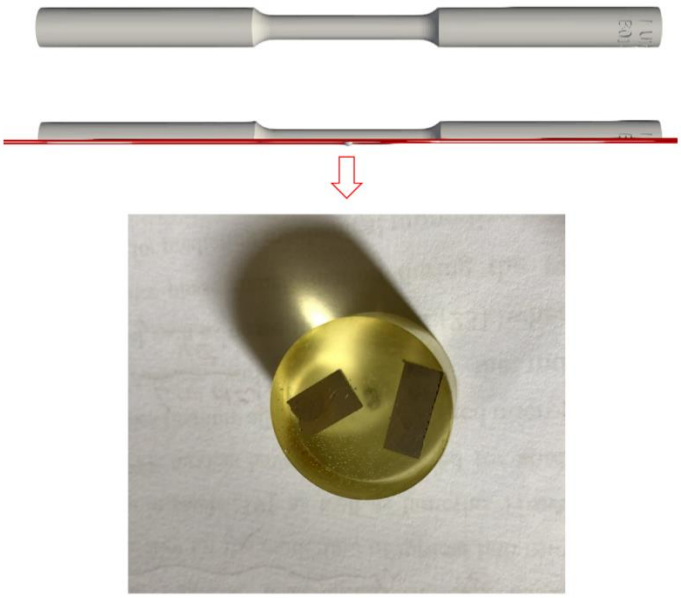

Figure 6-2. Sample cutting a from longitude cross-section surface, ready for SEM and EBSD scan.

6.2.2 EBSD-based PFM for grain growth prediction

Post-processing HT such as annealing and hot isostatic pressing, are necessary to homogenize microstructure and eliminate initial defects, and meanwhile, modify the lath size. Quantitative PFM is implemented to simulate grain growth during such process. Figure 6-3 shows the 9.6 um^2 square (same as model 1 below) converted PFM model from a cropped area of the original EBSD map. An adaptive mesh was used in this PFM work to allow denser mesh around the GB area, because GB evolution and migration behaviour was the focus of the PFM component of the simulation.

Table 6-1. PFM model information in various model size.

Sample	Size L (μm)	# of grains	# of elements	Meshing time (min)
1	9.6	88	36636	5
2	12	395	57400	20
3	14	2499	78400	55
4	17.6	3957	123904	180
5	25.8	8614	266256	720

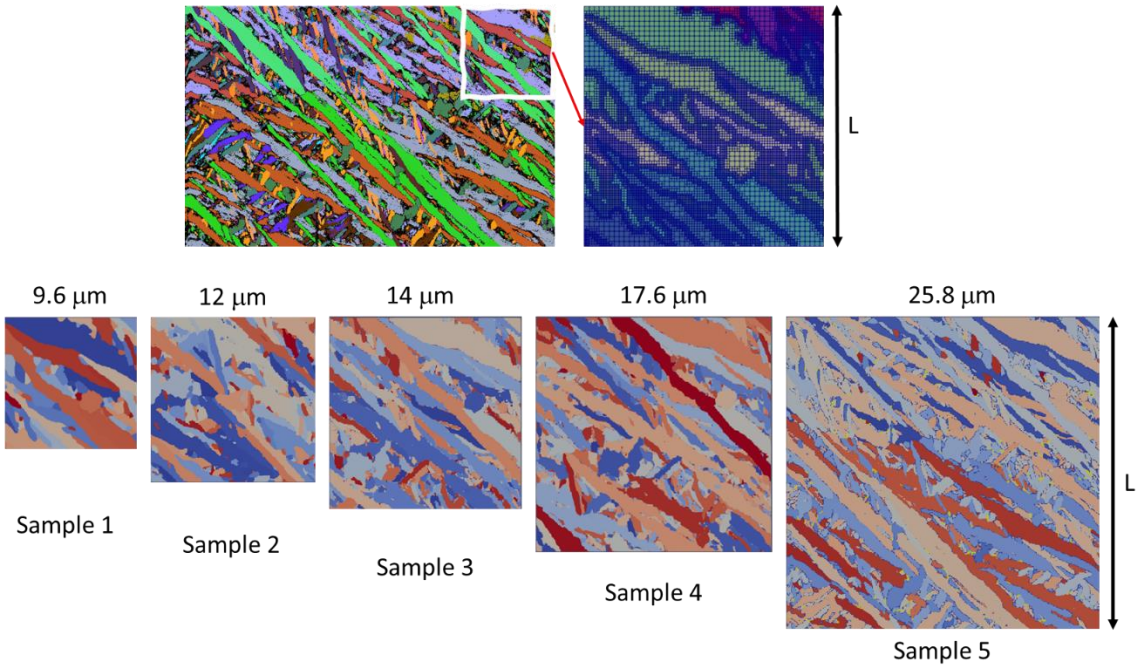

Figure 6-3. EBSD-PFM model generation, and convergence study.

The meshing of the EBSD image and conversion to PFM input files were conducted through a custom written C++ code. The EBSD image was cropped at various size L, to carry out the convergence study. Table 6-1 lists the sample details such as the number of grains and elements information for the five regions. The meshing process was first performed on a standard office PC with 32GB RAM, which turned out to be insufficient for samples 3-5. Thus, the meshing time listed in the table are all based on high performance ICHEC facility [351], with 4-core 2.4 GHz Intel Xeon Gold 6148 (Skylake) processors, and 192 GB of RAM. However, sample 5 failed to converge a single step after 144 hours (maximum allowance time when submitting job), without any temporary result to continue running. Consequently, all the following computational finite element modelling work in this chapter is based on sample 4 size.

Considering the balance between the computational cost and predicting accuracy, it is necessary to carry out a PFM convergence study. In this grain growth PFM model, it is

anticipated the lath area can grow 3-5 times after HT [324, 352, 353]. Take sample 1 for example, it is reasonable to anticipate that the evolved microstructure will contain fewer than 20 laths after HT, making it unfavourable for statistical comparison to EBSD measurement with regards to lath size, and lath area. Too small the cropped model also increases the uncertainty in the representative microstructure, due to limited lath information, which in turn, also influences the CPFE results in a later stage. From the CPFE perspective, one significant conclusion from the previous convergence study in Chapter 4 has confirmed a preferable model length L and grain diameter ratio *L/w* of higher than 21, for definitive EBSD-CPFE models. Based on this conclusion, 10.0 μm is calculated as the minimum model size while a bigger sample is always preferable if permitted considering that the lath width will increase after HT. Sample 5 has an overall dimension of 25.8 μm corresponding to the maximum available scan length in the EBSD scan.

The proposed PFM approach takes into account both temperature-dependent grain boundary (GB) mobility and thermal driving force. This PFM model was developed based on the open-access package MOOSE FRAMEWORK [247], and is designed according to MARMOT theory using the Allen-Cahn and Ginzburg-Landau equations, as were detailed in Section 2.9 of this thesis.

This PFM modelling tool predicts the microstructural evolution during heat treatment including grain nucleation and growth, based on the strain energy release theory and neighbouring grains' misorientation induced stored energy difference. Apart from the temperature, 1173 K operated in this annealing process, other parameters include molar volume which equals 2.846 e-5 m^3/mol for Ti-6Al-4V alloy, and the diffuse grain boundary width w_{GB} which is defined as the same as the minimum resolution distance between neighbouring lath in the EBSD scan, equalling 0.1 μm. Previous research on PFM of electron beam AM Ti-6Al-4V [168] has determined the values for GB energy σ_{gb} and activating migration energy Q, as shown in Table 6-2.

Table 6-2. Parameters used in PFM for grain growth prediction during HT.

Parameter	Value
m_{gb}	$4.0 \times 10^{-5}\, J/K$
σ_{gb}	$0.81\, J/m^2$
Q	$1.0\, eV$
T	$1173\, K$

The remaining parameter to determine the value for GB mobility m_{gb} which can vary from $1.8 \times 10^{-8}\, J/K$ to $2.42 \times 10^{-4}\, J/K$ for different alloys [171, 354]. A further complexity is the dependency of GB mobility on texture [355]. This could lead to different grain growth results for AM samples built in varying directions. The GB mobility was $4.0 \times 10^{-5}\, J/K$, calculated from a non-AM Ti-6Al-4V grain growth research [356].

6.2.3 CPFE modelling for mechanical property prediction

The CPFE modelling in this chapter uses the strain gradient constitutive laws introduced in Section 2.8.5 of this thesis. The PBF-LB Ti-6Al-4V, after HT, such as annealing, is believed to sacrifice strength for an increase in ductility [357]. In Section 5.5, a relationship between the Ti-6Al-4V lath width and the yield stress in the tensile test is summarized based on the Hall-Patch formula. Two constants were imported from size-sensitive yield strength study calibrated in Section 5.5, k_{HP} as 103.69 MPa, and the exponent constant n, as 0.2848. Then the initial critical resolved shear stress (CRSS) σ_0, was calibrated against the experimental tensile stress-strain curve obtained from as-built sample.

$$\tau_{c0}{}^{\alpha} = \sigma_0 + \frac{103.69}{w^{0.2848}}$$

The modified CRSS equation is now implemented to determine the $\tau_{c0}{}^{\alpha}$ of basal slip system of alpha phase, where w is the lath width.

σ_0 was fitted against the experimental tensile test on as-built sample, using the EBSD-based as-built CPFE model, which was calibrated as 220 MPa. The two constants, σ_0 and n, were then unchanged when modelling the heat-treated specimen, where $\tau_{c0}{}^{\alpha}$ was

automatically updated from the evolved lath width value. Periodic boundary conditions were applied to both PFM and CPFE models. In CPFE, the model deformed along the y-axis direction, with the maximum strain the same as the strain at fracture from the tests.

Both the PFM predicted microstructural information and the EBSD scans after HT are firstly compared, and then independently converted into CPFE inputs, ready for the grain-size sensitive and orientational-dependant mechanical response simulation. A comparison between these CPFE models and the experimental mechanical tests is conducted to confirm the reliability of the proposed PFM-CPFE methodology.

6.2.4 Tensile tests

The samples before annealing (EXP as-built) and after HT (EXP HT) were tested on an Instron 8500 servo hydraulic machine, equipped with a clip-on strain extensometer. The initial tensile speed was set at 1.25 mm/min and increased to 2.5 mm/min after yield.

6.3 Results

6.3.1 Quantitative PBF-LB Ti-6Al-4V EBSD measurement

Two 139×87 μm area lath images were scanned from the longitude cross-section surfaces, to plot a 3D schematic figure for the EBSD reconstruction, as shown in Figure 6-4. The reconstructed grain morphology indicates the main presence of Al-rich α phase, with a variety of lath morphologies, acicular, basket-weave or band shapes with varies of aspect ratios.

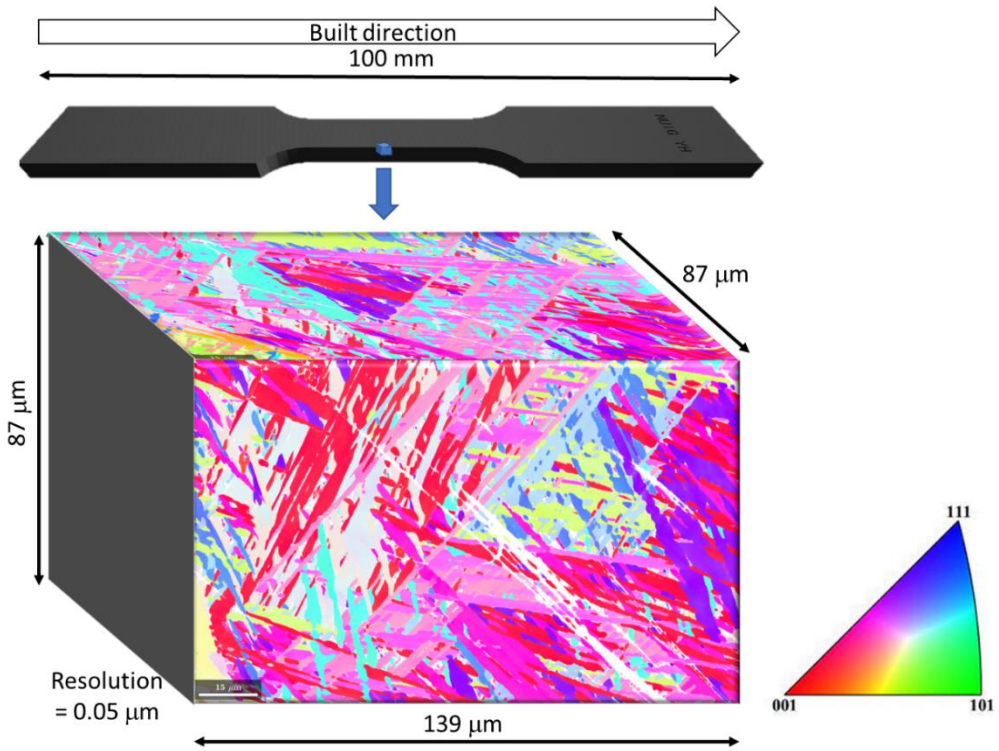

Figure 6-4. Reconstructed 3D schematic lath map, coloured in IPF legend, from EBSD scans.

Figure 6-5 compares the EBSD scan with area of 40 × 26 µm, for as-built and HT samples, respectively. The estimation of lath width again adopted the ellipse fit of alpha lath, from the aspect ratio and lath area, the algorithm and calculating methodology was detailed in Section 5.2.1.

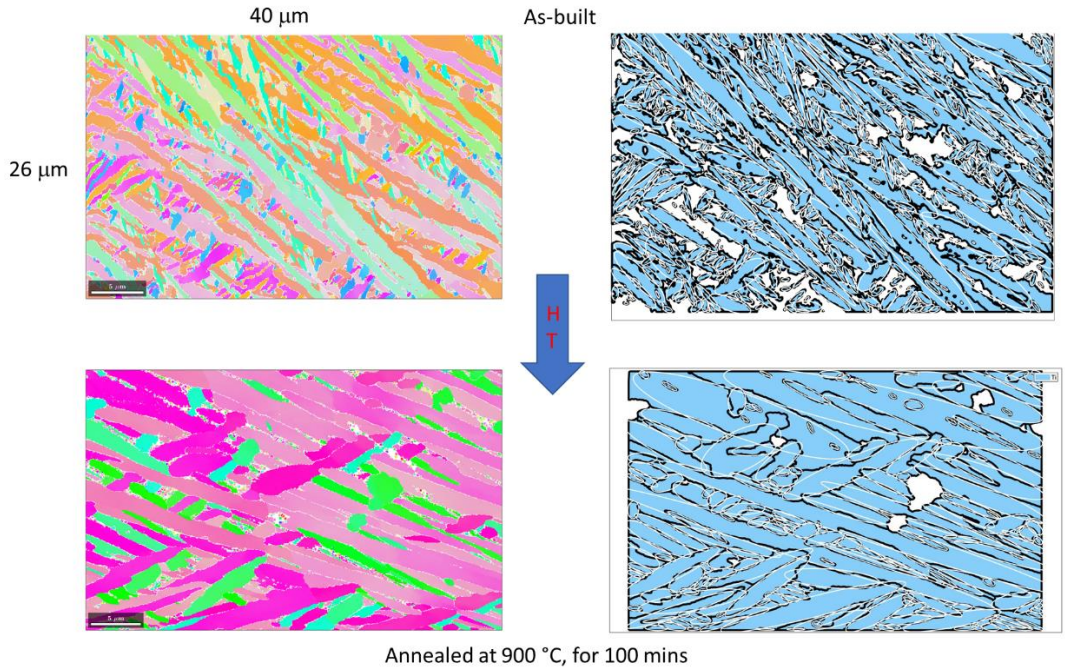

Figure 6-5. The EBSD map for as-built and annealed Ti-6Al-4V. Ellipse lath fit was adopted for lath width and aspect ratio estimation.

After annealing, the total number of grains has decreased from 1822 to 447 measured from EBSD scan, with the averaged lath width increasing from 0.52 µm 1.23 µm. The main changes of the microstructural features are quantified and summarized in Table 6-3. Figure 6-6 shows the lath area evolution during annealing, from the two EBSD measurements. This EBSD characterisation has indicated that the lath area growth is influenced by both lath width and the lath length, with obvious aspect ratio increase as well.

Table 6-3. Quantitative Ti-6Al-4V lath features from experimental EBSD measurement.

	As built	**HT**
Number of laths	1822	447
Lath area (um^2)	0.59	3.00
Lath width (um)	0.52	1.23
Aspect ratio	2.53	4.80

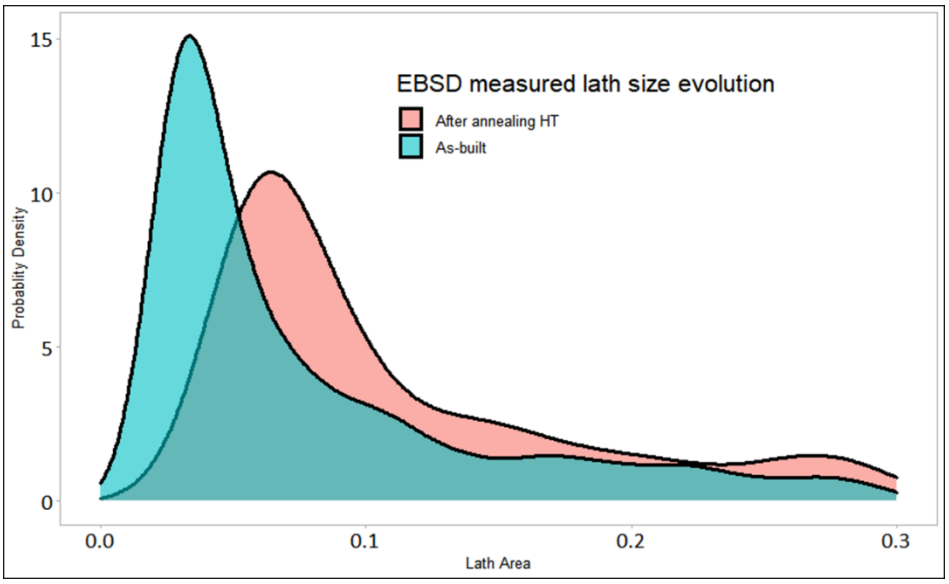

Figure 6-6. Probability density curves showing lath size distribution comparison between as-built and annealed EBSD measurements.

6.3.2 PFM microstructural evolution after HT

The grain growth is predicted based on the reduction of total grain boundary energy during the GB migrating behaviour under the annealing process. Figure 6-7 shows the evolved grain map after the simulated post-built annealing process, under a temperature of 1127 K. The small grains merge into their neighbouring grains to minimize the total local free energy caused by the high-temperature driving force. The EBSD map of the same size (17.6 μm in length) are listed on the right side, for a straightforward comparison. The PFM model and EBSD before HT are completely consistent because they are from direct conversion. However, the EBSD scan after annealing is not the same region due to two main reasons: (i) extremely precise operation requirement when mounting and placing sample in the SEM chamber to repeat the same coordinate setting and difficulty to locate the same region; and (ii) destructive tensile test that prevents using the same sample after HT.

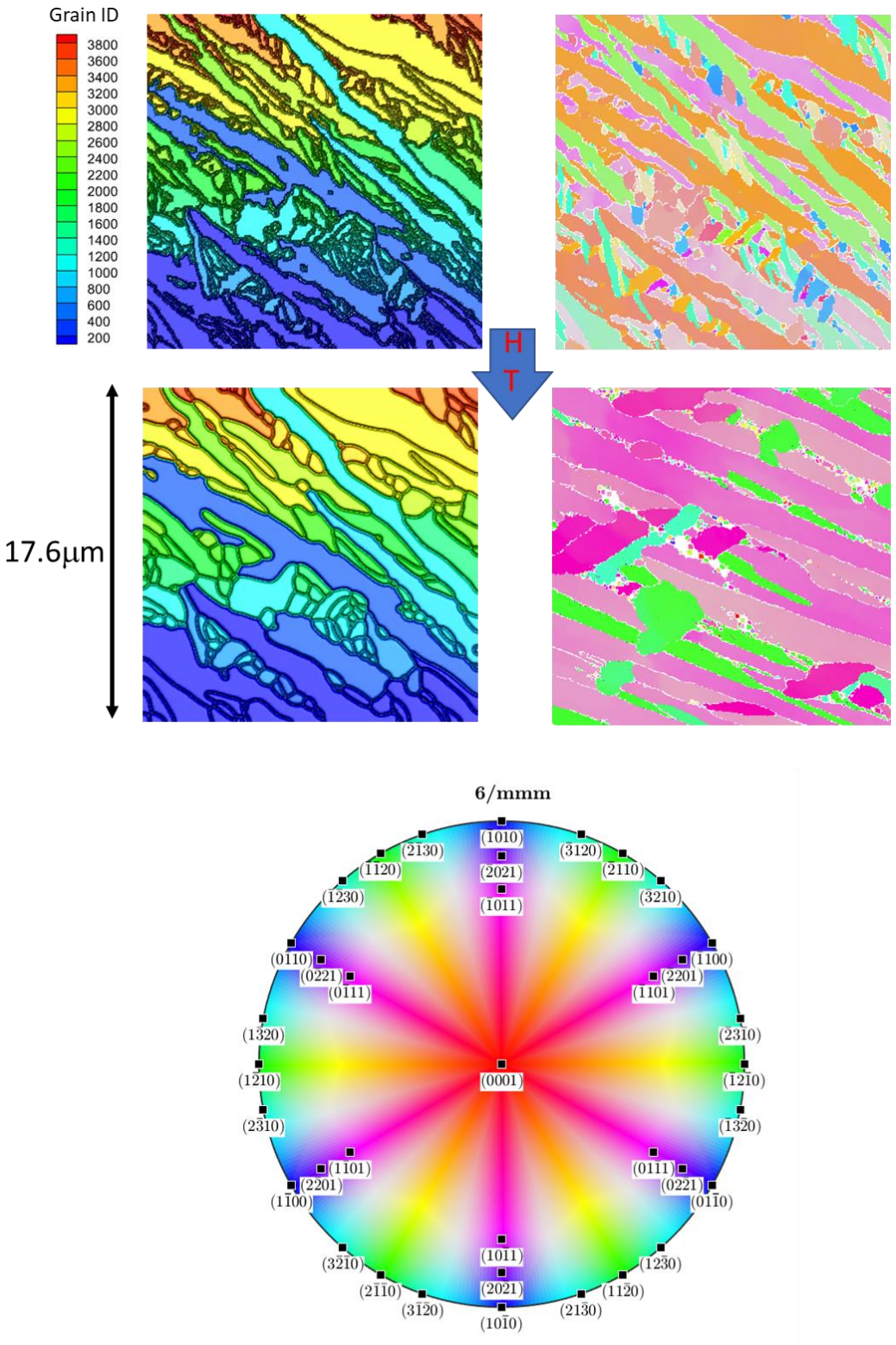

Figure 6-7. PFM predicted microstructural evolution under 1127 K for 100 minutes.

Figure 6-8 shows the probability density plot for the lath area distribution before and after HT in the PFM model. The PFM predicted lath size evolution was statistically compared and validated against the EBSD measurement. After HT, the EBSD measures the lath area between 0.01 to 77.86 μm^2, while the PFM predict the lath area varying from 0.01 to 143.10 μm^2. The averaged lath area predicted by PFM is 3.03 μm^2 with a standard deviation of 13.01, compared to 3.01 μm^2 and standard deviation of 8.13 from EBSD characterisation. From this microstructural validation, the averaged lath area reaches close agreement compared to EBSD, and the PFM prediction has a bigger maximum lath size, and a wider distribution range.

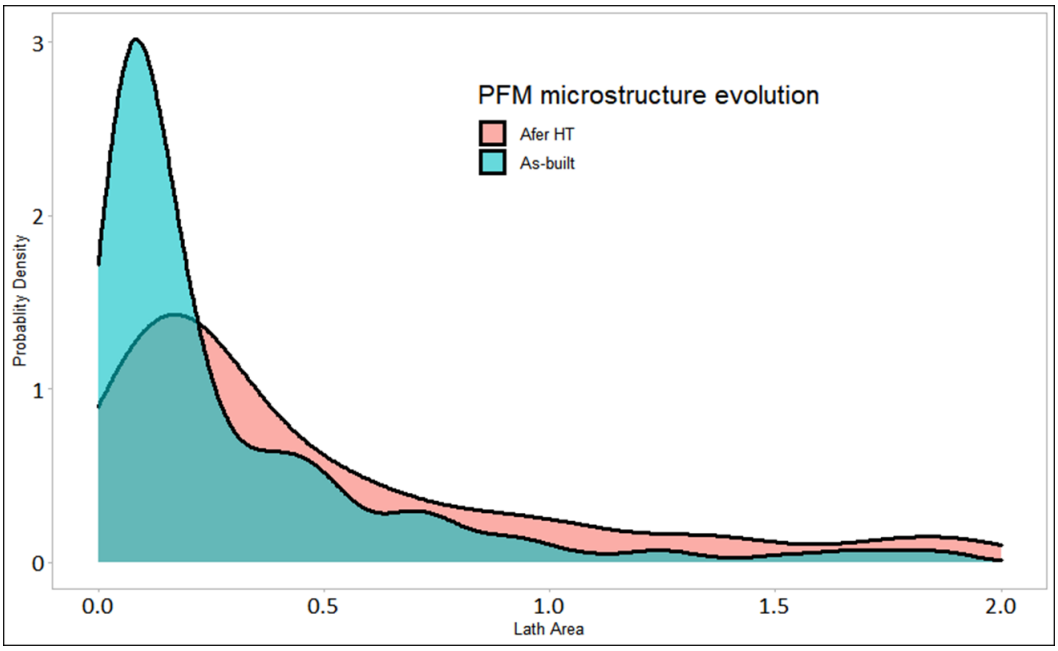

Figure 6-8. Probability density plot for the lath size distribution evolution by PFM.

6.3.3 Fractography and porosity.

The crack was uneven and not homogeneous in SEM observation. The fractography study indicates poor ductility of the PBF-LB Ti-6Al-4V parts under tensile loading. Figure 6-9 shows the abrupt cracking surface without necking. In the higher magnitude images (b) and (d), the cracking area is extended by a terraces or spindrift like region with few dimples. This terraces morphology region does not show obvious preferable direction,

making it hard to tell the actual crack propagation routine. A possible crack propagation step is marked by arrow in image (a). This fracture type is usually attributed by either porosity or lack of fusion near the surface [358].

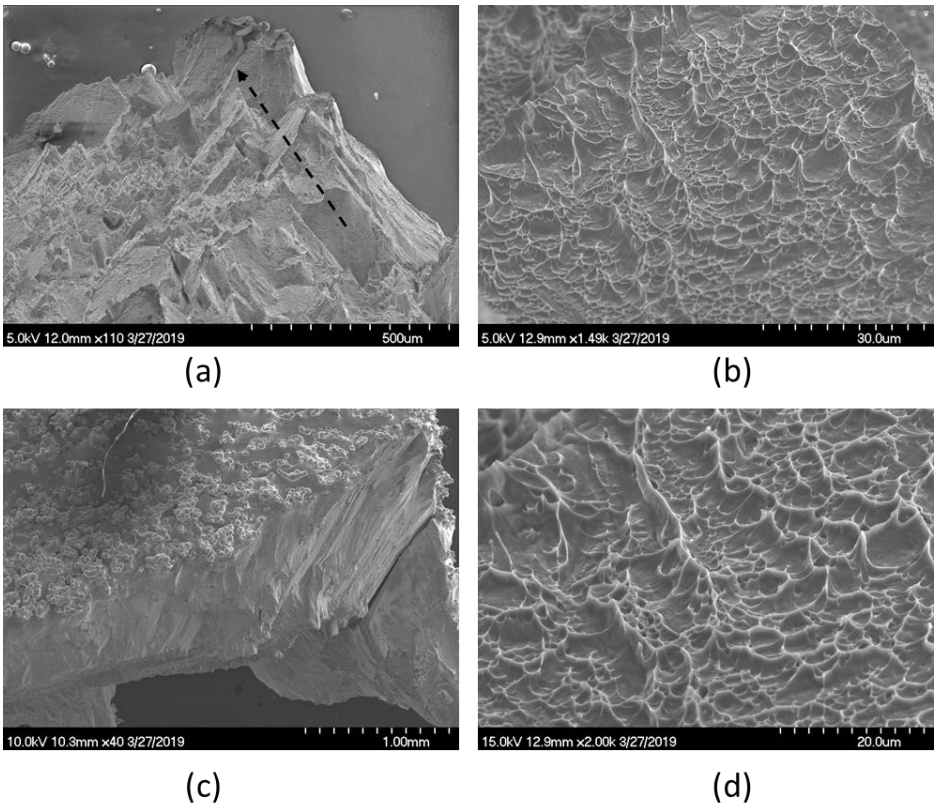

Figure 6-9. SEM images of the fracture surface after tensile test of the two plate ASTM-E8 Ti-6Al-4V samples.

Micro-CT is used to check the voids and porosity of the as-build samples, and the scanned 3D reconstruction is shown in Figure 6-10. The density of these samples was measured to be 4.39 g/cm^3, 99.1% of the theoretical value 4.43 g/cm^3. Micro-CT results showed no significant porosity or defect. However, potential pores might exist but cannot be detected due to the poor penetration of X-ray for Ti-6Al-4V alloy.

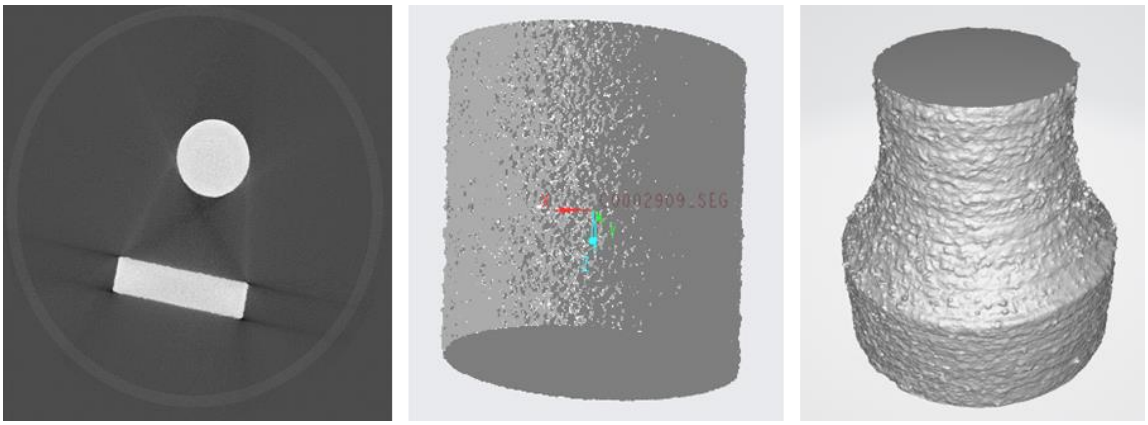

Figure 6-10. micro-CT slice image, and two reconstructed 3D stl models.

6.3.4 Tensile behaviour: tensile tests and CPFE comparison.

Both the original EBSD scan for the as-printed part and the PFM predicted microstructure after the grain growth evolution were imported for generating the CPFE models. Consequently, the following terms are defined for the ease of pointing to specific CPFE model types generated from different sources: (i) EBSD-AB for the model converted from the direct EBSD grain map image of the as-built sample; (ii) EBSD-HT for the model converted from EBSD image of the annealed sample; (iii) PFM-HT for the model generated from the PFM predicted microstructure after annealing. Figure 6-11 (a) shows the converted CPFE model in ABAQUS, using C3D20R hexagonal finite element mesh, for the EBSD-AB, EBSD-HT and PFM-HT, respectively. CPFE contour plots results from the three models are shown in Figure 6-11 (b) shows the von-Mises stress at 1% strain. At a deformed strain of 1%, the CPFE contour plots predicts a maximum von-Mises stress of over 2000 MPa, for the three samples, indicating severe stress localization in this lamellar PBF-LB alloy.

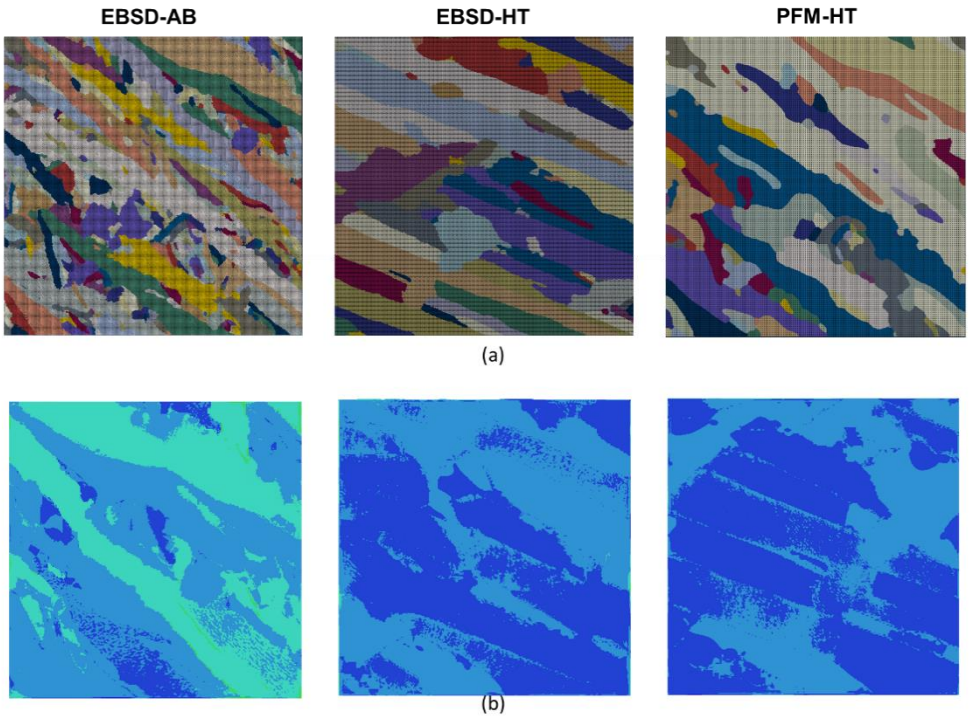

Figure 6-11. CPFE results from EBSD-AB, EBSD-HT, and PFM-HT, for (a) meshed polycrystalline model, (b) von-Mises contour plots at 1% strain.

The macroscopic tensile stress-strain curves were extracted from the three CPFE models, shown in Figure 6-12, for a comparison with the experimental tests. The two experimental tensile curves have confirmed the function of annealing on PBF alloys, to improve the ductility by increasing the strain at failure from 1.62% to 2.07%. Meanwhile, the strength including both yield stress, and ultimate stress are sacrificed due to lath size growth. This phenomenon is referred to as strength-ductility trade-off, which is successfully captured with the strain gradient CPFE models.

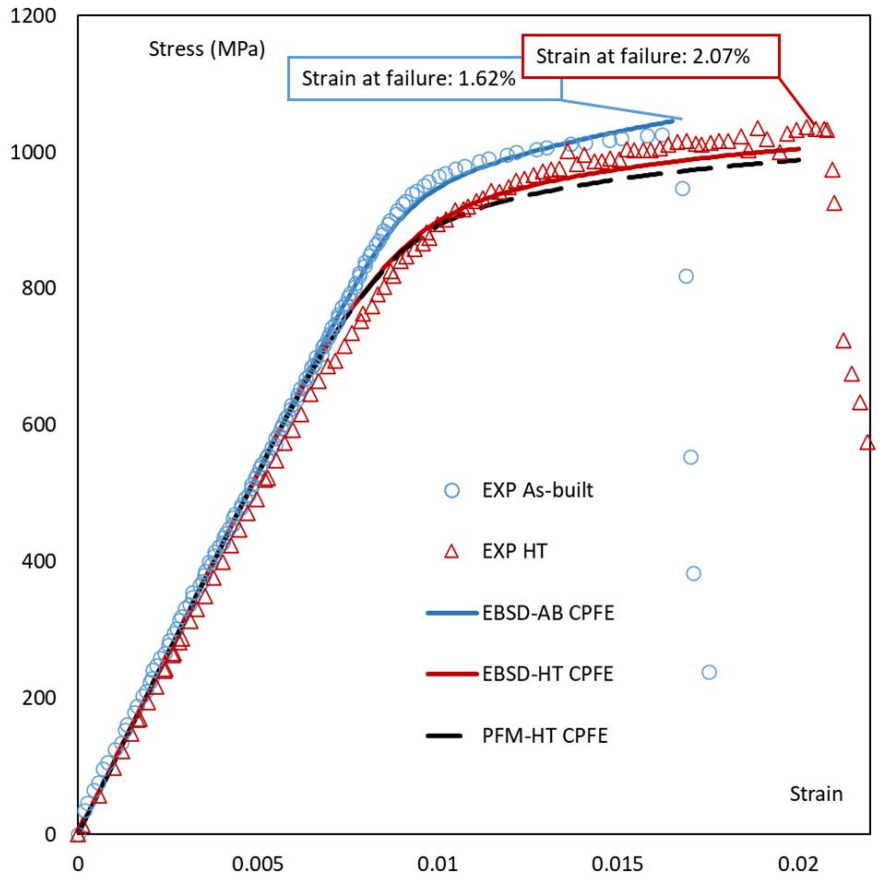

Figure 6-12. CPFE tensile stress-strain curves from EBSD- and PFM-based conversion, and validation against mechanical tests.

6.4 Discussion

The discussion on material mechanical performance is always linked to its structure, especially for PBF-LB manufactured alloy which has more complex thermal history and unique microstructure. The challenge in characterizing such process-structure-property relationship requires integrating interdisciplinary computational models to fulfil a through-process modelling framework. Typical coupled modelling examples can be found in Section 2.7 of this thesis.

To fulfil a balanced mechanical property, the AM Ti-6Al-4V is either coupled with hybrid manufacturing strategies such as forging and wrought, to generate bimodal microstructure [359, 360], or followed by HT to modify the lath size. Post-built HT modifies microstructure to reduced residual stress, and improve the ductility and fatigue

life [50]. Suitable HT process design, such as hot isotropic pressing, or tempering strategy can maintain the tensile strengths while improving the ductility or removing the heterogeneities [54, 361]. These findings further emphasize the significance and necessity of understanding the thermal process, microstructure, and the property relationship in AM fabrication. It is necessary to better understand the effect of such HT process on microstructural modification, thus the PFM on grain morphology evolution under high temperature was developed. The introduced PFM-CPFE provides a reliable tool in characterizing this relationship and is important for AM material tailoring and the AM process technological design.

The varying file format in EBSD characterisation, PFM, and CPFE (ABAQUS 2017 [303]) is one challenge in this coupled modelling work. Customized codes were written to allow seamless conversion and importing functions between the three sources. Such a real image-based PFM-CPFE framework has not been previously reported. However, this effort is worth considering the more detailed and higher fidelity information provided. For e.g., the Ti-6Al-4V grain growth behaviour was previously measured from SEM image [54, 362] to consider lath thickness change only. The common PFM research on grain growth also compares the averaged grain area with experiments only, some validate the number of grains. The image-based PFM introduced in this Chapter, besides the number of lath and area, also gives the value of lath width and aspect ratio, thanks to the developed EBSD grain fitting program. Lath width and aspect ratio is more important for the fully lamellar structure PBF-LB Ti-6Al-4V, the result shown in Chapter 5 also convinces the strain gradient CPFE model is more sensitive to the lath width compared to grain area. This capability guarantees higher reliability when validated against a microstructural image, taking into account both size and morphology. From the CPFE perspective, one important achievement is that the size effect is induced from geometrical sensitivity rather than material parameter modification. It can be anticipated that this MARMOT based PFM model [165] will predict slighter grain growth when a lower temperature or fewer HT time are defined. However, the CPFE model, once calibrated, can predict the mechanical response from products under ranges of HT process, without the need to change a material parameter, which is automatically updated accordingly from the coarsened structure.

In Chapter 4, it was found that the real image-based CPFE model does not show prominent improvement in stress prediction. However, it might be reasonable to propose that a realistic grain boundary representation is preferable in PFM model compared to CPFE, because the GB migration, and the neighbouring grain merging behaviour are the focus. To convince this suppose, the lamellar Voronoi tessellation (VT) model, introduced in Chapter 5 was converted to PFM model and predict the lath growth evolution using the same physical parameter, result shown in Figure 6-13. The VT-PFM underestimates the effect of HT on lath growth. Table 6-4 lists the three microstructural features, lath width, lath aspect ratio, and lath area from the three data. Here only the microstructural information after HT is compared, considering that the PFM model is converted directly from the EBSD scan, so their as-built features are consistent. The VT-based PFM is still the most common approach in recent grain growth research [363, 364]. However, in this modelling case for PBF-LB Ti-6Al-4V, the artificially generated VT, although whose morphology has lamellar structure, fails to generate very small grains which exists in EBSD. Besides, the aspect ratio is bigger which means longer laths are generated due to the limited lamellar VT algorithm. As for CPFE modelling case, the EBSD-based CPFE study introduced in Chapter 4, although finds no prominent improvement for predicting the bulk stress-strain curve, indicates the significance of representing realistic grain morphology and neighbouring grain relationship for a better understanding of localized behaviour, even for an equiaxed microstructure. For the same reason, recent years have witnessed the use of EBSD-CPFE method for complex hierarchical morphology size-effect study [191], and cyclic shear localized deformation modelling for steels [365]. Although the artificial VT method was able to capture the lath size effect in the CPFE study in Chapter 5, mainly because the developed strain gradient model is not sensitive to the aspect ratio. However, this is not the same case in the PFM modelling, where lath morphology, especially lath boundary becomes the focus of the simulation. Consequently, real image-based PFM, as well as the high-fidelity PFM-CPFE modelling become more significant, for precise microstructural evolution and the associated property prediction, to obtain an accurate result for the complex PBF-LB manufactured alloys.

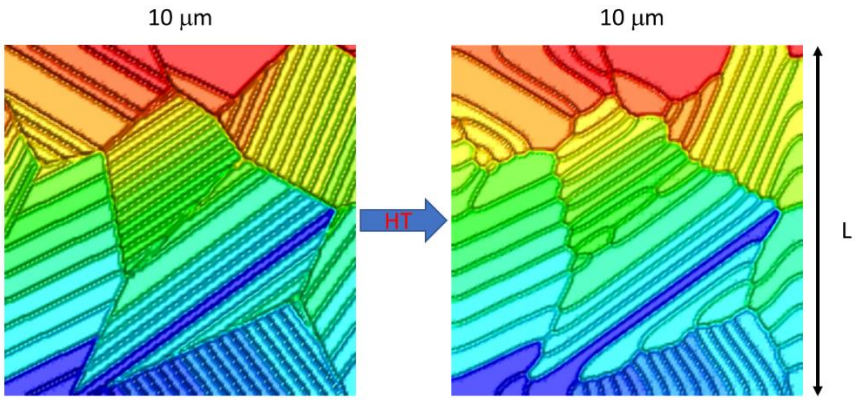

Figure 6-13. PFM lath growth evolution from lamellar Voronoi tessellation model.

Table 6-4. Lath information after HT, from experimental EBSD and two-types PFM models.

	Experiment	**EBSD-PFM**	**VT-PFM**
Lath area (um^2)	3.01	3.03	1.48
Aspect ratio	4.80	4.08	7.51
Lath width (um)	1.23	1.34	0.69

Crystallographic orientation does not evolve in the current PFM model, which means that the merged lath directly inherits the original orientation from its parent phase. This assumption is made to simplify the problem. In Figure 6-5, when the smaller lath merge to its neighbouring lath, its ID is labelled inactive, and the crystallographic orientation of that material in that space is updated to match the orientation of the new larger grain. Figure 6-14 plots the pole figures contour showing the texture distribution for the as-built and HT materials. Due to the simplified assumption, PFM after HT contains partial texture distribution and cannot have new texture compared to as-built EBSD, because it is generated from EBSD, and some texture information becomes inactive after sample cropping and lath growth and merging. Comparing as-built and HT EBSD pole figures,

there appear some new laths elongated perpendicular to the (1010) plane in the pole figure after HT, which are not taken into account by the introduced PFM.

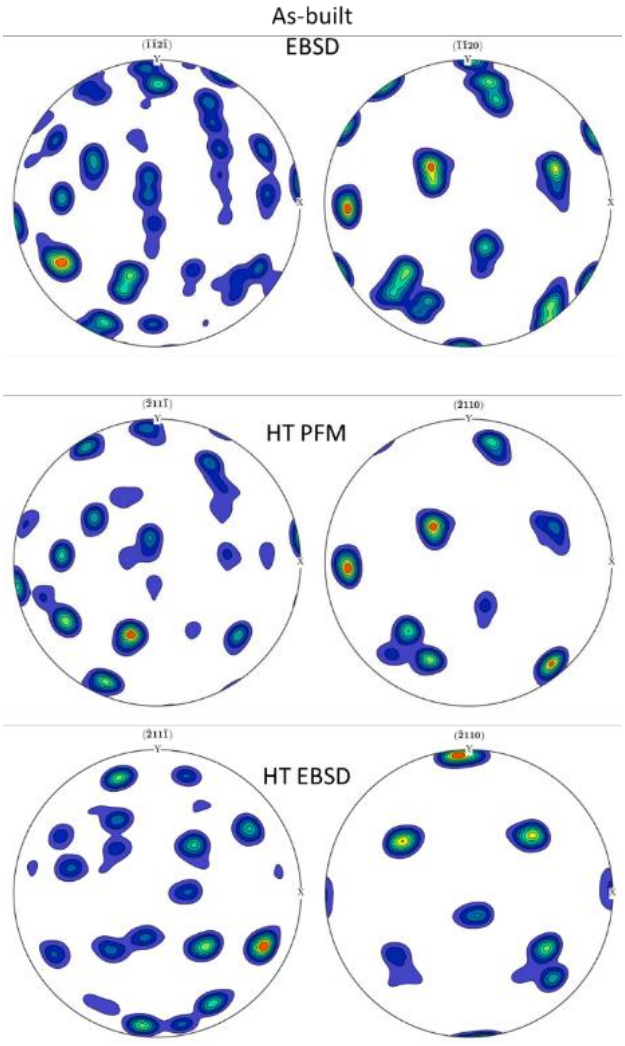

Figure 6-14. Pole figure comparison between the as-built EBSD scan, PFM model after HT, and EBSD scan after HT.

It is always important to be aware of the scatter caused by using non-converged RVE model to represent a large material. The scatter has been discussed several times in this thesis, which causes statistical microstructural-sensitive effect in CPFE, and undesirable texture strength and size distribution in PFM. In a single case, as shown in Figure 6-12, the EBSD-HT CPFE model seems to have a better predicting result compared to PFM-HT, but it should be noted that the two models are not based on the same sample region

due to technical difficulties. However, both models have successfully captured the most important strength-ductility change after HT for Ti-6Al-4V alloys, which is the key finding here. The current challenge in eliminating or limiting the undesired scatter lies in computational modelling capability. Thanks to the progress in EBSD plugin hardware, it takes 40 minutes to scan the two grain images (40×26 μm) for model generation, and 4 hours to complete the two bigger images for 3D reconstruction (139×87 μm), which is completely affordable. However, unlike the EBSD scan which has a linear time-size relationship, modelling cost increases exponentially as the size grows, especially for PFM as shown in Table 6-1. The EBSD-PFM-CPFE methodology can also be easily extended to real 3D given that the facility can fulfil the capability.

In this work, the PFM was used first because the objective was to study the HT effect (lath size effect) on mechanical properties. However, this order is not unalterable, e.g., reversing the workflow, it is also possible to run CPFE first to calculate the plastic dislocation and the relative generated stored energy along the grain boundary, which is then imported to PFM as a driving force, to calculate dynamic recrystallization during hot deformation [366] [367].

6.5 Conclusion

A through-process approach that integrates the phase-field method (PFM) with the crystal plasticity finite element (CPFE) modelling is presented for the prediction of microstructural evolution and the mechanical properties of powder bed fusion (PBF) manufacture Ti-6Al-4V alloy. This framework offers an efficient method for an in-depth understanding of the relationship between thermo-processing, microstructural evolution, and mechanical properties for additive manufactured alloys. The key achievements in this chapter are:

1. The PFM model is utilized for analysing the grain growth behaviour during the post-built heat treatment process through the simulation of grain boundary migration. It predicts five times growth in lath area from 0.59 to 3.0 um^2, after

100 minutes of annealing at 1127 K. The evolved lath prediction reaches close agreement compared to EBSD measurement.

2. Lath size sensitive CPFE models, generated from both direct EBSD-, and PFM-based conversions, are used to model the tensile behaviour of as-built and annealed samples. The CPFE models successfully observe the softening tensile property due to the lath growth after heat treatment and are validated against mechanical tests.
3. The developed geometrically strain gradient CPFE model has captured severe stress localization phenomenon in this lamellar morphology PBF Ti-6Al-4V alloy. The maximum localized principal stress can be up to 2790 MPa, approximately triple the value of yield stress.
4. This work introduces a realistic microstructure image-based phase-field method, as well as a PFM-to-CPFE bridging tool method. Together with the image-based CPFE methodology detailed in chapter 4, this tool has achieved a complete high fidelity micro-scale coupled modelling framework, to offer an important process-structure-property for predicting microstructural evolution and mechanical properties during the PBF thermal process.

7 An Instant Process Quality Control Tool for Additive Manufactured Dual-Phase Steel based on a Crystal Plasticity Trained Deep Learning Surrogate for Structure-Property Prediction

The core contents of this chapter has been published in Yuhui Tu, Zhongzhou Liu, Luiz Carneiro, Caitriona M. Ryan, Andrew C. Parnell, Seán B Leen, Noel M Harrison, Towards an instant structure-property prediction quality control tool for additive manufactured steel using a crystal plasticity trained deep learning surrogate, Materials & Design, Volume 213, 2022, https://doi.org/10.1016/j.matdes.2021.110345. The author of this thesis is the primary author of the paper led the following activity in this chapter / paper:

- *CPFE model development: model generation, constitutive law development, parameter calibration, and automatic big data modelling workflow design.*
- *Experimental test data post-processing: EBSD analysis.*
- *DL model development: TensorFlow code writing, CNN architecture optimization, accuracy assessment and comparison against CPFE and experimental data.*
- *Manuscript drafting.*

The contribution of each collaborator in this study is as follows:

- *Zhongzhou Liu (Singapore Management University) : Discussion on TensorFlow coding structure optimization.*
- *Luiz Carneiro (University of Nevada, Reno): Provision of experimental test data*
- *Caitriona M. Ryan, Andrew C. Parnell (Maynooth University): Discussion on DL application and theory.*

7.1 Introduction

Accurate computational simulation of the macroscale strength of metals or alloys typically requires microstructure definition. Finite element analysis, involving grain boundary and crystal orientation specifications, along with constitutive and damage model parameters, are referred to as crystal plasticity finite element (CPFE) methods [188, 216-218]. Such advanced modelling generally requires model development and simulation time in the order of hours and days, respectively. For e.g, the 190-grain model introduced in Chapter 4, requires 5 days to complete the simulation of low cyclic fatigue behaviour. Often high-end computer infrastructure is required to perform the computation, and once complete offers powerful insights into the contribution that individual microstructural features make to the local and bulk material response. CPFE methods have evolved to include increased slip system complexity [28, 136], allowing simulation of multi-phase alloy behaviour. These advances improve accuracy and broaden the applicability, but they also increase computational costs. The more advanced strain gradient model implemented in Chapter 5 and 6, has the capability of calculating dislocation density based on model geometry. However, the computational cost is also 10 times heavier compared to the phenomenological model in Chapter 4. This computational effort further increases when the loading condition is complex (e.g. cyclic) and further grows if a definitive RVE model (containing sufficient grain information and mesh density to represent a large sample) [318, 322] or a high-fidelity model (realistic microscopy image-based) is required. While accurate and insightful, finite element modelling is far removed from a live in-process property predictive tool, primarily due to model setup and simulation times.

Stainless steels have emerged as a common material for metal printing due to the low power requirement for melting and the non-reactive properties of the material in powder form [368]. The AM fabricated stainless steel exhibits different phase components (austenite, martensite, and ferrite) as well as the varying precipitate (carbides), leading to complex combination of microstructure and mechanical properties [25]. Studies on dual phase austenite-martensite steels have shown that chemical phase fraction has the bigger influence on mechanical behaviour, among a range of microstructural features examined in PBF additive manufactured 17-4PH stainless steel (SS17-4PH) and 316L stainless steel

(SS316L) [369]. It is known that spatial variations in phase fraction can occur during the PBF process due to small changes in (rapid) cooling rate and the complex thermal history involved [323]. SS17-4PH is a dual-phase steel strengthened by precipitation. As-built SS17-4PH contains mainly martensite phase together with the retained austenite phase [370], the precise fraction of which is highly dependent on the PBF process as well as post heat treatment parameters [99]. Studies have reported the retained austenite phase varying from 3% to 63% [37, 79, 197, 371]. Similar behaviour was also observed for other stainless steels such as SS316L, with more complex phase composition including the detected volume fraction of ferrite ranged from 0.83% to 7.83% [372, 373].

Variations in PBF process parameters, number of parts in a build or build layouts can lead to variations in as-built microstructure, and consequently variations in local mechanical performance [331]. Even when process parameters are held constant in a build, a gradient in microstructure can often be observed along the build direction [323]. This, along with the risk of defect occurrence, has led to some PBF equipment manufacturers developing live process monitoring quality tools that image and record sensor data for each individual solidified layer, before the next layer of loose powder is applied [92, 357, 374-376]. As optical imaging resolution and sensor technology continue to advance, it is anticipated that the next generation of quality control in PBF machines will go beyond melt-pool analysis and record as-solidified microstructural features, such as grain boundaries within the captured individual layer data. To take advantage of this live microstructural data, an ideal in-process PBF monitoring tool should have a structure-property prediction for each printed layer. However, live-CPFE modelling of the individual layers is impractical due to computational cost and the short time frame (generally seconds) between successive layer printing.

This study presents a data-driven deep learning (DL) model based on a CPFE predicted structure-property relationship database. This will provide an instant predictive capability to advance the development of a live process-structure-property quality tool based on real-time image and sensor data, giving real-time layer-by-layer strength prediction, once suitable in-situ microscopy technology is in place.

7.2 Methodology

The workflow is described in Figure 7-1. This process firstly generates a statistically equivalent VT-generated CPFE model from the EBSD measurement of an AM 17-4PH stainless steel sample. The input parameters are calibrated against experimental stress-strain behaviour under tensile and cyclic fatigue conditions (ASTM-E606). The dual phase CPFE model is then extended to five different martensite volume fractions ($V_{f,m}$) model sets. Each set contains 200 models, with different (random) grain morphologies, leading to the simulation of 1000 unique CPFE models in total. The resulting 1000 structure-property linkages are used for training and validating the DL model as a surrogate tool for CPFE to rapidly predict structure-property relationships.

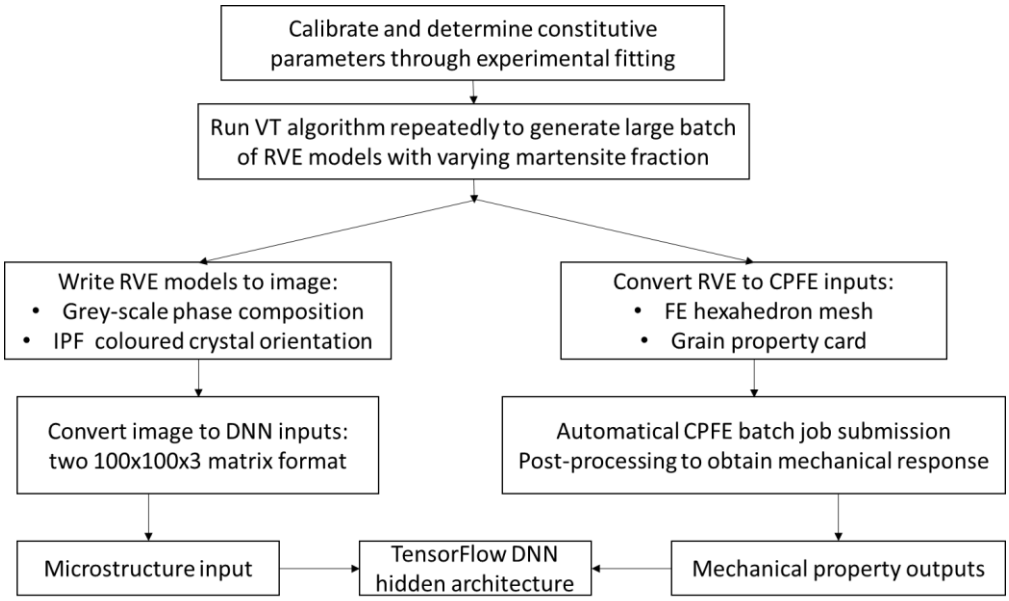

Figure 7-1. Schematic of the integrated CPFE-DNN architecture, two images containing phase fraction and orientation information act as input to predict mechanical properties.

7.2.1 CPFE based dataset generation.

The data-driven model requires structure-property relationship data for training of the DNN model. In the absence of large datasets of experimental testing for structure-property relationships of PBF-LB manufactured stainless steel, CPFE models are adopted here as a reasonable method to produce a broad map of property-structure linkage information for

the DL tool. The VT based grain maps were generated using DREAM3D [294]. The advantage of this tool is that it permits random grain nucleation while maintaining a constant phase fraction ratio. This feature is beneficial to imitate a batch of samples with the same print parameters.

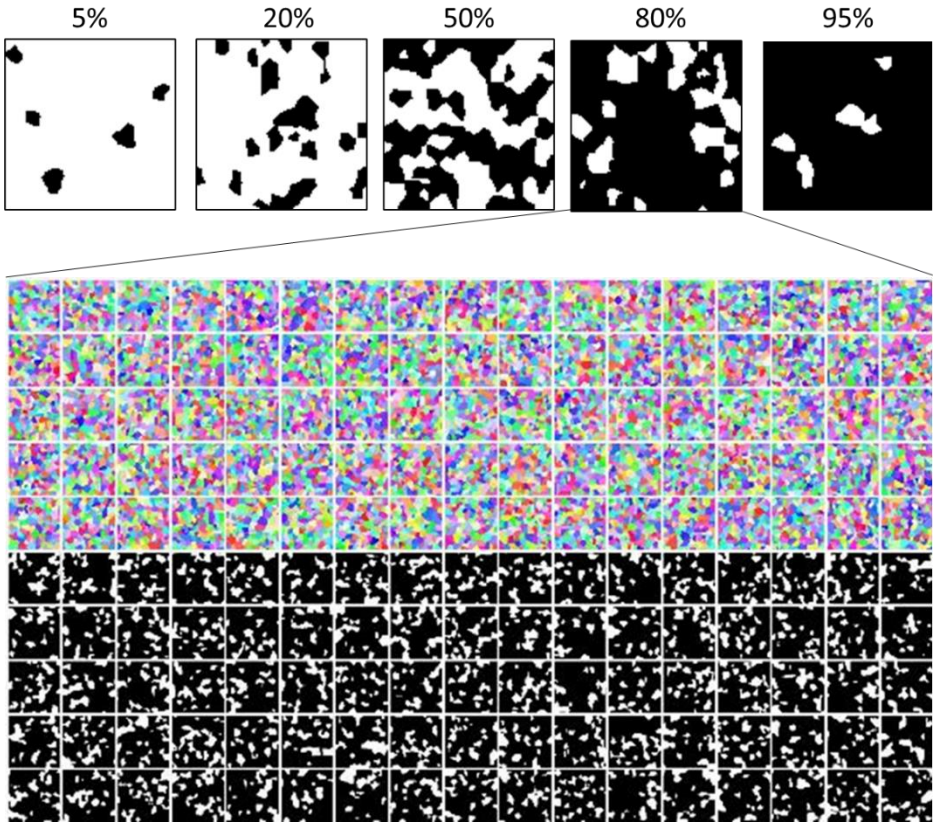

Figure. 7-2. A sample of 85 automatically generated CPFE big data generation results with unique grain morphology, crystallographic orientational and phase volume fraction information for five different martensite phase fractions. Each individual square represents a 100 × 100 μm sample

An efficient simulation framework was developed to batch generate and solve large groups of dual-phase VT models automatically. Each model contains approximately 100 grains of average grain size 10.36 μm and each grain is meshed with approximately 100 linear solid hexahedral (C3D8) finite elements in the general purpose finite element solver ABAQUS [303]. This voxel mesh permits directly conversion from image pixels to a finite element mesh [377] and also facilitates a consistent DNN input size for all model thus

minimizing the potential bias of DNN input size [378]. This three-dimensional solid element as a recommended stress/displacement element [379], has also been shown to have better accuracy compared to linear tetrahedron mesh for plasticity simulations [380]. 200 unique CPFE models were generated for each martensite volume fractions ($V_{f,m}$) of 5, 20, 50, 80, 95%, with a constant grain size distribution and phase fraction. Crystallographic orientation is assigned to individual grains according to the BCC and FCC inverse pole figures (IPFs), to generate 1000 unique polycrystalline realizations in total. Finally, a customized script analyses the phase and orientation definitions and generates the relevant CPFE and DNN material data cards for each model. Figure 7-2 shows sample models from the 80% $V_{f,m}$ model set, the martensite phase is shown in black with austenite in white and corresponding grain morphology and orientation data shown in colour. Materials consisting of more than two phases would require a colour map for complete phase data description.

The CPFE model implements large deformation theory, and the deformation is determined by crystallographic slip only. The yield and hardening behaviour are described by initial critical resolved shear stress g_0, saturated stress g_∞ when large plastic flow breaks out in stage I, is the initial self-hardening modules h_0, as detailed in Chapter 2.8.2. This dual phase CPFE model contains 24 slip systems, 12 for the FCC lattice structure austenite phase, and another 12 for the BCC martensite phase [381, 382], shown in Figure 7-3.

For this material research, it is found necessary to use a scale-consistent fatigue indicator parameter (FIP) to predict the FCI life here. In this case, based on previous work, two FIPs, namely accumulated effective crystallographic slip p [244], and accumulative energy dissipation W [138, 243] were calculated. Equations 5 to 7 define the calculation of these two FIPs. The two FIPs have successfully been utilized in previous research [6, 56] to determine fatigue crack initiation.

Accumulated effective crystal slip p, aggregated over all slip systems including the effects of mean stress, is successfully implemented with CPFE to predict fatigue behaviour as follows:

$$\dot{p} = \left(\frac{2}{3}\boldsymbol{L}^{\mathrm{p}} : \boldsymbol{L}^{\mathrm{p}}\right)^{\frac{1}{2}} \qquad (7-1)$$

$$p = \int_0^t \dot{p}\,dt \qquad (7-2)$$

Further development of this FCI prediction approach considers the accumulated strain energy dissipation parameter *W* which sums up the energy consumption on all the crystal slip systems by considering both microscale shear stress and slip rate, as follows:

$$W = \sum_{\alpha} \int_0^t \tau^{\alpha} \dot{\gamma}^{\alpha} dt \qquad (7-3)$$

It has been found that the two FIPs tend to evolve and finally reach a stabilised value during CPFE modelling. Thus, it is reasonable to predict the numbers of cycles for FCI by dividing a critical FIP value FIP_{crit} by that of the stabilized fatigue cycle FIP_{cyc}, as shown below:

$$p_{\mathrm{cyc}} = p_t - p_{(t-\Delta t_{cyc})} \qquad (7-4)$$

$$W_{cyc} = W_t - W_{(t-\Delta t_{cyc})} \qquad (7-5)$$

$$N_{i,p} = \frac{p_{\mathrm{crit}}}{(p_{\mathrm{cyc}})^{b_1}} \qquad (7-6)$$

$$N_{i,W} = \frac{W_{\mathrm{crit}}}{\left(W_{\mathrm{cyc}}\right)^{b_2}} \qquad (7-7)$$

where Δt_{cyc} is the modelling time consumed to finish one fatigue cycle.

The critical FIP values are identified and validated by comparing the CPFE-predicted and measured FCI data for certain sample tests. The component *b* is solved through the experimental data-fitting process by a nonlinear least-squares algorithm. This power-law approach was considered necessary to improve the fatigue prediction [182, 340, 383].

The integrated algorithm was written in a user material subroutine (UMAT) [231] for ABAQUS. More details about self-hardening and latent-hardening moduli definitions can be found in prior literature [234-236].

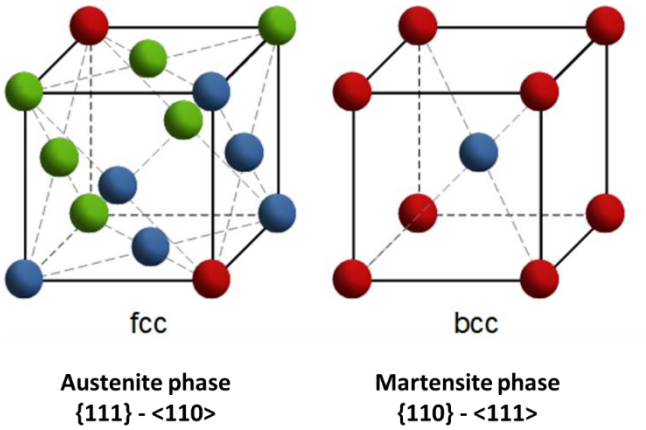

Figure. 7-3. Slip systems and crystallographic lattice of austenite and martensite phase.

Periodic boundary conditions (PBC) [234] were applied to the free surfaces in the CPFE models together with a strain of 1.0%, which is sufficient to calculate bulk yield strength value while keeping an acceptable CPFE running time. A customized script was applied to schedule the job and perform results extraction once the simulation finishes. These post-processed property data (stress-strain and fatigue data) act as the output of the DNN model.

Although the definitive RVE model is unfortunately not the suitable choice for running the big data batch jobs, due to the tremendous computational cost from thousands of models, it can be adopted for calibrating the material parameters in CPFE modelling. The CPFE model for calibration shown in Figure 7-5, contains 1078 grains with a mesh density of 111 elements per grain. This model has satisfied the minimum size and number of grain required for a converged definitive VT-based model, as previously quantified in Chapter 4.3.1.1 (190 grains and 98 elements per grain). This converged model helps avoid scatter caused by microstructural variation during the VT realization and texture definition, thus ensuring reliable calibration results.

The initial parameter values selected in the calibration step referred to relative dual phase steel studies using similar UMAT, as the starting variable combination in the

developed MATLAB non-linear square fit automatic calibration tool. Specifically, the initial elastic parameters for martensite phase were taken from a two-stage deformation modelling work on DP 780 steel [12] and the values for austenite were obtained from published data [50] [51]. Initial parameters for critical resolved shear stress g_0 and stage I saturated stress values g_∞ were determined through hardness tests [52], and the hardening modules from tensile tests for a transformation-induced plasticity steel [53]. These values were iteratively adjusted by the algorithm to suit the PBF-LB steel adopted in this chapter. The calibrated data set for PBF-LB built 17-4PH steel sample with 79% $V_{f,m}$, based on a comparison with the stabilized stress-strain curve [28] is given in Table 7-1.

Table 7-1. Calibrated parameters for dual phase CPFE model.

Parameter	**Martensite BCC**	**Austenite FCC**
$\dot{a}$	0.001 s^{-1}	0.001 s^{-1}
n	50	50
g_0	466 MPa	192.5
g_∞	740 MPa	402.5
h_0	20 MPa	20 MPa
C_{11}	262 GPa	204.6 GPa
C_{12}	150 GPa	137.7 GPa
C_{44}	112 GPa	126.2 GPa
C_1	10000	
D_1	200	
b	1.58	

7.2.2 DNN model optimization, training, and validation.

The DNN inputs consist of 1000 varying microstructural images including phase and crystallographic orientation variations, each with 10,000 pixels, thus 2×10^7 data features in total. There is no fixed value for optimal ratio of size of training sample dataset to size of validation sample dataset, as this parameter depends on the signal-to-noise ratio in the data and the training sample size. The effect of this ratio selection has been discussed in a previous study [378], showing that an increase in the training set percentage can lead to an unstable estimation of the true performance of the DNN model, while a reduced training set percentage can lead to a poor model due to insufficient amount of training data. In this study, a range of ratios was examined, as shown in Table 7-2, where a training to validation ratio of 75:25 was found to give the lowest mean absolute error (MAE) in yield strength predictions. Consequently, the CPFE predicted 1000 structure-property relationships are randomly divided into two groups: 750 for training and 250 for validation.

Table 7-2. Relationship between DNN performance and the training/validation ratio setting.

Training/validation ratio	MAE in YS (MPa)
50-50	332.0
60-40	317.8
70-30	45.3
75-25	37.1
80-20	38.6

Specifically, the inputs of the DL model are the microstructural images containing phase and orientation data, and the output value is the predicted bulk stress-strain curve. The 100×100 pixel (nodes in CPFE) microstructural images, representing phase

composition and orientation, were converted to DNN input data format, which contained the RGB values respectively, for the complete model. Thus, the phase map input and the orientation map use $100 \times 100 \times 3$ array sizes. A customized Python code was developed for calculating the macroscopic stress based on the CPFE predicted reaction force, and the result together with its strain value was recorded with an interval of 0.00025 strain. Consequently, 40 data points were extracted and used to plot the stress-strain curves, which also acted as the DNN output, with an array dimension of 40×2.

In this work, two different types of DNN architecture are considered. A standard sequence DNN network [269, 277] is first developed where inputs go through a single pipeline shown in Figure 7-4 (a). As the microstructural inputs have two variables, the sequence DNN design may not be appropriate. Thus, an optimized non-sequence (Siamese) DNN structure [384] with two pipelines, shown in Figure 7-4 (b), was also developed to capture the structural features of phase and crystallographic orientation (represented as IPF colour) data separately. Integrating the two different CNNs to extract the characteristic of phase and orientation separately while aggregating the outputs together at the last 3 layers (as shown in Figure 7-4) is a key novelty in this study. In a standard sequence DNN design, the two images are usually imported at the first layer where rich semantic information could be lost. However, in the new model, by aggregating the images in the last 3 layers, it can better capture their common points and differentiate their features thus leading to an improved prediction [77].

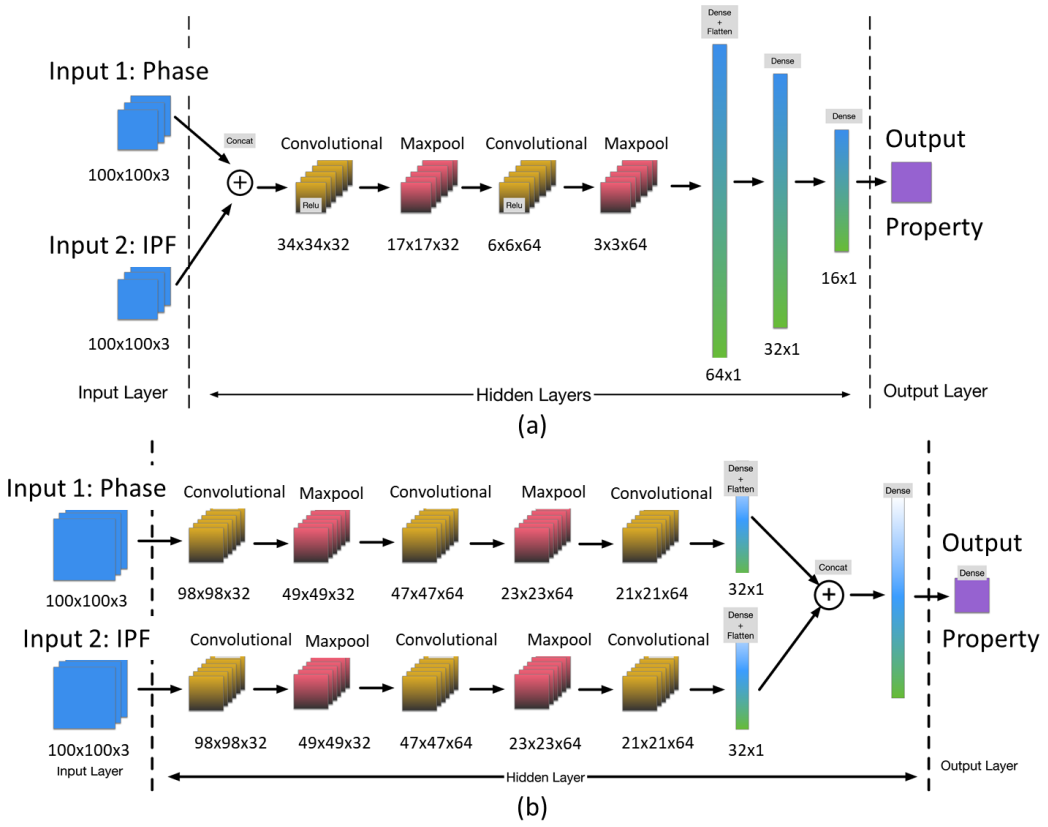

Figure. 7-4. (a) Single pipeline sequence DNN (before optimization) and (b) non-sequence multi-pipeline Siamese DNN (after optimization)

The base module of the DNN model implements convolution neural networks (CNN) as the kernels to extract information from the microstructure images. CNN is generally designed to handle the problem of processing grid-shaped data which are difficult to process via traditional deep learning models. It utilizes several small filters and pooling layers to efficiently extract features which are useful for downstream tasks. Further general information on convolution layer design can be found elsewhere [276]. In this study, the design of the CNN contains the following layers: convolution layer [279], pooling layer and dropout layer.

The convolution layer only needs a small part for each computation (usually 3×3 or 5×5), resulting in a much smaller number of parameters. It consists of several filters which capture the distributions of the specific characteristic on the data (i.e. in which part the characteristic is more significant when predicting the result, also denoted by a weight parameter) by performing matrix multiplication with a part of the data. In this way, the

filters are a set of matrices whose elements (parameters) are implicitly and automatically learned during the training process of model development. The stress-strain property of each instance is influenced by different characteristics of the data. The goal of the convolution layer is to determine the implicit characteristics that contribute to the stress property. The hyper-parameters were defined based on a (published) recommended stable value [385], without an explicit hyper-parameter search, as it was observed that the predicted output was not sensitive to minimal change in hyper-parameter.

The DNN architecture (i.e. the combination of DNN layers) was modified through parameter tuning during the training process to obtain a satisfactory accuracy and learning rate. Mean squared error (MSE) is adopted to train the model and optimize the parameters. The definition of MSE is presented in Equation 13 below:

$$MSE_{(y_{true},y_{pred})} = \left(y_{true} - y_{pred}\right)^2 \qquad (7-8)$$

where y_{true} is the ground truth of the stress property from CPFE modelling results, and y_{pred} is the predicted value by DNN, and L is the MSE loss function.

A back propagation (BP) algorithm was adopted for the training of the DNN. A BP algorithm is a general algorithm to update parameters in a DNN for supervised learning. The BP algorithm computes the gradient of each parameter, with respect to the loss function. For the DNN proposed in this model, the network architecture can be summarized in the formula below:

$$y_{pred} = \emptyset^L\left(\theta^L, \emptyset^{L-1}(\theta^{L-1} \cdots \emptyset^1(\theta^1, x) \cdots)\right) \qquad (7-9)$$

where x is the input into this model, θ^L is the L^{th} layer's parameters (note that there may more than 1 parameter existing in a neural network layer, but they are all represented by a single θ here), and $\emptyset^L$ means the activation function and layer type of the L^{th} layer.

Hence, the loss function can be rewritten as:

$$\begin{aligned} &L\left(y_{true}, \emptyset^L\left(\theta^L, \emptyset^{L-1}(\theta^{L-1} \cdots \emptyset^1(\theta^1, x) \cdots)\right)\right) \\ &= abs\left(y_{true} - \emptyset^L\left(\theta^L, \emptyset^{L-1}(\theta^{L-1} \cdots \emptyset^1(\theta^1, x) \cdots)\right)\right) \end{aligned} \qquad (7-10)$$

Therefore, for each θ, it is possible to compute its gradient with a chain rule. This back propagation (BP) algorithm was adopted for the training of the DNN [386]. For example, considering θ^1 the gradient is:

$$\frac{dL}{d\theta^1} = \frac{dL}{d\emptyset^L}\frac{d\emptyset^L}{d\emptyset^{L-1}}\cdots\frac{d\emptyset^1}{d\theta^1} \qquad (7-11)$$

After getting the gradient of parameter θ, it is updated as:

$$\theta' = \theta - \alpha\frac{dL}{d\theta} \qquad (7-12)$$

where α is referred to as a learning rate. The Keras library and the efficient implementation of BP (SGD) were adopted in this optimization process [250].

In general, BP algorithm intends to find a global optimal parameter $\hat{\theta}$ that minimizes the gap between the y_{pred} value and y_{true} extracted from CPFE modelling result. θ' is expected to finally converge to $\hat{\theta}$. The CPFE predicted training database is used to compute the loss as well as the gradient of each parameter. After multiple steps of updated iterations, the parameters finally converge to produce a minimized loss (e.g. MSE defined in Equation 13).

The remaining unseen unique 250 sets of CPFE predicted structure-property relationships are used to validate the reliability of the trained DNN model. Two criteria, mean absolute error (MAE) and regression residual are used for determining the DNN model performance in both efficiency and accuracy. MAE quantifies the loss between the predicted values and ground truth of the 250 data points. The regression residual is computed as $|y_{true} - y_{pred}|/y_{true}$ and reported in percentage terms. The standard and Siamese DNN architecture are trained to predict the property and then compared to CPFE, and the resulting preferred DNN type is adopted for subsequent runs.

7.2.3 DNN validation with new phase fraction dataset

Having determined the effectiveness of the DNN model in predicting the stress-strain response and fatigue life for the specific martensite-austenite phase fractions that it was

trained upon, the effectiveness of the DNN model's predictive capability for other phase fraction combinations was then assessed. Thus, 200 more synthetic microstructure images were generated for two martensite fractions ($V_{f,m}$ = 35%, 65%) that are between previous fraction values (5, 20, 50, 80, 95%). In this case, no re-training of the DNN model was performed, however CPFE analyses were performed for validation of the predicted yield strength.

7.2.4 DNN application on realistic microstructural images

CPFE modelling based directly on realistic microstructure images, (based on SEM or EBSD scans) is considered to more accurately represent microstructure with complex grain morphologies and special textures common in AM metals, [142, 143, 228, 387] than using synthetic (e.g. VT-based) images. However, this real image-based model usually has higher computational cost and larger computational memory requirements. Furthermore, time-consuming sample preparation and pre-processing of the raw data, including non-indexed fill and grain cleaning, is necessary to avoid excessive numbers of local singularities.

The DNN model is potentially capable of addressing the excessive computational cost issue associated with solving EBSD-CPFE models. To test this capability, a 400×400 pixel EBSD scan of 17-4PH material was performed. The EBSD images were converted to a grey scale image (for phase data) together with an IPF coloured orientation map (for texture data) with which the trained DNN is familiar. Meanwhile, an EBSD image-based CPFE model was constructed using a previously published approach [228]. To distinguish from the VT-generated CPFE model, all models from direct EBSD image-based conversion are subsequently denoted as CPFE-E. The DNN and CPFE-E predicted stress-strain curves using realistic microstructural images were compared to the experimental test to determine predictive accuracy. The computational costs were also measured to compare efficiency.

7.3 Results

7.3.1 CPFE model calibration and property prediction.

This study started with CPFE model calibration against the mechanical tests. Figure 7-5 shows a statistically equivalent RVE model (21% austenite phase and equivalent texture), based on microstructural characterisation from EBSD measurement, for this parameter calibration process. Figure 7-6 shows a comparison between CPFE-predicted and measured experimental tensile stress-strain response. This CPFE model shows close agreement up to the strain of 1%, including good agreement of yield stress (1066 and 1087 MPa).

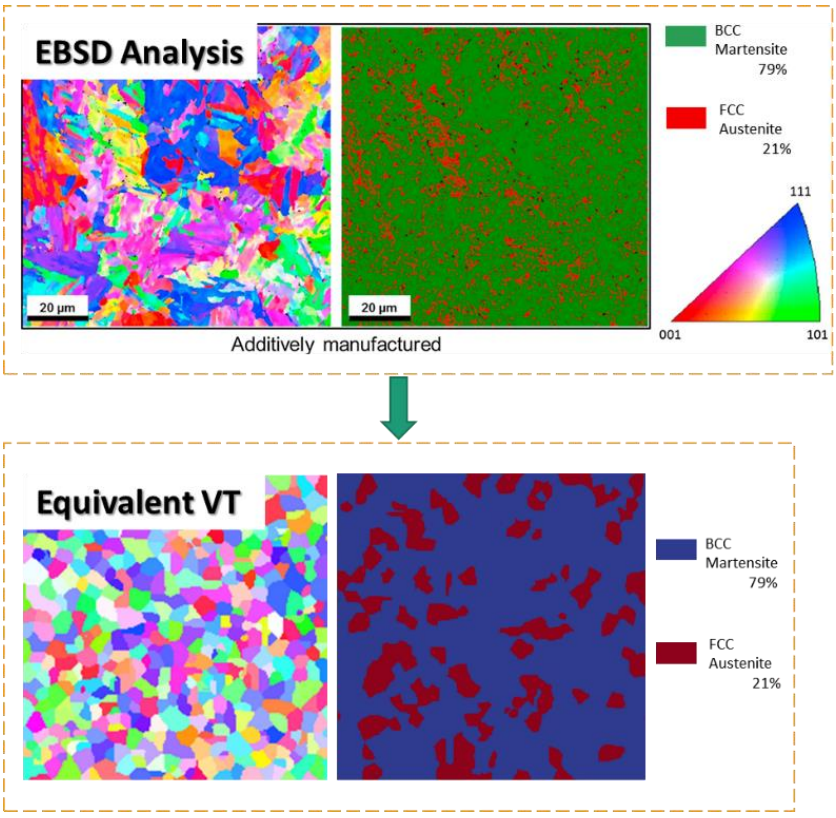

Figure. 7-5. Reconstructed EBSD crystallographic orientation map coloured in inverse pole figure (IPF), phase fraction map (79% martensite in green and 21% austenite in red), and the statistically equivalent VT-generated CPFE model.

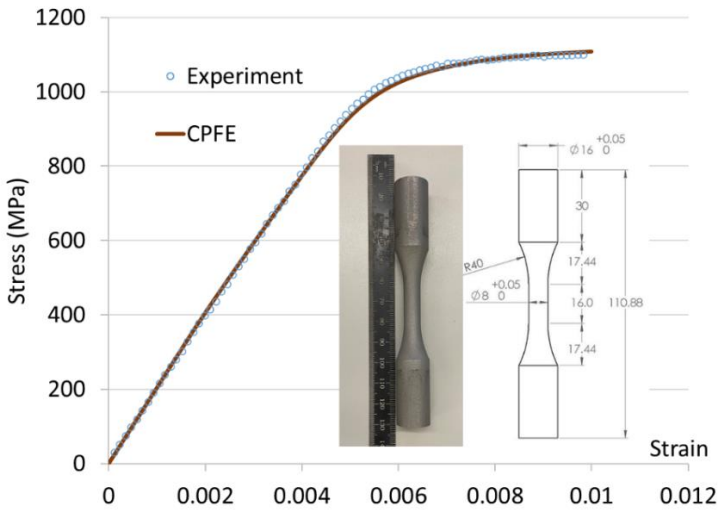

Figure 7-6. Experimental fit and CPFE parameters calibration for SLM manufactured 17-4PH steel.

The next step was to validate the performance of steels with different phase fractions. For ease of results visualization and comparison, Figure 7-7 shows the 0.2% offset yield stress (YS) values extracted from the 1000 CPFE models with five different phase fractions. The CPFE model predicted an increasing tensile strength as the martensite fraction increases with the predicted YS median values being 532 MPa, 567 MPa, 702 MPa, 1003 MPa and 1216 MPa for the groups with 5, 20, 50, 80, 95% martensite phase, respectively. The CPFE-predicted YS ranges are also compared with tensile test data for other AM steels for a range of martensite phase fractions in Table 7-3.

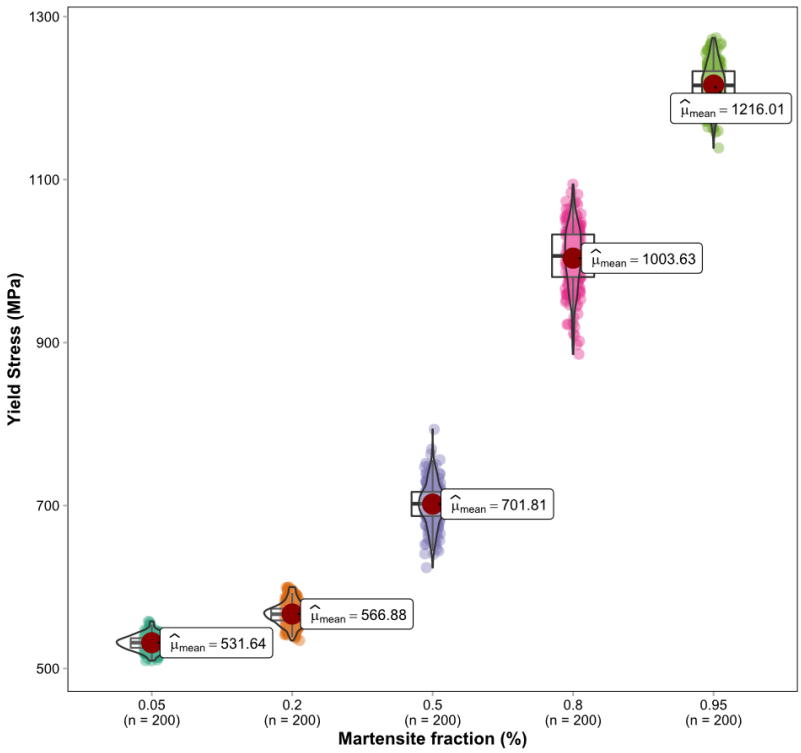

Figure. 7-7. CPFE predicted effect of martensite phase fraction on yield stress.

Table 7-3. Comparison of CPFE predicted results with literature on yield strength.

Martensite Fraction (%)	CPFE YS ranges (MPa)	Test YS (MPa)
5	509.7 - 557.9	440-520 [388-390]
20	534.4 - 600.0	570 [391]
50	623.8 - 793.5	750-798 [371, 392]
80	824.9 - 1094.3	1087 [79]
95	1138.8 - 1270.0	1170 [99]

Figure 7-8 shows the CPFE-predicted stabilized hysteresis stress-strain loop relationship at three strain amplitudes, $\pm 0.4\%$, $\pm 0.7\%$, and $\pm 1.0\%$. FCI is assumed to correspond to a critical FIP W value, which is calibrated against the $\pm 1.0\%$ CPFE result as $8.26 \times 10^5\ MJm^{-3}$. The maximum localized FIP W is adopted to indicate the predicted FCI life. Table 3 shows a comparison between predicted and measured stress amplitudes and FCI lives. Both FIPs show a decreasing trend until they finally become stable after 8 cycles. The FIP energy dissipation W result from the tensile test simulation can, to some extent, represent the cyclic FIP result by multiplying it by a factor of four while the plastic slip p result shows overestimation when predicting maximum

localization values. A previous study [234] also showed a more reliable prediction on fatigue behaviour using W rather than p. Due to the above reasons, this work only considers energy dissipation W values as the FIP and uses tensile CPFE modelling results for the DNN training to save computational cost.

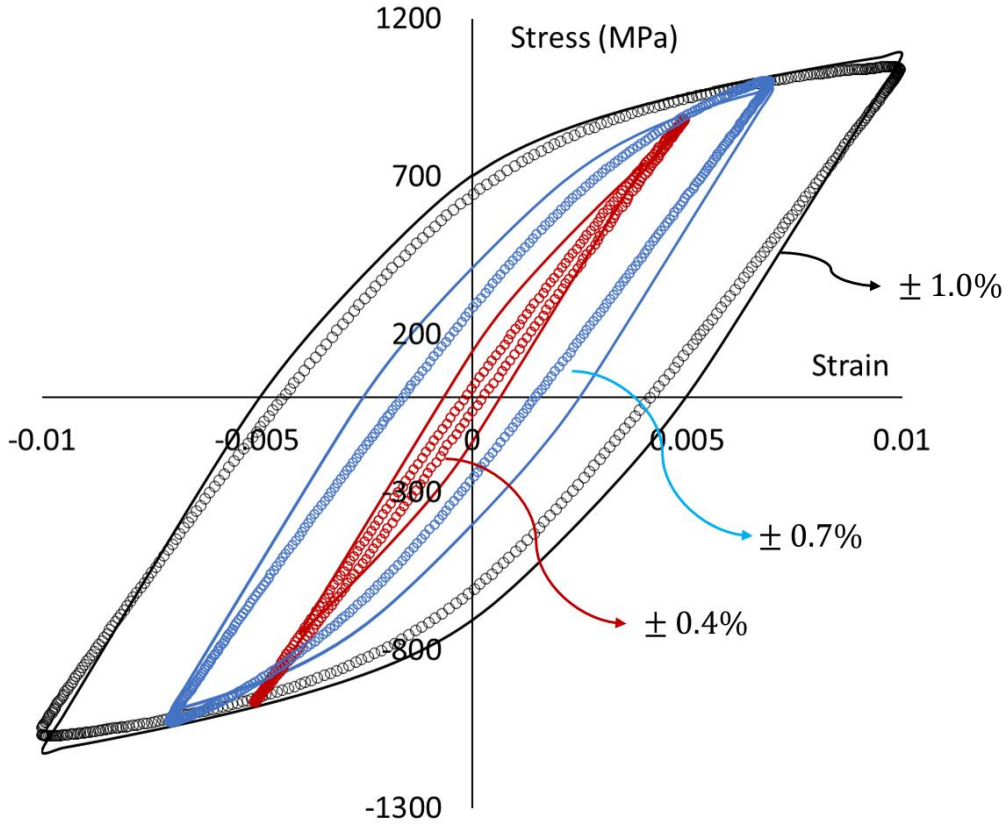

Figure. 7-8. Comparison of CPFE-predicted stabilized hysteresis loop (lines) with experimental data (symbols), for the 79% martensite phase fraction in 17-4PH AM steel, at 0.4%, 0.7% and 1.0% cyclic strain amplitudes.

Table 7-4. Comparison between experimental tests and CPFE predicted results on cyclic stress and fatigue crack initiation life.

Strain amplitude	Experiment $\Delta\sigma/2$	CPFE $\Delta\sigma/2$	N_iTest (cycles)	N_i CPFE (cycles)
±0.4%	792 MPa	748 MPa	11271	11399
±0.5%	921 MPa	862 MPa	4011	3352
±0.7%	1014 MPa	994 MPa	633	956
±1.0%	1060 MPa	1108 MPa	129	125

Figure 7-9 shows the 1000 maximum localized FIP W distribution results extracted from batch CPFE models at the strain of 1%. It can be observed that for a group of randomly generated models with a constant phase fraction definition but unique morphology and texture, there is approximately a 3% possibility for the CPFE models to predict double the localized FIP values compared to the mean FIP of the phase group. The CPFE models have predicted a wide range of FIPs although their phase compositions are statistically equivalent. One reason is the difference in RVE size for a monotonic stress-strain prediction and the RVE size for a maximum FIP value prediction. The RVE size used here meets the requirements for monotonic stress-strain but may not suffice for some model FIP predictions. It is known that the predicted fatigue life reduces as the RVE size increases [228]. However, the model size in this work (of 1000 CPFE models) had to be balanced with the computational costs of the CPFE analysis. In addition, the FIP prediction has proved to be more sensitive to the initial texture than to grain morphology. The texture is randomly assigned to the models within the same phase group and is unique in individual RVEs. In each phase group, there are approximately 5 FIP predictions considerably higher than the mean. It is worth noting that although a bigger RVE decreases the possibility of a large scatter in the FIP prediction, it is unlikely to account for all scatter [393]. Figure 7-10 shows von Mises stress, principal strain, and FIP W contour plots for phase fractions of 20% and 80% at the strain of 1%. The 80% martensite material gives a higher von Mises stress and fewer deformed regions due to increased harder phase components. The FIP W shows a similar distribution to the principal strain contour plot, while its magnitude is influenced by both stress and strain localization values.

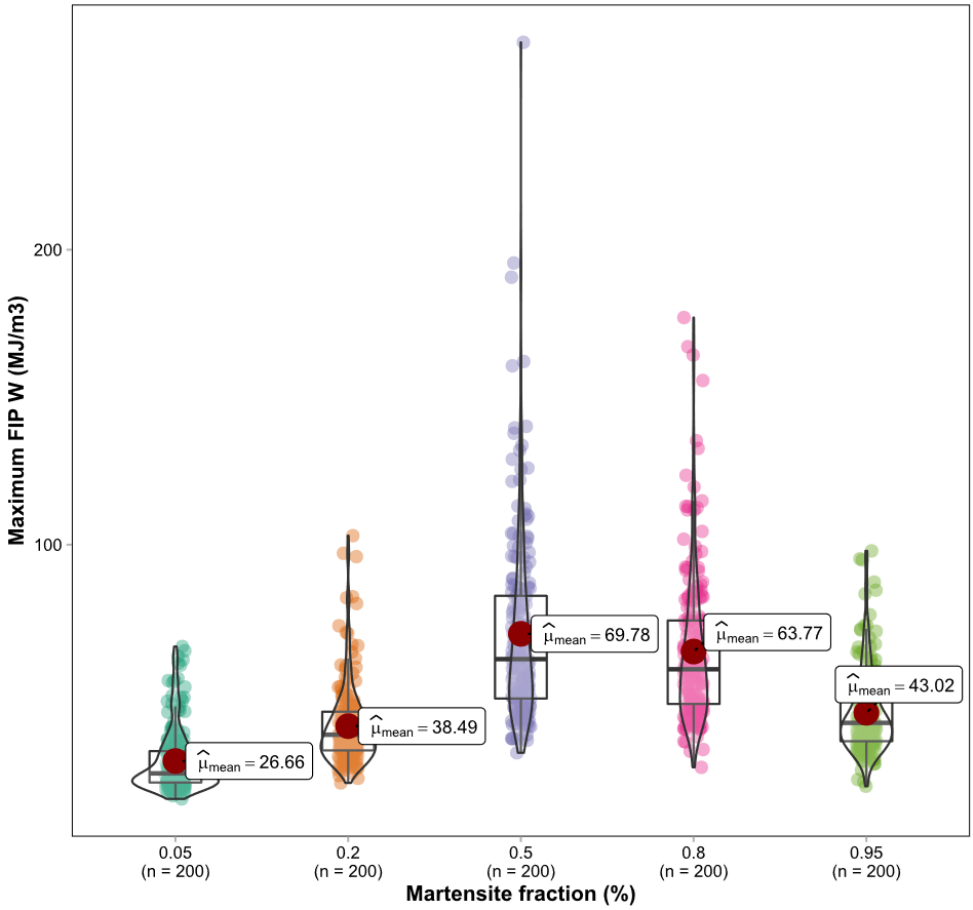

Figure. 7-9. Predicted effect of martensite phase fractions on the maximum localized energy dissipation FIP W over full RVE extracted from CPFE models.

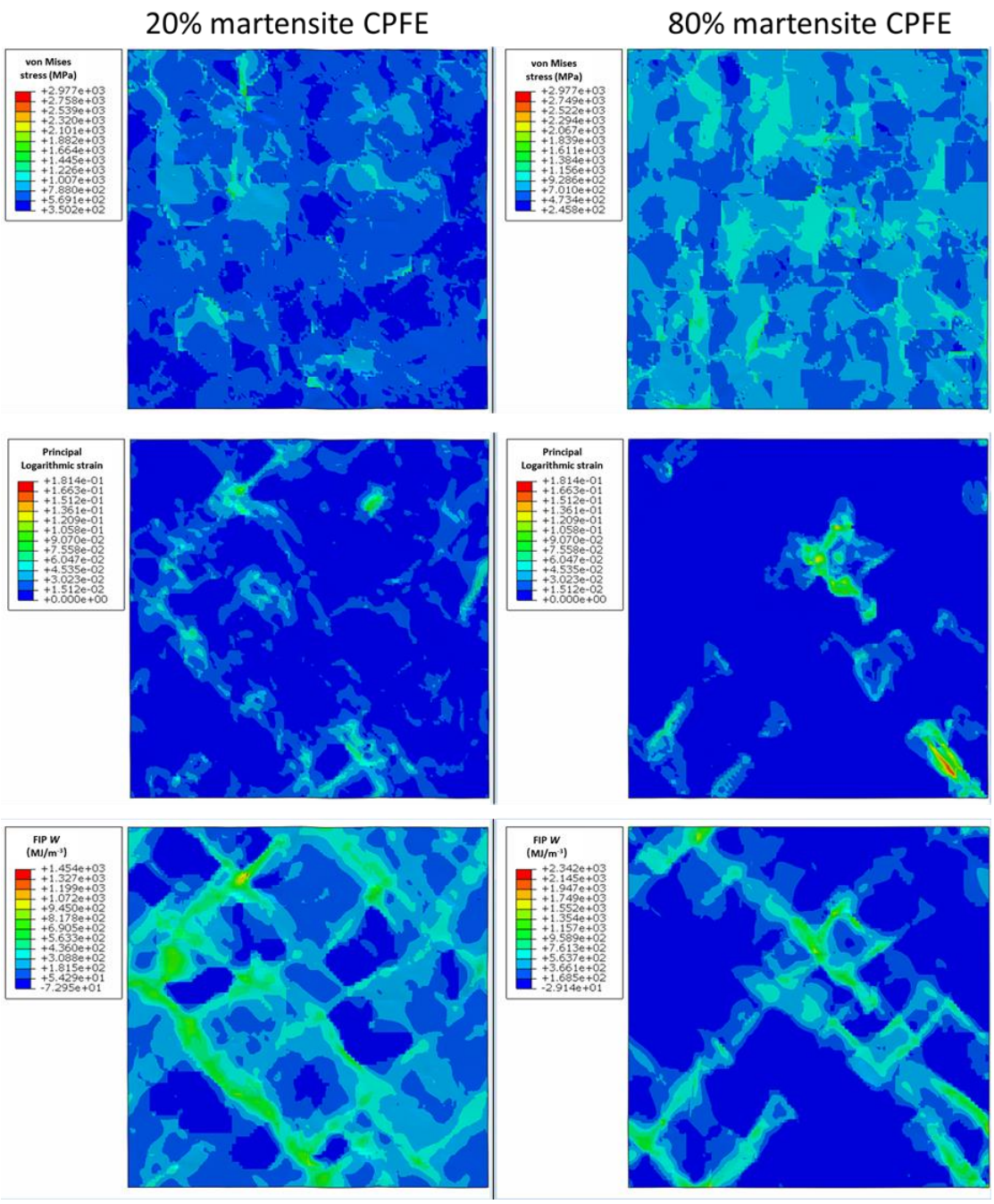

Figure. 7-10. Predicted effect of martensite phase fraction on CPFE-predicted distribution of von-Mises stress, maximum principal strain and W FIP.

7.3.2 DNN training and validation performance

The hardware requirement for the developed DNN model is low and all DNN code in this work runs on an office-grade laptop with 4-core CPU and 16 GB RAM. The design and arrangement of DNN layers have a significant impact on training time and convergence values, but not on the convergence speed. The optimised non-sequence DNN model in Figure 7-4 (b), with 2 input layers and 3 CNN layers for each branch, had an accuracy of 91% (compared to the standard sequence DNN model of 65%) but required a larger training time of 25 minutes (compared to 15 minutes).

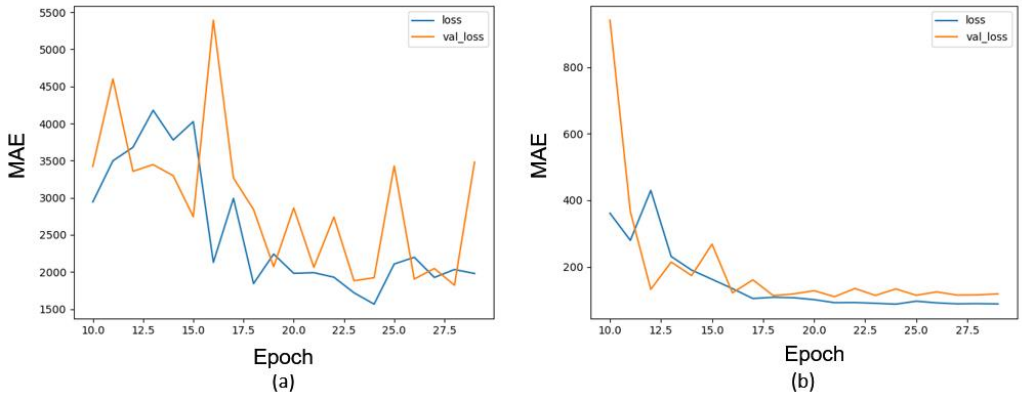

Fig. 7-11. MSE loss curves (loss for training group and val_loss for validation group) of the DNN network (a) before (standard DNN) and (b) after optimization (Non-sequential DNN).

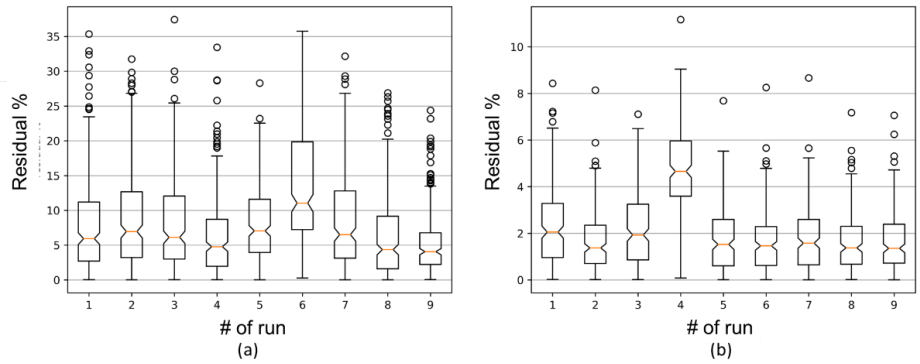

Fig. 7-12. Regression residual (residual %) boxplot of the DNN network performance (a) before (standard DNN) and (b) after optimization (Non-sequential DNN).

Figure 7-11 compares the training loss and validation loss curves for the standard sequence DNN (a) and the advanced non-sequence DNN after model optimization (b). From these two figures, it can be concluded that after optimization, the latter model creates far better predictions with significantly reduced MSE. The MSE curve for the model before optimization fails to converge, as shown in Figure 7-11 that after 25 epochs the validation loss is still not steady. After improving the DNN to non-sequence multi-pipeline type, the loss curves begin to converge after 20 epochs, giving a more robust model. To further distinguish the two DNN model types, Figure 7-12 plots the regression residual for the two network structures. Similar to the conclusion drawn by MSE, after optimization, the mean of regression residual has decreased, indicating that the model can perform more accurate prediction and the variance of the regression residual has also decreased indicating that the optimized model is less likely to produce outliers. Table 7-5 and Table 7-6 list the structural parameters of two models before and after optimization. Although the optimized model adds more parameters in total which may lead to slightly more training time, it results in largely improved performance. Thus, all DNN models run hereafter in this study employ the optimized non-sequence structure.

Table 7-5. Standard DNN structure design parameters before optimization.

Layer (type)	**Output Shape**	**Param #**
Conv2D	(BATCH, 98, 98, 32)	896
MaxPooling2D	(BATCH, 49, 49, 32)	0
Conv2D	(BATCH, 47, 47, 64)	18496
MaxPooling2D	(BATCH, 23, 23, 64)	0
Conv2D	(BATCH, 21, 21, 64)	36928
Flatten	(BATCH, 28224)	0
Dense	(BATCH, 64)	1806400
Dense	(BATCH, 1)	65
Total		1862785

Table 7-6 Non-sequence (Siamese) DNN structure design parameters after optimization.

Layer (type)	Output Shape	Param #
Conv2D	(BATCH, 98, 98, 32)	896
MaxPooling2D	(BATCH, 49, 49, 32)	0
Conv2D	(BATCH, 47, 47, 64)	18496
MaxPooling2D	(BATCH, 23, 23, 64)	0
Conv2D	(BATCH, 21, 21, 64)	36928
Flatten	(BATCH, 28224)	0
Dense	(BATCH, 32)	903200
Conv2D	(BATCH, 98, 98, 32)	896
MaxPooling2D	(BATCH, 49, 49, 32)	0
Conv2D	(BATCH, 47, 47, 64)	18496
MaxPooling2D	(BATCH, 23, 23, 64)	0
Conv2D	(BATCH, 21, 21, 64)	36928
Flatten	(BATCH, 28224)	0
Dense	(BATCH, 32)	903200
Concatenate	(BATCH, 64)	0
Dense	(BATCH, 64)	1040
Dense	(BATCH, 1)	17
Total		1920097

It takes 3 seconds for the DNN to give stress-strain relationships for all 250 models in the validation group, while it takes 4 days to complete CPFE modelling of the equivalent data set. Figure 7-13 show the stress-strain curve comparison from randomly picked models in 250 validation group of 80% martensite phase fraction. Figure 7-14 plots the comparison between 0.2% offset yield strength predicted by CPFE modelling and DNN machine learning, including both training and validation groups. The validation group tends to over predicts the YS value for the 50% phase fraction group, but the general predicting error is controlled within $\pm 15\%$ margin.

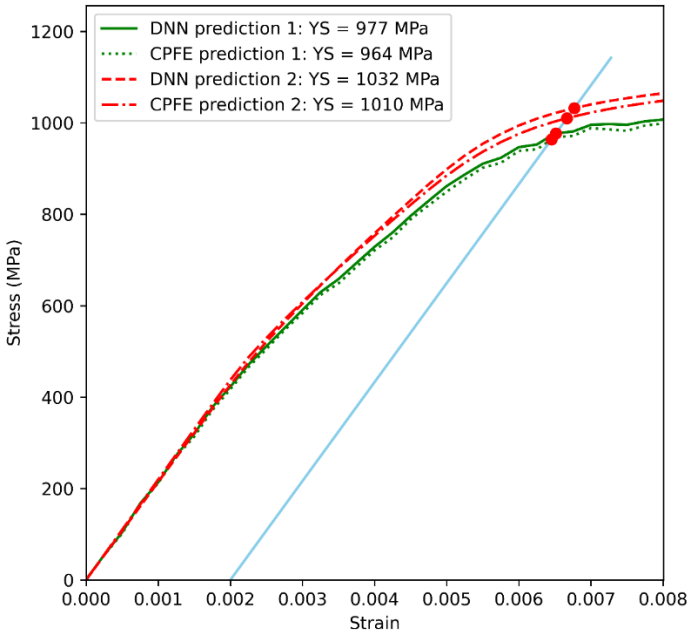

Fig. 7-13. Comparison between CPFE- and DNN-predicted tensile stress-strain response up to 0.8% strain for 80% phase fraction of martensite.

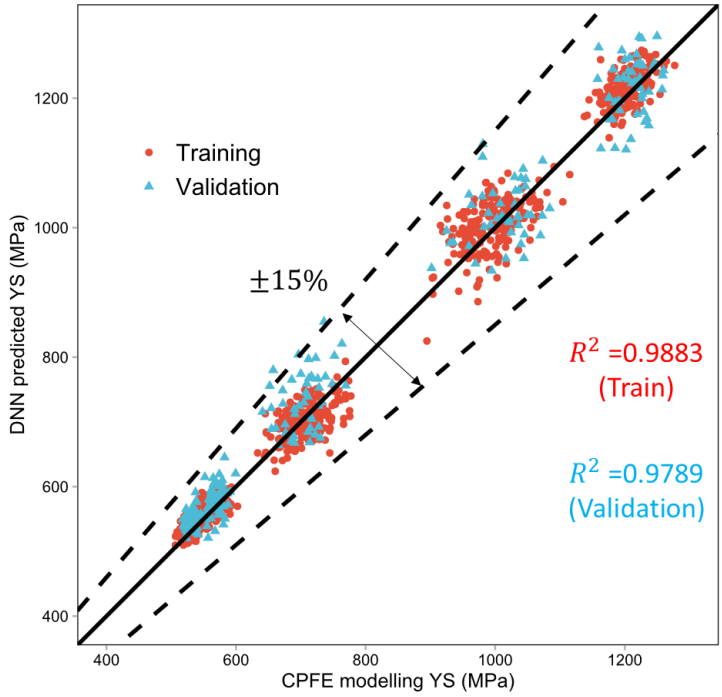

Fig. 7-14. Result Comparison between CPFE and DNN (optimized) predicted yield stress values in the training (red) and validation (blue) group.

Figure 7-15 shows the CPFE and DNN predicted contour plots of von Mises stress (CPFE) and heat-map for contributing pixels (DNN) at 1% strain for 20%, 50% and 80% models, respectively. The contour plots on the left side are directly from CPFE modelling showing von Mises stress, while the contour plots on the right side are the weight factor distribution extracted from the DNN convolutional layer to the overall stress-strain response. It should be noted that the DNN model is not designed to predict the von Mises stress contour plot, but these images are presented to indicate the relative contribution that each grain makes to the DNN response prediction. The weight factor heatmap shows the correlation of microstructural images to the stress property after DNN training, where the red regions contribute most to the overall stress (DNN output property) while the blue regions have the least positive effect on the property. It is obvious that the black phase (martensite) has the higher weight factor leading to a higher stress localization, which is consistent with the CPFE model prediction because martensite is defined to be harder. Figure 7-16 shows a similar comparison between the CPFE contour plot of FIP W and the corresponding DNN predicted heat map for FIP W. The CNN weight factor heatmap reveals what the DNN model has interpreted. The comparison between the heatmap and the relevant physical constitutive-based CPFE model stress contour plot, helps assess and improve the DNN performance. Besides, the localized mechanical property prediction, rather than a macroscopic stress-strain curve, offers a more visible and straightforward reference for tailored microstructure design or localized quality assessment.

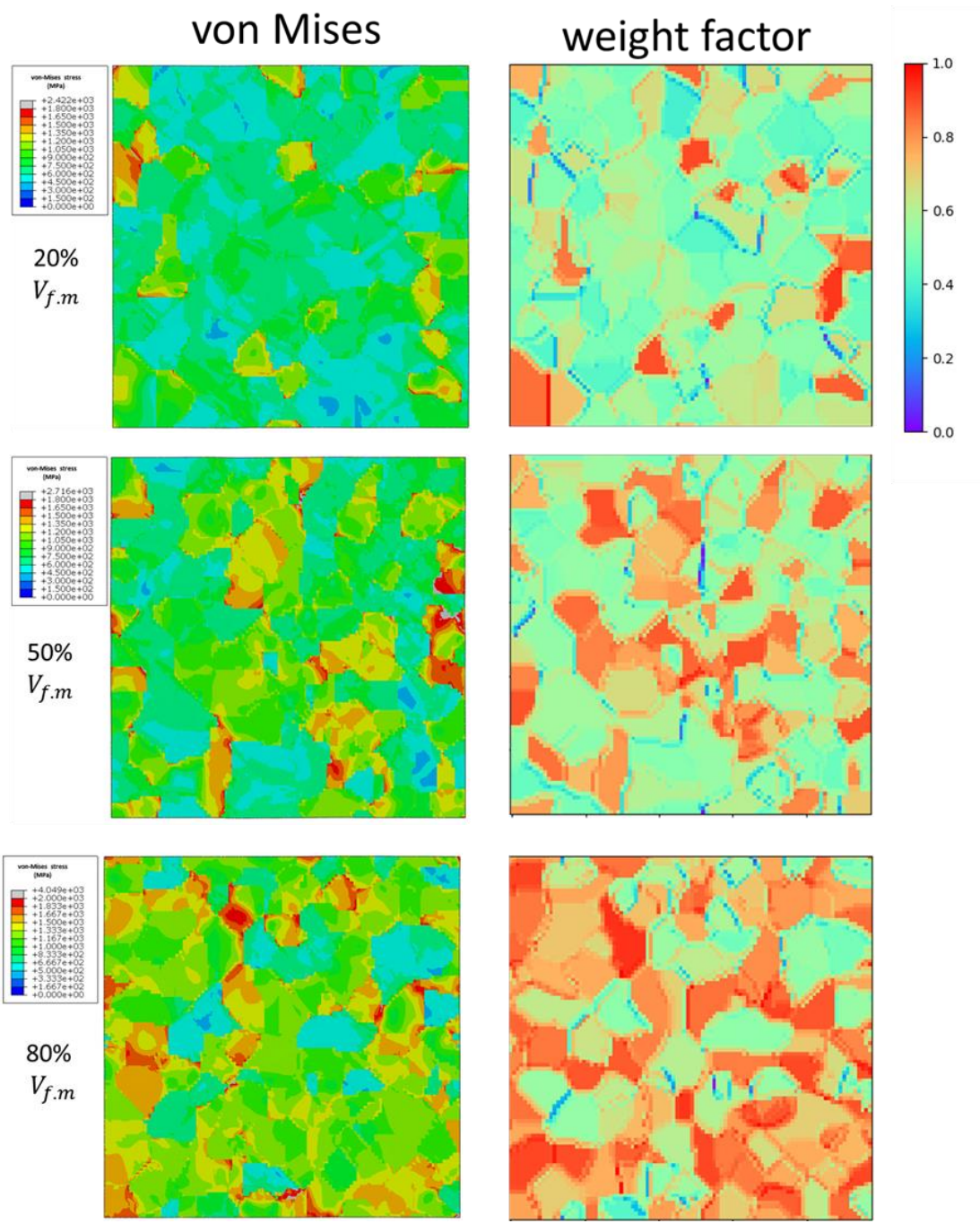

Fig. 7-15. CPFE Effect of martensite phase fraction on CPFE-predicted von Mises stress distribution (left) and corresponding weight factors for CNN layer (right).

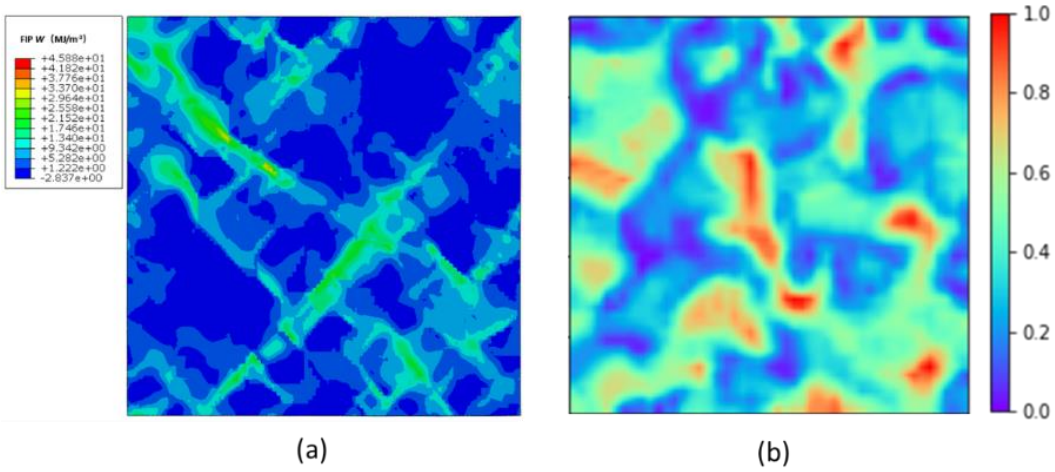

Fig. 7-16. A comparison of the predicted FIP W contour plot from (a) CPFE modelling and (b) CNN layer weight factor.

7.3.3 DNN structure-property prediction on customized multiphase steels.

The developed DNN tool was adopted for predicting the YS values out of the newly generated 400 models with 35% and 65% martensite fractions, respectively. CPFE modelling result with the same phase fraction was only adopted for validating the DNN predictions. Figure 7-17 shows a randomly selected example from the 200 models and compares the predicted stress localization contour plots. Together with the previous 1000 models for DNN training and validation, Figure 7-18 shows the DNN predicted structure-property relationship curve defined by YS and phase fraction including 7 phases totally. The averaged YS values from the two selected CPFE models in Figure 7-17 were plotted (in black diamonds) to validate the two new phase DNN predictions. A third order polynomial equation was implemented here to quantify the trend relationship as $YS = f(V_{f,m})$, which shows a similar trend compared to the hardness testing data for similar materials in the literature [394].

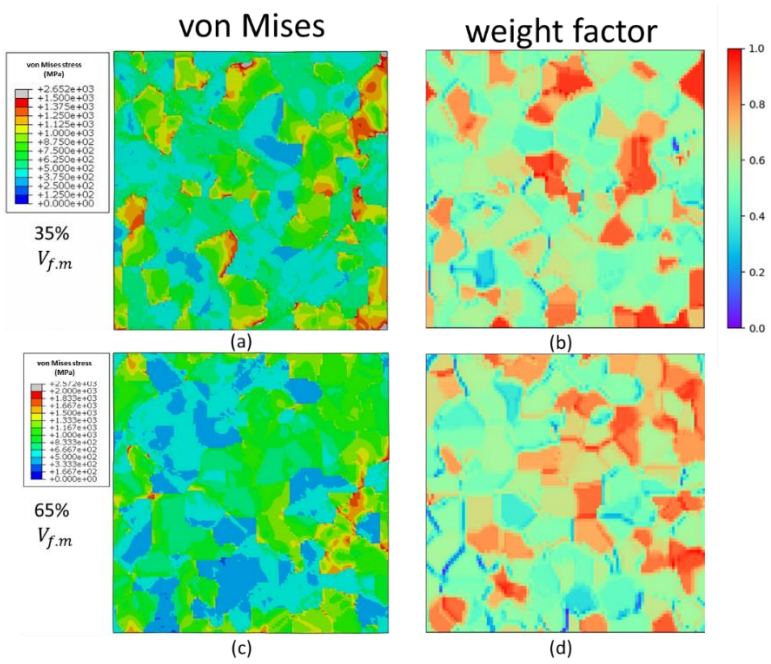

Fig. 7-17. CPFE and DNN predicted contour plot comparison. 35% martensite phase fraction model: (a) CPFE predicted von-Mises stress distribution and (b) CNN layer weight factor predicted from DNN model. 65% martensite phase fraction model: (c) CPFE predicted von-Mises stress and (d) DNN model weight factor.

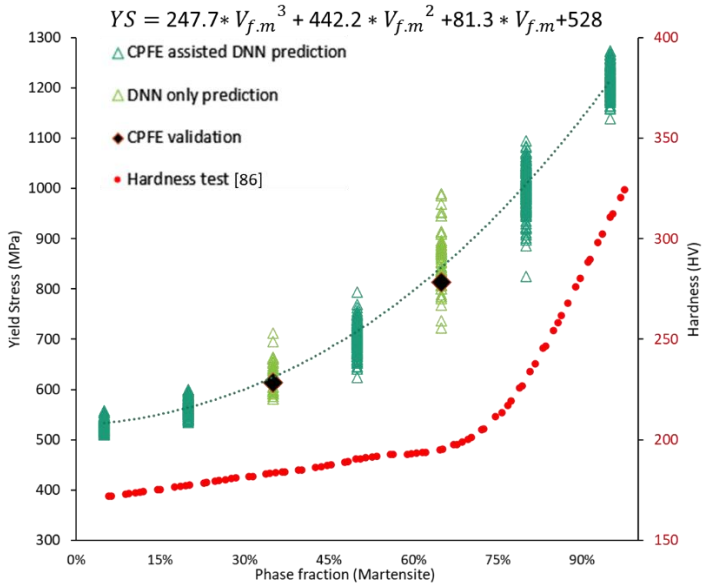

Fig. 7-18. DNN predicted relationship between martensite phase fraction and yield strength, and comparison with measured effect on hardness.

7.3.4 DNN structure-property prediction on a realistic EBSD scan.

Figure 7-19 (a) shows the EBSD data and images containing phase and orientation information as the DNN input. The realistic EBSD image has 321,602 pixels, equal to the number of nodes required in the converted CPFE-E model. The reconstructed EBSD map with 24,406 grains is meshed with C3D8 hexagonal voxels as shown in Figure 7-19 (b). One key benefit of the DNN model is again the much higher computational efficiency. It takes 45 minutes for the customized code to generate the necessary CPFE-E input file. It takes 13 hours to finish the real image-based CPFE-E modelling due to the model size and higher resolution. Yet it only takes 1.27 seconds for the trained DNN tool to output the stress prediction and most of that time is consumed with data transfer.

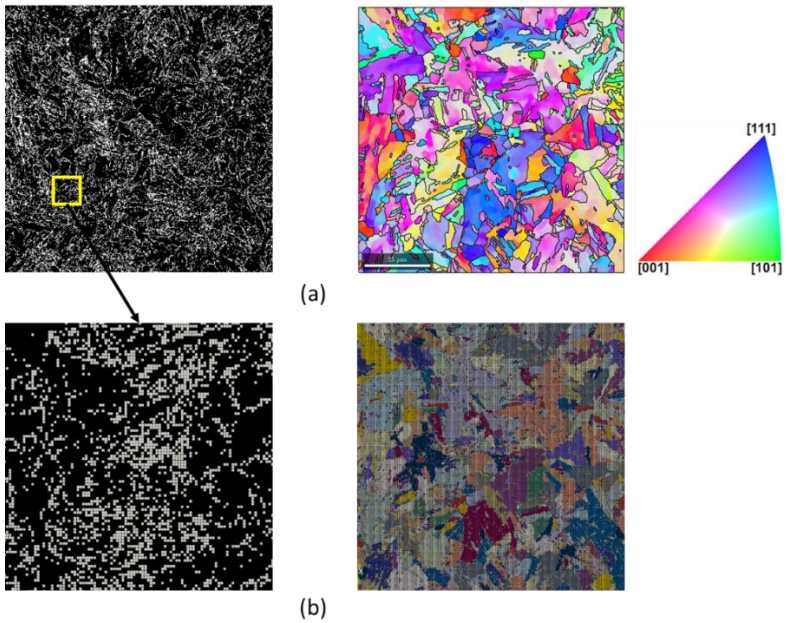

Fig 7-19. (a) EBSD map data inputs in DNN tool with 321602 pixels: grey scale phase composition and IPF coloured crystallographic orientation imaging information. (b) Direct EBSD converted CPFE-E model with 24406 grains using C3D8 hexagonal mesh.

Figure 7-20 shows the stress-strain curve comparison between CPFE-E, DNN prediction and the experiment test. The YS prediction from CPFE-E and DNN are 1049 MPa and 1095 MPa respectively, compared to the experimentally obtained 1087 MPa. The DNN predicted stress-strain behaviour after yield is slightly closer to the experimental test in this case. In this case, the higher predicted stress from CPFE-E might be due to the small size of some austenite grains and could be solved using a higher resolution.

However, this solution further increases the computational cost. In this real image-based study, while both CPFE-E and DNN models successfully predict stress-strain curves, the developed DNN model has shown higher efficiency and accuracy when predicting mechanical properties, albeit with a non-smooth computational stress-strain curve.

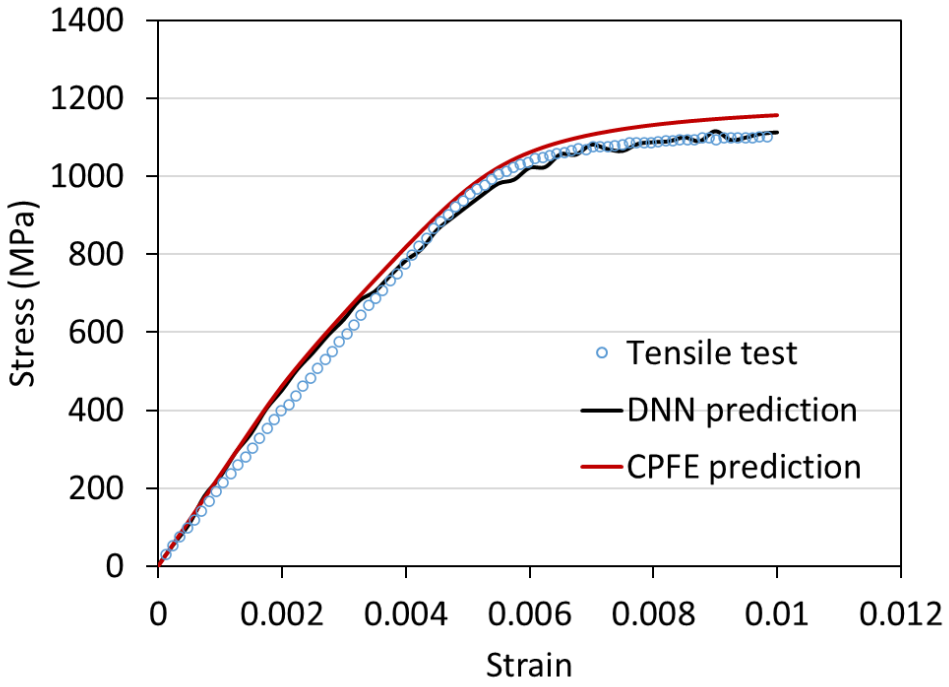

Fig. 7-20. A comparison of the bulk stress-strain relationship between EBSD image-based DNN model, CPFE-E model and the experimental test.

7.4 Discussion

This study has presented a CPFE trained DNN tool with the ability to predict mechanical response based on microstructural images. In CPFE, the phase and orientation data determine the individual grain properties in microscale finite element based modelling of grain deformation and interaction under a given loading condition. Within the DNN tool (trained from prior CPFE analyses), microstructural detail such as phase and orientation is regarded as a combination of pixels with different weight factors for the prediction. Every pixel in the image contributes to the prediction depending on this weight factor, and together they determine the mechanical response metrics. The predicted

contour plots and heat maps are shown in Figure 7-15 and Figure 7-17 to demonstrate this principle. Both CPFE contour plots represent the localised mechanical response while the hottest region in the DNN heatmap represents the pixels with the most significant influence (high weight factor) on the DNN predicted mechanical property. From these contours, the DNN successfully captures the stress localization at similar hot spots to the CPFE results. The difficulty lies around the grain boundary when DNN knows to assign different weight factors on the grain boundary curves but fails to always find the correct trends. Precise grain boundary modelling is also a challenge for CPFE modelling. The consistent fit between stress distribution maps explains the satisfying prediction of stress-strain behaviour and yield strength. Moreover, it can be deduced that the integrated CPFE-DNN tool developed in this study has the potential to predict hysteresis loops by extending current CPFE tensile models to fatigue, without the need to change the DNN model architecture.

When it comes to FIP prediction, see Figure 7-21, the MSE curve fails to converge, even with sufficient training iterations (200 epochs), using the same optimized DNN model. Figure 7-16 visually shows how the DNN model fails to identify the dominant grains for FIP W contribution (per the CPFE result). FIP is an extremely localized value for predicting strong mechanical behaviour such as crack initiation. Thus, fewer clues exist in the training data for the DNN which causes reduced predictive accuracy. This is in contrast to Figure 7-15, where most pixels in the structural input image appropriately contribute to a weight factor when determining bulk stress-strain behaviour as well as the stress localization distribution, resulting in a good stress-strain predictive accuracy.

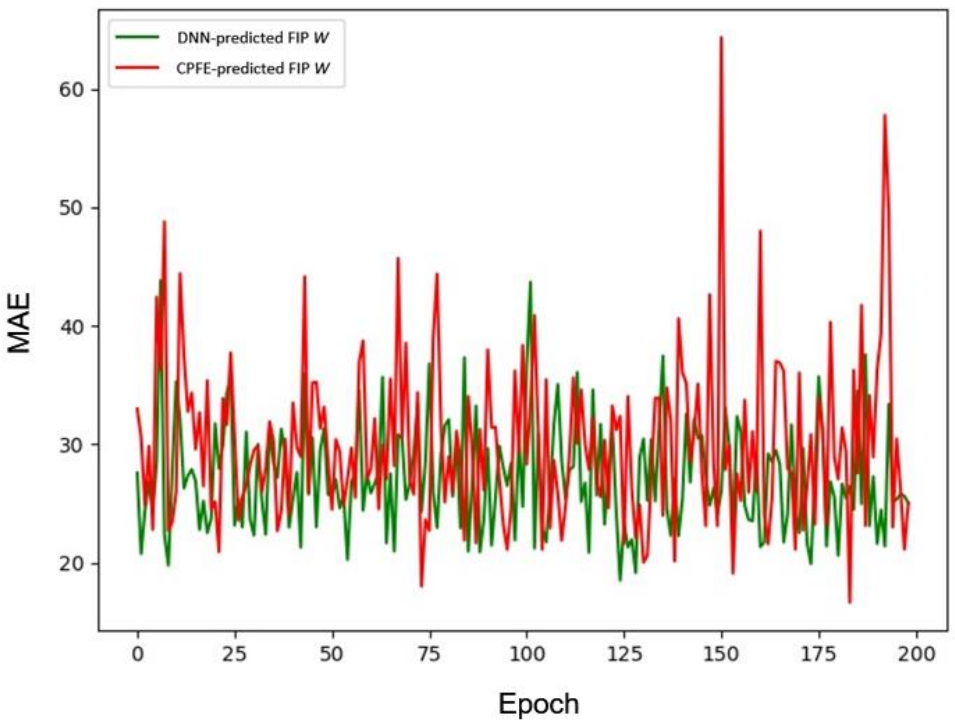

Fig. 7-21. MAE convergence curve for W FIP prediction during DNN training.

DNN architecture optimization has a significant effect on the predicting accuracy in this work. Despite the different settings of the standard and Siamese DNN, they are quite similar in layers and depth. However, the latter achieved lower MSE and regression residual as shown in Figures 7-11 and 7-12, which indicate a better capacity in prediction. The reasons for the results can be concluded as follows. (1) The Siamese DNN separate the microstructure inputs Phase and IPF data into two separate pipelines, which enables the model to capture their individual characteristics in different ways without interference. (2) The two different characteristics are merged in the last 3 layers, which guarantees that the model can also capture the common points between Phase and IPF data during the BP algorithm. (3) The Siamese DNN has more parameters compared to the standard type, providing better capability in fitting and predicting the more complex CPFE data.

Another key finding in this work is that the developed DNN model has the ability to predict the structure-property relationships for a real image within seconds, providing a rapid non-destructive testing solution once integrated with a high speed in-situ cameras

providing live microstructure imaging of a solidified layer. This potential application offers a step towards an instant / real-time determination of mechanical performance based on live process quality control data, for instance, the next generation of PBF machines could give a live read-out of the strength of the layer which has just solidified. It is noted that such in-process microstructural imaging captures as-solidified microstructure and so future code surrogates could be expanded to include microstructural evolution predictive steps to account for changes that may occur during cooling or subsequent post-built heat-treatment.

The two results introduced in sections 7.3.3 and 7.3.4 broaden the practical applications of the developed DNN tool. If the DNN model is designed for the purpose of predicting gradient or flexible phase composition, the phase fraction in training data can be specified to be continuous within the desired range, rather than the discrete values, to further improve the predicting accuracy. After sufficient training steps, the developed DNN model successfully recognizes the phase regions and the associated unique crystallographic orientation variations. It also captures the differences in macroscopic stress response due to the varying microstructures. Such DNN model exhibits as high accuracy compared to CPFE on structure-property relationship prediction while reducing the computational cost to seconds. The developed DNN model and its training procedure offer a new perspective for structure-property modelling. The developed DNN model has the ability to predict the structure-property relationships for a real image within milliseconds, providing a rapid non-destructive tensile testing solution once integrated with a high speed in-situ cameras providing live microstructure imaging of a solidified layer.

This potential application offers a step towards an instant / real-time determination of tensile mechanical performance based on live process quality control data, for instance, the next generation of PBF machines could give a live read-out of the tensile strength of the layer which has just solidified. It is noted that such in-process microstructural imaging captures as-solidified microstructure and so future code surrogates could be expanded to include microstructural evolution predictive steps to account for changes that may occur during cooling or subsequent post-built heat-treatment. In addition, this DNN tool could

be expanded to include PBF process-structure modelling capability [59, 395], to give a complete process-structure-property instant predictive capability based on selected process parameters and CAD layer/slice data. Further uptake of the developed CPFE-DNN method could be via a non-destructive inspection tool which gives quick and accurate reports on void and microstructural defect characterisation, to accompany the existing microscopy techniques [396, 397].

7.5 Conclusions

The Deep Learning model presented here demonstrates one future option for an instant non-destructive property predicting tool, trained by crystal plasticity finite element analysis of the microstructure-property relationship and experimental testing. The near-instant strength prediction performance makes it feasible to implement this DL model as a surrogate tool of CPFE and other computationally expensive models, to give a rapid prediction of additive manufacturing part performance within a process-monitoring quality control tool. The dual-phase crystal plasticity and DNN models have been developed for relating microstructural features and mechanical response including stress-strain and fatigue indicator parameter behaviour. The CPFE study was scripted and automated for big data generation and an optimized DNN model was implemented with the automated CPFE for data-driven model training. The key conclusions for this research are:

1. It is viable to develop and train a CPFE-DNN model to successfully predict the stress-strain curve and yield strength to within $\pm$15% error.
2. The DNN model, while predicting the structure-property relationship as a viable alternative tool for CPFE, enables significant computational cost savings (once trained). (The DNN takes 12 milliseconds for VT generated 100-grain predictions and 1.27 seconds for real EBSD image converted 24406-grain predictions compared to 25 mins and 13 hours, respectively, when using full CPFE modelling.)
3. A data driven DNN model requires a large number of CPFE predicted samples for training, with 75:25 training: validation ratio recommended. For dual-phase

materials, phase fraction and crystallographic texture are sufficient inputs to provide reliable yield stress for the AM steels.

4. The design of the DNN hidden layers architecture is important in machine learning parameter optimization. In this case, the prediction accuracy increases from 65% to 91% after improving the sequence DNN to multi-pipeline non-sequence architecture.
5. It is necessary to run multiple models of the same phase fraction for FIP characterisation to account for possible over-prediction of the maximum FIP values.
6. The DNN model, trained on VT-CPFE data, can identify the main contributing grains to the stress distribution profile, and can accurately predict the tensile stress-strain curve but is less accurate in predicting FIP localization results.
7. The trained DNN model can be applied to multiple ranges of phase fraction steels, including phase fractions not used in the training data. Most importantly, it is capable of predicting the mechanical response from real EBSD images, despite being trained only on VT models. This is a key step towards a tool for in-situ microstructure-property prediction in real-time.

8 Conclusion and Future Work

8.1 Conclusions

The main outputs of this thesis include the development of (i) 3D microstructural sensitive crystal plasticity finite element (CPFE) computational models to characterize the structure-property relationship; (ii) Integrated multi-physics phase-field method (PFM) and CPFE to establish dynamic and evolving structure-property modelling framework; and (iii) A deep learning (DL) model developed on multiple state-of-the-art computational methods. The thesis' multi-physics and interdisciplinary modelling work, with the associated experimental characterisation, complete a micromechanics-based investigation on the structure-property relationship for additive manufactured, particularly powder bed fusion (PBF) manufactured metals. The significant achievements of this thesis include:

- The development and implementation of high-fidelity and real image-based PFM and CPFE models for CoCr, Ti-6Al-4V, and 17-4PH stainless steel alloys. The models are calibrated and validated via experimental characterisation for the micromechanics-based investigation.
- A series of bridging tools were developed to fulfil a seamless data connection between computational mechanical modelling, material science and characterisation, deep learning. With these tools, data formats can be flexibly and easily converted between microscopy scans, finite element models, and convolutional neural network, to fulfil an interdisciplinary research capability. These tools are available open source at https://github.com/I-Form/Deep-learning---Crystal-plasticity-.
- Developing the coupled CPFE-PFM and CPFE-DL modelling frameworks for an efficient and reliable computational assessment system for the micromechanics characterisation of AM products and heat treatment processes. The core codes for these frameworks are available at the above link.

The main outputs of the above achievement are summarized as follows.

8.1.1 Microstructure sensitive CPFE models

Research of a variety of microstructural sensitive features, ranging from grain sizes, grain morphology, phase fraction, and crystallographic orientations, has been carried out to study and quantify the structure-property relationship for PBF metals. The single-phase CoCr alloy with equiaxed grain morphology and randomly orientated grain texture is studied with a phenomenological constitutive law as a straightforward starting point. Through this CoCr study, detailed methods for EBSD raw data proceeding and grain reconstruction, generating equiaxed Voronoi tessellation (VT), and converting EBSD images to high-fidelity CPFE models, have been developed. The methodologies have been applied to investigate micromechanics of low-cycle fatigue of CoCr alloy. The comparison between VT- and EBSD-based CPFE models has observed an improvement of up to 10% in fatigue life prediction from direct EBSD-CPFE modelling. Another contribution of this work is determining the converged definitive representative volume element (RVE) model size for the VT and EBSD types of CPFE model. The study indicates a preferable minimum grain number of 120 and 100 meshes in each grain, and a ratio of 14.5 between scan image size and grain size to avoid undesired prediction scatter, sometimes referred to as the statistical grain size effect. The proposed methodology, as well as the convergence study, offer important predicates for the subsequent studies of more complex PBF-LB alloys.

The VT model is then extended to a more advanced dual-phase lamellar lath RVE with statistically equivalent crystallographic texture and lath width validated against EBSD measurement. Meanwhile, a physically-based strain gradient constitutive law is incorporated to study the Ti-6Al-4V alloy with three different slip systems in the hexagonal crystal lattice alpha phase. The developed GND-induced length-scale model, reached close agreement with the experimental tensile test and predicted the impact on mechanical response difference caused by microstructural inhomogeneity along the built height, and the microstructural evolution due to post-built heat treatments. Models varying in lath width and phase fraction were generated respectively, to represent the microstructure observed in the bottom and top area of as-built samples, as well as the homogenous sample after heat treatment. The CPFE model predicts a minor decrease of

0.9% in yield stress of the top area compared to the bottom area in the same specimen, while a bigger drop in yield stress of 9% was predicted in a heat-treated specimen. The changes in the predicated tensile strength correspond with the experimental measurements. The benefit of using VT models in this work is the possibility of performing trial sensitivity analyses of individual microstructural features via a strain gradient CPFE model. The effects of lath width and grain size, and grain morphology on both GND density distribution and the macroscopic stress-strain behaviour are analysed and quantified. GND-induced size sensitive model has shown prominent sensitivity for the material with lath width less than 2 μm. The lath width has shown the greatest influence among these variables on the tensile behaviour, thus the predicted relationship is fitted using Hall-Petch equations, dislocation-based grain size equations, and a grain boundary strengthening equation, to further develop a relationship of PBF-LB titanium lath width and its macroscopic yield strength.

Although deep learning (DL) implementation is the primary focus of Chapter 7, the accurate prediction of SS 17-4 steel from dual-phase VT-CPFE model data is also a significant achievement. The CPFE model, while giving tensile stress-strain curve and the localized stress distribution contour, also provides accurate fatigue crack initiation life prediction for the testing strains ranging from ± 0.4 to ± 1.0 with the tested fatigue life varying from 129 to 11271 cycles. The crystallographic orientations and grain boundary misorientation information are also involved in the 1000 VT realizations within each phase set, and the resulting different mechanical responses have been captured by both CPFE and DL models.

8.1.2 Coupled PFM-CPFE modelling framework

A PFM model is developed based on the Allen-Cahn and Ginzburg-Landau theories, to predict the lath growth during annealing heat treatment (HT) process of PBF-LB Ti-6Al-4V. Then, the PFM evolved microstructure is imported into CPFE as a coupling PFM-CPFE model for HT-structure-property relationship characterisation. This work builds on the two previous thesis outputs: (i) EBSD direct conversion methodology and model convergence criteria determined in Chapter 4; and (ii) lath width sensitive strain gradient model developed in Chapter 5.

The PFM model successfully predict the lath growth during HT process, with the averaged lath area increasing from 0.59 to 3.01 μm^2 after annealing at 1127 K for 100 minutes. This result is validated against the EBSD measurement where the lath size is quantified through an ellipse fitting program, indicating the averaged lath area growing from 0.56 to 3.03 μm^2.. Both PFM-HT and EBSD-HT CPFE models successfully capture the decrease in tensile strength after HT, due to the martensite softening and lath size increase.

8.1.3 Interdisciplinary application of Deep learning (DL) and CPFE.

An instant material structure-property prediction tool for a metal additive manufacturing process based on a DL model is trained and validated with over 1,400 complex and computationally expensive CPFE simulations of microstructural deformation. The trained DL model reaches close agreement (85% accuracy on yield stress prediction) compared to the crystal plasticity modelling results. The deep learning model is capable of predicting a whole stress-strain curve and stress localization distribution. Besides, the trained code surrogate can predict mechanical response within milliseconds, making it feasible to be implemented as an industry powder bed fusion process quality control tool.

The two results introduced in sections 7.3.3 and 7.3.4 have broadened the practical applications of the developed deep neural network (DNN) tool. DNN successfully predicts the structure-property relationship of two new customized phase fraction dual phase steels, even though the DNN model was not specifically trained on that phase fraction or data (EBSD) type. This indicates strong potential for such tools to read in geometrically gradient microstructure images, e.g., growing martensite fraction along the built direction and predict the changing property from layer to layer.

Furthermore, this model could be reversed to assist microstructure design (determining required microstructural features) for the desired strength response or use in decision making on the powder mixture ratio for a desired functional gradient material product.

The CPFE-DNN method presented can also be easily extended to multiple-phase materials with other chemical compositions.

8.2 Future work recommendation.

The final objective of this thesis was to develop an effective and reliable process-structure-property predictive tool for additive manufacturing process. This thesis has achieved specific outcomes in this regarding a microstructural sensitive CPFE model for stress-strain curve and fatigue crack initiation prediction, as well as a solid-state grain growth phase-field method for AM heat treatment effect. Future work in this area could focus on the following aspects:

8.2.1 3D high-fidelity modelling

The EBSD-CPFE models in this thesis are all defined as Quasi-3D models where the single slice EBSD scan is extended to one-element thickness along the out-of-plane direction. This Quasi-3D RVE approach has been previously adopted by a number of authors, such as O'Dowd and co-workers [146, 191], Dunne and co-workers [29, 136], Shollock and co-workers [137, 398] etc. However, the grain size measured from 2D EBSD image assumption has potential errors since not all grains in the 2D slice are sectioned through their exact middle section. This issue could be solved using 3D EBSD data which combines a set of 2D slices to provide more reliable grain size distribution information.

It is also anticipated that the higher fidelity 3D EBSD-CPFE provides a more accurate prediction on the localized behaviour such as fatigue performance because it offers more grain boundary information along the z axis direction. The EBSD-based methodology discussed in Chapter 4 could be extended to 3D by suitably combining a sequence of EBSD scan slices [399]. The tool developed in this thesis has confirmed the capability of switching and converting the multiple EBSD scans into a 3D EBSD-CPFE model. Figure 8-1 shows the constructed IN-100 alloy from 117 scan layers where each slice size is of 189 x 201 pixels (supplied by DARPA AIM program). Such an approach can also be easily adapted for constructing 3D realistic PFM models.

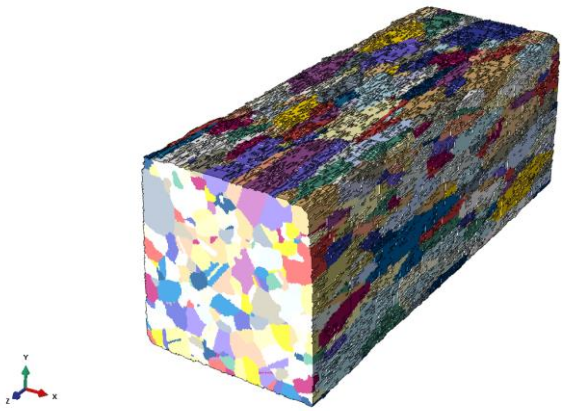

Figure 8-1. The schematic of a reconstructed high-fidelity 3D EBSD-CPFE model using developed converting tool on 117-layers IN-100 nickel alloy scans.

One existing challenge is the difficulty when preparing multiple sample slices required for 3D EBSD reconstruction [400, 401]. The requirements of file size and model reconstructing executions have been solved with a cloud-based infrastructure solution [402], for anisotropic additive manufactured materials. Another solution is using 3D X-ray tomography microscopy instead, which provides grain structure without the need of cutting the sample. The remaining problem is the heavy CPFE and PFM computational cost.

8.2.2 Full physically-based CPFE model development.

The commonly-adopted method for calibrating the constitutive parameters of CPFE and PFM are still based on trial and error, which could be time consuming and sometimes unreliable. A previous study [403] and Chapter 5 in this thesis have applied MATLAB toolbox to perform an automatic non-linear fitting. This program is also used to calibrate lath effect equation constants and fatigue indicate parameter calculation in Chapter 7. However, this fitting method still requires multiple CPFE runs to optimize the suitable parameter set and thus is not feasible for modelling with heavy computational cost, such as the EBSD-CPFE and EBSD-PFM works.

One solution is the direct measurement from micro-scale experiments, such as microhardness tests to obtain the elastic modulus [76, 404]. Some parameters like critical

resolved shear stress (CRSS) of different slip system, grain boundary width and mobility in PFM are difficult to obtain from experimental work. Another possible solution is through first-principal calculation. For example, the calculation of stacking fault energy during plastic deformation has been utilised for calculating CRSS in different slipping modes [405, 406]. It is reasonable to anticipate this method can also be used for calculating the CRSS of basal, pyramidal, and prismatic slip systems in Ti6Al4V alpha phase, and even the twining slip system [219, 407] induced from PBF solidification or large deformation.

8.2.3 Inhomogeneous behaviour of PBF-LB built direction

Although an anisotropic texture case study is carried out on CoCr EBSD map, the experimental fatigue tests on PBF-LB samples are still incomplete. It would be worthwhile constructing EBSD-CPFE models for samples varying in printing direction and study this directional effect on the predicted stress-strain curve, GND distribution, and fatigue indicator parameters. Another limitation of the CPFE and PFM models in this thesis is that crystallographic orientation of each grain is constant and does not evolve during the deformation and heat treatment. This assumption is acceptable when all the strain ranges studied in this thesis are small, and heat treatment is unlikely to largely alter the texture. However, it is anticipated that adding texture evolution will improve the accuracy of representing neighbouring grain boundary angles.

Gradient grain size VT model has been successfully constructed (shown in Figure 8-2) but unfortunately, there is a mismatch in size between the gradient in a whole specimen and the gradient achievable within a single CPFE model (usually in hundreds to thousands of microns). The model developed in this thesis could be further employed and validated once more microscopy data is available.

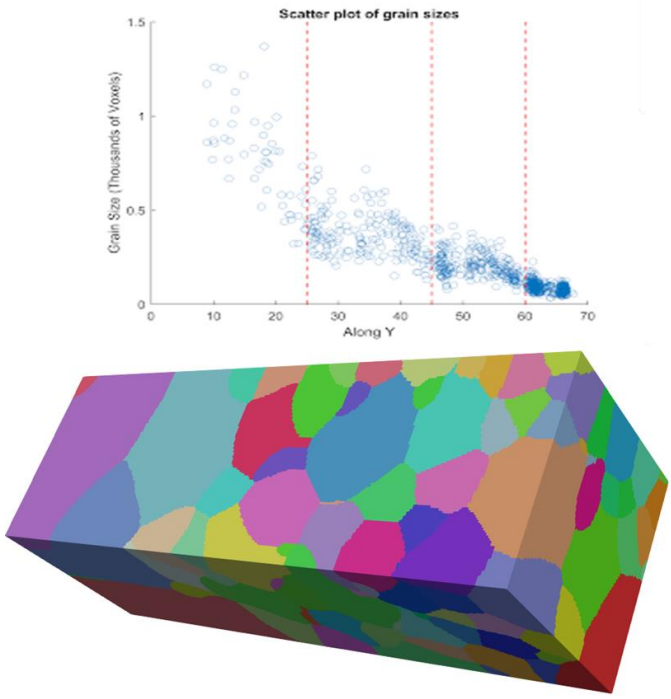

Figure 8-2. Gradient grain size VT model with a decreasing grain size along y axis.

8.2.4 Damaged crystal plasticity model

The CPFE models introduced in thesis are all non-damaged models. However, it is known that strength-ductility trade-off is one significant feature for additive manufactured metals, which is also captured in Chapter 6 tensile tests. A damaged model helps characterizing this trade-off especially when comparing AM products with its conventionally fabricated counterparts. The damaged model is also helpful when studying the crack propagation behaviour, as well as the effect of defects such as voids and surface roughness, which leads to a significant decrease in ductility and fatigue life.

8.2.5 Expansion of load case scenarios

The mechanical test and the corresponding CPFE modelling in this thesis include static axial tensile test and fully reversed low cyclic fatigue test. There are still very few CPFE results for torque or fretting fatigue, and microhardness (nanoindentation) loading

condition simulations. The author so far has not found existed literature on CPFE modelling of Charpy impact toughness behaviour of AM metals.

8.2.6 Microstructural evolution including phase transition

The highest HT temperature encountered in this thesis is 1127 K, and minor phase change after cooling is observed for Ti-6Al-4V alloy. The PFM model in this work is simplified as a solid-state grain growth model considering the relatively low volume fraction changes (approximately 5%) of the beta phase detected during heat treatment. However, when the temperature is high, or for titanium alloys with fewer alpha phase stabilizer elements, the phase transformation and solidification behaviour cannot be ignored. To assist experimental validation of such phase transition behaviour, a parent phase reconstruction code (to reveal prior beta grain before PBF solidification in Ti-6Al-4V), has been developed according to the neighbouring orientation relationship when alpha laths segregate from the prior beta boundaries. The EBSD scan used in Chapter 6 is 30 μm in length and thus only captures two prior-beta grains along the built direction. The parent phase reconstruction method can assist the validation process once a bigger EBSD scan and a phase transition PFM (example shown in figure 8-3a) are available. The dynamic structure-property predicting ability is also possible through other modelling approaches at a similar scale such as coupled cellular automata and CPFE (shown in figure 8-3b). Further integration of AM process modelling which provides thermal history and temperature cycles will help establish a more complete process-structure-property interdependency framework.

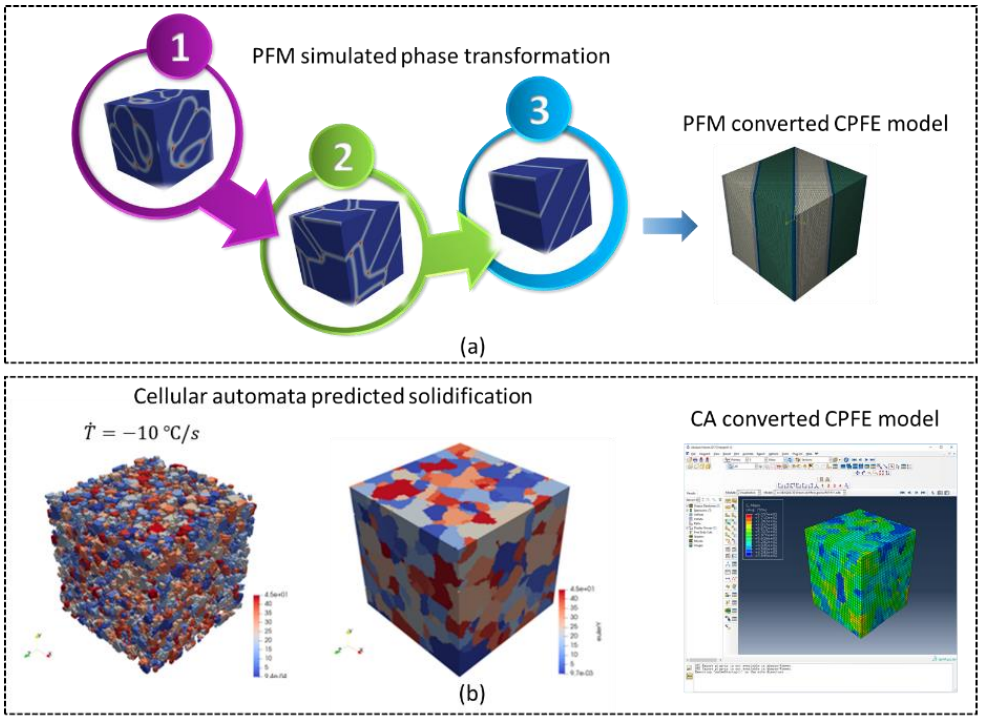

Figure 8-3. (a) An example of PFM simulation of austenite-martensite transformation. (b) Cellular automata predicted single crystal material solidification and grain nucleation.

8.2.7 Machine learning capability investigation

The DL surogate developed in this thesis not as accurate for fatigue life prediction, as it was for stress-strain perdiction. This limitation has been attributed to too few clues indicating fatigue life from the input images. Based on this reason, an improvement could be made by providing more information from both the input microstructure and CPFE predicted fatigue indicator parameter distributions. The fatigue cracking, while being a localized behaviour, is also sensitive to discontinuities in the microstructure. Thus, the suggested improvement includes adding another microstructure image showing the misorientation angles along the grain boundary curves with colours. The CPFE output could give the location of the maximum energy dissipation, as well as the value itself.

Further uptake of the developed CPFE-DL method could be via a non-destructive inspection tool which gives quick and accurate reports on void and microstructural defect characterisation, to accompany the existing microscopy techniques [396, 397]. The

potential and further application of EBSD-DL approach could offer a step towards an instant / real-time determination of mechanical performance based on live process quality control data, for instance, the next generation of PBF machines could give a live read-out of the strength of the layer which has just solidified. It is noted that such in-process microstructural imaging captures as-solidified microstructure and so future code surrogates could be expanded to include microstructural evolution predictive steps to account for changes that may occur during cooling or subsequent post-built heat-treatment.

8.2.8 User-friendly interface development

Customized codes have been written to assist model construction and running, as well as the post-processing and visualization. These codes contain: (i) EBSD analysis and direct EBSD-CPFE conversion, CPFE element aggregates inverse pole figure colouring and 3D periodic boundary condition assignment codes in Chapter 4; (ii) 3D dual-phase sub-tessellation, tessellation grain texture analysis, and parameter non-linear fitting program implemented in Chapter 5; (iii) PFM predicted morphology importing tool and CPFE grain boundary highlighting tool in Chapter 6; and (iv) automatic batch CPFE generation-running-postprocessing workflow command and DNN optimization codes in Chapter 7. The codes mentioned here were developed in python, MATLAB, and C++, and sometimes call each other to fulfil the multiple functions. Converting these codes to a user-friendly interface could help simplify the operation and encourage adoption by the industry. Early implementation of a GUI is avaiable here:

https://github.com/I-Form/PERCEPT_Microscopy-Stress-Tool
https://github.com/littlelazy6/PERCEPT_Microscopy-Stress-Tool

8.3 Summary Reflection

In summary, the work presented in this thesis has advanced the speed (Chapter 7), accuracy (Chapter 5) and fidelity (Chapter 4) of computational microstructural modelling

for metal additive manufacturing (Chapters 5 &7) and post-built heat treatment (Chapter 6) for a range of common PBF alloys. Real image based modelling is more sensitive to heterogeneous behaviour, such as fatigue crack, and localized behaviour around the grain boundary. This approach is helpful in PBF-LB inhomogeneity study and grain boundary evolution research. However VT-based is sufficient to represent macroscopic behaviour. On the other hand, RVE has the benefit of representing microstructures that have not been manufactured, to assist material optimization with custom-designed structure-property [123]. This thesis studies three different alloys, CoCr, Ti-6Al-4V and 17-4PH SS. Not only because they are widely used in PBF industries, they also cover complete slip system definitions (crystallographic lattice types), thus the models are universal and can be easily extended to other alloys without major modifications.

9 References

[1] A. 8, BS EN ISO/ASTM 52900:2017 - Additive manufacturing. General principles, Terminology, 2021.
[2] D. Gu, Laser additive manufacturing of high-performance materials, Springer2015.
[3] N.N. Kumbhar, A.V. Mulay, Post Processing Methods used to Improve Surface Finish of Products which are Manufactured by Additive Manufacturing Technologies: A Review, Journal of The Institution of Engineers (India): Series C 99(4) (2018) 481-487.
[4] M. Qian, W. Xu, M. Brandt, H.P. Tang, Additive manufacturing and postprocessing of Ti-6Al-4V for superior mechanical properties, MRS Bulletin 41(10) (2016) 775-784.
[5] M.-A. de Pastre, Y. Quinsat, C. Lartigue, Effects of additive manufacturing processes on part defects and properties: a classification review, International Journal on Interactive Design and Manufacturing (IJIDeM) (2022).
[6] B. Mueller, Additive manufacturing technologies–Rapid prototyping to direct digital manufacturing, Assembly Automation (2012).
[7] L. Löber, S. Biamino, U. Ackelid, S. Sabbadini, P. Epicoco, P. Fino, J. Eckert, Comparison off selective laser and electron beam melted titanium aluminides, 2011 International Solid Freeform Fabrication Symposium, University of Texas at Austin, 2011.
[8] W. Zhang, Process modelling and experimental validation of residual stress in metal additive manufacturing, NUI Galway, 2021.
[9] V. Bhavar, P. Kattire, V. Patil, S. Khot, K. Gujar, R. Singh, A review on powder bed fusion technology of metal additive manufacturing, Additive manufacturing handbook (2017) 251-253.
[10] D. Herzog, V. Seyda, E. Wycisk, C. Emmelmann, Additive manufacturing of metals, Acta Materialia 117 (2016) 371-392.
[11] L. Bian, N. Shamsaei, J. Usher, Laser-Based Additive Manufacturing of Metal Parts: Modeling, Optimization, and Control of Mechanical Properties, CRC Press2017.
[12] L. Gherman, A. Gleadall, O. Bakker, S. Ratchev, Manufacturing technology: micro-machining, Micro-manufacturing technologies and their applications, Springer2017, pp. 97-127.
[13] N. Harrison, J.R. Field, F. Quondamatteo, W. Curtin, P.E. McHugh, P. Mc Donnell, Preclinical trial of a novel surface architecture for improved primary fixation of cementless orthopaedic implants, Clinical Biomechanics 29(8) (2014) 861-868.
[14] N. Harrison, P.E. McHugh, W. Curtin, P. Mc Donnell, Micromotion and friction evaluation of a novel surface architecture for improved primary fixation of cementless orthopaedic implants, Journal of the Mechanical Behavior of Biomedical Materials 21 (2013) 37-46.
[15] D.S. Thomas, S.W. Gilbert, Costs and cost effectiveness of additive manufacturing, NIST special publication 1176 (2014) 12.
[16] I. Kelbassa, T. Wohlers, T. Caffrey, Quo vadis, laser additive manufacturing?, Journal of Laser Applications 24(5) (2012) 050101.
[17] J.C. Najmon, S. Raeisi, A. Tovar, 2 - Review of additive manufacturing technologies and applications in the aerospace industry, in: F. Froes, R. Boyer (Eds.), Additive Manufacturing for the Aerospace Industry, Elsevier2019, pp. 7-31.

[18] L.J. Kumar, C. Krishnadas Nair, Current trends of additive manufacturing in the aerospace industry, Advances in 3D printing & additive manufacturing technologies, Springer2017, pp. 39-54.
[19] D.I. Wimpenny, P.M. Pandey, L.J. Kumar, Advances in 3D printing & additive manufacturing technologies, Springer2017.
[20] M. Neikter, Microstructure and Texture of Additive Manufactured Ti-6Al-4V, 2017.
[21] G. Nolze, Fundamentals and applications of EBSD, 2015.
[22] R. Quey, L. Renversade, Optimal polyhedral description of 3D polycrystals: Method and application to statistical and synchrotron X-ray diffraction data, Computer Methods in Applied Mechanics and Engineering 330 (2018) 308-333.
[23] F. Roters, P. Eisenlohr, T.R. Bieler, D. Raabe, Crystal plasticity finite element methods: in materials science and engineering, John Wiley & Sons2011.
[24] L.-Q. Chen, Phase-field models for microstructure evolution, Annual review of materials research 32(1) (2002) 113-140.
[25] P. Bajaj, A. Hariharan, A. Kini, P. Kürnsteiner, D. Raabe, E.A. Jägle, Steels in additive manufacturing: A review of their microstructure and properties, Materials Science and Engineering: A 772 (2020) 138633.
[26] J.D. Eshelby, The determination of the elastic field of an ellipsoidal inclusion, and related problems, Proceedings of the royal society of London. Series A. Mathematical and physical sciences 241(1226) (1957) 376-396.
[27] J. Qu, M. Cherkaoui, Fundamentals of micromechanics of solids, Wiley Hoboken2006.
[28] P.J. Ashton, T.-S. Jun, Z. Zhang, T.B. Britton, A.M. Harte, S.B. Leen, F.P.E. Dunne, The effect of the beta phase on the micromechanical response of dual-phase titanium alloys, International Journal of Fatigue 100(P1) (2017) 377-387.
[29] F.P.E. DUNNE, D. RUGG, On the mechanisms of fatigue facet nucleation in titanium alloys, Fatigue & Fracture of Engineering Materials & Structures 31(11) (2008) 949-958.
[30] F.-. BEA, Accident to the AIRBUS A380-861 registered F-HPJE and operated by Air France on 30/09/2017 en route over Greenland [Investigation delegated to BEA by the authorities of Denmark], En croisière, 2017.
[31] F.P.E. Dunne, D. Rugg, A. Walker, Lengthscale-dependent, elastically anisotropic, physically-based hcp crystal plasticity: Application to cold-dwell fatigue in Ti alloys, International Journal of Plasticity 23(6) (2007) 1061-1083.
[32] T. DebRoy, H.L. Wei, J.S. Zuback, T. Mukherjee, J.W. Elmer, J.O. Milewski, A.M. Beese, A. Wilson-Heid, A. De, W. Zhang, Additive manufacturing of metallic components – Process, structure and properties, Progress in Materials Science 92 (2018) 112-224.
[33] J. Pelleg, Additive and Traditionally Manufactured Components: A Comparative Analysis of Mechanical Properties, Additive Manufacturing Materia2020.
[34] C. Leyens, M. Peters, W. John, Sons, I. Wiley, Titanium and titanium alloys : fundamentals and applications, Wiley-VCH ; [John Wiley] [distributor], Weinheim; [Chichester], 2003.
[35] M. Shunmugavel, A. Polishetty, G. Littlefair, Microstructure and Mechanical Properties of Wrought and Additive Manufactured Ti-6Al-4V Cylindrical Bars, Procedia Technology 20 (2015) 231-236.
[36] J.H. Rao, N. Stanford, A survey of fatigue properties from wrought and additively manufactured Ti-6Al-4V, Materials Letters 283 (2021) 128800.

[37] Y. Sun, R.J. Hebert, M. Aindow, Effect of heat treatments on microstructural evolution of additively manufactured and wrought 17-4PH stainless steel, Materials & Design 156 (2018) 429-440.
[38] F. Khodabakhshi, M.H. Farshidianfar, A.P. Gerlich, M. Nosko, V. Trembošová, A. Khajepour, Effects of laser additive manufacturing on microstructure and crystallographic texture of austenitic and martensitic stainless steels, Additive Manufacturing 31 (2020) 100915.
[39] D.J. Jensen, Y. Zhang, Impact of 3D/4D methods on the understanding of recrystallization, Current Opinion in Solid State and Materials Science 24(2) (2020) 100821.
[40] M. Mani, S. Feng, B. Lane, A. Donmez, S. Moylan, R. Fesperman, Measurement science needs for real-time control of additive manufacturing powder bed fusion processes, (2015).
[41] M. Mani, B.M. Lane, M.A. Donmez, S.C. Feng, S.P. Moylan, A review on measurement science needs for real-time control of additive manufacturing metal powder bed fusion processes, International Journal of Production Research 55(5) (2017) 1400-1418.
[42] D. Gu, 7 - New metallic materials development by laser additive manufacturing, in: J. Lawrence, D.G. Waugh (Eds.), Laser Surface Engineering, Woodhead Publishing2015, pp. 163-180.
[43] C. Tang, K.Q. Le, C.H. Wong, Physics of Humping Formation in Laser Powder Bed Fusion, International Journal of Heat and Mass Transfer 149 (2020).
[44] D. Grossin, A. Montón, P. Navarrete-Segado, E. Özmen, G. Urruth, F. Maury, D. Maury, C. Frances, M. Tourbin, P. Lenormand, G. Bertrand, A review of additive manufacturing of ceramics by powder bed selective laser processing (sintering / melting): Calcium phosphate, silicon carbide, zirconia, alumina, and their composites, Open Ceramics 5 (2021) 100073.
[45] L.E. Criales, Y.M. Arısoy, B. Lane, S. Moylan, A. Donmez, T. Özel, Laser powder bed fusion of nickel alloy 625: Experimental investigations of effects of process parameters on melt pool size and shape with spatter analysis, International Journal of Machine Tools and Manufacture 121 (2017) 22-36.
[46] A. Keshavarzkermani, E. Marzbanrad, R. Esmaeilizadeh, Y. Mahmoodkhani, U. Ali, P.D. Enrique, N.Y. Zhou, A. Bonakdar, E. Toyserkani, An investigation into the effect of process parameters on melt pool geometry, cell spacing, and grain refinement during laser powder bed fusion, Optics & Laser Technology 116 (2019) 83-91.
[47] H. Gong, K. Rafi, H. Gu, T. Starr, B. Stucker, Analysis of defect generation in Ti–6Al–4V parts made using powder bed fusion additive manufacturing processes, Additive Manufacturing 1 (2014) 87-98.
[48] Y.H. Zhou, W.P. Li, L. Zhang, S.Y. Zhou, X. Jia, D.W. Wang, M. Yan, Selective laser melting of Ti–22Al–25Nb intermetallic: Significant effects of hatch distance on microstructural features and mechanical properties, Journal of Materials Processing Technology 276 (2020) 116398.
[49] Q. Luo, L. Yin, T.W. Simpson, A.M. Beese, Effect of processing parameters on pore structures, grain features, and mechanical properties in Ti-6Al-4V by laser powder bed fusion, Additive Manufacturing 56 (2022) 102915.

[50] Ó. Teixeira, F.J.G. Silva, L.P. Ferreira, E. Atzeni, A Review of Heat Treatments on Improving the Quality and Residual Stresses of the Ti–6Al–4V Parts Produced by Additive Manufacturing, Metals 10(8) (2020).
[51] X. Wang, K. Chou, The effects of stress relieving heat treatment on the microstructure and residual stress of Inconel 718 fabricated by laser metal powder bed fusion additive manufacturing process, Journal of Manufacturing Processes 48 (2019) 154-163.
[52] E. Edin, F. Svahn, P. Åkerfeldt, M. Eriksson, M.-L. Antti, Rapid method for comparative studies on stress relief heat treatment of additively manufactured 316L, Materials Science and Engineering: A (2022) 143313.
[53] H. Li, M. Wang, D. Lou, W. Xia, X. Fang, Microstructural features of biomedical cobalt–chromium–molybdenum (CoCrMo) alloy from powder bed fusion to aging heat treatment, Journal of Materials Science & Technology 45 (2020) 146-156.
[54] J. Benzing, N. Hrabe, T. Quinn, R. White, R. Rentz, M. Ahlfors, Hot isostatic pressing (HIP) to achieve isotropic microstructure and retain as-built strength in an additive manufacturing titanium alloy (Ti-6Al-4V), Materials Letters 257 (2019) 126690.
[55] V. Chastand, P. Quaegebeur, W. Maia, E. Charkaluk, Comparative study of fatigue properties of Ti-6Al-4V specimens built by electron beam melting (EBM) and selective laser melting (SLM), Materials Characterization 143 (2018) 76-81.
[56] S. Cheruvathur, E.A. Lass, C.E. Campbell, Additive Manufacturing of 17-4 PH Stainless Steel: Post-processing Heat Treatment to Achieve Uniform Reproducible Microstructure, JOM 68(3) (2016) 930-942.
[57] X. Yu, L. Wang, T6 heat-treated AlSi10Mg alloys additive-manufactured by selective laser melting, Procedia Manufacturing 15 (2018) 1701-1707.
[58] R. Wauthle, B. Vrancken, B. Beynaerts, K. Jorissen, J. Schrooten, J.-P. Kruth, J. Van Humbeeck, Effects of build orientation and heat treatment on the microstructure and mechanical properties of selective laser melted Ti6Al4V lattice structures, Additive Manufacturing 5 (2015) 77-84.
[59] X. Yang, R.A. Barrett, M. Tong, N.M. Harrison, S.B. Leen, Towards a process-structure model for Ti-6Al-4V during additive manufacturing, Journal of Manufacturing Processes 61 (2021) 428-439.
[60] C. Li, Z.Y. Liu, X.Y. Fang, Y.B. Guo, Residual Stress in Metal Additive Manufacturing, Procedia CIRP 71 (2018) 348-353.
[61] P. Rangaswamy, M. Griffith, M. Prime, T. Holden, R. Rogge, J. Edwards, R. Sebring, Residual stresses in LENS® components using neutron diffraction and contour method, Materials Science and Engineering: A 399(1-2) (2005) 72-83.
[62] S. Götelid, T. Ma, C. Lyphout, J. Vang, E. Stålnacke, J. Holmberg, S. Hosseini, A. Strondl, Effect of post-processing on microstructure and mechanical properties of Alloy 718 fabricated using powder bed fusion additive manufacturing processes, Rapid Prototyping Journal (2021).
[63] E. Eschner, T. Staudt, M. Schmidt, Correlation of spatter behavior and process zone formation in powder bed fusion of metals, CIRP Annals 69(1) (2020) 209-212.
[64] A. Sola, A. Nouri, Microstructural porosity in additive manufacturing: The formation and detection of pores in metal parts fabricated by powder bed fusion, Journal of Advanced Manufacturing and Processing 1(3) (2019) e10021.
[65] C. Chen, Y. Xie, X. Yan, S. Yin, H. Fukanuma, R. Huang, R. Zhao, J. Wang, Z. Ren, M. Liu, H. Liao, Effect of hot isostatic pressing (HIP) on microstructure and mechanical

properties of Ti6Al4V alloy fabricated by cold spray additive manufacturing, Additive Manufacturing 27 (2019) 595-605.
[66] A. du Plessis, E. Macdonald, Hot isostatic pressing in metal additive manufacturing: X-ray tomography reveals details of pore closure, Additive Manufacturing 34 (2020) 101191.
[67] J. Li, X. Zhou, M. Brochu, N. Provatas, Y.F. Zhao, Solidification microstructure simulation of Ti-6Al-4V in metal additive manufacturing: A review, Additive Manufacturing 31 (2020) 100989.
[68] L.E. Murr, Metallurgy of additive manufacturing: Examples from electron beam melting, Additive Manufacturing 5 (2015) 40-53.
[69] Y.-Y. Zhu, H.-B. Tang, Z. Li, C. Xu, B. He, Solidification behavior and grain morphology of laser additive manufacturing titanium alloys, Journal of Alloys and Compounds 777 (2019) 712-716.
[70] R. Padrós, M. Punset, M. Molmeneu, A.B. Velasco, M. Herrero-Climent, E. Rupérez, F.J. Gil, Mechanical properties of cocr dental-prosthesis restorations made by three manufacturing processes. influence of the microstructure and topography, Metals 10(6) (2020) 788.
[71] J. Chen, Y. Yang, S. Wu, M. Zhang, S. Mai, C. Song, D. Wang, Selective laser melting dental CoCr alloy: microstructure, mechanical properties and corrosion resistance, Rapid Prototyping Journal (2021).
[72] M.V. Mergulhão, C.E. Podestá, M.D.M. das Neves, Mechanical properties and microstructural characterization of cobalt-chromium (CoCr) obtained by casting and selective laser melting (SLM), Materials Science Forum, Trans Tech Publ, 2017, pp. 534-539.
[73] M. Neikter, P. Åkerfeldt, R. Pederson, M.-L. Antti, Microstructure characterisation of Ti-6Al-4V from different additive manufacturing processes, IOP conference series: materials science and engineering, IOP Publishing, 2017, p. 012007.
[74] N. Guennouni, A. Barroux, C. Grosjean, D. Maisonnette, E. Nivet, E. Andrieu, D. Poquillon, L. Laffont, C. Blanc, Comparative study of the microstructure between a laser beam melted 17-4PH stainless steel and its conventional counterpart, Materials Science and Engineering: A 823 (2021) 141718.
[75] J.-C. Yoon, M.-G. Lee, C.-Y. Choi, D.-H. Kim, M.-S. Jeong, Y.-J. Choi, D.-H. Kim, Evaluation of microstructure and mechanical properties in 17-4PH stainless steels fabricated by PBF and DED processes, Journal of the Korean Society of Manufacturing Process Engineers 17(2) (2018) 83-88.
[76] Y. Geng, É. McCarthy, D. Brabazon, N. Harrison, Ti6Al4V functionally graded material via high power and high speed laser surface modification, Surface and Coatings Technology 398 (2020) 126085.
[77] T.a.C. Voisin, N and Khairallah, S and Forien, JB and Balogh, L and Cunningham, R and Rollett, AD and Wang, Y, Ti-6Al-4V by Selective Laser Melting: How Microstructure and Porosity Influence the Mechanical Properties, Lawrence Livermore National Lab.(LLNL), Livermore, CA (United States), 2018.
[78] S.M.J. Razavi, F. Berto, Directed Energy Deposition versus Wrought Ti-6Al-4V: A Comparison of Microstructure, Fatigue Behavior, and Notch Sensitivity, Advanced Engineering Materials 21(8) (2019) 1900220.

[79] L. Carneiro, B. Jalalahmadi, A. Ashtekar, Y. Jiang, Cyclic deformation and fatigue behavior of additively manufactured 17–4 PH stainless steel, International Journal of Fatigue 123 (2019) 22-30.
[80] X. Zhang, B. Mao, L. Mushongera, J. Kundin, Y. Liao, Laser powder bed fusion of titanium aluminides: An investigation on site-specific microstructure evolution mechanism, Materials & Design 201 (2021) 109501.
[81] M.S. Moyle, N. Haghdadi, X.Z. Liao, S.P. Ringer, S. Primig, On the microstructure and texture evolution in 17-4 PH stainless steel during laser powder bed fusion: Towards textural design, Journal of Materials Science & Technology 117 (2022) 183-195.
[82] N. Gey, M. Humbert, The calculation of a parent grain orientation from inherited variants for approximate (b.c.c.– h.c.p.) orientation relations, Journal of Applied Crystallography 35(4) (2002) 401-405.
[83] R. Acharya, J.A. Sharon, A. Staroselsky, Prediction of microstructure in laser powder bed fusion process, Acta Materialia 124 (2017) 360-371.
[84] K.S. Cruz, E.S. Meza, F.A.P. Fernandes, J.M.V. Quaresma, L.C. Casteletti, A. Garcia, Dendritic Arm Spacing Affecting Mechanical Properties and Wear Behavior of Al-Sn and Al-Si Alloys Directionally Solidified under Unsteady-State Conditions, Metallurgical and Materials Transactions A 41(4) (2010) 972-984.
[85] S. Louhenkilpi, Chapter 1.8 - Continuous Casting of Steel, in: S. Seetharaman (Ed.), Treatise on Process Metallurgy, Elsevier, Boston, 2014, pp. 373-434.
[86] H.L. Wei, J. Mazumder, T. DebRoy, Evolution of solidification texture during additive manufacturing, Scientific Reports 5 (2015).
[87] W. Chen, T. Voisin, Y. Zhang, J.-B. Florien, C.M. Spadaccini, D.L. McDowell, T. Zhu, Y.M. Wang, Microscale residual stresses in additively manufactured stainless steel, Nature Communications 10(1) (2019) 4338.
[88] T. Niendorf, S. Leuders, A. Riemer, H.A. Richard, T. Tröster, D. Schwarze, Highly anisotropic steel processed by selective laser melting, Metallurgical and materials transactions B 44(4) (2013) 794-796.
[89] M. Simonelli, Y.Y. Tse, C. Tuck, On the Texture Formation of Selective Laser Melted Ti-6Al-4V, Metallurgical and Materials Transactions A 45(6) (2014) 2863-2872.
[90] V.A. Popovich, E.V. Borisov, A.A. Popovich, V.S. Sufiiarov, D.V. Masaylo, L. Alzina, Impact of heat treatment on mechanical behaviour of Inconel 718 processed with tailored microstructure by selective laser melting, Materials & Design 131 (2017) 12-22.
[91] C. Balagna, S. Spriano, M. Faga, Characterization of Co–Cr–Mo alloys after a thermal treatment for high wear resistance, Materials Science and Engineering: C 32(7) (2012) 1868-1877.
[92] F.R. Kaschel, R.K. Vijayaraghavan, A. Shmeliov, E.K. McCarthy, M. Canavan, P.J. McNally, D.P. Dowling, V. Nicolosi, M. Celikin, Mechanism of stress relaxation and phase transformation in additively manufactured Ti-6Al-4V via in situ high temperature XRD and TEM analyses, Acta Materialia 188 (2020) 720-732.
[93] U. Ali, R. Esmaeilizadeh, F. Ahmed, D. Sarker, W. Muhammad, A. Keshavarzkermani, Y. Mahmoodkhani, E. Marzbanrad, E. Toyserkani, Identification and characterization of spatter particles and their effect on surface roughness, density and mechanical response of 17-4 PH stainless steel laser powder-bed fusion parts, Materials Science and Engineering: A 756 (2019) 98-107.

[94] R. Molaei, A. Fatemi, N. Phan, Multiaxial fatigue of LB-PBF additive manufactured 17–4 PH stainless steel including the effects of surface roughness and HIP treatment and comparisons with the wrought alloy, International Journal of Fatigue 137 (2020) 105646.
[95] N. Sanaei, A. Fatemi, Analysis of the effect of surface roughness on fatigue performance of powder bed fusion additive manufactured metals, Theoretical and Applied Fracture Mechanics 108 (2020) 102638.
[96] G. Strano, L. Hao, R.M. Everson, K.E. Evans, Surface roughness analysis, modelling and prediction in selective laser melting, Journal of Materials Processing Technology 213(4) (2013) 589-597.
[97] J.S. Weaver, J. Whiting, V. Tondare, C. Beauchamp, M. Peltz, J. Tarr, T.Q. Phan, M.A. Donmez, The effects of particle size distribution on the rheological properties of the powder and the mechanical properties of additively manufactured 17-4 PH stainless steel, Additive Manufacturing 39 (2021) 101851.
[98] Y. Sun, S. Gulizia, C. Oh, D. Fraser, M. Leary, Y. Yang, M. Qian, The influence of as-built surface conditions on mechanical properties of Ti-6Al-4V additively manufactured by selective electron beam melting, Jom 68(3) (2016) 791-798.
[99] H.K. Rafi, D. Pal, N. Patil, T.L. Starr, B.E. Stucker, Microstructure and Mechanical Behavior of 17-4 Precipitation Hardenable Steel Processed by Selective Laser Melting, Journal of Materials Engineering and Performance 23(12) (2014) 4421-4428.
[100] S. Liu, Y.C. Shin, Additive manufacturing of Ti6Al4V alloy: A review, Materials & Design 164 (2019) 107552.
[101] X.D. Nong, X.L. Zhou, J.H. Li, Y.D. Wang, Y.F. Zhao, M. Brochu, Selective laser melting and heat treatment of precipitation hardening stainless steel with a refined microstructure and excellent mechanical properties, Scripta Materialia 178 (2020) 7-12.
[102] Z. Zhu, F.L. Ng, H.L. Seet, S.M.L. Nai, Tailoring the microstructure and mechanical property of laser powder bed fusion fabricated Ti–6Al–2Sn–4Zr–2Mo via heat treatment, Journal of Alloys and Compounds 895 (2022) 162648.
[103] M. Braun, E. Mayer, I. Kryukov, C. Wolf, S. Böhm, A. Taghipour, R.E. Wu, S. Ehlers, S. Sheikhi, Fatigue strength of PBF‐LB/M and wrought 316L stainless steel: effect of post‐treatment and cyclic mean stress, Fatigue & Fracture of Engineering Materials & Structures 44(11) (2021) 3077-3093.
[104] T. Vilaro, C. Colin, J.D. Bartout, As-Fabricated and Heat-Treated Microstructures of the Ti-6Al-4V Alloy Processed by Selective Laser Melting, Metallurgical and Materials Transactions A 42(10) (2011) 3190-3199.
[105] D.B. Witkin, D.N. Patel, H. Helvajian, L. Steffeney, A. Diaz, Surface treatment of powder-bed fusion additive manufactured metals for improved fatigue life, Journal of Materials Engineering and Performance 28(2) (2019) 681-692.
[106] D. Agius, K.I. Kourousis, C. Wallbrink, T. Song, Cyclic plasticity and microstructure of as-built SLM Ti-6Al-4V: The effect of build orientation, Materials Science and Engineering: A 701 (2017) 85-100.
[107] Z.W. Xu, A. Liu, X.S. Wang, The influence of building direction on the fatigue crack propagation behavior of Ti6Al4V alloy produced by selective laser melting, Materials Science and Engineering: A 767 (2019) 138409.
[108] G. Nicoletto, Anisotropic high cycle fatigue behavior of Ti–6Al–4V obtained by powder bed laser fusion, International Journal of Fatigue 94 (2017) 255-262.

[109] S. Sasaoka, J. Arakawa, H. Akebono, A. Sugeta, Y. Shirai, E. Nakayama, Y. Kimura, The effects of crystallographic orientation on fatigue crack initiation behavior in Ti-6Al-4V, International Journal of Fatigue 117 (2018) 371-383.
[110] F. Briffod, A. Bleuset, T. Shiraiwa, M. Enoki, Effect of crystallographic orientation and geometrical compatibility on fatigue crack initiation and propagation in rolled Ti-6Al-4V alloy, Acta Materialia 177 (2019) 56-67.
[111] J. Maierhofer, R. Pippan, H.-P. Gänser, Modified NASGRO equation for physically short cracks, International Journal of fatigue 59 (2014) 200-207.
[112] M. Grasso, B.M. Colosimo, Process defects and in situ monitoring methods in metal powder bed fusion: a review, Measurement Science and Technology 28(4) (2017) 044005.
[113] A.G. Demir, B. Previtali, Investigation of remelting and preheating in SLM of 18Ni300 maraging steel as corrective and preventive measures for porosity reduction, The International Journal of Advanced Manufacturing Technology 93(5) (2017) 2697-2709.
[114] C. Barrett, E. MacDonald, B. Conner, F. Persi, Micron-level layer-wise surface profilometry to detect porosity defects in powder bed fusion of Inconel 718, Jom 70(9) (2018) 1844-1852.
[115] M. Seifi, M. Gorelik, J. Waller, N. Hrabe, N. Shamsaei, S. Daniewicz, J.J. Lewandowski, Progress towards metal additive manufacturing standardization to support qualification and certification, Jom 69(3) (2017) 439-455.
[116] P. Singh, R. M.Singari, R.S. Mishra, A review of study on modeling and simulation of additive manufacturing processes, Materials Today: Proceedings 56 (2022) 3594-3603.
[117] V.E. Küng, R. Scherr, M. Markl, C. Körner, Multi-material model for the simulation of powder bed fusion additive manufacturing, Computational Materials Science 194 (2021) 110415.
[118] B. Cheng, L. Loeber, H. Willeck, U. Hartel, C. Tuffile, Computational investigation of melt pool process dynamics and pore formation in laser powder bed fusion, Journal of Materials Engineering and Performance 28(11) (2019) 6565-6578.
[119] D. Tourret, H. Liu, J. Llorca, Phase-field modeling of microstructure evolution: Recent applications, perspectives and challenges, Progress in Materials Science 123 (2022) 100810.
[120] W. Zhang, M. Tong, N.M. Harrison, Resolution, energy and time dependency on layer scaling in finite element modelling of laser beam powder bed fusion additive manufacturing, Additive Manufacturing 28 (2019) 610-620.
[121] B. Radhakrishnan, S. Gorti, S.S. Babu, Phase Field Simulations of Autocatalytic Formation of Alpha Lamellar Colonies in Ti-6Al-4V, Metallurgical and Materials Transactions A 47(12) (2016) 6577-6592.
[122] F.-J. Gallardo-Basile, Y. Naunheim, F. Roters, M. Diehl, Lath Martensite Microstructure Modeling: A High-Resolution Crystal Plasticity Simulation Study, Materials 14(3) (2021) 691.
[123] S. Bargmann, B. Klusemann, J. Markmann, J.E. Schnabel, K. Schneider, C. Soyarslan, J. Wilmers, Generation of 3D representative volume elements for heterogeneous materials: A review, Progress in Materials Science 96 (2018) 322-384.
[124] I.M. Gitman, H. Askes, L.J. Sluys, Representative volume: Existence and size determination, Engineering Fracture Mechanics 74(16) (2007) 2518-2534.
[125] F. Han, F. Roters, D. Raabe, Microstructure-based multiscale modeling of large strain plastic deformation by coupling a full-field crystal plasticity-spectral solver with an implicit finite element solver, International Journal of Plasticity (2019).

[126] S.E. Perdahcıoğlu, C. Soyarslan, E.E. Aşık, T. Van den Boogaard, S. Bargmann, A Class of Rate-Independent Lower-Order Gradient Plasticity Theories: Implementation and Application to Disc Torsion Problem, Materials 11(8) (2018).
[127] P. Efthymiadis, C. Pinna, J.R. Yates, Fatigue crack initiation in AA2024: A coupled micromechanical testing and crystal plasticity study, Fatigue & Fracture of Engineering Materials & Structures 0(0) (2018).
[128] H. Abdolvand, J.P. Wright, A.J. Wilkinson, On the state of deformation in a polycrystalline material in three-dimension: Elastic strains, lattice rotations, and deformation mechanisms, International Journal of Plasticity 106 (2018) 145-163.
[129] E.A. Bonifaz, J. Baus, A. Czekanski, Finite element modelling of dual-phase polycrystalline Nickel-base alloys, Mechanics of Materials 98 (2016) 134-141.
[130] T.J. Barrett, D.J. Savage, M. Ardeljan, M. Knezevic, An automated procedure for geometry creation and finite element mesh generation: Application to explicit grain structure models and machining distortion, Computational Materials Science 141 (2018) 269-281.
[131] H.K. Park, J. Jung, H.S. Kim, Three-dimensional microstructure modeling of particulate composites using statistical synthetic structure and its thermo-mechanical finite element analysis, Computational Materials Science 126 (2017) 265-271.
[132] O. Diard, S. Leclercq, G. Rousselier, G. Cailletaud, Distribution of normal stress at grain boundaries in multicrystals: application to an intergranular damage modeling, Computational Materials Science 25(1) (2002) 73-84.
[133] M. Jahedi, M. Ardeljan, I.J. Beyerlein, M.H. Paydar, M. Knezevic, Enhancement of orientation gradients during simple shear deformation by application of simple compression, Journal of Applied Physics 117(21) (2015) 214309.
[134] R. Bandyopadhyay, V. Prithivirajan, M.D. Sangid, Uncertainty Quantification in the Mechanical Response of Crystal Plasticity Simulations, JOM 71(8) (2019) 2612-2624.
[135] X. Tu, A. Shahba, J. Shen, S. Ghosh, Microstructure and property based statistically equivalent RVEs for polycrystalline-polyphase aluminum alloys, International Journal of Plasticity (2018).
[136] D. Wilson, W. Wan, F.P.E. Dunne, Microstructurally-sensitive fatigue crack growth in HCP, BCC and FCC polycrystals, Journal of the Mechanics and Physics of Solids 126 (2019) 204-225.
[137] F. Farukh, L.G. Zhao, R. Jiang, P. Reed, D. Proprentner, B.A. Shollock, Realistic microstructure-based modelling of cyclic deformation and crack growth using crystal plasticity, Computational Materials Science 111 (2016) 395-405.
[138] D.L. McDowell, F.P.E. Dunne, Microstructure-sensitive computational modeling of fatigue crack formation, International Journal of Fatigue 32(9) (2010) 1521-1542.
[139] A. Rovinelli, H. Proudhon, R.A. Lebensohn, M.D. Sangid, Assessing the reliability of fast Fourier transform-based crystal plasticity simulations of a polycrystalline material near a crack tip, International Journal of Solids and Structures (2019).
[140] H. Proudhon, J. Li, P. Reischig, N. Guéninchault, S. Forest, W. Ludwig, Coupling Diffraction Contrast Tomography with the Finite Element Method Advanced Engineering Materials 18(6) (2016) 903-912.
[141] D.-F. Li, R.A. Barrett, P.E. O'Donoghue, N.P. O'Dowd, S.B. Leen, A multi-scale crystal plasticity model for cyclic plasticity and low-cycle fatigue in a precipitate-strengthened steel at elevated temperature, Journal of the Mechanics and Physics of Solids 101 (2017) 44-62.

[142] D.-F. Li, B.J. Golden, N.P. O'Dowd, Multiscale modelling of mechanical response in a martensitic steel: A micromechanical and length-scale-dependent framework for precipitate hardening, Acta Materialia 80 (2014) 445-456.
[143] C.A. Bronkhorst, J.R. Mayeur, V. Livescu, R. Pokharel, D.W. Brown, G.T. Gray, Structural representation of additively manufactured 316L austenitic stainless steel, International Journal of Plasticity 118 (2019) 70-86.
[144] K. Kapoor, Y.S.J. Yoo, T.A. Book, J.P. Kacher, M.D. Sangid, Incorporating grain-level residual stresses and validating a crystal plasticity model of a two-phase Ti-6Al-4 V alloy produced via additive manufacturing, Journal of the Mechanics and Physics of Solids 121 (2018) 447-462.
[145] K. Kapoor, R. Noraas, V. Seetharaman, M.D. Sangid, Modeling Strain Localization in Microtextured Regions in a Titanium Alloy: Ti–6Al–4V, Integrating Materials and Manufacturing Innovation (2019).
[146] D.-F. Li, R.A. Barrett, P.E. O'Donoghue, C.J. Hyde, N.P. O'Dowd, S.B. Leen, Micromechanical finite element modelling of thermo-mechanical fatigue for P91 steels, International Journal of Fatigue 87 (2016) 192-202.
[147] Y. Li, V. Aubin, C. Rey, P. Bompard, Microstructural modeling of fatigue crack initiation in austenitic steel 304L, Procedia Engineering 31(C) (2012) 541-549.
[148] J. Schwartz, O. Fandeur, C. Rey, Fatigue crack initiation modeling of 316LN steel based on non local plasticity theory, Procedia Engineering 2(1) (2010) 1353-1362.
[149] Z. Zhang, D. Lunt, H. Abdolvand, A.J. Wilkinson, M. Preuss, F.P.E. Dunne, Quantitative investigation of micro slip and localization in polycrystalline materials under uniaxial tension, International Journal of Plasticity 108 (2018) 88-106.
[150] R. Hielscher, C.B. Silbermann, E. Schmidl, J. Ihlemann, Denoising of crystal orientation maps, Journal of Applied Crystallography 52(5) (2019) 984-996.
[151] C. Panwisawas, C. Qiu, M.J. Anderson, Y. Sovani, R.P. Turner, M.M. Attallah, J.W. Brooks, H.C. Basoalto, Mesoscale modelling of selective laser melting: Thermal fluid dynamics and microstructural evolution, Computational Materials Science 126 (2017) 479-490.
[152] W. Zhang, M. Tong, N.M. Harrison, Scanning strategies effect on temperature, residual stress and deformation by multi-laser beam powder bed fusion manufacturing, Additive Manufacturing 36 (2020).
[153] N.P. Karapatis, J.P.S. Van Griethuysen, R. Glardon, Direct rapid tooling: A review of current research, Rapid Prototyping Journal 4(2) (1998) 77-89.
[154] Y. Zhang, X. Xiao, J. Zhang, Kinetic Monte Carlo simulation of sintering behavior of additively manufactured stainless steel powder particles using reconstructed microstructures from synchrotron X-ray microtomography, Results in Physics 13 (2019) 102336.
[155] T.M. Rodgers, J.D. Madison, V. Tikare, Simulation of metal additive manufacturing microstructures using kinetic Monte Carlo, Computational Materials Science 135 (2017) 78-89.
[156] C.A. Gandin, M. Rappaz, A coupled finite element-cellular automaton model for the prediction of dendritic grain structures in solidification processes, Acta Metallurgica et Materialia 42(7) (1994) 2233-2246.
[157] Y. Zhang, J. Zhang, Modeling of solidification microstructure evolution in laser powder bed fusion fabricated 316L stainless steel using combined computational fluid dynamics and cellular automata, Additive Manufacturing 28 (2019) 750-765.

[158] J.A. Koepf, M.R. Gotterbarm, M. Markl, C. Körner, 3D multi-layer grain structure simulation of powder bed fusion additive manufacturing, Acta Materialia 152 (2018) 119-126.
[159] K. Teferra, D.J. Rowenhorst, Optimizing the cellular automata finite element model for additive manufacturing to simulate large microstructures, Acta Materialia 213 (2021) 116930.
[160] J.H.K. Tan, Modelling of grain structure using cellular automata-finite element method for additive manufacturing of metals.
[161] S.A. Etesami, M. Laradji, E. Asadi, Reliability of molecular dynamics interatomic potentials for modeling of titanium in additive manufacturing processes, Computational Materials Science 184 (2020) 109883.
[162] S. Cummins, P.W. Cleary, G. Delaney, A. Phua, M. Sinnott, D. Gunasegaram, C. Davies, A Coupled DEM/SPH Computational Model to Simulate Microstructure Evolution in Ti-6Al-4V Laser Powder Bed Fusion Processes, Metals 11(6) (2021) 858.
[163] M.J.M. Krane, D.R. Johnson, S. Raghavan, The development of a cellular automaton-finite volume model for dendritic growth, Applied Mathematical Modelling 33(5) (2009) 2234-2247.
[164] Y. Li, S. Hu, X. Sun, M. Stan, A review: applications of the phase field method in predicting microstructure and property evolution of irradiated nuclear materials, npj Computational Materials 3(1) (2017) 16.
[165] B. Fromm, Y. Zhang, D. Schwen, D. Brown, R. Pokharel, Assessment of MARMOT Grain Growth Model, United States, 2015.
[166] C.J. Permann, M.R. Tonks, B. Fromm, D.R. Gaston, Order parameter re-mapping algorithm for 3D phase field model of grain growth using FEM, Computational Materials Science 115 (2016) 18-25.
[167] B. Chen, Y. Sun, B.R. Barboza, A.R. Barron, C. Li, Phase-field simulation of hydraulic fracturing with a revised fluid model and hybrid solver, Engineering Fracture Mechanics 229 (2020) 106928.
[168] S. Sahoo, K. Chou, Phase-field simulation of microstructure evolution of Ti–6Al–4V in electron beam additive manufacturing process, Additive Manufacturing 9 (2016) 14-24.
[169] X. Wang, P.W. Liu, Y. Ji, Y. Liu, M.H. Horstemeyer, L. Chen, Investigation on Microsegregation of IN718 Alloy During Additive Manufacturing via Integrated Phase-Field and Finite-Element Modeling, Journal of Materials Engineering and Performance 28(2) (2019) 657-665.
[170] Z. Huang, Z. Fan, H. Wang, B. Li, Numerical Study of Grain Growth in Laser Powder Bed Fusion Additive Manufacturing of Metals, International Journal of Computational Methods (2021) 2141012.
[171] L. Shi, S.A. Alexandratos, N.P. O'Dowd, Prediction of prior austenite grain growth in the heat-affected zone of a martensitic steel during welding, International Journal of Pressure Vessels and Piping 166 (2018) 94-106.
[172] Y. Liu, M. Militzer, M. Perez, Phase field modelling of abnormal grain growth, Materials 12(24) (2019) 4048.
[173] K.E. Ahmed, Phase field modeling of grain growth in porous polycrystalline solids, Purdue University, 2015.
[174] S. Yoder, S. Morgan, C. Kinzy, E. Barnes, M. Kirka, V. Paquit, P. Nandwana, A. Plotkowski, R.R. Dehoff, S.S. Babu, Characterization of topology optimized Ti-6Al-4V

components using electron beam powder bed fusion, Additive Manufacturing 19 (2018) 184-196.
[175] J. Li, Z. Huang, G. Liu, Q. An, M. Chen, Topology optimization design and research of lightweight biomimetic three-dimensional lattice structures based on laser powder bed fusion, Journal of Manufacturing Processes 74 (2022) 220-232.
[176] F.H. Kim, S.P. Moylan, T.Q. Phan, E.J. Garboczi, Investigation of the Effect of Artificial Internal Defects on the Tensile Behavior of Laser Powder Bed Fusion 17–4 Stainless Steel Samples: Simultaneous Tensile Testing and X-Ray Computed Tomography, Experimental Mechanics 60(7) (2020) 987-1004.
[177] S. Plimpton, Fast Parallel Algorithms for Short-Range Molecular Dynamics, Journal of Computational Physics 117(1) (1995) 1-19.
[178] C. Kloss, C. Goniva, A. Hager, S. Amberger, S. Pirker, Models, algorithms and validation for opensource DEM and CFD–DEM, Progress in Computational Fluid Dynamics, an International Journal 12(2-3) (2012) 140-152.
[179] Y. Zhang, W.H. Lee, L. Wu, L. Meng, Y.-G. Jung, J. Zhang, 7 - Multiscale multiphysics modeling of laser powder bed fusion process, in: J. Zhang, Y.-G. Jung (Eds.), Additive Manufacturing, Butterworth-Heinemann2018, pp. 215-259.
[180] Y. Geng, N. Harrison, Functionally graded bimodal Ti6Al4V fabricated by powder bed fusion additive manufacturing: Crystal plasticity finite element modelling, Materials Science and Engineering: A 773 (2020) 138736.
[181] T. Park, L.G. Hector, X. Hu, F. Abu-Farha, M.R. Fellinger, H. Kim, R. Esmaeilpour, F. Pourboghrat, Crystal plasticity modeling of 3rd generation multi-phase AHSS with martensitic transformation, International Journal of Plasticity 120 (2019) 1-46.
[182] A. Cruzado, S. Lucarini, J. Llorca, J. Segurado, Crystal plasticity simulation of the effect of grain size on the fatigue behavior of polycrystalline Inconel 718, International Journal of Fatigue 113 (2018) 236-245.
[183] C.A. Sweeney, B. O'Brien, F.P.E. Dunne, P.E. McHugh, S.B. Leen, Strain-gradient modelling of grain size effects on fatigue of CoCr alloy, Acta Materialia 78(C) (2014) 341-353.
[184] S. Haouala, S. Lucarini, J. Llorca, J. Segurado, Simulation of the Hall-Petch effect in FCC polycrystals by means of strain gradient crystal plasticity and FFT homogenization, Journal of the Mechanics and Physics of Solids 134 (2020) 103755.
[185] F. Barbe, L. Decker, D. Jeulin, G. Cailletaud, Intergranular and intragranular behavior of polycrystalline aggregates. Part 1: F.E. model, International Journal of Plasticity 17(4) (2001) 513-536.
[186] F.P.E. Dunne, A. Walker, D. Rugg, A systematic study of hcp crystal orientation and morphology effects in polycrystal deformation and fatigue, Proceedings of the Royal Society A: Mathematical, Physical and Engineering Sciences 463(2082) (2007) 1467-1489.
[187] L. Li, L. Shen, G. Proust, A texture-based representative volume element crystal plasticity model for predicting Bauschinger effect during cyclic loading, Materials Science and Engineering: A 608 (2014) 174-183.
[188] F. Roters, P. Eisenlohr, L. Hantcherli, D.D. Tjahjanto, T.R. Bieler, D. Raabe, Overview of constitutive laws, kinematics, homogenization and multiscale methods in crystal plasticity finite-element modeling: Theory, experiments, applications, Acta Materialia 58(4) (2010) 1152-1211.

[189] Q. Zhang, J. Xie, T. London, D. Griffiths, I. Bhamji, V. Oancea, Estimates of the mechanical properties of laser powder bed fusion Ti-6Al-4V parts using finite element models, Materials & Design 169 (2019) 107678.
[190] A. Fatemi, R. Molaei, S. Sharifimehr, N. Shamsaei, N. Phan, Torsional fatigue behavior of wrought and additive manufactured Ti-6Al-4V by powder bed fusion including surface finish effect, International Journal of Fatigue 99 (2017) 187-201.
[191] F. Sun, E.D. Meade, N.P. O'Dowd, Strain gradient crystal plasticity modelling of size effects in a hierarchical martensitic steel using the Voronoi tessellation method, International Journal of Plasticity (2019).
[192] J. Paris, New ideas concerning the physiology, physiopathology and pharmacology of the bile ducts, Revue médico-chirurgicale des maladies du foie 36 (1961) 9-16.
[193] N. Pugno, M. Ciavarella, P. Cornetti, A. Carpinteri, A generalized Paris' law for fatigue crack growth, Journal of the Mechanics and Physics of Solids 54(7) (2006) 1333-1349.
[194] O.H. Basquin, Proceedings of the American Society of Testing and Materials (1910) 625-630.
[195] L.F. Coffin, J.F. Tavernelli, The cyclic straining and fatigue of metals, Trans. Metall. Soc. AIME 215(5) (1959) 794-807.
[196] M. Zhang, C.-N. Sun, X. Zhang, J. Wei, D. Hardacre, H. Li, Predictive models for fatigue property of laser powder bed fusion stainless steel 316L, Materials & Design 145 (2018) 42-54.
[197] A. Yadollahi, M. Mahmoudi, A. Elwany, H. Doude, L. Bian, J.C. Newman, Effects of crack orientation and heat treatment on fatigue-crack-growth behavior of AM 17-4 PH stainless steel, Engineering Fracture Mechanics 226 (2020) 106874.
[198] A. Yadollahi, N. Shamsaei, S. Thompson, A. Elwany, L. Bian, M. Mahmoudi, Fatigue behavior of selective laser melted 17-4 PH stainless steel, 2015.
[199] A. Yadollahi, M. Mahmoudi, A. Elwany, H. Doude, L. Bian, J.C. Newman Jr, Fatigue-life prediction of additively manufactured material: Effects of heat treatment and build orientation, Fatigue & Fracture of Engineering Materials & Structures 43(4) (2020) 831-844.
[200] A. Padmanabhan, Fatigue Analysis of 3D Printed 15-5 PH Stainless Steel-A Combined Numerical and Experimental Study, 2019.
[201] J.L. Bartlett, X. Li, An overview of residual stresses in metal powder bed fusion, Additive Manufacturing 27 (2019) 131-149.
[202] R.K. Ganeriwala, M. Strantza, W.E. King, B. Clausen, T.Q. Phan, L.E. Levine, D.W. Brown, N.E. Hodge, Evaluation of a thermomechanical model for prediction of residual stress during laser powder bed fusion of Ti-6Al-4V, Additive Manufacturing 27 (2019) 489-502.
[203] T. Mishurova, K. Artzt, J. Haubrich, G. Requena, G. Bruno, Exploring the correlation between subsurface residual stresses and manufacturing parameters in laser powder bed fused Ti-6Al-4V, Metals 9(2) (2019) 261.
[204] I. Yeo, S. Bae, A. Amanov, S. Jeong, Effect of laser shock peening on properties of heat-treated Ti–6Al–4V manufactured by laser powder bed fusion, International Journal of Precision Engineering and Manufacturing-Green Technology 8(4) (2021) 1137-1150.
[205] X. Wang, O. Sanchez-Mata, S.E. Atabay, J.A. Muñiz-Lerma, M.A. Shandiz, M. Brochu, Crystallographic orientation dependence of Charpy impact behaviours in

stainless steel 316L fabricated by laser powder bed fusion, Additive Manufacturing (2021) 102104.
[206] S. Karnati, A. Khiabhani, A. Flood, F. Liou, J. Newkirk, Anisotropy in impact toughness of powder bed fused AISI 304L stainless steel, Material Design & Processing Communications (2019) e59.
[207] P. Kumar, Z. Zhu, S.M.L. Nai, R.L. Narayan, U. Ramamurty, Fracture toughness of 304L austenitic stainless steel produced by laser powder bed fusion, Scripta Materialia 202 (2021) 114002.
[208] G.R. Johnson, A constitutive model and data for materials subjected to large strains, high strain rates, and high temperatures, Proc. 7th Inf. Sympo. Ballistics (1983) 541-547.
[209] S. Sagar, Y. Zhang, L. Wu, H.-Y. Park, J.-H. Lee, Y.-G. Jung, J. Zhang, Room-temperature charpy impact property of 3d-printed 15-5 stainless steel, Journal of Materials Engineering and Performance 27(1) (2018) 52-56.
[210] M. Bayat, C.G. Klingaa, S. Mohanty, D. De Baere, J. Thorborg, N.S. Tiedje, J.H. Hattel, Part-scale thermo-mechanical modelling of distortions in Laser Powder Bed Fusion – Analysis of the sequential flash heating method with experimental validation, Additive Manufacturing 36 (2020) 101508.
[211] C. Bruna-Rosso, A.G. Demir, B. Previtali, Selective laser melting finite element modeling: Validation with high-speed imaging and lack of fusion defects prediction, Materials & Design 156 (2018) 143-153.
[212] M. Bayat, A. Thanki, S. Mohanty, A. Witvrouw, S. Yang, J. Thorborg, N.S. Tiedje, J.H. Hattel, Keyhole-induced porosities in Laser-based Powder Bed Fusion (L-PBF) of Ti6Al4V: High-fidelity modelling and experimental validation, Additive Manufacturing 30 (2019) 100835.
[213] M. Bayat, S. Mohanty, J.H. Hattel, Multiphysics modelling of lack-of-fusion voids formation and evolution in IN718 made by multi-track/multi-layer L-PBF, International Journal of Heat and Mass Transfer 139 (2019) 95-114.
[214] L.Y. Liu, Q.S. Yang, Y.X. Zhang, Plastic damage of additive manufactured aluminium with void defects, Mech Res Commun 95 (2019) 45-51.
[215] W. Yan, Y. Qian, W. Ge, S. Lin, W.K. Liu, F. Lin, G.J. Wagner, Meso-scale modeling of multiple-layer fabrication process in Selective Electron Beam Melting: Inter-layer/track voids formation, Materials & Design 141 (2018) 210-219.
[216] R.J. Asaro, Crystal Plasticity, Journal of Applied Mechanics 50(4b) (1983) 921-934.
[217] B. Dutta, S. Babu, B. Jared, Metal additive manufacturing process modeling and simulation, in: B. Dutta, S. Babu, B. Jared (Eds.), Science, Technology and Applications of Metals in Additive Manufacturing, Elsevier2019, pp. 145-191.
[218] M. Lindroos, T. Pinomaa, A. Antikainen, J. Lagerbom, J. Reijonen, T. Lindroos, T. Andersson, A. Laukkanen, Micromechanical modeling approach to single track deformation, phase transformation and residual stress evolution during selective laser melting using crystal plasticity, Additive Manufacturing 38 (2021) 101819.
[219] S. Xu, P. Zhou, G. Liu, D. Xiao, M. Gong, J. Wang, Shock-induced two types of $\{101\bar{2}\}$ sequential twinning in Titanium, Acta Materialia 165 (2019) 547-560.
[220] A. Abd El-Aty, Y. Xu, S. Ha, S.-H. Zhang, Computational homogenization of tensile deformation behaviors of a third generation Al-Li alloy 2060-T8 using crystal plasticity finite element method, Materials Science and Engineering: A 731 (2018) 583-594.

[221] M. Zhang, J. Zhang, D.L. McDowell, Microstructure-based crystal plasticity modeling of cyclic deformation of Ti–6Al–4V, International Journal of Plasticity 23(8) (2007) 1328-1348.
[222] J.R. Mayeur, D.L. McDowell, R.W. Neu, Crystal plasticity simulations of fretting of Ti-6Al-4V in partial slip regime considering effects of texture, Computational Materials Science 41(3) (2008) 356-365.
[223] M. Wronski, K. Wierzbanowski, S. Wronski, B. Bacroix, P. Lipinski, Texture variation in asymmetrically rolled titanium. Study by Finite Element Method with implemented crystalline model, International Journal of Mechanical Sciences 87 (2014) 258-267.
[224] Y. Guilhem, S. Basseville, F. Curtit, J.M. Stéphan, G. Cailletaud, Investigation of the effect of grain clusters on fatigue crack initiation in polycrystals, International Journal of Fatigue 32(11) (2010) 1748-1763.
[225] R.K. Verma, P. Biswas, T. Kuwabara, K. Chung, Two stage deformation modeling for DP 780 steel sheet using crystal plasticity, Materials Science and Engineering: A 604 (2014) 98-102.
[226] S. Zarei, R.J. Nedoushan, M. Atapour, The sources of the micro stress and strain inhomogeneity in dual phase steels, Materials Science and Engineering: A 674 (2016) 384-396.
[227] J. Kadkhodapour, A. Butz, S. Ziaei-Rad, S. Schmauder, A micro mechanical study on failure initiation of dual phase steels under tension using single crystal plasticity model, International Journal of Plasticity 27(7) (2011) 1103-1125.
[228] Y. Tu, S.B. Leen, N.M. Harrison, A high-fidelity crystal-plasticity finite element methodology for low-cycle fatigue using automatic electron backscatter diffraction scan conversion: Application to hot-rolled cobalt–chromium alloy, Proceedings of the Institution of Mechanical Engineers, Part L: Journal of Materials: Design and Applications (2021) 14644207211010836.
[229] R. Bandyopadhyay, A.W. Mello, K. Kapoor, M.P. Reinhold, T.F. Broderick, M.D. Sangid, On the crack initiation and heterogeneous deformation of Ti-6Al-4V during high cycle fatigue at high R ratios, Journal of the Mechanics and Physics of Solids 129 (2019) 61-82.
[230] F. Dunne, N. Petrinic, Introduction to Computational Plasticity, OUP Oxford2005.
[231] Y. Huang, A user-material subroutine incroporating single crystal plasticity in the ABAQUS finite element program, Harvard Univ.1991.
[232] C.A. Sweeney, P.E. McHugh, J.P. McGarry, S.B. Leen, Micromechanical methodology for fatigue in cardiovascular stents, International Journal of Fatigue 44 (2012) 202-216.
[233] D. Pierce, R.J. Asaro, A. Needleman, An analysis of non-uniform and localized deformation in ductile single crystals, Acta Metall. 31 (1983).
[234] P.J. Ashton, A.M. Harte, S.B. Leen, Statistical grain size effects in fretting crack initiation, Tribology International 108 (2017) 75-86.
[235] C.A. Sweeney, B. O'Brien, P.E. McHugh, S.B. Leen, Experimental characterisation for micromechanical modelling of CoCr stent fatigue, Biomaterials 35(1) (2014) 36-48.
[236] J.A. Grogan, S.B. Leen, P.E. McHugh, Influence of statistical size effects on the plastic deformation of coronary stents, J Mech Behav Biomed Mater 20 (2013) 61-76.
[237] R. Kiwanuka, Micro-deformation and Texture in Engineering Materials, University of Oxford, UK, 2013.

[238] M.F. Ashby, The deformation of plastically non-homogeneous materials, The Philosophical Magazine: A Journal of Theoretical Experimental and Applied Physics 21(170) (1970) 399-424.
[239] H. Liang, F.P.E. Dunne, GND accumulation in bi-crystal deformation: Crystal plasticity analysis and comparison with experiments, International Journal of Mechanical Sciences 51(4) (2009) 326-333.
[240] G.B. Gibbs, Thermodynamic analysis of dislocation glide controlled by dispersed local obstacles, Materials Science and Engineering 4(6) (1969) 313-328.
[241] F. Dunne, R. Kiwanuka, A. Wilkinson, Crystal plasticity analysis of micro-deformation, lattice rotation and geometrically necessary dislocation density, Proceedings of the Royal Society a-Mathematical Physical and Engineering Sciences 468 (2012) 2509-2531.
[242] G.I. Taylor, The mechanism of plastic deformation of crystals. Part I.—Theoretical, Proceedings of the Royal Society of London. Series A, Containing Papers of a Mathematical and Physical Character 145(855) (1934) 362-387.
[243] F.P.E. Dunne, Fatigue crack nucleation: Mechanistic modelling across the length scales, Current Opinion in Solid State and Materials Science 18(4) (2014) 170-179.
[244] A. Manonukul, F.P.E. Dunne, High– and low–cycle fatigue crack initiation using polycrystal plasticity, Proceedings of the Royal Society of London. Series A: Mathematical, Physical and Engineering Sciences 460(2047) (2004) 1881-1903.
[245] A. Muth, R. John, A. Pilchak, S.R. Kalidindi, D.L. McDowell, Analysis of Fatigue Indicator Parameters for Ti-6Al-4V microstructures using extreme value statistics in the transition fatigue regime, International Journal of Fatigue 153 (2021) 106441.
[246] H. Hallberg, S.K. Ås, B. Skallerud, Crystal plasticity modeling of microstructure influence on fatigue crack initiation in extruded Al6082-T6 with surface irregularities, International Journal of Fatigue 111 (2018) 16-32.
[247] N. Moelans, B. Blanpain, P. Wollants, Quantitative analysis of grain boundary properties in a generalized phase field model for grain growth in anisotropic systems, Physical Review B 78(2) (2008) 024113.
[248] J.W. Cahn, On spinodal decomposition, Acta metallurgica 9(9) (1961) 795-801.
[249] A. Schmid, A time dependent Ginzburg-Landau equation and its application to the problem of resistivity in the mixed state, Physik der kondensierten Materie 5(4) (1966) 302-317.
[250] A. Gulli, A. Kapoor, S. Pal, Deep learning with TensorFlow 2 and Keras: regression, ConvNets, GANs, RNNs, NLP, and more with TensorFlow 2 and the Keras API, Packt Publishing Ltd2019.
[251] H. Baumgartl, J. Tomas, R. Buettner, M. Merkel, A deep learning-based model for defect detection in laser-powder bed fusion using in-situ thermographic monitoring, Progress in Additive Manufacturing (2020) 1-9.
[252] A. Gaikwad, F. Imani, H. Yang, E. Reutzel, P. Rao, In Situ Monitoring of Thin-Wall Build Quality in Laser Powder Bed Fusion Using Deep Learning, Smart and Sustainable Manufacturing Systems 3(1) (2019).
[253] L. Scime, J. Beuth, A multi-scale convolutional neural network for autonomous anomaly detection and classification in a laser powder bed fusion additive manufacturing process, Additive Manufacturing 24 (2018) 273-286.

[254] D.S. Nguyen, H.S. Park, C.M. Lee, Optimization of selective laser melting process parameters for Ti-6Al-4V alloy manufacturing using deep learning, Journal of Manufacturing Processes 55 (2020) 230-235.
[255] H. Baumgartl, J. Tomas, R. Buettner, M. Merkel, A deep learning-based model for defect detection in laser-powder bed fusion using in-situ thermographic monitoring, Progress in Additive Manufacturing 5(3) (2020) 277-285.
[256] A. Chowdhury, E. Kautz, B. Yener, D. Lewis, Image driven machine learning methods for microstructure recognition, Computational Materials Science 123 (2016) 176-187.
[257] J. Fu, S. Cui, S. Cen, C. Li, Statistical characterization and reconstruction of heterogeneous microstructures using deep neural network, Computer Methods in Applied Mechanics and Engineering 373 (2021) 113516.
[258] Y. Han, R.J. Griffiths, H.Z. Yu, Y. Zhu, Quantitative microstructure analysis for solid-state metal additive manufacturing via deep learning, Journal of Materials Research 35(15) (2020) 1936-1948.
[259] W. Halsey, J. Ferguson, A. Plotkowski, R. Dehoff, V. Paquit, Geometry-independent microstructure optimization for electron beam powder bed fusion additive manufacturing, Additive Manufacturing 35 (2020) 101354.
[260] S.A. Razavi, F. Ashrafizadeh, S. Fooladi, Prediction of age hardening parameters for 17-4PH stainless steel by artificial neural network and genetic algorithm, Materials Science and Engineering: A 675 (2016) 147-152.
[261] S. Kotha, D. Ozturk, S. Ghosh, Parametrically homogenized constitutive models (PHCMs) from micromechanical crystal plasticity FE simulations, part I: Sensitivity analysis and parameter identification for Titanium alloys, International Journal of Plasticity 120 (2019) 296-319.
[262] A. Rovinelli, M.D. Sangid, H. Proudhon, W. Ludwig, Using machine learning and a data-driven approach to identify the small fatigue crack driving force in polycrystalline materials, npj Computational Materials 4(1) (2018).
[263] C. Wang, X.P. Tan, S.B. Tor, C.S. Lim, Machine learning in additive manufacturing: State-of-the-art and perspectives, Additive Manufacturing 36 (2020) 101538.
[264] E. Westphal, H. Seitz, A machine learning method for defect detection and visualization in selective laser sintering based on convolutional neural networks, Additive Manufacturing 41 (2021) 101965.
[265] B. Zhang, S. Liu, Y.C. Shin, In-Process monitoring of porosity during laser additive manufacturing process, Additive Manufacturing 28 (2019) 497-505.
[266] A. Cecen, H. Dai, Y.C. Yabansu, S.R. Kalidindi, L. Song, Material structure-property linkages using three-dimensional convolutional neural networks, Acta Materialia 146 (2018) 76-84.
[267] J. Jung, J.I. Yoon, H.K. Park, J.Y. Kim, H.S. Kim, An efficient machine learning approach to establish structure-property linkages, Computational Materials Science 156 (2019) 17-25.
[268] X. Li, Z. Liu, S. Cui, C. Luo, C. Li, Z. Zhuang, Predicting the effective mechanical property of heterogeneous materials by image based modeling and deep learning, Computer Methods in Applied Mechanics and Engineering 347 (2019) 735-753.

[269] A. Yamanaka, R. Kamijyo, K. Koenuma, I. Watanabe, T. Kuwabara, Deep neural network approach to estimate biaxial stress-strain curves of sheet metals, Materials & Design 195 (2020) 108970.
[270] Y. Miyazawa, F. Briffod, T. Shiraiwa, M. Enoki, Prediction of Cyclic Stress-Strain Property of Steels by Crystal Plasticity Simulations and Machine Learning, Materials (Basel) 12(22) (2019).
[271] A.L. Frankel, R.E. Jones, C. Alleman, J.A. Templeton, Predicting the mechanical response of oligocrystals with deep learning, Computational Materials Science 169 (2019) 109099.
[272] M. Yuan, S. Paradiso, B. Meredig, S.R. Niezgoda, Machine Learning–Based Reduce Order Crystal Plasticity Modeling for ICME Applications, Integrating Materials and Manufacturing Innovation 7(4) (2018) 214-230.
[273] A. Mangal, E.A. Holm, Applied machine learning to predict stress hotspots II: Hexagonal close packed materials, International Journal of Plasticity 114 (2019) 1-14.
[274] N.G. Paterakis, E. Mocanu, M. Gibescu, B. Stappers, W.v. Alst, Deep learning versus traditional machine learning methods for aggregated energy demand prediction, 2017 IEEE PES Innovative Smart Grid Technologies Conference Europe (ISGT-Europe), 2017, pp. 1-6.
[275] I. Baturynska, O. Semeniuta, K. Martinsen, Optimization of Process Parameters for Powder Bed Fusion Additive Manufacturing by Combination of Machine Learning and Finite Element Method: A Conceptual Framework, Procedia CIRP 67 (2018) 227-232.
[276] J. Wu, Introduction to convolutional neural networks, National Key Lab for Novel Software Technology. Nanjing University. China 5(23) (2017) 495.
[277] Z. Zhang, Artificial Neural Network, in: Z. Zhang (Ed.), Multivariate Time Series Analysis in Climate and Environmental Research, Springer International Publishing, Cham, 2018, pp. 1-35.
[278] N. Coskun, T. Yildirim, The effects of training algorithms in MLP network on image classification, Proceedings of the International Joint Conference on Neural Networks, 2003., 2003, pp. 1223-1226 vol.2.
[279] S. Albawi, T.A. Mohammed, S. Al-Zawi, Understanding of a convolutional neural network, 2017 International Conference on Engineering and Technology (ICET), 2017, pp. 1-6.
[280] L. Dowling, J. Kennedy, S. O'Shaughnessy, D. Trimble, A review of critical repeatability and reproducibility issues in powder bed fusion, Materials & Design 186 (2020) 108346.
[281] F. R. Kaschel, M. Celikin, D.P. Dowling, Effects of laser power on geometry, microstructure and mechanical properties of printed Ti-6Al-4V parts, Journal of Materials Processing Technology 278 (2020) 116539.
[282] S.-J. Chang, Z.-X. Wei, Influences of the scanning strategy on surface roughness in selective laser melting, Proceedings of the Institution of Mechanical Engineers, Part B: Journal of Engineering Manufacture (2020) 0954405420978119.
[283] Y. Tu, Z. Liu, L. Carneiro, C.M. Ryan, A.C. Parnell, S.B. Leen, N.M. Harrison, Towards an instant structure-property prediction quality control tool for additive manufactured steel using a crystal plasticity trained deep learning surrogate, Materials & Design 213 (2022) 110345.
[284] A. INTERNATIONAL, ASTM E8 / E8M-21, Standard Test Methods for Tension Testing of Metallic Materials, West Conshohocken, PA, 2021.

[285] A. International, ASTM E606 / E606M-21, Standard Test Method for Strain-Controlled Fatigue Testing, West Conshohocken, PA, 2021.
[286] N.M. Harrison, P.F. McDonnell, D.C. O'Mahoney, O.D. Kennedy, F.J. O'Brien, P.E. McHugh, Heterogeneous linear elastic trabecular bone modelling using micro-CT attenuation data and experimentally measured heterogeneous tissue properties, Journal of Biomechanics 41(11) (2008) 2589-2596.
[287] S. Buehler, The science behind materials preparation, Buehler Ltd (2004).
[288] P. Lehto, H. Remes, T. Saukkonen, H. Hänninen, J. Romanoff, Influence of grain size distribution on the Hall–Petch relationship of welded structural steel, Materials Science and Engineering: A 592 (2014) 28-39.
[289] A. Winkelmann, C. Trager-Cowan, F. Sweeney, A.P. Day, P. Parbrook, Many-beam dynamical simulation of electron backscatter diffraction patterns, Ultramicroscopy 107(4-5) (2007) 414-421.
[290] S.b. Oxford Instrument, EBSD Training Document, 2009.09.
[291] F. Bachmann, R. Hielscher, H. Schaeben, Texture Analysis with MTEX – Free and Open Source Software Toolbox, Solid State Phenomena 160 (2010) 63-68.
[292] A. Loeb, M. Ferry, L. Bassman, Segmentation of 3D EBSD data for subgrain boundary identification and feature characterization, Ultramicroscopy 161 (2016) 83-89.
[293] B. Beausir, J. Fundenberger, Analysis Tools for Electron and X-ray diffraction, ATEX—software, Université de Lorraine, www. atex-software. eu (2017).
[294] M.A. Groeber, M.A. Jackson, DREAM.3D: A Digital Representation Environment for the Analysis of Microstructure in 3D, Integrating Materials and Manufacturing Innovation 3(1) (2014) 56-72.
[295] C.A. Sweeney, Micromechanics of fatigue with application to stents, PhD Thesis, National University of Ireland Galway, 2014.
[296] C.A. Sweeney, B. O'Brien, F.P. Dunne, P.E. McHugh, S.B. Leen, Micro-scale testing and micromechanical modelling for high cycle fatigue of CoCr stent material, J Mech Behav Biomed Mater 46(C) (2015) 244-60.
[297] N. Bonnheim, H. Gramling, M. Ries, S. Shukla, B. Iliescu, L. Pruitt, Fatigue fracture of a cemented Omnifit CoCr femoral stem: implant and failure analysis, Arthroplasty Today 3(4) (2017) 234-238.
[298] A. Cutolo, B. Neirinck, K. Lietaert, C. de Formanoir, B. Van Hooreweder, Influence of layer thickness and post-process treatments on the fatigue properties of CoCr scaffolds produced by laser powder bed fusion, Additive Manufacturing 23 (2018) 498-504.
[299] T.B. Britton, J. Jiang, Y. Guo, A. Vilalta-Clemente, D. Wallis, L.N. Hansen, A. Winkelmann, A.J. Wilkinson, Tutorial: Crystal orientations and EBSD — Or which way is up?, Materials Characterization 117 (2016) 113-126.
[300] A.J. Schwartz, M. Kumar, B.L. Adams, D.P. Field, Electron backscatter diffraction in materials science, Springer2000.
[301] MATLAB, 9.3.0.713579 (R2017b) ed., Natick, Massachusetts: The MathWorks Inc. 2018.
[302] DREAM.3D v6 User Manual.
[303] ABAQUS, Dassault Systèmes Simulia Corp.
[304] Y. Bhandari, S. Sarkar, M. Groeber, M.D. Uchic, D.M. Dimiduk, S. Ghosh, 3D Polycrystalline Microstructure Reconstruction From FIB Generated Serial Sections for FE Analysis, Computational Materials Science 41 (2007) 222-235.

[305] F. Bachmann, R. Hielscher, H. Schaeben, Grain detection from 2d and 3d EBSD data—Specification of the MTEX algorithm, Ultramicroscopy 111(12) (2011) 1720-1733.
[306] X. Li, A. Ramazani, U. Prahl, W. Bleck, Quantification of complex-phase steel microstructure by using combined EBSD and EPMA measurements, Materials Characterization 142 (2018) 179-186.
[307] A.C. Magee, L. Ladani, Representation of a microstructure with bimodal grain size distribution through crystal plasticity and cohesive interface modeling, Mechanics of Materials 82 (2015) 1-12.
[308] M. Knezevic, B. Drach, M. Ardeljan, I.J. Beyerlein, Three dimensional predictions of grain scale plasticity and grain boundaries using crystal plasticity finite element models, Computer Methods in Applied Mechanics and Engineering 277 (2014) 239-259.
[309] O.E. Jones E, Peterson P, et al, SciPy: Open Source Scientific Tools for Python, 2001-.
[310] M. Jiang, K. Alzebdeh, I. Jasiuk, M. Ostoja-Starzewski, Scale and boundary conditions effects in elastic properties of random composites, Acta Mechanica 148(1) (2001) 63-78.
[311] R. Zabihyan, J. Mergheim, A. Javili, P. Steinmann, Aspects of computational homogenization in magneto-mechanics: Boundary conditions, RVE size and microstructure composition, International Journal of Solids and Structures 130-131 (2018) 105-121.
[312] J. Lu, W. Sun, A. Becker, Material characterisation and finite element modelling of cyclic plasticity behaviour for 304 stainless steel using a crystal plasticity model, International Journal of Mechanical Sciences 105 (2016) 315-329.
[313] M. Henning, H. Vehoff, Statistical size effects based on grain size and texture in thin sheets, Materials Science and Engineering: A 452-453 (2007) 602-613.
[314] H. Lim, C.C. Battaile, J.E. Bishop, J.W. Foulk, Investigating mesh sensitivity and polycrystalline RVEs in crystal plasticity finite element simulations, International Journal of Plasticity 121 (2019) 101-115.
[315] C.A. Sweeney, B. O'Brien, P.E. McHugh, S.B. Leen, Experimental characterisation for micromechanical modelling of CoCr stent fatigue, Biomaterials 35(1) (2013).
[316] F.J. Harewood, P.E. McHugh, Investigation of finite element mesh independence in rate dependent materials, Computational Materials Science 37(4) (2006) 442-453.
[317] M. Ostoja-Starzewski, X. Du, Z.F. Khisaeva, W. Li, Comparisons of the size of the representative volume element in elastic, plastic, thermoelastic, and permeable random microstructures, International Journal for Multiscale Computational Engineering 5(2) (2007) 73-82.
[318] C.A. Sweeney, W. Vorster, S.B. Leen, E. Sakurada, P.E. McHugh, F.P.E. Dunne, The role of elastic anisotropy, length scale and crystallographic slip in fatigue crack nucleation, Journal of the Mechanics and Physics of Solids 61(5) (2013) 1224-1240.
[319] B.J. Golden, D.F. Li, N.P. O'Dowd, P. Tiernan, Microstructural Modeling of P91 Martensitic Steel Under Uniaxial Loading Conditions, Journal of Pressure Vessel Technology 136(2) (2014).
[320] İ. Özdemir, Grain statistics induced size effect in the expansion of metallic micro rings, International Journal of Mechanical Sciences 87 (2014) 52-59.
[321] C. Sun, X. Zhang, X. Liu, Y. Hong, Effects of specimen size on fatigue life of metallic materials in high-cycle and very-high-cycle fatigue regimes, Fatigue & Fracture of Engineering Materials & Structures 39 (2016) n/a-n/a.

[322] S. Lucarini, J. Segurado, An upscaling approach for micromechanics based fatigue: from RVEs to specimens and component life prediction, International Journal of Fracture 223(1-2) (2019) 93-108.
[323] S.L. Lu, H.P. Tang, Y.P. Ning, N. Liu, D.H. StJohn, M. Qian, Microstructure and Mechanical Properties of Long Ti-6Al-4V Rods Additively Manufactured by Selective Electron Beam Melting Out of a Deep Powder Bed and the Effect of Subsequent Hot Isostatic Pressing, Metallurgical and Materials Transactions A 46(9) (2015) 3824-3834.
[324] B. Vrancken, L. Thijs, J.-P. Kruth, J. Van Humbeeck, Heat treatment of Ti6Al4V produced by Selective Laser Melting: Microstructure and mechanical properties, Journal of Alloys and Compounds 541 (2012) 177-185.
[325] J. Yu, M. Rombouts, G. Maes, F. Motmans, Material Properties of Ti6Al4V Parts Produced by Laser Metal Deposition, Physics Procedia 39 (2012) 416-424.
[326] T. Ahmed, H.J. Rack, Phase transformations during cooling in α+β titanium alloys, Materials Science and Engineering: A 243(1) (1998) 206-211.
[327] W. Xu, M. Brandt, S. Sun, J. Elambasseril, Q. Liu, K. Latham, K. Xia, M. Qian, Additive manufacturing of strong and ductile Ti–6Al–4V by selective laser melting via in situ martensite decomposition, Acta Materialia 85 (2015) 74-84.
[328] H. Sharma, D. Parfitt, A.K. Syed, D. Wimpenny, E. Muzangaza, G. Baxter, B. Chen, A critical evaluation of the microstructural gradient along the build direction in electron beam melted Ti-6Al-4V alloy, Materials Science and Engineering: A 744 (2019) 182-194.
[329] X. Tan, Y. Kok, Y.J. Tan, M. Descoins, D. Mangelinck, S.B. Tor, K.F. Leong, C.K. Chua, Graded microstructure and mechanical properties of additive manufactured Ti–6Al–4V via electron beam melting, Acta Materialia 97 (2015) 1-16.
[330] T.H. Becker, P. Kumar, U. Ramamurty, Fracture and fatigue in additively manufactured metals, Acta Materialia 219 (2021) 117240.
[331] A. Azarniya, X.G. Colera, M.J. Mirzaali, S. Sovizi, F. Bartolomeu, M.k. St Weglowski, W.W. Wits, C.Y. Yap, J. Ahn, G. Miranda, F.S. Silva, H.R. Madaah Hosseini, S. Ramakrishna, A.A. Zadpoor, Additive manufacturing of Ti–6Al–4V parts through laser metal deposition (LMD): Process, microstructure, and mechanical properties, Journal of Alloys and Compounds 804 (2019) 163-191.
[332] A.H. Chern, P. Nandwana, T. Yuan, M.M. Kirka, R.R. Dehoff, P.K. Liaw, C.E. Duty, A review on the fatigue behavior of Ti-6Al-4V fabricated by electron beam melting additive manufacturing, International Journal of Fatigue 119 (2019) 173-184.
[333] M.-T. Tsai, Y.-W. Chen, C.-Y. Chao, J.S.C. Jang, C.-C. Tsai, Y.-L. Su, C.-N. Kuo, Heat-treatment effects on mechanical properties and microstructure evolution of Ti-6Al-4V alloy fabricated by laser powder bed fusion, Journal of Alloys and Compounds (2019) 152615.
[334] L. Chen, T.E. James Edwards, F. Di Gioacchino, W.J. Clegg, F.P.E. Dunne, M.-S. Pham, Crystal plasticity analysis of deformation anisotropy of lamellar TiAl alloy: 3D microstructure-based modelling and in-situ micro-compression, International Journal of Plasticity 119 (2019) 344-360.
[335] P.W. Liu, Z. Wang, Y.H. Xiao, R.A. Lebensohn, Y.C. Liu, M.F. Horstemeyer, X.Y. Cui, L. Chen, Integration of phase-field model and crystal plasticity for the prediction of process-structure-property relation of additively manufactured metallic materials, International Journal of Plasticity (2020) 102670.

[336] C.C. Tasan, M. Diehl, D. Yan, C. Zambaldi, P. Shanthraj, F. Roters, D. Raabe, Integrated experimental–simulation analysis of stress and strain partitioning in multiphase alloys, Acta Materialia 81 (2014) 386-400.
[337] Y. Geng, W. Xie, Y. Tu, S. Deng, D. Egan, D.P. Dowling, H. Song, S. Zhang, N. Harrison, Ti–6Al–4V microstructural functionally graded material by additive manufacturing: Experiment and computational modelling, Materials Science and Engineering: A 823 (2021) 141782.
[338] S. Haouala, J. Segurado, J. Llorca, An analysis of the influence of grain size on the strength of FCC polycrystals by means of computational homogenization, Acta Materialia 148 (2018) 72-85.
[339] P.J. Ashton, A.M. Harte, S.B. Leen, A strain-gradient, crystal plasticity model for microstructure-sensitive fretting crack initiation in ferritic-pearlitic steel for flexible marine risers, International Journal of Fatigue 111 (2018) 81-92.
[340] P.J. Ashton, PhD Thesis: Micromechanical modelling of size effects in crack initiation with application to fretting fatigue and cold dwell fatigue, Mechanical Engineering, National University of Ireland, Galway, 2018.
[341] M. Kasemer, R. Quey, P. Dawson, The Influence of Mechanical Constraints Introduced by β Annealed Microstructures on the Yield Strength and Ductility of Ti-6Al-4V, Journal of the Mechanics and Physics of Solids 103 (2017).
[342] E.M. O'Hara, N.M. Harrison, B.K. Polomski, R.A. Barrett, S.B. Leen, Fatigue damage characterisation of MarBN steel for high temperature flexible operating conditions, Proceedings of the Institution of Mechanical Engineers, Part L: Journal of Materials: Design and Applications 231(1-2) (2016) 23-37.
[343] Z. Zhan, J. Tong, A study of creep-fatigue interaction in a new nickel-based superalloy, WIT Press2004.
[344] E. Hall, The deformation and ageing of mild steel: III discussion of results, Proceedings of the Physical Society. Section B 64(9) (1951) 747.
[345] N. Petch, The cleavage strength of polycrystals, Journal of the Iron and Steel Institute 174 (1953) 25-28.
[346] A.M. Beese, B.E. Carroll, Review of Mechanical Properties of Ti-6Al-4V Made by Laser-Based Additive Manufacturing Using Powder Feedstock, JOM 68(3) (2016) 724-734.
[347] J. El-Awady, Unravelling the physics of size-dependent dislocation-mediated plasticity, Nature Communications 6 (2015) 5926.
[348] K.M. Min, W. Jeong, S.H. Hong, C.A. Lee, P.R. Cha, H.N. Han, M.G. Lee, Integrated crystal plasticity and phase field model for prediction of recrystallization texture and anisotropic mechanical properties of cold-rolled ultra-low carbon steels, International Journal of Plasticity 127 (2020) 102644.
[349] J. Zhang, X. Li, D. Xu, R. Yang, Recent progress in the simulation of microstructure evolution in titanium alloys, Progress in Natural Science: Materials International 29(3) (2019) 295-304.
[350] Y. Li, S. Hu, E. Barker, N. Overman, S. Whalen, S. Mathaudhu, Effect of grain structure and strain rate on dynamic recrystallization and deformation behavior: A phase field-crystal plasticity model, Computational Materials Science 180 (2020) 109707.
[351] Irish Centre for High-End Computing (ICHEC).

[352] Y. Zhang, L. Feng, T. Zhang, H. Xu, J. Li, Heat treatment of additively manufactured Ti-6Al-4V alloy: Microstructure and electrochemical properties, Journal of Alloys and Compounds 888 (2021) 161602.
[353] Z. Zou, M. Simonelli, J. Katrib, G. Dimitrakis, R. Hague, Microstructure and tensile properties of additive manufactured Ti-6Al-4V with refined prior-β grain structure obtained by rapid heat treatment, Materials Science and Engineering: A 814 (2021) 141271.
[354] Y. Huang, F.J. Humphreys, Measurements of grain boundary mobility during recrystallization of a single-phase aluminium alloy, Acta Materialia 47(7) (1999) 2259-2268.
[355] S.L. Semiatin, P.N. Fagin, M.G. Glavicic, I.M. Sukonnik, O.M. Ivasishin, Influence on texture on beta grain growth during continuous annealing of Ti–6Al–4V, Materials Science and Engineering: A 299(1) (2001) 225-234.
[356] A. SEKI, M. SAWADA, K. MORIGUCHI, Y. SHIRAI, Simulations of Grain Growth in Titanium and Stainless Steels.
[357] R. McCann, M.A. Obeidi, C. Hughes, É. McCarthy, D.S. Egan, R.K. Vijayaraghavan, A.M. Joshi, V. Acinas Garzon, D.P. Dowling, P.J. McNally, D. Brabazon, In-situ sensing, process monitoring and machine control in Laser Powder Bed Fusion: A review, Additive Manufacturing 45 (2021) 102058.
[358] C. Qiu, N.J.E. Adkins, M.M. Attallah, Microstructure and tensile properties of selectively laser-melted and of HIPed laser-melted Ti–6Al–4V, Materials Science and Engineering: A 578 (2013) 230-239.
[359] J. Ma, Y. Zhang, J. Li, D. Cui, Z. Wang, J. Wang, Microstructure and mechanical properties of forging-additive hybrid manufactured Ti–6Al–4V alloys, Materials Science and Engineering: A 811 (2021) 140984.
[360] O. Dolev, S. Osovski, A. Shirizly, Ti-6Al-4V hybrid structure mechanical properties—Wrought and additive manufactured powder-bed material, Additive Manufacturing 37 (2021) 101657.
[361] E.W. Lui, A.E. Medvedev, D. Edwards, M. Qian, M. Leary, M. Brandt, Microstructure modification of additive manufactured Ti-6Al-4V plates for improved ballistic performance properties, Journal of Materials Processing Technology 301 (2022) 117436.
[362] M. Shao, S. Vijayan, P. Nandwana, J.R. Jinschek, The effect of beam scan strategies on microstructural variations in Ti-6Al-4V fabricated by electron beam powder bed fusion, Materials & Design 196 (2020) 109165.
[363] T.F. Flint, Y.L. Sun, Q. Xiong, M.C. Smith, J.A. Francis, Phase-Field Simulation of Grain Boundary Evolution In Microstructures Containing Second-Phase Particles with Heterogeneous Thermal Properties, Scientific Reports 9(1) (2019) 18426.
[364] Y. You, M. Yan, C. Zhang, Phase field simulation for grains evolution of 17-4PH steel during cyclic heat treatment, Acta Metallurgica Sinica (English Letters) 26(2) (2013) 183-187.
[365] Y. Gui, D. An, F. Han, X. Lu, G. Kang, X. Zhang, Multiple-mechanism and microstructure-based crystal plasticity modeling for cyclic shear deformation of TRIP steel, International Journal of Mechanical Sciences 222 (2022) 107269.
[366] M. Jafari, M. Jamshidian, S. Ziaei-Rad, D. Raabe, F. Roters, Constitutive modeling of strain induced grain boundary migration via coupling crystal plasticity and phase-field methods, International Journal of Plasticity 99 (2017) 19-42.

[367] N.Y. Zhu, C.Y. Sun, Y.L. Li, L.Y. Qian, S.Y. Hu, Y. Cai, Y.H. Feng, Modeling discontinuous dynamic recrystallization containing second phase particles in magnesium alloys utilizing phase field method, Computational Materials Science 200 (2021) 110858.
[368] W.E. Frazier, Metal Additive Manufacturing: A Review, Journal of Materials Engineering and Performance 23(6) (2014) 1917-1928.
[369] T.M. Mower, M.J. Long, Mechanical behavior of additive manufactured, powder-bed laser-fused materials, Materials Science and Engineering: A 651 (2016) 198-213.
[370] H. Irrinki, J.S.D. Jangam, S. Pasebani, S. Badwe, J. Stitzel, K. Kate, O. Gulsoy, S.V. Atre, Effects of particle characteristics on the microstructure and mechanical properties of 17-4 PH stainless steel fabricated by laser-powder bed fusion, Powder Technology 331 (2018) 192-203.
[371] A. Kudzal, B. McWilliams, C. Hofmeister, F. Kellogg, J. Yu, J. Taggart-Scarff, J. Liang, Effect of scan pattern on the microstructure and mechanical properties of Powder Bed Fusion additive manufactured 17-4 stainless steel, Materials & Design 133 (2017) 205-215.
[372] K. Benarji, Y. Ravi Kumar, A.N. Jinoop, C.P. Paul, K.S. Bindra, Effect of Heat-Treatment on the Microstructure, Mechanical Properties and Corrosion Behaviour of SS 316 Structures Built by Laser Directed Energy Deposition Based Additive Manufacturing, Metals and Materials International 27(3) (2020) 488-499.
[373] X. Chen, J. Li, X. Cheng, H. Wang, Z. Huang, Effect of heat treatment on microstructure, mechanical and corrosion properties of austenitic stainless steel 316L using arc additive manufacturing, Materials Science and Engineering: A 715 (2018) 307-314.
[374] N. Raghavan, S. Simunovic, R. Dehoff, A. Plotkowski, J. Turner, M. Kirka, S. Babu, Localized melt-scan strategy for site specific control of grain size and primary dendrite arm spacing in electron beam additive manufacturing, Acta Materialia 140 (2017) 375-387.
[375] N. Boone, C. Zhu, C. Smith, I. Todd, J.R. Willmott, Thermal near infrared monitoring system for electron beam melting with emissivity tracking, Additive Manufacturing 22 (2018) 601-605.
[376] D.S. Egan, D.P. Dowling, Influence of process parameters on the correlation between in-situ process monitoring data and the mechanical properties of Ti-6Al-4V non-stochastic cellular structures, Additive Manufacturing 30 (2019) 100890.
[377] N.M. Harrison, P.F. McDonnell, D.C. O'Mahoney, O.D. Kennedy, F.J. O'Brien, P.E. McHugh, Heterogeneous linear elastic trabecular bone modelling using micro-CT attenuation data and experimentally measured heterogeneous tissue properties, J Biomech 41(11) (2008) 2589-96.
[378] J.H. Friedman, The elements of statistical learning: Data mining, inference, and prediction, springer open2017.
[379] D. Systèmes, ABAQUS Documentation.
[380] W.G. Feather, H. Lim, M. Knezevic, A numerical study into element type and mesh resolution for crystal plasticity finite element modeling of explicit grain structures, Computational Mechanics 67(1) (2020) 33-55.
[381] K. Shoemake, Euler Angle Conversion, in: P.S. Heckbert (Ed.), Graphics Gems, Academic Press1994, pp. 222-229.
[382] K.M.K. Anthony Kelly, Appendix 5: Slip Systems in C.C.P. and B.C.C. Crystals, Crystallography and Crystal Defects, Wiley2012, pp. 481-486.

[383] A. Cruzado, S. Lucarini, J. Llorca, J. Segurado, Microstructure-based fatigue life model of metallic alloys with bilinear Coffin-Manson behavior, International Journal of Fatigue 107 (2018) 40-48.
[384] D. Chicco, Siamese Neural Networks: An Overview, in: H. Cartwright (Ed.), Artificial Neural Networks, Springer US, New York, NY, 2021, pp. 73-94.
[385] M. Abadi, A. Agarwal, P. Barham, E. Brevdo, Z. Chen, C. Citro, G.S. Corrado, A. Davis, J. Dean, M. Devin, Tensorflow: Large-scale machine learning on heterogeneous distributed systems, arXiv preprint arXiv:1603.04467 (2016).
[386] A. Zhang, Z.C. Lipton, M. Li, A.J. Smola, Dive into deep learning, arXiv preprint arXiv:2106.11342 (2021).
[387] V. Herrera-Solaz, L. Patriarca, S. Foletti, J. Segurado, M. Niffenegger, Microstructure-based modelling and Digital Image Correlation measurement of strain fields in austenitic stainless steel 316L during tension loading, Materials Science and Engineering: A 751 (2019) 99-106.
[388] J. Suryawanshi, K.G. Prashanth, U. Ramamurty, Mechanical behavior of selective laser melted 316L stainless steel, Materials Science and Engineering: A 696 (2017) 113-121.
[389] Y.J. Yin, J.Q. Sun, J. Guo, X.F. Kan, D.C. Yang, Mechanism of high yield strength and yield ratio of 316 L stainless steel by additive manufacturing, Materials Science and Engineering: A 744 (2019) 773-777.
[390] M.S. Pham, B. Dovgyy, P.A. Hooper, Twinning induced plasticity in austenitic stainless steel 316L made by additive manufacturing, Materials Science and Engineering: A 704 (2017) 102-111.
[391] K. Guan, Z. Wang, M. Gao, X. Li, X. Zeng, Effects of processing parameters on tensile properties of selective laser melted 304 stainless steel, Materials & Design 50 (2013) 581-586.
[392] X.H. Hu, X. Sun, L.G. Hector, Y. Ren, Individual phase constitutive properties of a TRIP-assisted QP980 steel from a combined synchrotron X-ray diffraction and crystal plasticity approach, Acta Materialia 132 (2017) 230-244.
[393] M. Yaghoobi, K.S. Stopka, A. Lakshmanan, V. Sundararaghavan, J.E. Allison, D.L. McDowell, PRISMS-Fatigue computational framework for fatigue analysis in polycrystalline metals and alloys, npj Computational Materials 7(1) (2021) 38.
[394] P.G.E. Jerrard, L. Hao, K.E. Evans, Experimental investigation into selective laser melting of austenitic and martensitic stainless steel powder mixtures, Proceedings of the Institution of Mechanical Engineers, Part B: Journal of Engineering Manufacture 223(11) (2009) 1409-1416.
[395] X. Yang, R.A. Barrett, M. Tong, N.M. Harrison, S.B. Leen, Prediction of microstructure evolution for additive manufacturing of Ti-6Al-4V, Procedia Manufacturing 47 (2020) 1178-1183.
[396] N.H. Paulson, B. Gould, S.J. Wolff, M. Stan, A.C. Greco, Correlations between thermal history and keyhole porosity in laser powder bed fusion, Additive Manufacturing 34 (2020) 101213.
[397] C. Gobert, A. Kudzal, J. Sietins, C. Mock, J. Sun, B. McWilliams, Porosity segmentation in X-ray computed tomography scans of metal additively manufactured specimens with machine learning, Additive Manufacturing 36 (2020) 101460.

[398] T. Zhang, D.M. Collins, F.P.E. Dunne, B.A. Shollock, Crystal plasticity and high-resolution electron backscatter diffraction analysis of full-field polycrystal Ni superalloy strains and rotations under thermal loading, Acta Materialia 80 (2014) 25-38.
[399] M. Sitko, M. Mojzeszko, L. Rychlowski, G. Cios, P. Bala, K. Muszka, L. Madej, Numerical Procedure of Three-Dimensional Reconstruction of Ferrite-Pearlite Microstructure Data from SEM/EBSD Serial Sectioning, Procedia Manufacturing 47 (2020) 1217-1222.
[400] S. Hémery, A. Naït-Ali, M. Guéguen, J. Wendorf, A.T. Polonsky, M.P. Echlin, J.C. Stinville, T.M. Pollock, P. Villechaise, A 3D analysis of the onset of slip activity in relation to the degree of micro-texture in Ti–6Al–4V, Acta Materialia 181 (2019) 36-48.
[401] S. Kalácska, Z. Dankházi, G. Zilahi, X. Maeder, J. Michler, P.D. Ispánovity, I. Groma, Investigation of geometrically necessary dislocation structures in compressed Cu micropillars by 3-dimensional HR-EBSD, Materials Science and Engineering: A 770 (2020) 138499.
[402] A.T. Polonsky, C.A. Lang, K.G. Kvilekval, M.I. Latypov, M.P. Echlin, B.S. Manjunath, T.M. Pollock, Three-dimensional Analysis and Reconstruction of Additively Manufactured Materials in the Cloud-Based BisQue Infrastructure, Integrating Materials and Manufacturing Innovation 8(1) (2019) 37-51.
[403] E.M.H. BE, An experimental and computational investigation of the high temperature behaviour of MarBN steel with application to effects of manufacturing, National University of Ireland Galway, 2018.
[404] F. Han, B. Tang, H. Kou, J. Li, Y. Feng, Experiments and crystal plasticity finite element simulations of nanoindentation on Ti–6Al–4V alloy, Materials Science and Engineering: A 625 (2015) 28-35.
[405] S. Sinha, J.A. Szpunar, N.A.P. Kiran Kumar, N.P. Gurao, Tensile deformation of 316L austenitic stainless steel using in-situ electron backscatter diffraction and crystal plasticity simulations, Materials Science and Engineering: A 637 (2015) 48-55.
[406] A. Ojha, H. Sehitoglu, Critical Stresses for Twinning, Slip, and Transformation in Ti-Based Shape Memory Alloys, Shape Memory and Superelasticity 2(2) (2016) 180-195.
[407] X. Zhang, S. Li, X. Guo, H. Wang, Q. Yu, P. Wu, Effects of texture and twinning on the torsional behavior of magnesium alloy solid rod: A crystal plasticity approach in comparison with uniaxial tension/compression, International Journal of Mechanical Sciences (2020) 106062.

10 Appendices

Appendix A: Etching comparison for PBF-LB Titanium alloys.

The standard immersion method was used for this TiAl sample. Four different immersion times were used in this etching procedure with Kroll's reagent (187). Immersed for 5s 10s 15s and 25s

Table 0-1. Ti-Al etchant test matrix

TiAl- 1	Immerse for 10 seconds
TiAl- 2	Immerse for 15 seconds
TiAl- 3	Immerse for 20 seconds
TiAl- 4	Immerse for 25 seconds

Figure 0-1. TiAl Etched samples, sample 1 (10 Seconds), 2 (15 Seconds), 3 (20 Seconds), 4 (25 Seconds).

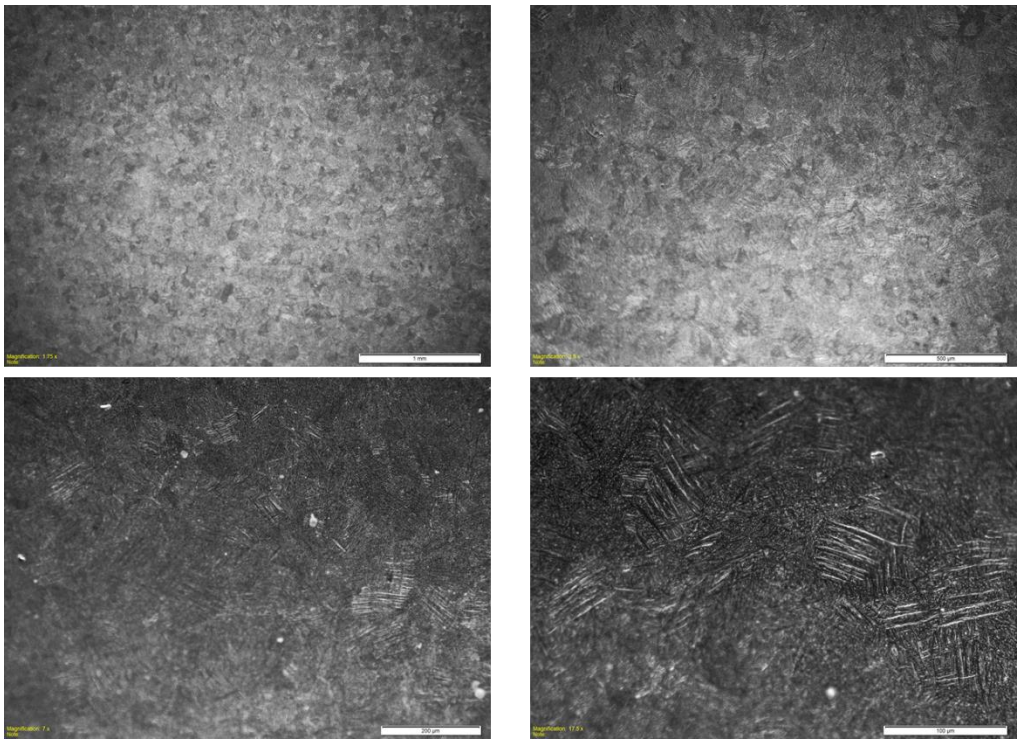

Figure 0-2.Clear microstructural images visible on an optical microscope image for TiAl-2

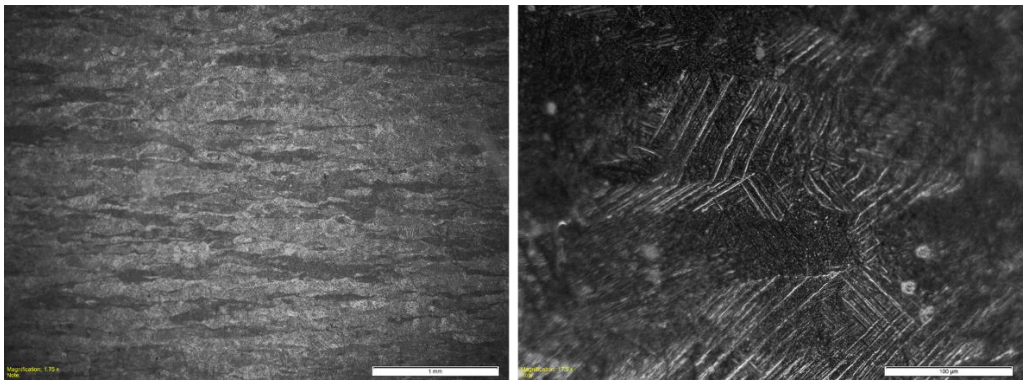

Figure 0-3. Higher resolution optical microscope images for TiAl-3, showing darker structure more difficult to discern microstructural boundaries

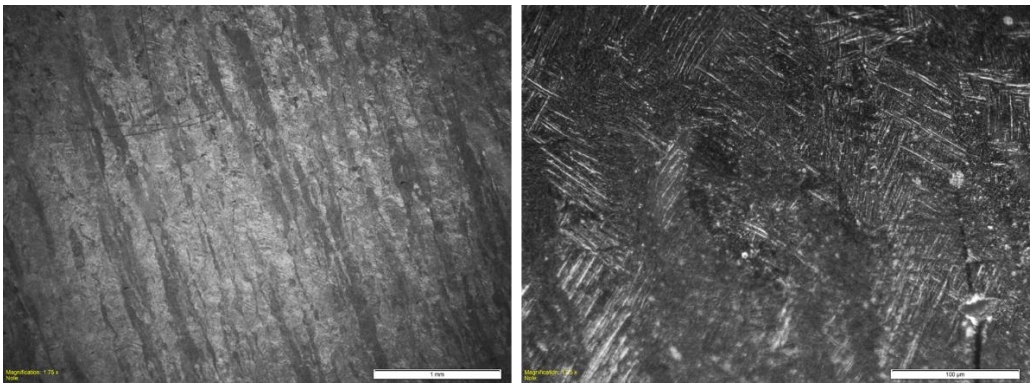

Figure 0-4. Large areas of dark regions visible in optical microscope images for TiAl-4

Five different etching strategies were employed and compared for PBF-LB Ti-6Al-4V.

Table 0-2. Ti6Al4V etchant test matrix.

Ti6Al4V- 1	3 drops. Dropping interval = 1 second.
Ti6Al4V- 2	3 drops. Dropping interval = 2 second.
Ti6Al4V- 3	5 drops. Dropping interval = 1 second.
Ti6Al4V- 4	Immerse for 10 seconds
Ti6Al4V- 5	Immerse for 20 seconds

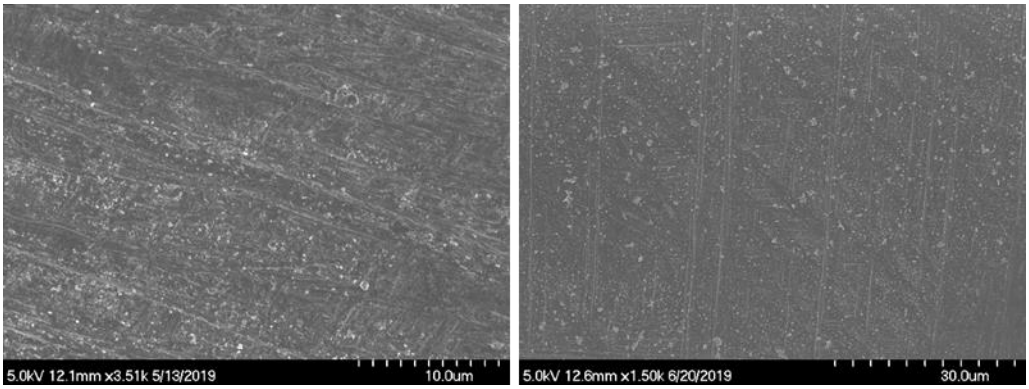

Figure 0-5. Sample Ti6Al4V- 1 revealed lamellar grain morphology, but not with a very obvious contrast, especially for the secondary lath grain between the thicker primary alpha grain.

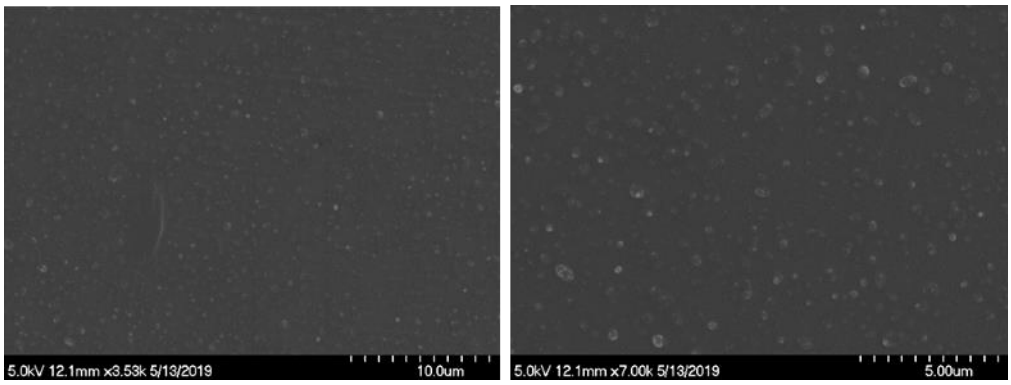

Figure 0-6. Sample 4 is hard to see clear features; the etching depth is very shallow.

The etching strategies for Sample 2, 3 and 5 have similar results: visible long and thin columnar grains formed during cooling from high temperature, elongated along 3D printing direction with obvious texture. The dark regions correspond to the α (HCP) phase and the light white region is the β (BCC) phase. Secondary α phase (smaller and thinner needle-shape martensite structure) forms in-between the primary α phase laths.

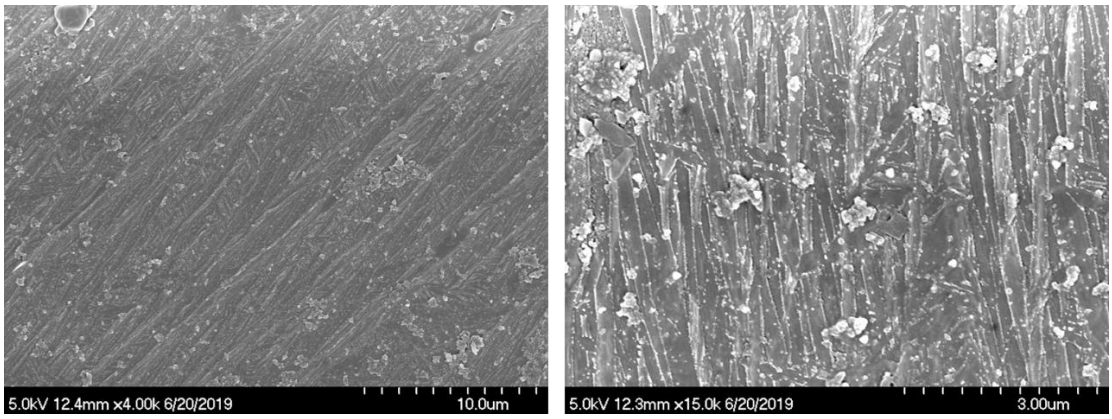

Figure 0-7. SEM image of Ti6Al4V- 2. 3 drops. Dropping interval = 2 second.

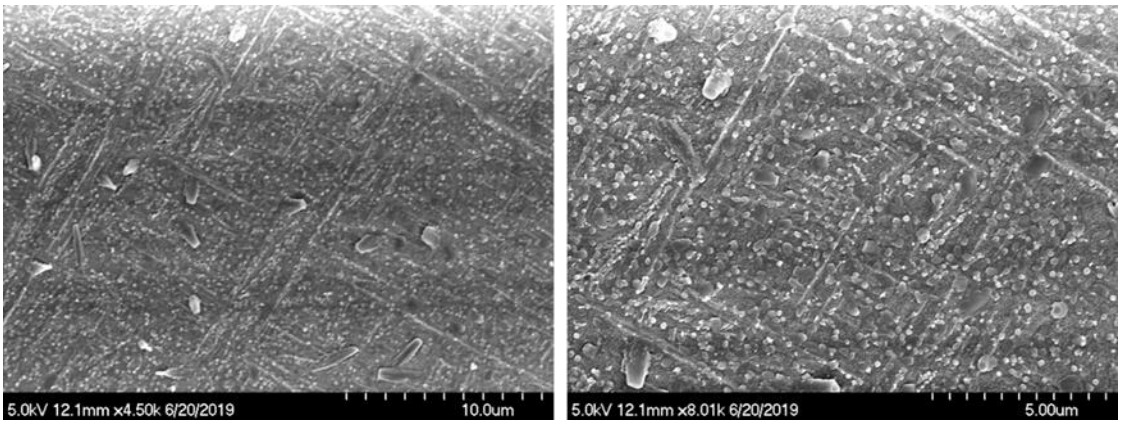

Figure 0-8. SEM image of Ti6Al4V- 5. Dip for 20 seconds

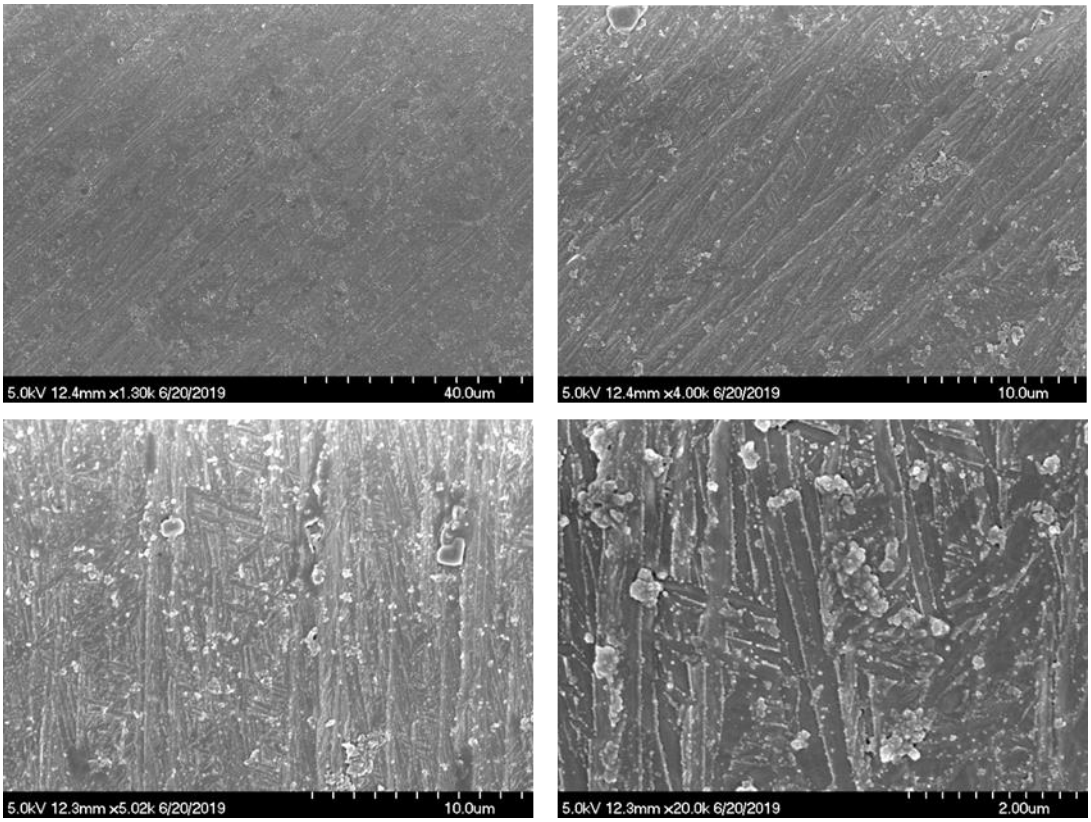

Figure 0-9. SEM images for Ti6Al4V- 3. 5 drops with a 1 second interval

Appendix B: Tensile and Fatigue test on PBF-LB Ti6Al-4V.

B1 Tensile test

The test was carried out on Instron-4467 (without extensometer), with the crosshead speed of 4.0 mm/min and the same speed after yield. The data points were recorded at the rate of 20 points per second. Table B1 shows the average testing result. A huge variation of elongation at fracture measurement was observed, varying from 2.3 to 4%, probably due to the build layout design or the powder freshness condition. The measured elastic modulus is about half the value compared to generally reported property. This test protocol provides reasonable material strength, but not accurate strain values due to the lack of an extensometer.

Table B1. Tensile testing result of PBF-LB Ti-6Al-4V from Instron-4467, without extensometer.

Ultimate Stress (MPa)	Stress at 0.2% (MPa)	Ultimate Strain (%)	Strain at fracture (%)	Young's Modulus (GPa)
1167.76	1033.53	3.028	3.557	48.6

B2 Fatigue test

The test was firstly set by $\pm 1.0\%$ strain, however, the sample break immediately after the first cycle. The fatigue test setting had to turn to a lower strain amplitude at $\pm 0.5\%$. At this strain range, as shown in Figure 20, the Ti-6Al-4V material does not reach the yield stage. The fatigue life was measured as 1108 cycles. The martensite softening phenomenon was observed, as the maximum tensile stress decreases from 545.3 MPa to 494.3 MPa at 1% strain during the last cycle of this test. Similar downwards of cyclic

strength were observed in Agius [106] work as the applied strain range became over ±1.5%, also in other fatigue behaviour of lath structure and martensite phase predominate metals such as P91 steel [146].

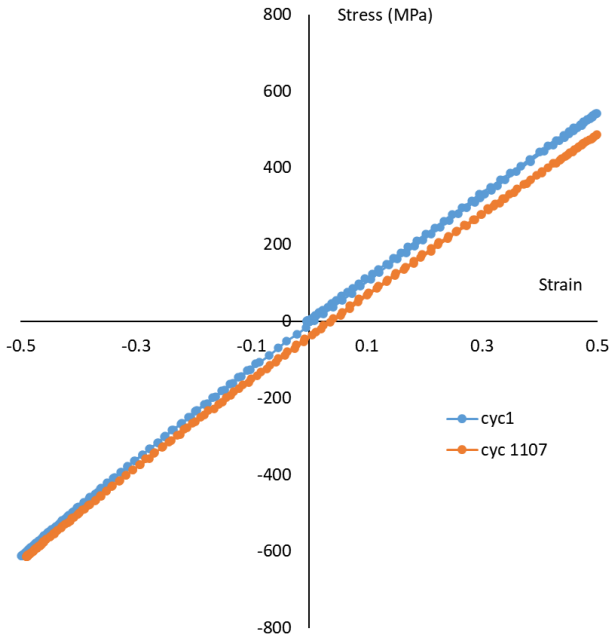

Figure 10-10. LCF test of as-build PBF Ti-6Al-4V, under a strain magnitude of ±0.5%.

Appendix C: Software and customized codes summary.

This appendix summarises the codes used or developed within this thesis.

Software	Custom codes written to extend function
Microstructure analysis	
MTEX (MATLAB plugin)	Ctf cleaning, cropping, non-indexed data filling. Grain reconstruction. Texture analysis. Parent phase prediction. Dislocation density measurement.
AzTec (Oxford Instrument)	N/A
Model construction and meshing	
DREAM3D	C++ plugin for EBSD conversion and C3D20 meshing capability. Convert inp to ctf, convert 3D mesh to 2D.
Neper	C++ Multi-VT, lamellar structure, voids.
Computational tool	
ABAQUS 2017	Python codes for post-processing (stress-strain, contour plot printing, SDV evolution, maximum/averaged value extraction). Grain boundary visualization. Batch job automatic manage.
MOOSE FRAMWORK	MATLAB codes for PFM exodus mesh to ABAQUS inp, and to ctf.
TensorFlow	Python for DNN optimization